Surficial Investigations of Hargraves Crater and Siloe Patera, Mars

by

Al Emran

A thesis submitted to the Graduate Faculty of
Auburn University
in partial fulfillment of the
requirements for the Degree of
Master of Science

Auburn, Alabama
August 03, 2019

Keywords: Mars, Impact Crater, Morphology, Thermophysics, Mineralogy

Copyright © 2019 by Al Emran

Approved by

Luke J. Marzen, Chair, Professor of Geosciences
David T. King Jr., Co-chair, Professor of Geosciences
Masatoshi Hirabayashi, Assistant Professor of Aerospace Engineering
Chadana Mitra, Associate Professor of Geosciences

Abstract

This study investigates Hargraves crater and Siloe Patera of Mars. Individual barchan and barchanoids dunes in Hargraves were almost accurately identified using a semi-automated object-based image analysis technique. The dunes have an effective grain-size of ~230 μm (fine sand) and are composed of a mixture of feldspar, olivine, pyroxene, and relatively lower bulk-silica phase. Having a debated geologic history of Siloe Patera, this study resolved the possible origin hypothesis. The feature has experienced multiple geologic processes; initially formed as an impact crater, followed by subsequent modification by fluvial activities and/or periglacial reworking and, then, followed by a major collapse event due to primarily cryospheric subsurface ice-removal resulting in melting of accumulated subsurface snow and ice deposits that formed boomerang lake and fresh shallow valley system in conjunction with possible effusive lava flow and volcanic heating. Later, the depression underwent glacial reworking and recent aeolian modification.

Acknowledgments

None of this work would have been accomplished without the advice, patience, and assistance of my advisors Dr. Luke J. Marzen and Dr. David T. King Jr. They have made a great contribution for their invaluable guidance during this study and for their kind help with information, ideas, and in providing me organizational support in completing this thesis. I am also thankful to two other committee members Dr. Masatoshi Hirabayashi (Aerospace Engineering) and Dr. Chandana Mitra (Geosciences). Special gratitude goes to my family members: parents (Nurul Islam and Mahmuda Khatun) and siblings (Asma Akter Sheuly, Mahbubul Alam, and Al Quium).

Next, I would like to thank the team members of 2001 Mars Odyssey, Mars Global Surveyor (MGS), and Mars Reconnaissance Orbiter (MRO) spacecraft missions for targeting, collecting, and archiving THEMIS, CRISM, TES, MOLA, MOC, CTX, and HiRISE datasets used in this study. JMARS, ISIS3, NASA Ames Stereo Pipelines (ASP), Davinci, GDAL, THMPROC, MARSTHERM, ENVI, ArcGIS, and QGIS software/tools were used for data processing and analysis. Special thanks to the team of Arizona State University (ASU)'s Mars Space Flight Facility. I am also grateful to Dr. Bethany L. Ehlmann (CalTech), Dr. Raymond E. Arvidson (Washington University in St. Louis), Dr. Mark R. Salvatore (Northern Arizona University), Dr. Amber Gullikson (USGS), and Dr. Joshua L. Bandfield (Space Science Institute) for providing useful information on data processing.

Lastly, I am grateful to the entirety of the faculty and staff in the Department of Geosciences at Auburn University and other people who helped me directly and indirectly to complete this thesis.

Table of Contents

List of Tables

List of Figures

List of Abbreviations

ASP	Ames Stereo Pipeline
ASU	Arizona State University
ATI	Apparent Thermal Inertia
AU	Astronomical Unit
CCD	Charged Coupled Device
CRISM	Compact Reconnaissance Imaging Spectrometer for Mars
CTX	Context Camera
DCS	Decorrelation Stretch
DEM	Digital Elevation Models
DN	Digital Number
EM	Electromagnetic Radiation
ESA	European Space Agency
FoV	Field of View
HiRISE	High Resolution Imaging Science Experiment
HRL	Half Resolution Long
HRS	Half Resolution Short
HRSC	High Rise Stereo Camera
ISIS	Integrated Software for Imagers and Spectrometers
ISRO	Indian Space Research Organization
MEx	Mars Expresses

MGS	Mars Global Surveyor
MOC	Mars Orbiter Camera
MOLA	Mars Orbiter Laser Altimeter
MRO	Mars Reconnaissance Orbiter
MSP	Multi-spectral Survey Products
MTRDR	Map-projected Targeted Reduced Data Record
NASA	National Aeronautics and Space Administration
NIR	Near-Infrared
NW	North West
OMEGA	The Observatoire pour la Minéralogie, l'Eau, les Glaces et l'Activité
PDS	Planetary Data System
POLA	Polar Stereographic
RDR	Reduced Data Record
SIMP	Simple Cylindrical
SINU	Sinusoidal Equal Area
SWIR	Shortwave Infrared
TES	Thermal Emission Spectrometer
THEMIS	Thermal Emission Imaging System
TI	Thermal Inertia
TRDR	Targeted Reduced Data Records
USGS	United States Geological Survey
VIS	Visible
VISALB	Visible Albedo
VNIR	Visible Near-Infrared

Chapter 1: Introduction

Mars is a terrestrial planet (second-smallest) in the solar system. It is the fourth planet from the Sun. Iron oxide is rife on the surface of Mars, and therefore it is rightly called the 'Red Planet'. Mars is the planet, besides Earth, that has attracted the highest level of human curiosity, not only because it has similar characteristics of the Earth such as eccentricity, orbital inclination, seasonality, and some Earth-like geomorphology (e.g., Carr, 1980; Faure and Mensing, 2008; Barlow, 2008), but because Mars was thought for a long time to harbor an alien civilization (Hoyt, 1976). The planet has undergone different geological processes and modifications over time such as impact cratering, volcanism, fluvial, aeolian activities, etc. The imprints of these geological processes are present on the martian surface as evident from morphology and mineralogy extracted from the remote sensing data of different spacecraft missions. Determining the relationship between different exposed units and stratigraphy allows an analyst to reconstruct the geological and environmental history (as well as the processes involved in shaping the surface) of Mars (Golder, 2013). The presence of sinuous channels, large outflow channels, and shorelines (oceanic or lacustrine) suggest that the planet has substantially experienced periods with large quantities of surface water (e.g., Carr, 1979; Carr, 1996; Head et al., 1999; Carr and Head, 2003; Irwin et al., 2004; Fassett and Head, 2008). The martian geological timescales are divided into three major epochs: the Noachian, the Hesperian, and the Amazonian (e.g., Hartmann and Neukum, 2001; Nimmo and Tanaka, 2005). These epochs have their distinctive characteristics in terms of dominant geological processes involved and their absolute ages are determined from crater counting or superposition techniques (e.g., Tanaka et al., 1992). The Noachian surfaces are the basement materials of the rugged and heavily cratered surface.

The Hesperian surfaces involve the base of the ridged materials whereas the Amazonian surfaces are smooth moderately cratered plain materials and polar deposits (e.g., Scott and Carr, 1978; Tanaka, 1986; Tanaka et al., 1992).

Studying Mars adds to the knowledge about the earlier history of the solar system. The surface of Mars is the blueprint of its earlier history. Mars has been a major spacecraft destination since the early days of space exploration (Barlow, 2008). Mars has formed during the same time (~4.56 Ga) as the solar system (e.g., Carr, 1980; Faure and Mensing, 2008). Like other terrestrial planets, e.g., Earth, Mars has gone through three formation stages: formation of kilometer-sized planetesimals, the formation of planetary embryos, and collisional formation of larger planets (e.g., Canup and Agnor, 2000; Chambers, 2004). The ongoing space mission investigation and future exploration are focused on assessing whether Mars had harbored any kind of life form as well as will it support life forms in future (e.g., MER, 2013; Jarrel, 2015). Study of Mars demands details on thermophysical, morphological, stratigraphic, and mineralogical characterization. Combining morphological, thermophysical, and mineralogical information allows ascertaining promises on landforms and climate of early Mars. Over the past few decades, the surface of Mars has been studied using information from orbital spacecraft, telescopes, and *in-situ* lander and rovers. However, orbital spacecraft datasets are the most used data covering the planet at global scales. Moreover, orbital data are the reconnaissance information for the future manned missions or rover missions (e.g., Mars 2020) to the surface of Mars. The characterizations of the martian surfaces are accomplished using orbital data of visible (VIS), near-infrared (NIR), shortwave infrared (SWIR), and thermal infrared (TIR) data. The prominent sensors for deriving these orbital data are the most recent mission of the Mars Reconnaissance Orbiter (MRO) mission on boards the High Resolution Imaging Science Experiment (HiRISE; McEwen et al., 2007), the Context Camera (CTX; Malin et al., 2007), and the

Compact Reconnaissance Imaging Spectrometer for Mars (CRISM; Murchie et al., 2007) instruments. The European Space Agency (ESA) operated the Mars Express (MEx) mission which carried the instruments of the High Rise Stereo Camera (HRSC; Neukum et al., 2004) and The Observatoire pour la Minéralogie, l'Eau, les Glaces et l'Activité (OMEGA; Bibring et al., 2004). The 2001 Mars Odyssey mission on boards The Thermal Emission Imaging System (THEMIS; Christensen et al., 2004) whereas the Mars Global Surveyor (MGS) mission carried the instrument payloads the Thermal Emission Spectrometer (TES; Christensen et al., 2001), the Mars Orbiter Camera (MOC), and the Mars Orbiter Laser Altimeter (MOLA; Smith et al., 2001). In this research, orbital datasets were used for characterizing the surficial geology of different parts of Mars e.g., Siloe Patera in Arabia Terra and Hargraves crater in Nili Fossae area.

On Mars, few areas received substantial attention for the future exploration of the rover and manned missions because of their astrobiological significances. The region of Northwest Isidis, hereafter NW Isidis, is one of the prominent interests in planetary exploration. NW Isidis area of the planet has been extensively studied area over the past decades (e.g., Salvatore et al., 2018). Jezero crater, the final site for Mars 2020 rover mission, is in the NW Isidis region (Goudge et al., 2017). The area includes the Nili Fossae which is a suite of grabens (Salvatore et al., 2018 and references therein). The Nili Fossae is hypothesized to have been formed from the result of crustal fracture associated with the nearby Isidis basin formation (e.g., Wichman and Schultz, 1989; Schultz and Frey, 1990). Jezero crater has a diameter of ~45 km which hosts two inlet channels of deltaic remnants with an outlet channel, and contains hydrated minerals i.e., phyllosilicates and carbonates (e.g., Fassett and Head, 2005; Ehlmann et al., 2008; Ehlmann et al., 2009; Schon et al., 2012; Goudge et al., 2015). An approximately 2,500 km^2 area is named as North Eastern Syrtis, hereafter NE Syrtis, located just south of the Jezero crater. NE Syrtis area has a wide mineralogical diversity as identified

from the spectroscopic information of visible and near-infrared (VNIR) data (e.g., Mangold et al., 2007; Mustard et al., 2009; Ehlmann and Mustard, 2012; Quinn and Ehlmann, 2014; Bramble et al., 2017; Salvatore et al., 2018). One of the study areas of the present research i.e., Hargraves crater is in the Nili Fossae region of NW Isidis (Fig. 1.1). Hargraves crater is home to a dune field of barchan and barchanoids dunes as seen with visible images. The Mars Global Digital Dune Database (MGD^3) (e.g., Hayward et al., 2007; Hayward et al., 2014) delineated the dune fields at Hargraves crater but did not include individual dunes and their geometry and morphologies. The delineation of dune fields in MGD^3 was manually prepared through visual photo-interpretation from the THEMIS imagery at 100 m/pixel spatial resolution, including digitized dune parameters and mapped dune slipface orientations. However, the manual digitizing of the dune parameters from low-resolution THEMIS images is a very tedious and time-consuming task. Moreover, the outline of the dune field delineated by MGD^3 is not accurate as seen from the higher resolution data (the details and maps are given in the corresponding chapter). Thus, an auto/semi-automated method with higher resolution images e.g., CTX at ~6 m/pixel are more efficient in the extraction of maximum important morphological information of the martian dune fields. The present study employs a semi-automated object-based image analysis (OBIA) technique to extract dunes at Hargraves crater as a test case of OBIA application and validation. A validated and accurate result renders the applicability of the OBIA method on the entire surface of Mars. Besides identifying dunes, the study analyzes the thermal infrared (TIR) spectral responses of the surface dune materials for characterizing the constituent materials of the dune field. The project has been titled *"Semi-Automated Identification and Thermal Infrared Response of Dunes Materials at Hargraves Crater, Mars"*.

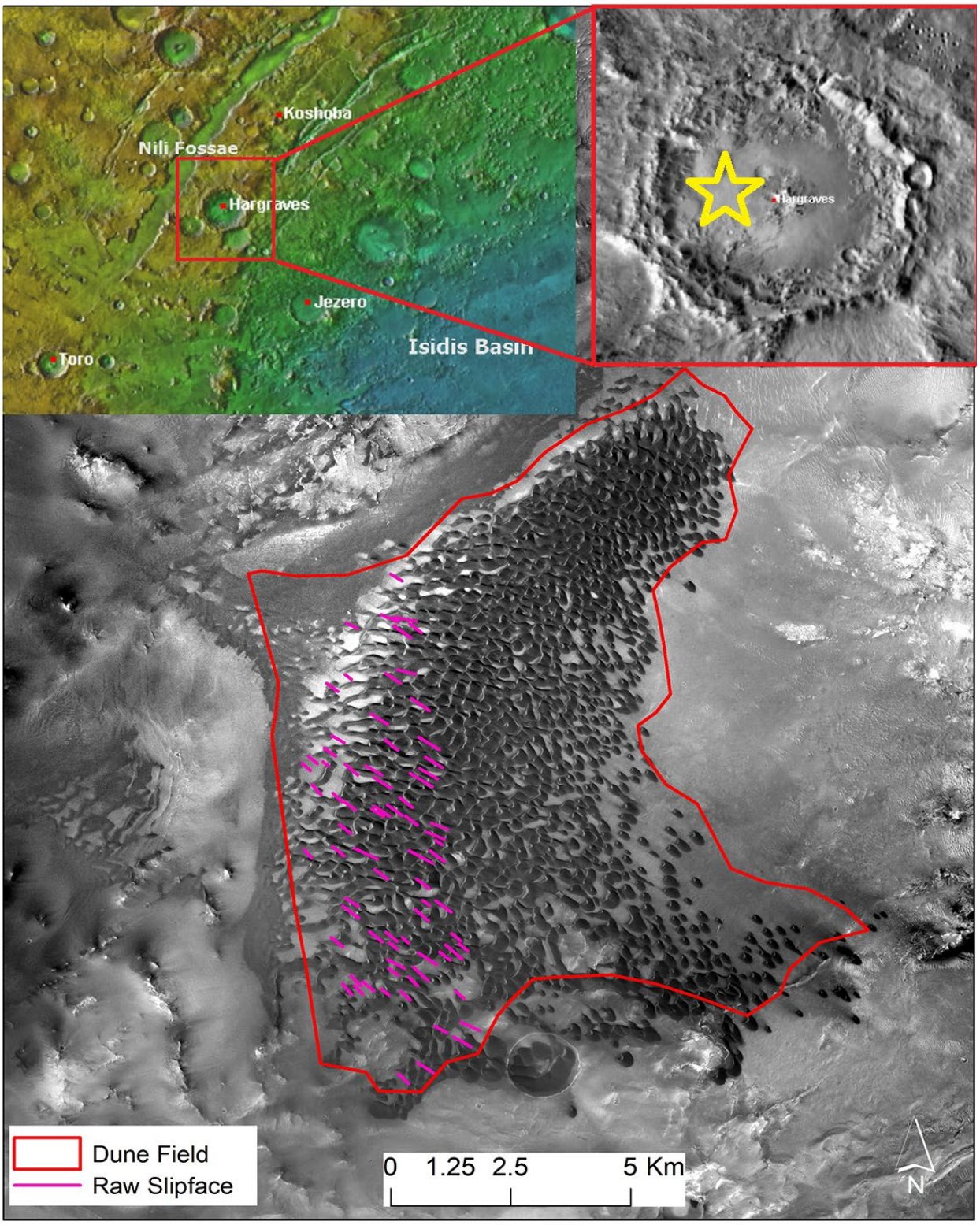

Fig. 1.1: The location of the Hargraves crater is on the east side of the Nili Fossae Trough (NFT) and northwest of the Isidis Basin. The dune field in CTX image resolution, inset the reference map (the yellow star is the location of dune inside the crater). The red outline is the dune field boundary and magenta transect are the raw slipface as defined by MGD[3].

The second project is aimed at resolving the disputed geological history of Siloe Patera in the Arabia Terra region. Siloe Patera is in heavily cratered Arabia Terra region and has a debated geological history. The abundance of layered ejecta suggests that the region has been developed through explosive volcanism. However, the absence of nearby source vents for repeated eruptions, necessary for layered ejecta formation, suggests an alternative explanation of the presence of possible supervolcano complexes in the region (Michalski and Bleacher, 2013). The existing study of Michalski and Bleacher (2013) suggested seven irregularly shaped volcanic constructs or supervolcanic caldera complexes including Siloe Patera, Eden Patera, etc. Siloe Patera has a set of nested craters that resemble an impact crater like other typical craters on the entire martian surface or other planetary bodies (Fig. 1.2). However, absence of direct evidence of impact ejecta around its structure, and the absence of a central uplift and a raised or overturned rim do not support the impact crater origin (details of the geological characteristics of the study area are given in the corresponding chapter). Siloe Patera has a confused geologic history among planetary researchers; whether it was formed as an impact crater versus supervolcano caldera (Fig. 1.3). This study, therefore, aimed at resolving these issues from the analyses of thermal infrared (TIR) and near-infrared (NIR) data. Having the specific sensitivity of TIR and NIR spectra in analyzing the martian surface, utilizing a single dataset may mislead the conclusion. Simultaneous use of NIR and TIR data can render a robust and complete scenario of Siloe Patera. The study result reveals the geological history of Siloe Patera and more broadly the north-eastern part of Arabia Terra region. The project is titled *"NIR-TIR Spectral Investigations of Siloe Patera on Arabia Terra, Mars"*.

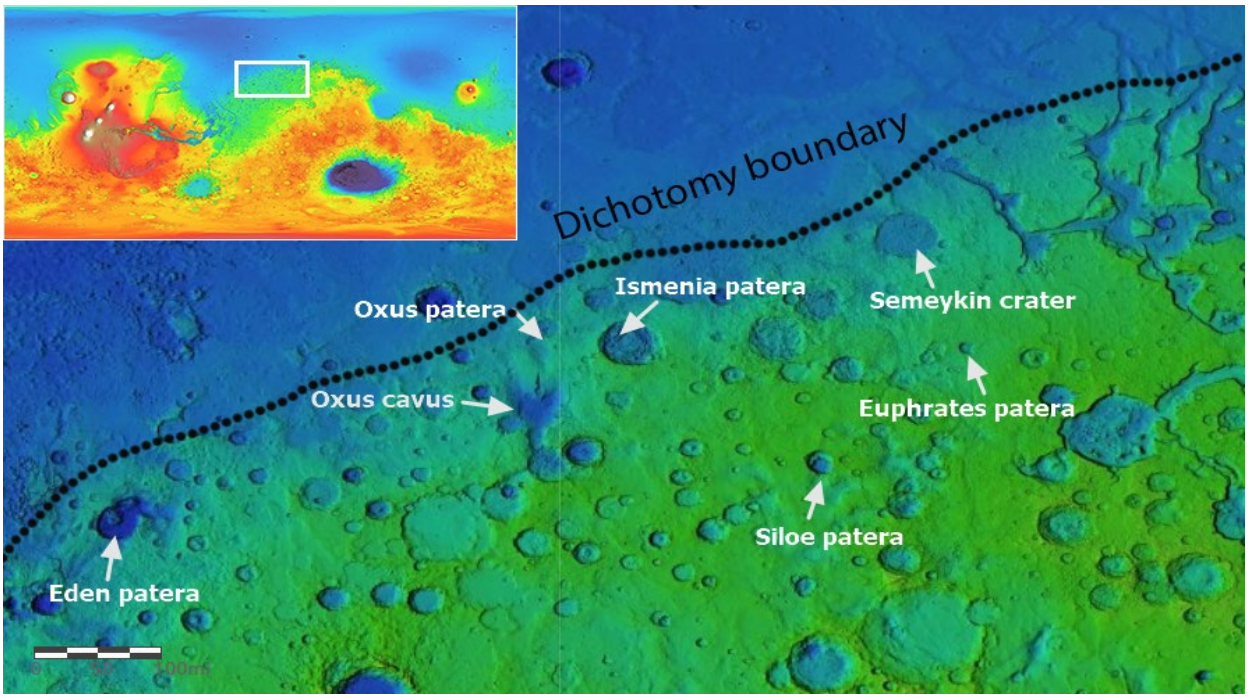

Fig. 1.2: Context map of HRSC colorized elevation overlain on THEMIS daytime IR image mosaic showing seven calderas in northwestern Arabia Terra, Mars. Inset is the MOLA colorized global elevation map of Mars showing the context of the northern Arabia Terra indicated in a white rectangular box. The seven calderas, namely Eden Patera, Oxus Patera, Oxus Cavus, Ismenia Patera, Siloe Patera, Euphrates Patera, and Semeykin crater, are indicated by the white arrows. The dichotomy boundary is outlined as a black dashed line that separates northern lowland to the southern highland.

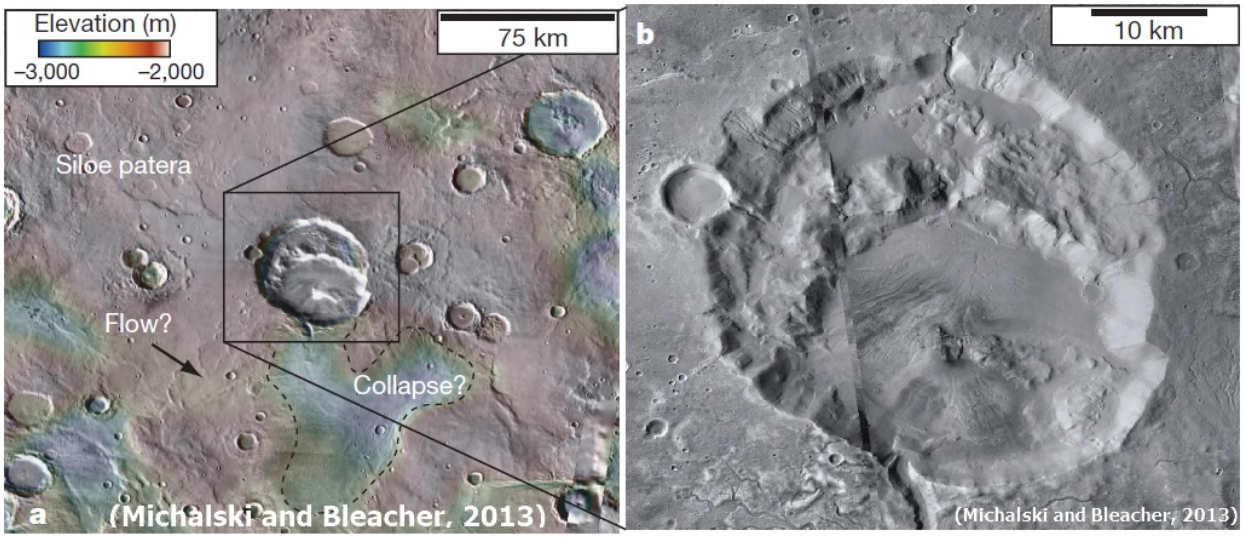

Fig. 1.3: Context map showing the morphology of Siloe Patera. a) MOLA topographic data overlain on CTX images showing the morphologies. The black rectangle outlines the area of interest. b) Mosaic produced using CTX grayscale observations, corresponding to the black rectangle in (a). The figures were adopted from Michalski and Bleacher (2013).

1.1. Research objectives

Since the study is comprised of two different projects in two different areas, the objectives of the study are also divided into two different sections:

1.1.1 Semi-Automated Identification and Thermal Infrared Response of Dune Materials at Hargraves Crater, Mars

a) Delineating individual dunes using a semi-automated object-based image analysis technique in a quick and accurate fashion.

b) Validating the objected based image analysis method for further investigation on the martian studies.

c) Updating existing the Mars digital dune database (MGD^3) for a more detailed understanding of the martian surface and its atmospheric mechanisms at the local scale.

d) Identifying the grain-size distribution of constituent dune materials from the thermal inertia measurements.

e) Explaining compositional (e.g., mineral abundances and bulk-silica content) characteristics of the dune materials and inferring the source provenance of the dune materials.

1.1.2 NIR-TIR Spectral Investigations of Siloe Patera on Arabia Terra, Mars

a) Interpreting surficial geology of Siloe Patera at Arabia Terra from visible and near-infrared (VNIR) and thermal infrared (TIR) data.

b) Resolving, in specific, the debated geological history of Siloe Patera and broadly the history of northeastern Arabia Terra.

c) Determining the thermal inferred (TIR) spectral units and their characteristics in the study areas for the analyzing surface geology.

d) Analyzing mineral composition and bulk-silica content of the surface materials to come up with geological history.

1.2. Significance of the study

Applying the relatively newer approach of object-based image analysis for identifying dune features at Hargraves crater is the main significance of the first project. Since the existing dune database was prepared from the lower resolution THEMIS images through manual photo interpretation and, therefore, is less detailed and less accurate (as seen from higher resolution data), and more time demanding in dune parameters identification. This research uses a newer method of object-based image analysis technique with higher resolution CTX dataset aiming to lessen effort in dune identification and to render more detailed information about dune parameters. The project makes a new database for the dunes and their geometric parameters at Hargraves which (the same method) can be applied on the entire martian surface to produce a more detailed dune database at the global scale. The study also determines the grain-size distribution of the dune materials at Hargraves crater. The grain-size distribution of dune materials helps in characterizing sedimentary environment present and understanding the sediment transport dynamics of an area. Finally, the study identifies the mineral composition of the dune materials for understanding mineral distribution in constituent dune materials at Hargraves crater. Identification of mineral composition helps to constrain the evolution, history, and sources of sediment supply for a dune field. Combining all these analyses help to characterize the nature of the dune field and source of constituent dune materials at a local scale.

The key significance of the second project is to resolve the debated geological history of Siloe Patera. Determining the surface materials characteristics helps to understand the geological history of an area. The present research constrains the characteristics of surface materials in the study area by combining the investigations of spectral units, bulk-silica content, colorized nighttime IR overlain daytime IR mosaic, and thermal inertia characteristics. The information for these analyses was derived from the thermal-infrared (TIR) images from the Thermal Emission Imaging System (THEMIS) sensor. Minerals are blueprints of past surface processes, environment, and climate, and therefore, identifying minerals provides insight about the geological history. In this study, a mineral index map from near-infrared (NIR) data of the Compact Reconnaissance Imaging Spectrometer for Mars (CRISM) image was used to identify mineralogy of surficial materials at Siloe Patera. Combining the analysis of the findings resolve the debated geological history of Siloe Patera; providing evidence on whether it is an impact crater verses supervolcanic caldera or any other probable origin and its subsequent geologic processes responsible for the formation, evolution, and modifications. The results help not only to determine the geologic history of Siloe Patera but also gives an idea of the geologic history of the broader Arabia Terra region.

References

Barlow, N., 2008. Mars: An Introduction to its Interior, Surface and Atmosphere. Cambridge University Press, Cambridge: UK. ISBN 978-0-521-85226-5.

Bibring, J.-P., A. Soufflot, M. Berthé, Y. Langevin, B. Gondet, P. Drossart, M. Bouyé, et al., 2004. OMEGA: Observatoire Pour La Minéralogie, l'Eau, Les Glaces et l'Activité. In Mars Express - The Scientific Payload, European Space Agency Special Publication, SP-1240, edited, pp. 37-49, ESA. http://adsabs.harvard.edu/abs/2004ESASP1240...37B.

Bramble, Michael S., John F. Mustard, and Mark R. Salvatore., 2017. The Geological History of Northeast Syrtis Major, Mars. Icarus 293 (Supplement C):66–93. https://doi.org/10.1016/j.icarus.2017.03.030.

Canup, R.M. and C.B. Agnor., 2000. Accretion of the terrestrial planets and the Earth–Moon system. In Origin of the Earth and Moon, edt. R.M. Canup and K. Righter. Tucson, AZ: University of Arizona Press.

Carr, M.H., 1980. The Morphology of the Martian Surface. Space Science Review 25 (3): 231-284 https://doi.org/10.1007/BF00221929

Carr, M.H., 2012. Formation of Martian flood features by release of water from confined aquifers. Journal of Geophysical Research: Solid Earth 2995–3007. https://doi.org/10.1029/JB084iB06p02995@10.1002/(ISSN)2169-9356.MARSVOL1

Carr, M.H., Head, J.W., 2003. Oceans on Mars: An assessment of the observational evidence and possible fate. Journal of Geophysical Research: Planets 108. https://doi.org/10.1029/2002JE001963

Chambers, John E., 2004. Planetary Accretion in the Inner Solar System. Earth and Planetary Science Letters 223 (3):241–52. https://doi.org/10.1016/j.epsl.2004.04.031.

Christensen, P.R., Bandfield, J.L., Hamilton, V.E., Ruff, S.W., Kieffer, H.H., Titus, T.N., Malin, M.C., Morris, R.V., Lane, M.D., Clark, R.L., Jakosky, B.M., Mellon, M.T., Pearl, J.C., Conrath, B.J., Smith, M.D., Clancy, R.T., Kuzmin, R.O., Roush, T., Mehall, G.L., Gorelick, N., Bender, K., Murray, K., Dason, S., Greene, E., Silverman, S., Greenfield, M., 2001. Mars Global Surveyor Thermal Emission Spectrometer experiment: Investigation description and surface science results. Journal of Geophysical Research: Planets 106, 23823–23871. https://doi.org/10.1029/2000JE001370

Christensen, P.R., Jakosky, B.M., Kieffer, H.H., Malin, M.C., McSween, H.Y., Nealson, K., Mehall, G.L., Silverman, S.H., Ferry, S., Caplinger, M., Ravine, M., 2004. The Thermal Emission Imaging System (THEMIS) for the Mars 2001 Odyssey Mission. Space Science Reviews 110, 85–130. https://doi.org/10.1023/B:SPAC.0000021008.16305.94

Ehlmann, Bethany L., and John F. Mustard., 2012. An In-Situ Record of Major Environmental Transitions on Early Mars at Northeast Syrtis Major. Geophysical Research Letters 39 (11):L11202. https://doi.org/10.1029/2012GL051594

Ehlmann, Bethany L., John F. Mustard, Caleb I. Fassett, Samuel C. Schon, James W. Head III, David J. Des Marais, John A. Grant, and Scott L. Murchie., 2008. Clay Minerals in Delta Deposits and Organic Preservation Potential on Mars. Nature Geoscience 1 (6):ngeo207. https://doi.org/10.1038/ngeo207.

Ehlmann, Bethany L., John F. Mustard, Gregg A. Swayze, Roger N. Clark, Janice L. Bishop, Francois Poulet, David J. Des Marais, et al., 2009. Identification of Hydrated Silicate Minerals on Mars Using MRO-CRISM: Geologic Context near Nili Fossae and Implications for Aqueous Alteration. Journal of Geophysical Research: Planets 114 (E2):E00D08. https://doi.org/10.1029/2009JE003339.

Fassett, C.I., Head, J.W., 2008. Valley network-fed, open-basin lakes on Mars: Distribution and implications for Noachian surface and subsurface hydrology. Icarus 198, 37–56. https://doi.org/10.1016/j.icarus.2008.06.016

Fassett, Caleb I., and James W. Head., 2005. Fluvial Sedimentary Deposits on Mars: Ancient Deltas in a Crater Lake in the Nili Fossae Region. Geophysical Research Letters 32 (14):L14201. https://doi.org/10.1029/2005GL023456.

Faure, G and T.M. Mensing., 2008. Introduction to Planetary Science: The Geological Prspective. Springer Netherlands. doi 10.1007/978-1-4020-5544-7

Golder, K., 2013. Geomorphology of Eridania Basin, Mars: A Study of the Evolution of Chaotic Terrain and a Paleolake. Masters Theses. Wesleyan University, Connecticut, USA.

Goudge, T.A., Milliken, R.E., Head, J.W., Mustard, J.F., Fassett, C.I., 2017. Sedimentological evidence for a deltaic origin of the western fan deposit in Jezero crater, Mars and implications for future exploration. Earth and Planetary Science Letters 458, 357–365. https://doi.org/10.1016/j.epsl.2016.10.056

Goudge, Timothy A., John F. Mustard, James W. Head, Caleb I. Fassett, and Sandra M. Wiseman., 2015b. Assessing the Mineralogy of the Watershed and Fan Deposits of the Jezero Crater Paleolake System, Mars. Journal of Geophysical Research: Planets 120 (4):2014JE004782. https://doi.org/10.1002/2014JE004782.

Hartmann, W.K., Neukum, G., 2001. Cratering Chronology and the Evolution of Mars. Space Science Reviews 96, 165–194. https://doi.org/10.1023/A:1011945222010

Hayward, R.K., Fenton, L., Titus, T.N., 2014. Mars Global Digital Dune Database (MGD3): Global dune distribution and wind pattern observations. Icarus 230, 9. https://doi.org/10.1016/j.icarus.2013.04.011

Hayward, R.K., Mullins, K.F., Fenton, L.K., Hare, T.M., Titus, T.N., Bourke, M.C., Colaprete, A., Christensen, P.R., 2007. Mars global digital dune database and initial science results. Journal of Geophysical Research E: Planets 112. https://doi.org/10.1029/2007JE002943

Head, J.W., Hiesinger, H., Ivanov, M.A., Kreslavsky, M.A., Pratt, S., Thomson, B.J., 1999. Possible Ancient Oceans on Mars: Evidence from Mars Orbiter Laser Altimeter Data. Science 286, 2134–2137. https://doi.org/10.1126/science.286.5447.2134

Hoyt, W.G., Wesley, W.G., 1977. Lowell and Mars. American Journal of Physics 45, 316–317. https://doi.org/10.1119/1.10630

Irwin, R.P., Howard, A.D., Maxwell, T.A., 2004. Geomorphology of Ma'adim Vallis, Mars, and associated paleolake basins. Journal of Geophysical Research: Planets 109. https://doi.org/10.1029/2004JE002287

Jarell, Elizabeth M .2015. Using Curiosity to Search for Life. Mars Daily. Last Accessed October 25, 2017. http://www.marsdaily.com/reports/Using_Curiosity_to_Search_for_Life_999.html.

Mangold, N., Poulet, F., Mustard, J.F., Bibring, J.-P., Gondet, B., Langevin, Y., Ansan, V., Masson, P., Fassett, C., Head, J.W., Hoffmann, H., Neukum, G., 2007. Mineralogy of the Nili Fossae region with OMEGA/Mars Express data: 2. Aqueous alteration of the crust. Journal of Geophysical Research: Planets 112. https://doi.org/10.1029/2006JE002835

McEwen, A.S., Eliason, E.M., Bergstrom, J.W., Bridges, N.T., Hansen, C.J., Delamere, W.A., Grant, J.A., Gulick, V.C., Herkenhoff, K.E., Keszthelyi, L., Kirk, R.L., Mellon, M.T., Squyres, S.W., Thomas, N., Weitz, C.M., 2007. Mars Reconnaissance Orbiter's High Resolution Imaging Science Experiment (HiRISE). Journal of Geophysical Research: Planets 112. https://doi.org/10.1029/2005JE002605

Mellon, M.T., Jakosky, B.M., Kieffer, H.H., Christensen, P.R., 2000. High-Resolution Thermal Inertia Mapping from the Mars Global Surveyor Thermal Emission Spectrometer. Icarus 148, 437–455. https://doi.org/10.1006/icar.2000.6503

MER., 2013. The Mars Exploration Rover Mission. NASA Report. November 2013, 20. Last Accessed October 25, 2017. https://mars.nasa.gov/mer/home/resources/MERLithograph.pdf

Michalski, J.R., Bleacher, J.E., 2013. Supervolcanoes within an ancient volcanic province in Arabia Terra, Mars. Nature 502, 47–52. https://doi.org/10.1038/nature12482

Murchie, S., Arvidson, R., Bedini, P., Beisser, K., Bibring, J.-P., Bishop, J., Boldt, J., Cavender, P., Choo, T., Clancy, R.T., Darlington, E.H., Marais, D.D., Espiritu, R., Fort, D., Green, R., Guinness, E., Hayes, J., Hash, C., Heffernan, K., Hemmler, J., Heyler, G., Humm, D., Hutcheson, J., Izenberg, N., Lee, R., Lees, J., Lohr, D., Malaret, E., Martin, T., McGovern, J.A., McGuire, P., Morris, R., Mustard, J., Pelkey, S., Rhodes, E., Robinson, M., Roush, T., Schaefer, E., Seagrave, G., Seelos, F., Silverglate, P., Slavney, S., Smith, M., Shyong, W.-J., Strohbehn, K., Taylor, H., Thompson, P., Tossman, B., Wirzburger, M., Wolff, M., 2007. Compact Reconnaissance Imaging Spectrometer for Mars (CRISM) on Mars Reconnaissance Orbiter (MRO). Journal of Geophysical Research: Planets 112. https://doi.org/10.1029/2006JE002682

Mustard, J. F., B. L. Ehlmann, S. L. Murchie, F. Poulet, N. Mangold, J. W. Head, J.-P. Bibring, and L. H. Roach., 2009. Composition, Morphology, and Stratigraphy of Noachian Crust around the Isidis Basin. Journal of Geophysical Research: Planets 114 (E2):E00D12. https://doi.org/10.1029/2009JE003349.

Neukum, G., R. Jaumann, HRSC Co-Investigator and Experiment Team., 2004. HRSC: The High-Resolution Stereo Camera of Mars Express. In A. Wilson (Ed.), Mars Express: The Scientific Payload, ESA, Noordwijk, The Netherlands (2004), pp. 17-35.

Nimmo, F., Tanaka, K., 2005. Early Crustal Evolution of Mars. Annual Review of Earth and Planetary Sciences 33, 133–161. https://doi.org/10.1146/annurev.earth.33.092203.122637

Quinn, D. P., and B. L. Ehlmann., 2014. Structural Constraints on the Origin of the Sulfate-Bearing Unit at Northeast Syrtis Major. In 8th International Conference on Mars, held July 14-18, 2014 in Pasadena, California. LPI Contribution No. 1791 (1437). http://adsabs.harvard.edu/abs/2014LPICo1791.1437Q.

Salvatore, M.R., Goudge, T.A., Bramble, M.S., Edwards, C.S., Bandfield, J.L., Amador, E.S., Mustard, J.F., Christensen, P.R., 2018. Bulk mineralogy of the NE Syrtis and Jezero crater regions of Mars derived through thermal infrared spectral analyses. Icarus 301, 76–96. https://doi.org/10.1016/j.icarus.2017.09.019

Schon, Samuel C., James W. Head, and Caleb I. Fassett., 2012. An Overfilled Lacustrine System and Progradational Delta in Jezero Crater, Mars: Implications for Noachian Climate. Planetary and Space Science 67 (1):28–45. https://doi.org/10.1016/j.pss.2012.02.003.

Schultz, Richard A., and Herbert V. Frey., 1990. A New Survey of Multiring Impact Basins on Mars. Journal of Geophysical Research: Solid Earth 95 (B9):14175–89.

Scott, D.H., and Carr, M.H., (1978) Geologic map of Mars. USGS Miscellaneous Investigations Series, Map I-1083. https://www.usgs.gov/media/images/geologic-map-mars (accessed 4.11.19).

Smith, David E., Maria T. Zuber, Herbert V. Frey, James B. Garvin, James W. Head, Duane O. Muhleman, Gordon H. Pettengill, et al., 2001. Mars Orbiter Laser Altimeter: Experiment Summary after the First Year of Global Mapping of Mars. Journal of Geophysical Research: Planets 106 (E10): 23689–722. https://doi.org/10.1029/2000JE001364.

Tanaka, K.L., 1986. The stratigraphy of Mars. Proceedings of Lunar Planetary Science Conference, 17th, Part 1. Journal of Geophysical Research, 91, supplemental, E139-E158.
Tanaka, K.L., Scott, D.H., Greeley, R., 1992. Global Stratigraphy. Mars, edited by H.H. Hieffer et al., pp. 345-382, University of Arizona Press, Tuscon.
Wichman, R.W., Schultz, P.H., 1989. Sequence and mechanisms of deformation around the Hellas and Isidis Impact Basins on Mars. Journal of Geophysical Research 94, 17333. https://doi.org/10.1029/JB094iB12p17333

Chapter 2: Literature Review

2.1: Introduction

Mars is a terrestrial planet in the inner solar system. The planet has some Earth-like geomorphology (e.g., Carr, 1980; Barlow, 2008; Faure and Mensing, 2008). In addition, like Earth, it has an atmosphere though very tenuous with 95% of CO_2 and other trace gases with a surface temperature minimum of -123°C to the maximum -33°C (e.g., Carr, 2007). Over time the planet has been studied through many space exploration missions (Barlow, 2008) with a goal of finding organic lifeform. Is another planet conducive for sustaining life forms? This question has long been, even today, a mystery. However, the planet Mars is the best bet for resolving that mystery since it has many Earth-like geomorphologies and an atmosphere. The surface of Mars is the blueprint of its past environment, whether it had sustained or will embrace life form in the future. Water is thought to have flowed on the surface of the planet around 3.8 Ga ago or before as evident from the presence of valley and valley networks (e.g., Carr and Head, 2010). The history of Mars is allied with the formation of the solar system as it is thought to have formed around the same time of solar system formation ~4.5 Ga ago (e.g., Carr, 1980; Faure and Mensing, 2008). The formation history of Mars is consistent with other terrestrial planets and has gone through different planet formation mechanisms (e.g., Canup and Agnor, 2000; Chambers, 2004). Mars is approximately half of the diameter of Earth and the surface is broadly divided into two regions: the southern highland and northern lowland (Fig. 2.1a). The southern highland is highly cratered and pitted in comparison to the northern lowland. The northern lowland is thought to the home of an ancient sea with relatively few impact craters visible. The two regions have an elevation difference about 1 to 3 km. Because of

these observed differences in topography and geology, there is a dichotomy between the northern lowland and southern highland. The surface of Mars is comprised of large volcanoes, rift channels, river beds and valleys, and dune fields like the surface of Earth. The martian surface is home to three clearly visible impact basins such as two basins called Argyre and Hellas in the southern hemisphere, and Isidis basin near the equator. The global geological map of martian surface (Fig. 2.1b) has been prepared by many planetary scientists, freely available at the United States Geological Survey (USGS)'s media website, that describes detail on the distribution of the geological units and landforms (Tanaka et al., 2014). The geological map was prepared using the remote sensing dataset acquired over time since the Viking orbiter (Tanaka et al., 2014). The remote sensing dataset was used to derive the morphological, topographical, thermophysical, spectral, radar, and other observations that have been analyzed and interpreted to prepare the detail global geological map of the planet Mars (Tanaka et al., 2014). Thermal infrared data were efficiently used to prepare the geological map since thermal infrared wavelengths are less affected by atmospheric interferences e.g., haze. The geological history of the planet has broadly been divided into three eras (from old to the recent): the Noachian, the Hesperian, and the Amazonian (Fig. 2.2; e.g., Hartmann and Neukum, 2001; Nimmo and Tanaka, 2005). The Noachian period has spanned around 4.1 to 3.8 Ga ago and the era is characterized by higher impact cratering, erosion, valley formation, and consists of hydrous weathering products e.g., phyllosilicates (e.g., Nimmo and Tanaka, 2005, Carr and Head, 2010). A substantial drop of impact cratering, weathering and erosion, and valley formation are attributed to the Hesperian epoch (around 3.7 to 3 Ga ago), although the rate of volcanism culminated at a higher rate than the previous epoch (e.g., Carr and Head, 2010 and the references therein). During the Amazonian period (3.0 Ga to the present), the rate of volcanism dropped, and valley formation became restricted, but ice-related activities (e.g., presence, movement, and accumulation) were dominant during this recent era of the planet (e.g., Carr and Head, 2010).

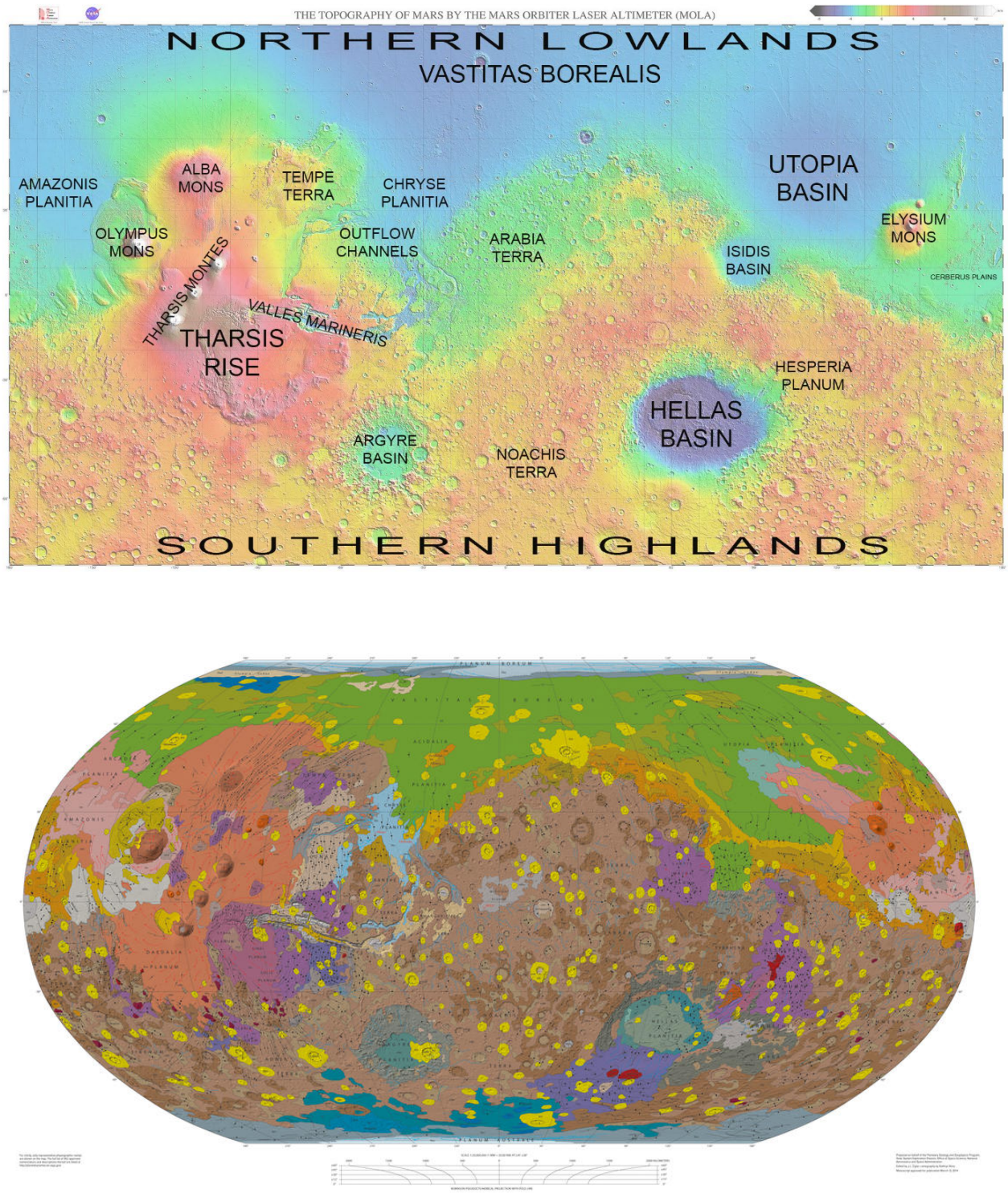

Fig. 2.1: The surface regions of Mars: southern highland and northern lowland (a). The three large impact basins e.g., Hellas, Argyre, and Isidis are shown on the map (Source: MOLA map by NASA/JPL/GSFC). (b) The global geological map of Mars as prepared by Tanaka et al. (2014), the figure was adopted from USGS. For detail of the martian global geological map and landform units, the readers are referred to the online version of the map at https://dx.doi.org/10.3133/sim3292.

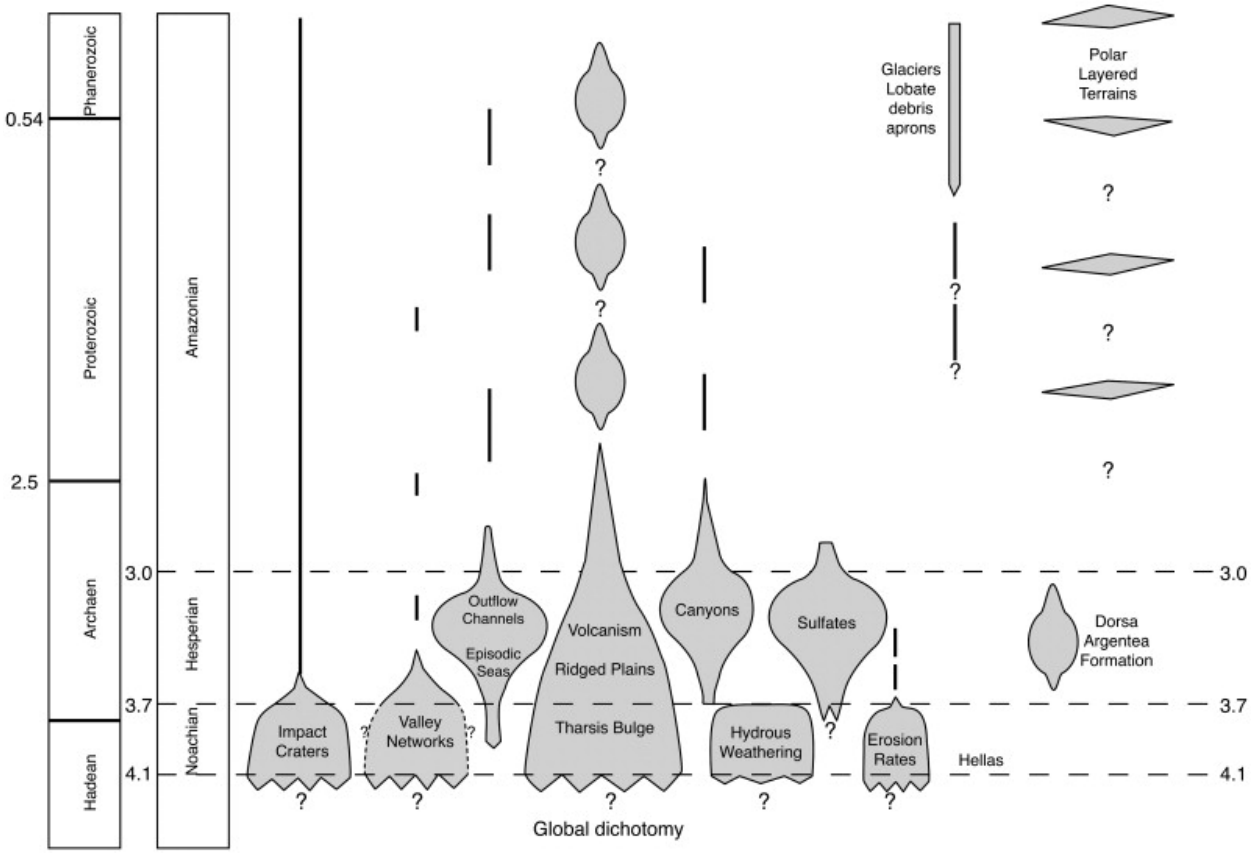

Fig. 2.2: The geological timescale of Mars. The timescale of the planet has broadly been divided into three eras (from old to the recent): the Noachian, Hesperian, and Amazonian (e.g., Hartmann and Neukum, 2001; Nimmo and Tanaka, 2005). The figure was adopted from Carr and Head (2010).

Studying Mars adds knowledge not only for a better understanding of the evolution and history of Earth but also helps us to understand the information of the earlier solar system. Over the past decades, Mars has been studied in different perspectives in detail on thermophysical properties (e.g., thermal inertia, albedo, and diurnal temperature variations), as well as morphological, stratigraphic, and mineralogical characteristics. Combining this information helps to constrain the environmental history and evolution of surface and climate of the planet. The data from the martian research come from the orbital spacecraft, rover, and lander missions. Over time, different space agencies, such as the National Aeronautics and Space Administration (NASA), the Soviet Union, the European Space

Agency (ESA), and the Indian Space Research Organization (ISRO) have sent spacecraft with different instrument arrangements of visible (VIS), near-infrared (NIR), shortwave infrared (SWIR), and thermal infrared (TIR) sensors. Though rover and lander missions are very useful since these can collect *in-situ* data directly from the surface of Mars, the areal extent of these *in-situ* data is very minimum (and limited) in amount. In contrast, the orbital spacecraft data are the most extensive data used for the martian study covering the entire global surface of Mars. The most recent of these orbiter missions is NASA's Mars Reconnaissance Orbiter (MRO) which has the instruments platforms of the High Resolution Imaging Science Experiment (HiRISE; McEwen et al., 2007), the Context Camera (CTX; Malin et al., 2007), and the Compact Reconnaissance Imaging Spectrometer for Mars (CRISM; Murchie et al., 2007). While HiRISE and CTX sensor images are used to identify the local geology at very high spatial resolutions (local scale), the CRISM data are used for identifying surface mineralogy and atmospheric properties of the planet (details are described in the subsequent sections). ESA has sent a mission named the Mars Express (MEx) that on boards the instruments of the High Rise Stereo Camera (HRSC; Neukum et al., 2004) and The Observatoire pour la Minéralogie, l'Eau, les Glaces et l'Activité (OMEGA; Bibring et al., 2004). The HRSC produces digital elevation models to characterize the topography and surface geology while the OMEGA is a hyperspectral spectroscopic instrument used to detect mineralogy of Mars as CRISM does. Earlier, NASA sent another mission named the 2001 Mars Odyssey with the instrument payload of the Thermal Emission Imaging System (THEMIS; Christensen et al., 2004). The Mars Global Surveyor (MGS) mission by NASA carried the thermal infrared (TIR) instrument of the Thermal Emission Spectrometer (TES; Christensen et al., 2001), the Mars Orbiter Camera (MOC), and the Mars Orbiter Laser Altimeter (MOLA; Smith et al., 2001) sensors.

This chapter first describes the thermophysical, morphological and stratigraphic, and mineralogical characterizations of Mars and then describes the orbital sensors characteristics and their usability for characterizing the environmental and geologic history of Mars.

2.2: Thermophysical characteristics

The thermophysical properties of the martian surface represent the spectral response (absorption and reflection) of the surface materials to thermal energy. The thermophysical characteristics are evaluated through determining thermal inertia, albedo, and diurnal temperature changes on the surface of the planet (e.g., Jakosky et al., 2000). On Mars, thermal inertia is considered as the primary physical property that is a function of resistance of the materials to a temperature change and can be used as an indicator of surface geological characteristics for the upper few centimeters (e.g., Edgett and Christensen, 1991; Jakosky et al., 2000; Mellon et al., 2000; Putzig et al., 2005). In other words, the thermal inertia of the surface of the planet is the physical property involving the diurnal thermal response (emission) to solar heating (e.g., Jakosky et al., 2000). Thermal inertia is associated with the thermal conductivity and the physical structure of top few decimeters-to-centimeters of surficial materials or 'soil' (e.g., Kieffer et al., 1973; Jakosky, 1986; Putzig et al., 2005). The thermal inertia (TI) of a material *(I)* can be defined and calculated using the following equation (1):

$$I = \sqrt{kpc} \quad \ldots\ldots\ldots\ldots\ldots\ldots \quad (1)$$

Where, k = the thermal conductivity, p = the density, and c = the specific heat (e.g., Edgett and Christensen, 1991). The Mars Global Surveyor (MGS) onboard the Thermal Emission Spectrometer (TES) instrument measures emitted infrared (IR) energy (Christensen et al., 2001). The brightness

and surface kinetic temperature (surface temperature) are inferred from this measured infrared energy (Christensen et al., 2001). With the determination of brightness (and surface) temperature and thermal inertia, one can map the surface physical properties of the planet to understand the spatial distribution and transport of surface materials (e.g., Kieffer et al., 1977; Palluconi and Kieffer, 1981). Thermal inertia helps in determining the surface temperature which is considered as a function of the seasons for long periods of time (Mellon and Jakosky, 1993). On Mars, the thermal inertia is determined remotely (i.e., using orbital spacecraft data) from measurements of the thermal emission at a point on the martian surface by comparing the measured temperature with the temperature inferred from a thermal model (e.g., Jakosky et al., 2000; Putzig et al., 2005). The temperature of the surface is influenced by the physical and thermal properties of surface materials to a few centimeters (Mellon et al., 2000; Jakosky et al., 2000). Therefore, thermal inertia is an indicator of surface geological characteristics for a few centimeters (e.g., Jakosky et al., 2000; Mellon et al., 2000; Putzig et al., 2005). In general, a lower thermal inertia represents a loose, fine surface dust particles, and/or very few rocks (mechanically weak surface); medium/moderate thermal inertia means a combination of coarser loose particles, crusted fine-grained materials, a reasonable amount of scattered rocks; whereas a higher thermal inertia indicates a combination of mechanically strong coarse-grained sand (dune sand), strongly-crusted or indurated fines with abundant rocks, and/or scattered bedrocks (e.g., Kieffer et al., 1977; Palluconi and Kieffer, 1981; Jakosky et al., 2000; Mellon et al., 2000; Putzig et al., 2005). A higher value of thermal inertia involves a surface with more extreme thermophysical properties or mechanically strong materials (Murphy et al., 2005). The details of thermal inertia calculation and its applications are thoroughly described in the subsequent chapters.

The albedo of the surface of Mars (or any other planetary bodies) provides a measure of the amount of sunlight absorbed by the surface. It is considered as an important component influencing the total energy balance of the planet (Putzig and Mellon, 2007). Thermal inertia can be retrieved without knowing surface albedo either by fitting multiple daytime measurements of the emitted thermal energy (Palluconi and Kieffer, 1981; Hayashi et al., 1995) or considering a constant albedo and attributing the variations in nighttime surface temperature (Christensen, 1988). The thermal inertia and albedo are derived by combining infrared (IR) radiation of the 2001 Mars Odyssey's the Thermal Emission Imaging System (THEMIS) and the Mars Global Surveyor (MGS) on boards the Thermal Emission Spectrometer (TES) data (e.g., Mellon et al., 2000; Christensen et al., 2001; Putzig et al., 2005; Putzig and Mellon, 2007). The thermal infrared (TIR) 9 band of THEMIS is used for detecting the brightness and surface diurnal temperature changes on Mars (Pelkey et al., 2003; Rogers and Bandfield, 2009). TES albedo product has lower resolutions (3x6 km) compared to THEMIS (100 m/pixel) albedo product. Therefore, studying local scale geology of Mars uses THEMIS albedo data. The higher spatial resolution albedo of the martian surface is derived from THEMIS projected visible albedo product (VISALB). The albedo is calculated using the visible radiance from a single band standard planetary data system (PDS). The Lambert albedo (*L*) of the surface of the planet is calculated from the measured THEMIS visible radiance using the following equation (2) (THEMIS User Guide, 2006):

$$L = \frac{R}{\left(\frac{J}{d^2\pi}\right) * cos(i)} \quad \ldots\ldots\ldots\ldots\ldots (2)$$

Where, R = the calibrated spectral radiance data (VISRDR) in [W m^{-2} st^{-1} μm^{-1}], J = the solar irradiance in [W m^{-2} μm^{-1}] at the Mars-Sun distance (d) in the astronomical unit (AU), and i = the incidence angle of the Sun on the surface of Mars (THEMIS User Guide, 2006). The values for solar

distance (*d*) and incidence angle (*i*) are computed at the image center whereas the solar irradiance values are convoluted from the individual visible bands as given in the following table 2.1 (THEMIS User Guide, 2006). The albedo images are derived from visible band V-3. However, if band V-3 is not available, band V-4 or the first available band is used.

Table 2.1: Solar irradiance values in THEMIS visible wavelengths (THEMIS User Guide, 2006).

THEMIS Band	J [W m^{-2} μm^{-1}]
V-1	1714.882
V-2	1854.915
V-3	1567.595
V-4	1268.324
V-5	981.8372

There are few thermophysical models and methods to derive thermal inertia, albedo, and temperature change information (Putzig et al., 2013; Putzig et al., 2014). The key questions asked in terms of thermophysical characteristics on the martian surface are: (a) what type of surface presents higher and lower thermal inertia?; (b) what is the relationship between thermal inertia and albedo characteristics?; (c) what are the correlation between elevation and thermophysical characteristics e.g., thermal inertia and albedo?; (d) what are the mineral composition (as identified by orbital sensors) in thermal spectral units?; and (e) what are the differences, if any, in thermal inertia between TES and THEMIS products? The existing studies have used the Thermal Emission Imaging System (THEMIS) (Christensen et al., 2004) and MGS on boards the Thermal Emission Spectrometer (TES) (Christensen et al., 2001) to derive thermophysical properties. The Mars Orbiter Laser Altimeter (MOLA; Smith et al., 2001) point cloud data of 128 ppd (pixels per degree), derived from the Planetary Data System (PDS), are used to constrain elevation map.

The THMPROC, a THEMIS processing web interface developed by Arizona State University (ASU), is used to run the THEMIS standard processing routine e.g., signal drift corrections (UnDrifft/DeWoobble – UDDW), image rectification (unslant), correlated noise removal (deplaid), and automated radiance correction (auto-radcorr) (THMPROC, http://thmproc.mars.asu.edu). Different projections system such as sinusoidal equal area (SINU), simple cylindrical (SIMP), and polar stereographic (POLA) projections can be used to project the data. THEMIS radiance images are processed, atmospherically corrected, and then converted to the surface emissivity using the methods described by Christensen (1998) and Bandfield et al. (2004). In addition, some prior studies calculated two other temperature measurements e.g., brightness temperature and surface temperature from THEMIS IR data. In THMPROC, the available THEMIS infrared (IR) radiance bands are converted to the blackbody temperature equivalent radiance for each band to get the brightness temperature values of THEMIS pixels. On the other hand, the surface temperature is calculated as a function of the highest brightness temperature for every pixel in THEMIS bands. The tool calculates an approximate surface temperature albeit the martian atmosphere is not transparent entirely. Colder surfaces (<220 K) put some uncertainties in deriving the surface temperature and, therefore, are not preferred in surface temperature calculation. In general, the THEMIS band 9 is used to calculate the brightness temperature and produces more accurate results. Thus, the existing studies have used THEMIS band 9 for surface temperature calculation. All the outputs e.g., radiance, emissivity, brightness, and surface temperature derived from THEMIS images are rescaled to a 0-255 value ranges to produce 8-bit stretched images to the better enhancement and interpretation the surface features at a local scale. The tool employs a standard deviation or linear stretch for all images with an average digital number (DN) of 127 and a specific standard deviation of 40 by default. Moreover, the tool applies a decorrelation stretch (DCS; Gillespie et al., 1986; Gillespie, 1992; Edwards et al., 2011) using bands 8 (11.79 μm), 7 (11.04 μm), and 5 (9.35 μm), bands

9 (12.57 μm), 6 (10.21 μm), and 4 (8.56 μm), or bands 6 (10.21 μm), 4 (8.56 μm), and 2 (6.78 μm) of THEMIS images assigned to red, green, and blue bands, respectively, to investigate the spectral variability in different parts of the martian surface, for instance NW Syrtis (Salvatore et al., 2018).

The thermal inertia of the martian surface is calculated from the nighttime thermal emission measurements (Murphy et al., 2007). This study calculates the thermal inertia from both TES and THEMIS images. The study uses MARSTHERM, a thermophysical analysis tool for Mars research developed by researchers at the Planetary Science Institute in Tucson, Arizona (Putzig et al., 2013), to derive TES thermal inertia and albedo, THEMIS thermal inertia, and reference MOLA elevation map of the study area. The thermal inertia from TES measurement is produced using the method developed by Putzig et al. (2014). The details of the method and calculation routine are described in the subsequent chapters.

2.3: Morphology and stratigraphy

The surface of Mars has a dichotomy as most of the southern highland is densely cratered with 1-3 km topographic rise whereas northern lowland is more sparsely cratered with the elevation below the martian datum (e.g., Carr, 1980). Like the Earth, Mars has distinct geologic features such as mountain ridges (e.g., Olympus Mons), young lava flows, valleys (e.g., Valles Marineris), channels of alluvial origin, deltaic sedimentary deposits (e.g., Faure 2007; Salvatore et al., 2018), etc. The valley networks are seen around the Noachian densely cratered upland areas (e.g., Carr and Head, 2010 and references therein). The visible images from the orbital dataset suggest that the surface has experienced water-related fluvial activities for during the ancient martian history (e.g., Hynek and Phillips, 2003; Carr, 2012). Remote sensing with visible images in combination with digital elevation models has been to analyze ancient fluvial systems of the planet (e.g. Rangarajan et al., 2018 and

references therein). The topography and geomorphology of the martian surface have been analyzed using the radar system and measurement from the Mariner and Viking dataset in the earlier era. However, the advent of high-resolution dataset paved the ways to sophisticatedly and comprehensively analyze the geologic features (more especially fluvial features) of the martian surface. The surface of the planet has a distinct records of sedimentary processes e.g., transport, deposition, and accumulation of sediments in a wide variety of environments (e.g., Ori et al., 2000; Malin et al., 2003; Fassett and Head, 2005; Howard et al., 2005; Irwin et al., 2005; Lewis and Aharonson, 2006; Goudge et al., 2017). However, construction of sedimentary records in surface requires details on stratigraphic architecture and morphological characterization (Goudge et al., 2017). In addition, for some areas, such as Jezero crater of Nili Fossae region, there is a debate on the origins of these sedimentary environments (i.e., erosion, transportation, and deposition), specifically in the different parts of the northern hemisphere; whether these sedimentary environments are an alluvial fan or deltaic deposit. Identifying distinct differences between deltas and alluvial fans demands an analysis of surface morphology and topographic aspects carefully (Blair et al., 1994) because alluvial fans have distinct shapes whereas deltas have distinct clinoforms (e.g., Goudge et al., 2017). These differences on the martian surface can be identified by using high-resolution images such as the Mars Reconnaissance Orbiter (MRO) on boards the High Resolution Imaging Science Experiment (HiRISE) (McEwen et al., 2007) and the Context Camera (CTX) (Malin et al., 2007).

HiRISE image produces a high-resolution digital elevation models or DEMs (spatial resolution around 1 meter per pixel) and orthorectified images (spatial resolution about 0.25 per pixel) (McEwen et al., 2007). DEM of HiRISE can be processed through different interfaces following a standard routine procedure such as using NASA's Ames Stereo Pipeline (ASP) stereogrammetry

software (Broxton and Edwards, 2008; Moratto et al., 2010; Beyer et al., 2014). Details of the HiRISE image processing are described in the subsequent chapters. The dip-strike characteristics of the bedding or surface layers are also derived from the stereo photogrammetry of the different datasets (e.g., Goudge et al., 2017). The global geological map of Mars can be produced using daytime IR data from the 2001 Mars Odyssey on boards the Thermal Emission Imaging System (THEMIS) instrument (Christensen et al., 2003; Pelkey et al., 2003; Christensen et al., 2004) since the sensor data cover the entire martian surface. For large spatial scale (regional and planetary scale), the radar and laser data sets are used to map the subsurface topographic (and subsurface) profile from data such as point shots or point clouds of the Mars Orbiter Laser Altimeter (MOLA; Smith et al., 2001) data. In addition, the Context Camera (CTX) is used to get the context morphology for the regional and local scale of the surface since the sensor has a spatial resolution of ~6 meters/pixel (Malin et al., 2007). Therefore, the integration of the High Resolution Imaging Science Experiment (McEwen et al., 2007), the Context Camera (Malin et al. 2007), the High Resolution Stereo Camera (Neukum et al., 2004), the Thermal Emission Imaging System (Christensen et al., 2003; Christensen et al., 2004; Pelkey et al., 2003), and the Mars Orbiter Laser Altimeter (Smith et al., 2001) data allow a comprehensive understanding and mapping details of the morphology, geologic units, and stratigraphy of the surface of Mars.

2.4: Mineralogy

Minerals on the martian surface represent the ancient environment and landform processes involved. Therefore, identification of mineral composition is key to determining the environment, landform, and climate of ancient Mars. Determining the surface mineralogical composition provides, therefore, a means of understanding and constraining the origin and geological history of the planet (e.g., Pelkey et al., 2007). The determination of mineralogy is, therefore, the key to interpreting the

environmental history and atmospheric characteristics of Mars (e.g., Ehlmann and Edwards, 2014). Spectroscopy is used for obtaining mineralogic information and over time the tool has been widely used in the missions (orbiters, landers, and rovers) to the planet (e.g., Pelkey et al., 2007; Ehlmann and Edwards, 2014). The identification of minerals has been carried out using the MRO's CRISM data; the most recent orbital spectrometer revolving around the planet (Murchie et al., 2007). The CRISM instrument is a hyperspectral imager including visible to near-infrared wavelengths (spectral wavelength range of 0.37–3.92 mm at a spectral sampling of 6.55 nm per channel) and has two modes of operation e.g., targeted hyperspectral and mapped multispectral (Murchie et al., 2007). There are different versions of the data set (Viviano-Beck et al., 2014; Pelkey et al., 2007; Murchie et al., 2007) used to derive surface mineralogical information. However, a new version called map-projected targeted reduced data record (MTRDR) products is derived by the standard processing routine of CRISM hyperspectral targeted observations (TRDR). The TRDR product records radiance at the sensor and processed through a set of standard routine of spectral corrections (e.g., atmospheric correction, volcanic scan correction, etc.), spatial transforms (e.g., geometric correction), and renderings that are used to identify the minerals (Viviano-Beck et al., 2014 and 2017). The details of the CRISM data processing are described in the subsequent chapters. Different phases of minerals such as ices (e.g., carbon ice and water ice), iron oxides and primary mafic silicates (e.g., olivine and pyroxene), sulfates, phyllosilicates, carbonates, halides, other hydrated silicates, etc. are identified using CRISM data (e.g., Pelkey et al., 2007; Viviano-Beck et al., 2014; Ehlmann and Edwards, 2014). The identification of minerals has been done using different spectral summery products and displaying these summery products in 3-bands composite of browse products (Pelkey et al., 2007; Viviano-Beck et al., 2014). However, the mineral identification through CRISM analysis does not produce the quantitative or the exact amount of mineral present on the surface rather it displays qualitative information about the types of mineral present in the surface

(Pelkey et al., 2007; Viviano-Beck et al., 2014). Noted here that, both CRISM and OMEGA are used by planetary researchers in detecting and analyzing the primary and altered mineral of variety of mineral species (e.g., Pelkey et al. 2007; Viviano-Beck et al. 2014; Ehlmann and Edwards, 2014).

Besides CRISM, mineralogical identification (at local spatial scale), mineral bulk abundance, can be identified using IR spectrum of the 2001 Mars Odyssey mission on boards the Thermal Emission Imaging System (THEMIS) and the Mars Global Surveyor (MGS) on boards the Thermal Emission Spectrometer (TES) data (e.g., Rogers and Bandfield, 2009; Salvatore et al., 2018) at regional and global scale. For identifying bulk-mineralogy using TES and THEMIS data, a spectral unit map is highlighted first from THEMIS data (Rogers and Bandfield, 2009). Then quantitative bulk-mineralogy are extracted from representative areas that show high concentrations of THEMIS-derived spectral units (e.g., Rogers and Bandfield, 2009). Spectral deconvolution (both linear and non-linear) methods are used to quantitatively detect surface mineralogy from THEMS and TES data. Previous studies that used a non-negative least square minimization routine (e.g., Lawson and Hanson, 1995; Seelos and Arvidson, 2003; Rogers and Aharonson, 2008; Salvatore et al., 2014, Salvatore et al., 2016) is different from the techniques that of developed by Ramsey and Christensen (1998) (Salvatore et al., 2018) using THEMIS and TES data. A detail of atmospheric correction and mineral identification using spectral deconvolution method (i.e., non-negative least square minimization) are described in the subsequent chapters. The minerals are detected and then the analysis is carried out through spectral investigations of NIR and TIR datasets from multi-spectral THEMIS and hyperspectral TES and CRISM sensors data. The following section discusses in detail the spectral characteristics of different minerals (e.g., primary and altered) and rocks (e.g., igneous, sedimentary, and metamorphic).

2.4.1: Spectra of minerals and rocks[a]

Electromagnetic radiation (EM) interacts with mineral and rocks at the atomic-molecular level through some selective reflection, absorption, and emission. This interaction of EM with materials can be expressed as the relationship between the wavelength versus intensity of radiation; often called as a spectral response curve (alternatively spectral signature). Identification of minerals and rocks are done from the detection of a diagnostic single feature (shape) at a particular wavelength or a group of features (pattern) in a spectral signature curve at different wavelengths. This spectral behavior can be expressed as three types: a) selective absorption, b) selective reflection, and c) selective higher or lower emission (Gupta, 1991). Spectral information is crucial for identifying materials from the remote sensing data. Moreover, spectral arrangement plays an imperative role in designing the remote sensing system (e.g., Rangarajan et al., 2018). Measured spectral information from remote sensing system is then compared with the laboratory spectra of known materials (e.g., minerals and rocks) to identify and to be confirmed about the remotely measured materials types and their constituents. The methods for laboratory spectral data measurement differs in terms of ranges of wavelength used (VIS, IR, or TIR) and physical phenomena (reflection, absorption, or emission) under investigation. Reflection measurement, that is the most widely used arrangement, contains an optical region of EM spectrum such as visible [VIS] and near and short-wave infrared [NIR-SWIR]. Emission measurement requires the object under investigation must be above zero Kelvin (°k) temperature (most commonly several hundred degrees) to emit radiation. Alternatively, transmission happens with gases or liquids and is generally used for atmospheric constituent analysis. Spectral curves comprise positive and negative slopes; the negative peaks are alternatively designated as the absorption bands for all types of spectral signature regardless of the type of

[a] This section is a summary of the chapter titled 'Spectra of Minerals and Rocks' in the book 'Remote Sensing of Geology' by R. Gupta, 1991 (and the references therein). For detail of this section, readers are referred to: Gupta, R.P., 1991. Remote Sensing Geology. Springer-Verlag, Berlin Heidelberg.

spectral behavior e.g., reflection, absorption, emission or transmission. In other words, the spectral curve may imply high or low spectral absorptivity.

Energy interaction with minerals or rocks is attributed to energy states and transition of objects. The relative position, as well as the state of the constituent particles of matters at a given time, determines the energy state of a mineral or rock. There are four different types of energy states (e.g., translational, rotational, vibrational, and electronic) in an object that constitutes its sum energy of an atomic-molecular system. However, among these four energy states, only vibrational and electronic energy states of an object are important in the spectroscopic analysis. The vibrational energy state of an object involves the movement of atoms about a fixed position relative to each other is caused by thermal infrared (TIR) and short-wave infrared (SWIR) radiations (e.g., Gupta, 1991). Most terrestrial rock-forming minerals such as silicates, hydroxyls, oxides, phosphates, carbonates, sulphates, and nitrates are sensitive to and, therefore, marked by atomic-molecular vibrational processes at the SWIR and TIR wavelength regions (Gupta, 1991). Vibrational processes result from bending and stretching molecular motion distinguished as fundamental, overtones, and combinations primarily in the thermal infrared region at > 3.5 μm along with overtones in the short-wave infrared region at 1-3 μm (Gupta, 1991). The configuration of electrons surrounding the nucleus defines the electronic energy state of a matter and its transition involves a higher amount of energy predominantly at visible-near infrared (VIS-NIR), ultraviolet (UV), or X-ray regions (Gupta, 1991). The electronic process leads to selective absorption that can be explained by different models e.g., charge-transfer effects, conduction-bands absorption effects, electronic transition in transitional metals, and crystal effects. For details of these models, the readers are suggested to see Gupta (1991) and the references therein.

2.4.1.1: Spectral features of mineralogical constituents

Minerals are naturally occurring solid inorganic compound and contain cations (+ ion) and anions (- ion) (e.g., Wenk and Bulakh, 2016). The chemical composition of minerals can be simple or complicatedly complex while the constituent ions prevail as major, minor or trace components. The spectral response curve of a mineral is determined by the spectral effect of dominant anions and cations, spectra of trace constituent ions, and crystal field effect of the mineral (Gupta, 1991). The discussion on spectral features of a mineral constituent can be divided into three different parts regarding different spectrum e.g., VNIR, SWIR, and TIR regions.

Visible and Near Infrared (VNIR; 0.4-1.0 μm): Although electronic processes in many transition metals (i.e. Fe, Mn, Cu, Ni, Cr, etc.) are predominantly marked by spectral features of VNIR wavelengths, bulk of the terrestrial rock elements (e.g., Si and Al) as well as various anion groups (for instances, oxides, silicates, hydroxides, phosphates, carbonates, etc.) lack spectral features in VNIR region (Gupta, 1991). Ferric-ion in Fe-O exhibits strong absorption in UV-blue wavelengths resulting in a steep reflectance fall towards blue and a rise towards IR rendering a reflectance peak in the 1.3-1.6 μm region (Gupta, 1991).

Short-wave Infrared (SWIR; 1-3 μm): The spectral features of hydroxyls (OH^-) and carbonates (CO_3^{2-}) minerals are marked by SWIR region. The hydroxyl ion (OH^-) is a common constituent of secondary hydrated weathered minerals (e.g., micas, clays, chlorite, etc.) displaying a 2.74-2.77 μm fundamental vibrational absorption along with a 1.44 μm overtone feature at like water (H_2O) molecule (e.g., Gupta, 1991; Viviano-Beck et al., 2014). However, hydroxyl ion combining with aluminum and magnesium i.e., as AI-OH and Mg-OH in clays and hydrated silicates display sharp absorption features at 2.1 - 2.4 μm region

(Gupta, 1991). Although a vibrational band combination occurs at 2.2 μm for Al-OH and at 2.3 μm for Mg-OH, a combination of these Al-OH and Mg-OH displays a doublet of the stronger peak at 2.3 μm with a 2.2 μm weaker band such as in kaolinite (Gupta, 1991; Viviano-Beck et al., 2014). The absorption bands at 2.1 - 2.4 μm in Al-OH and Mg-OH bearing clay is responsible for the sharp decrease in spectral reflectance beyond the wavelength of 1.6 μm (Gupta, 1991). SWIR wavelength is also a powerful spectral range in identifying clay mineral assemblages and potential hydrothermal alteration zones since many of the clay minerals such as kaolinite, muscovite, pyrophyllite, montmorillonite, etc. are related to the hydrothermal alternation. Short-wave infrared region is considered as an important absorption band since water molecules show absorption at 1.4 and 1.9 μm. Carbonates minerals such as calcite ($CaCO_3$), magnesite ($MgCO_3$), dolomite [(Ca-Mg) CO_3], and siderite ($FeCO_3$) show important absorption bands at 1.9 μm, 2.35 μm, and 2.55 μm of SWIR region (e.g., Gupta, 1991 and the references therein; Viviano-Beck et al., 2014).

Thermal Infrared (TIR; ~6.25-50 μm): Terrestrial rock-forming minerals groups such as silicates, oxides, phosphates, carbonates, sulphates, hydroxyls, etc. are commonly marked by the spectral features at thermal infrared wavelengths. Noting here that since this study is using CRISM data which does not have TIR bands, therefore, this discussion does not cover spectral features in thermal infrared (TIR) extensively. Though carbonate minerals display a broad absorption at 7 μm, remote sensing data cannot be used in this range since the wavelength is beyond the atmospheric windows (8–14 μm). However, a weak 11.3 μm absorption can be marked by carbonate minerals. The presence of SiO_4- in the most abundant silicate minerals of earth crust responsible for displaying a vibrational spectral feature in thermal infrared wavelengths (Gupta, 1991).

2.4.1.1: Spectral features of rock constituents

Rocks are aggregates of different minerals. Being compositionally more variable as well as intricate than minerals makes it sometimes very difficult to clearly attribute the diagnostic spectral response curves of rocks. However, the spectral response of terrestrial rocks is broadly constructed upon on the spectral features of the constituent mineral components. The spectral response of rocks can be described in terms of two spectra: solar reflectance region (VNIR and SWIR) and emission region of thermal infrared (TIR) wavelengths. Since the thermal-IR region for rock spectra are readily interpreted in terms of relative or bulk mineral abundances and CRISM does not have TIR bands, therefore, this discussion confines extensively on VNIR and SWIR wavelengths.

The mineral constituents of rocks and their textual properties (e.g., grain size, packing, and mixing) determine the spectral curve of rocks. In the case of igneous rock, for instance, the graphic granites are marked by the absorption bands at 1.4 μm, 1.9 μm, and 2.2 μm which are the characteristic OH and H_2O molecules absorption bands (Gupta, 1991). Iron, pyroxenes, amphiboles, and magnetite (mafic minerals) constitute the basic constituents of mafic rocks (basaltic) and their absorption bands are marked at 0.7 μm and 1.0 μm which are diagnostic features for the ferrous (Fe^{2+}) and ferric (Fe^{3+}) ions, respectively (e.g., Viviano-Beck et al., 2014). Almost all sedimentary rocks display a diagnostic absorption at 1.4 μm and 1.9 μm wavelengths whereas clay-shales display an additional 2.1-2.3 μm absorption feature (e.g., Gupta, 1991; Viviano-Beck et al., 2014). Usually, carbonaceous shales and pure siliceous sandstone are featureless. Having some iron-oxide stains in sandstones appears a spectral feature at 0.87 μm. The absorption bands in carbonate rocks display diagnostic spectral shapes at 1.9 μm and 2.35 μm; very common for limestones and calcareous rocks (e.g., Viviano-Beck et al., 2014). The dolomites display a ferrous ion absorption band at 1.0 μm due to the substitution of Mg^{2+} by Fe^{2+} (Gupta, 1991). In the case of metamorphic

rock, for instance, tremolite schists display a broad absorption due to dominant ferrous ion. Schists, marbles, and quartzites display water (H_2O) and hydroxyl (OH^-) absorption bands at 1.4 μm and 1.9 μm whereas marbles are marked by carbonate bands at 1.9 μm and 2.35 μm (e.g., Gupta, 1991; Viviano-Beck et al., 2014).

Alternated minerals such as kaolinite, sericite, montmorillonite, muscovite, chlorite, biotite, epidote, pyrophyllite, alunite, zeolite, albite, quartz, goethite, jarosite, hematite, metal hydroxyls, calcite and other carbonates, actinolite-tremolite, serpentine, and talc display distinct spectral features in VNIS and SWIR bands that are broadly described into five groups (e.g., Gupta, 1991 and references therein; Pelkey et al., 2007; Viviano-Beck et al., 2014):

- Quartz and feldspar (framework silicates): spectrally featureless in VNIR-SWIR range with an increased reflectance in general.
- Clays (sheet silicates): displays absorption bands at 2.1-2.3 μm.
- Carbonates: shows spectral features at 1.9 μm and 2.35 μm.
- Hydroxyls, water and metal hydroxides: absorption features at 1.4 μm and 1.9 μm.
- Iron oxides: spectral features may occur in VNIR.

Though laboratory spectra are used as the representative mineral spectral endmembers, the laboratory spectra are generally pure, less complex, and without the interference of weathering, water, vegetation organic matter, etc. On the other hand, field spectra collected by remote sensing techniques influenced by abovementioned factors (or impurities) are, therefore, complex in nature. Thus, while comparing the spectral signature of remote sensing data with the laboratory endmember spectra (or during the spectral deconvolution) the degree to which field spectra are indistinguishable to the laboratory spectra should be interpreted with care.

2.5: Orbital sensors characteristics and their utilities

Characterizations of the surface of Mars are carried out using data derived from orbital remote sensing and *in-situ* data of rover or lander missions. A large number of spacecraft missions including flyby and orbiters have been sent to the planet Mars. The details of the Mars missions conducted by NASA and other space agencies are given in Table 2.2.

Table 2.2: A complete list of successful Mars missions (orbiter, lander, and rovers) to date with their scientific instrument payloads, as adopted and then recreated after Rangarajan et al. (2018).

Spacecraft	Launch date	Operator	Mission	Payloads
Mariner 4	28-Nov-64	NASA	Flyby	Helium Magnetometer, Geiger Counter, Trapped Radiation detector, Cosmic ray telescope, Solar plasma probe, Cosmic dust detector, Television camera
Mariner 6	25-Feb-69	NASA	Flyby	IR Spectrometer, Two Channel IR Radiometer, UV Spectrometer, S-Band Occultation, Conical Radiometer, Mars TV Camera
Mariner 7	27-Mar-69	NASA	Flyby	IR Spectrometer, Two Channel IR Radiometer, UV Spectrometer, S-Band Occultation, Conical Radiometer, Mars TV Camera
Mariner 9	30-May-71	NASA	Orbiter	UV Spectrometer, IR Interferometer Spectrometer, S-Band Occultation, IR Radiometer, Visual Imaging System
Mars 2	19-May-71	Soviet Union	Orbiter	IR Radiometer, Visible, IR and UV Photometer, Lyman-alpha sensor, Radiotelescope, IR Spectrometer, Phototelevision unit, Magnetometer
Mars 3	28-May-71	Soviet Union	Orbiter	IR Radiometer, Visible, IR and UV Photometer, Lyman-alpha sensor, Radiotelescope, IR Spectrometer, Phototelevision unit, Magnetometer
Viking 1 orbiter	20-Aug-75	NASA	Orbiter	Viking Imaging System, Atmospheric water detector, IR Thermal Mapper

Viking 1 lander	20-Aug-75	NASA	Lander	Imaging System, Gas Chromatograph Mass Spectrometer, Seismometer, X-ray Fluorescence Spectrometer, Biological Laboratory, Weather Instrument Package, Remote Sampler Arm
Viking 2 orbiter	09-Sep-75	NASA	Orbiter	Viking Imaging System, Atmospheric water detector, IR Thermal Mapper
Viking 2 lander	09-Sep-75	NASA	Lander	Imaging System, Gas Chromatograph Mass Spectrometer, Seismometer, X-ray Fluorescence Spectrometer, Biological Laboratory, Weather Instrument Package, Remote Sampler Arm
Mars Global Surveyor	07-Nov-96	NASA	Orbiter	Mars Orbiter Camera, Mars Orbiter Laser Altimeter, Thermal Emission Spectrometer, Magnetometer and Electron Reflectometer, Ultrastable Oscillator, Mars Relay
Mars Pathfinder	04-Dec-96	NASA	Lander	Imager for Mars Pathfinder, Magnetometer, Anemometer, Atmospheric and Meteorological Sensors
Sojourner	04-Dec-96	NASA	Rover	Imaging System, Laser Striper Hazard Detection System, Alpha Proton X-ray Spectrometer, Wheel Abrasion Experiment, Materials Adherence Experiment, Accelerometers
Mars Odyssey	07-Apr-01	NASA	Orbiter	Thermal Emission Imaging System, Gamma Ray Spectrometer, Mars Radiation Environment Experiment
Mars Express	02-Jun-03	ESA	Orbiter	Visible and IR Mineralogical Mapping Spectrometer, UV and IR Atmospheric Spectrometer, Sub-surface Sounding Radar altimeter, Planetary Fourier Spectrometer, Analyzer of Space Plasmas and Energetic Atoms, High Resolution Stereo Camera, Mars Express Lander Communications, Mars Radio Science Experiment

Spirit (MER-A)	10-Jun-03	NASA	Rover	Panaromic Camera, Navigation Camera, Miniature Thermal Emission Spectrometer, Hazard Cameras, Mossbauer Spectrometer, Alpha particle X-ray Spectrometer, Microscopic Imager, Rock abrasion Tool
Opportunity (MER-B)	08-Jul-03	NASA	Rover	Panaromic Camera, Navigation Camera, Miniature Thermal Emission Spectrometer, Hazard Cameras, Mossbauer Spectrometer, Alpha particle X-ray Spectrometer, Microscopic Imager, Rock abrasion Tool
MRO	12-Aug-05	NASA	Orbiter	High Resolution Imaging Science Experiment, Context Camera, Mars Color Imager, Compact Reconnaissance Imaging Spectrometer for Mars, Mars Climate Sounder, Shallow Subsurface Radar
Phoenix	04-Aug-07	NASA	Lander	Surface Stereo Imager, Robotic Arm Camera, Thermal and Evolved Gas Analyzer, Mars Descent Imager, Microscopy, Electrochemistry and Conductivity Analyzer, Thermal and Electrical Conductivity Probe, Meteorological Station
Curiosity (Mars Science Laboratory)	26-Nov-11	NASA	Rover	Alpha Particle X-ray Spectrometer, CheMin, Sample Analysis at Mars, Radiation Assessment Detector, Dynamic Albedo of Neutrons, Rover Environmental Monitoring Station, PanCam, NavCam, HazCam, Mastcam, Mars Hand Lens Imager, ChemCam, Mars Descent Imager
Mars Orbiter Mission	05-Nov-13	ISRO	Orbiter	Lyman-Alpha Photometer, Methane Sensor for Mars, Mars Exospheric Neutral Composition Analyser, Thermal Infrared Imaging Spectrometer, Mars Colour Camera

MAVEN	18-Nov-13	NASA	Orbiter	Solar Wind Electron Analyser, Solar Wind Ion Analyser, SupraThermal and Thermal Ion Composition, Solar Energetic Particle, Langmuir Probe and Waves, Magnetometer, Imaging UV Spectrometer, Neutral Gas and Ion Mass Spectrometer
ExoMars Trace Gas Orbiter	14-Mar-16	ESA/Roscosmos	Orbiter	Nadir and Occultation for Mars Discovery, Atmospheric Chemistry Suite, Colour and Stereo Surface Imaging System, Fine Resolution Epithermal Neutron Detector
NASA InSight	08-May-2018	NASA	Lander	Seismic Experiment for Interior Structure (SEIS), Heat Flow and Physical Properties Package (HP3), Rotation and Interior Structure Experiment (RISE), Rotation and Interior Structure Experiment (RISE), Laser RetroReflector for InSight (LaRRI), Instrument Deployment Arm (IDA), Instrument Deployment Camera (IDC), and Instrument Context Camera (ICC)

Remote sensing datasets for Mars were at a coarse or lower spatial resolution in the earlier era of exploration. However, over the decades the resolutions and domains of the remote sensing datasets have improved and increased. Remote sensing datasets cover from visible (VIS) to microwave wavelengths. The characterizations of martian surface are accomplished using orbital data of visible (VIS), near-infrared (NIR), shortwave infrared (SWIR), and thermal infrared (TIR) domains. A schematic figure of the commonly used wavelength and associated sensors for the Mars exploration are given in figure 2.2 (adopted from Rangarajan et al., 2018).

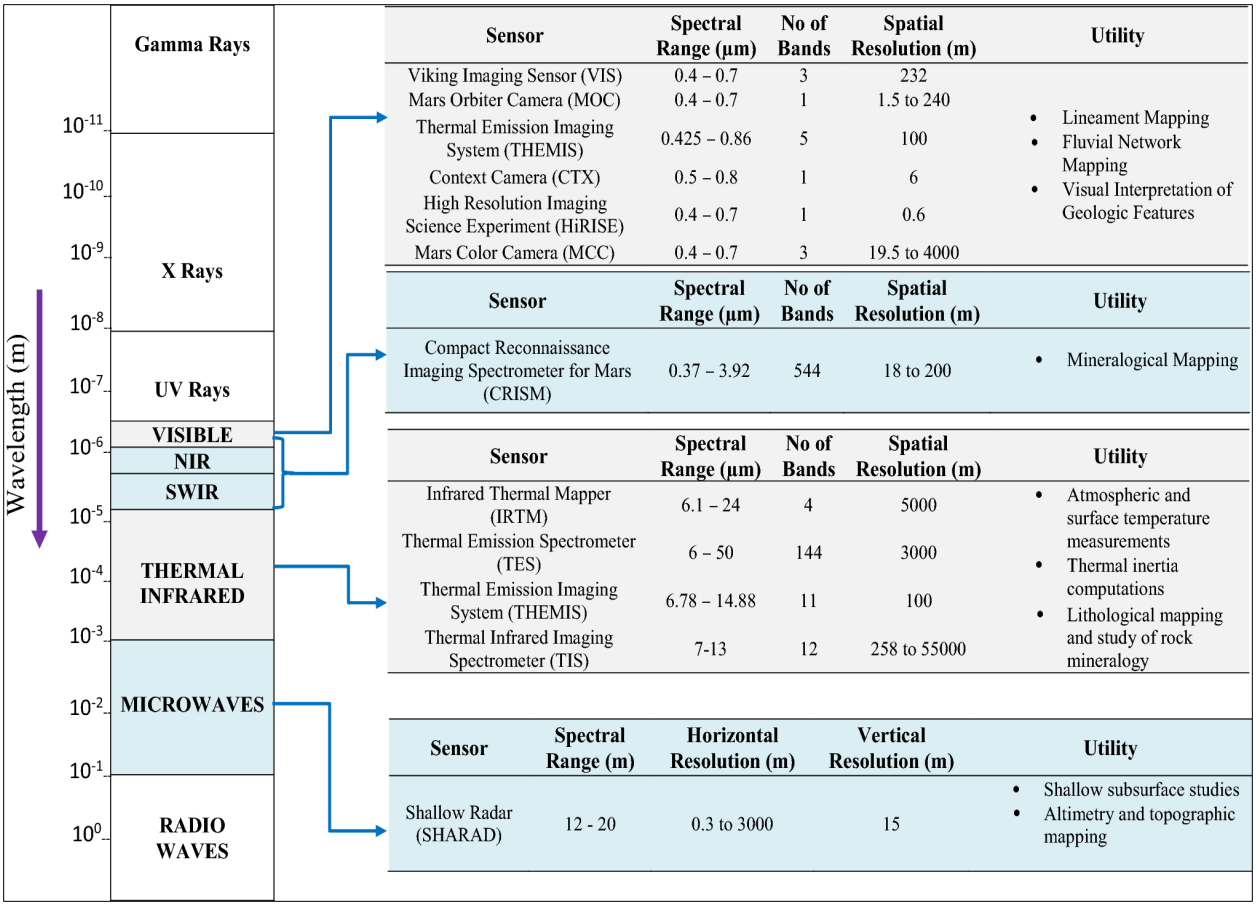

Sensor	Spectral Range (µm)	No of Bands	Spatial Resolution (m)	Utility
Viking Imaging Sensor (VIS)	0.4 – 0.7	3	232	• Lineament Mapping • Fluvial Network Mapping • Visual Interpretation of Geologic Features
Mars Orbiter Camera (MOC)	0.4 – 0.7	1	1.5 to 240	
Thermal Emission Imaging System (THEMIS)	0.425 – 0.86	5	100	
Context Camera (CTX)	0.5 – 0.8	1	6	
High Resolution Imaging Science Experiment (HiRISE)	0.4 – 0.7	1	0.6	
Mars Color Camera (MCC)	0.4 – 0.7	3	19.5 to 4000	

Sensor	Spectral Range (µm)	No of Bands	Spatial Resolution (m)	Utility
Compact Reconnaissance Imaging Spectrometer for Mars (CRISM)	0.37 – 3.92	544	18 to 200	• Mineralogical Mapping

Sensor	Spectral Range (µm)	No of Bands	Spatial Resolution (m)	Utility
Infrared Thermal Mapper (IRTM)	6.1 – 24	4	5000	• Atmospheric and surface temperature measurements • Thermal inertia computations • Lithological mapping and study of rock mineralogy
Thermal Emission Spectrometer (TES)	6 – 50	144	3000	
Thermal Emission Imaging System (THEMIS)	6.78 – 14.88	11	100	
Thermal Infrared Imaging Spectrometer (TIS)	7-13	12	258 to 55000	

Sensor	Spectral Range (m)	Horizontal Resolution (m)	Vertical Resolution (m)	Utility
Shallow Radar (SHARAD)	12 - 20	0.3 to 3000	15	• Shallow subsurface studies • Altimetry and topographic mapping

Figure 2.3: A list of commonly used wavelength and the associated sensors for the Mars exploration, adopted from Rangarajan et al. (2018). The domain of the orbital data covers visible (VIS), near-infrared (NIR), shortwave infrared (SWIR), thermal infrared (TIR), gamma rays, X-rays, microwave, and radio wavelengths.

The prominent sensors for deriving these orbital data are from the most recent mission of Mars Reconnaissance Orbiter (MRO) High Resolution Imaging Science Experiment (HiRISE) (McEwen et al., 2007), the Context Camera (CTX) (Malin et al., 2007), and the Compact Reconnaissance Imaging Spectrometer for Mars (CRISM) (Murchie et al., 2007); the 2001 Mars Odyssey spacecraft on boards The Thermal Emission Imaging System (THEMIS) (Christensen et al., 2004); the Mars Global Surveyor (MGS) on boards the Thermal Emission Spectrometer (TES) (Christensen et al., 2001), Mars Orbiter Camera (MOC), and Mars Orbiter Laser Altimeter (MOLA; Smith et al., 2001)

data; and Mars Expresses (MEx) on boards the High Rise Stereo Camera (HRSC; Neukum et al., 2004) and The Observatoire pour la Minéralogie, l'Eau, les Glaces et l'Activité (OMEGA; Bibring et al., 2004). These sensors have a different spectral and spatial resolution as schematically showing in a nutshell in Fig. 2.3 (adopted from Jaumann et al., 2015).

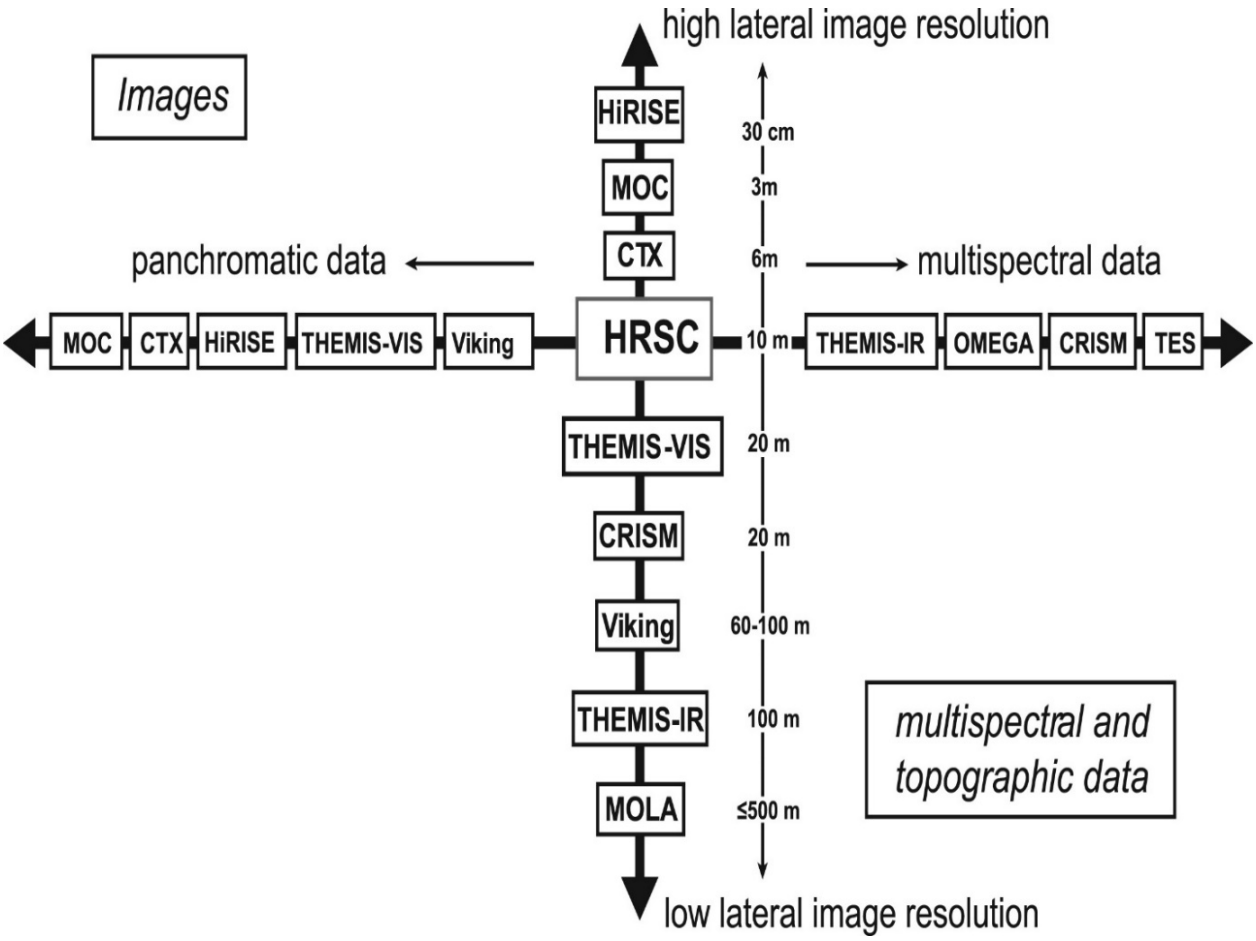

Fig. 2.4: The schematic diagram showing spectral and spatial resolution of orbital spacecraft data of Mars as adopted from Jaumann et al. (2015). The spectral resolution covers from single-band panchromatic data to multi-and-hyperspectral data. The spatial resolution of the orbital data sets ranging from the highest resolution of ~25 cm to the ≤ 500 m as a coarser resolution.

2.5.1: Mars Reconnaissance Orbiter (MRO)

2.5.1.1: High Resolution Imaging Science Experiment (HiRISE)

The High Resolution Imaging Science Experiment (HiRISE) onboard the Mars Reconnaissance Orbiter (MRO) is a telescope working in orbit at the visible and near-infrared (VNIR) wavelengths (McEwen et al., 2007; Zurek and Smrekar, 2007; Delamere et al., 2010). HiRISE produces high-resolution images for identifying or detecting surface details at a spatial resolution of 1-meter size or 0.25 to 1.3 m/pixel (McEwen et al., 2007). The HiRISE camera includes a total of 14 charged coupled device (CCD) of 3 different colors; red (RED), blue-green (BG), and near-infrared (NIR). The wavelength ranges of RED, BG, and NIR are 570-830 nm, <580 nm, and >790 nm, respectively (McEwen et al., 2007). The high-resolution color images enable the estimations of surface compositions and albedo heterogeneities which are directly correlated to the geomorphology and complementary to the mineralogic results from other orbital images such as CRISM, HRSC, OMEGA, and THEMIS instruments (Zurek and Smrekar, 2007; Quantin-Nataf et al., 2018). The images from the red detectors are used for a local scale geomorphologic and stereo-analysis (Quantin-Nataf et al. 2018). The other detector (i.e., blue-green and near-infrared) images are used to create false-color imaging of the martian surface (McEwen et al., 2007; Delamere et al., 2010). HiRISE images produce a high-resolution digital elevation model or DEM (spatial resolution around 1 meter per pixel) and it also produces an orthorectified image (spatial resolution about 0.25 per pixel) (McEwen et al., 2007). The details about HiRISE image processing to create HiRISE DTMs are described in Kirk et al. (2008). DEMs of HiRISE can be processed through different interfaces and procedures such as using NASA Ames Stereo Pipeline (ASP) stereogrammetry software (Broxton and Edwards, 2008; Moratto et al., 2010; Beyer et al., 2014). HiRISE images enable an analyst to not only study, for instance, the martian geomorphology but also seasonal surface changes

if any (Quantin-Nataf et al., 2018). The dip-strike characteristics of bedding are also derived from stereo photogrammetry of the HiRISE dataset (Goudge et al., 2017).

2.5.1.2: Compact Reconnaissance Imaging Spectrometers for Mars (CRISM)

The Mars Reconnaissance Orbiters (MRO) onboard the Compact Reconnaissance Imaging Spectrometer for Mars (CRISM) is a hyperspectral imager including visible and infrared wavelengths (Murchie et al., 2007). The observations enable the extraction of mineralogy information of the martian surface at a spatial resolution of ~20 m/pixel at the highest resolution (Murchie et al., 2007). The CRISM instrument acquires hyperspectral images of visible to near-infrared wavelengths (VNIR; spectral wavelength range of 0.37–3.92 mm at a spectral sampling of 6.55 nm per channel) and has two data acquisition modes of operation: targeted hyperspectral and mapped multispectral (Murchie et al., 2007). The hyperspectral targeted mode tracks the targets and takes 11 hyperspectral images (544 bands from 362 to 3920 nm) at different emission angles whereas multispectral untargeted mode with 72 bands chosen over the 544 spectral bands to identify principal minerals (Murchie et al., 2007). The half resolution short (HRS) and half resolution long (HRL) observations at a spatial resolution of 40 m/pixel are produced by reducing the spatial resolution (by a factor of 2) of the central images of observations (Murchie et al., 2007). The push scanner of the instrument stacks multiple scan lines to produce the hyperspectral image as the MRO spacecraft orbits over the surface (Murchie et al., 2007). The scanner acquires at a highest 18 m spatial resolution images with a swath about 10 km width from an altitude of 300 km (Murchie et al., 2007). There are also different versions of datasets available in the Planetary Data System (PDS) website such as targeted reduced data records (TRDR), map projected targeted reduced data records (MTRDR), etc. (e.g., Pelkey et al., 2007; Murchie et al., 2007; Viviano-Beck et al., 2014). However, the new version called Map-projected Targeted Reduced Data Record (MTRDR) products is derived by processing CRISM

hyperspectral targeted observations (TRDR) products. The TRDR records radiance at the sensor which is processed through a set of standard spectral corrections routines (e.g., atmospheric correction, volcanic scan correction, etc.), spatial transforms (e.g., geometric correction), and then rendered to identify the minerals (Viviano-Beck et al., 2014 and 2017).

2.5.1.3: Context Camera (CTX)

The Context Camera (CTX) onboard the Mars Reconnaissance Orbiters (MRO) is a grayscale camera (panchromatic) that acquires images at ~6 m/pixel spatial resolution (Malin et al., 2007). The CTX instrument consists of a digital electronics arrangement of 5.7° field of view (FOV) and a swath width of ~30-km enabling to capture images from a ~290 km altitude. The sensor has a bandpass of 500–700 nm that acquires images at ~6 m/pixel at a highest spatial resolution from a nearly polar circular mapping orbit (Malin et al., 2007). CTX provides context images for the MRO's HiRISE and CRISM observations and the images are used to monitor potential changes that happen on the surface of the planet at the very local scale if any (e.g., geological and meteorological). The CTX sensor acquires stereo pairs of selected as well as important science targets such as observational features of interest to Mars exploration programs of NASA or other space agencies like ESA, for instance, selection and characterization of candidate landing sites e.g., Mars 2020 (Malin et al., 2007). The stereo-pair of CTX is used to produce digital elevation models (DEMs) for topographic and morphologic mapping and provides the wider context for the images collected by the other two abovementioned instruments (Malin et al., 2007). ISIS3 and Ames Stereo pipelines (ASP) software are used for CTX data calibration, projection and producing the DEMs (Quantin-Nataf et al., 2018). The detail of the CTX image processing and producing a digital elevation model (DEM) from the stereo pairs are described in the subsequent chapters (for detail the readers are also referred to the subsequent chapters).

2.5.2: Mars Express (MEX)

2.5.2.1: High Resolution Stereo Camera (HRSC)

The High Resolution Stereo Camera (HRSC) is a multi-channel stereo color push-broom camera onboard the European Space Agency (ESA)'s Mars Express (MEx) spacecraft mission. HRSC captures global imagery of martian surface in both panchromatic and color images which pave the way to produce stereo-imagery for DTM production (e.g., Neukum et al., 2004; Jaumman et al., 2007; Gwinner et al., 2016). HRSC comprises multiple charge coupled device (CCD) line sensors for capturing multiple data products in multiphase images (e.g., emergence angles). In each observation, the sensor acquires 5 panchromatic images (grayscale) at different emergence angles. Among these 5 images, one is captured in the nadir channel and rest of 4 are taken with 4 different color filters at different emergence angles (Neukum et al., 2004). The highest resolution image generally comes from the nadir image than the other images. The multiple color images are used to produce the stereo-derived DEM which enables one to characterize the martian surface at different viewing angles (Jaumann et al., 2007; Quantin-Nataf et al., 2018). HRSC images are acquired at minimum 10 m/pixel to 100's m/pixel spatial resolution at different parts of the martian surface. Typically, the nadir channel images are 8-bit orthoimages whereas the stereo-derived DEM are produced in16-bit (e.g., Gwinner et al., 2016; Quantin-Nataf et al., 2018). HRSC images cover the entire planet and are used in the topographical and morphologic mapping (Neukum et al., 2004).

2.5.2.2: Observatoire pour la Minéralogie, l'Eau, les Glaces et l'Activité (OMEGA)

The Observatoire pour la Minéralogie, l'Eau, les Glaces et l'Activité (OMEGA) onboard Mars Express (MEx) spacecraft is a visible and near-infrared (VNIR) imaging spectrometer (Bibring et al., 2004). OMEGA captures images with 352 spectral channels at the wavelengths 0.38-5.1 μm at a spectral sampling of 7 to 20 nm (Bibring et al., 2004). Depending on spacecraft altitude and

acquisition time, the spatial resolution varies image to images ranging from ~300 m to 5 km per pixel (Bibring et al., 2004). OMEGA instrument has two different spectrometers in visible-near infrared (VNIR) and another short wavelength infrared (SWIR). The visible and near infrared (VNIR) sensor works in the wavelength range of 0.38-1.05 μm (Bibring et al., 2004). The short wavelength infrared (SWIR) captures images in 0.93-5.1 μm (Bibring et al., 2004). The instrument has two different modes in different spectral arrangements: the VNIR spectrometer acquires data in push-broom mode whereas the SWIR spectrometers is a whiskbroom sensor (Bibring et al., 2004). The VNIR captures data with a spectral dimension of 96 elements whereas SWIR acquires images with two 128-element line detectors (Bibring et al., 2004; Quantin-Nataf et al., 2018). The instrument captures data with various spatial resolutions, different widths under various incidence and emission conditions for identifying the mineral diversity of Mars (Quantin-Nataf et al., 2018). Both CRISM and OMEGA are used by planetary researchers in detecting and analyzing the primary and altered minerals of a variety of mineral species (e.g., Pelkey et al., 2007; Viviano-Beck et al., 2014).

2.5.3: Mars Odyssey (ODY)

2.5.3.1: Thermal Emission Imaging System (THEMIS)

The Thermal Emission Imaging System (THEMIS) onboard the 2001 Mars Odyssey (ODY) spacecraft is a multispectral imager for Mars. The sensor data are used in analyzing morphology, thermophysical and composition, and physical characteristics of the martian surface (Christensen et al., 2004). THEMIS has 9 channels in the thermal infrared (TIR) bands with a range between 6.78 μm and 14.88 μm (Christensen et al., 2004). The sensor has also 5 channels in the visible (VIS) bands 0.42μm through 0.86μm (Christensen et al., 2004). THEMIS acquires data in different (and spatial resolution) modes such as thermal infrared (TIR) data at a spatial resolution of 100 m/pixel

both in daytime and nighttime, and visible (VIS) images with a spatial resolution of 18 to 35 m/pixel in daytime (Christensen et al., 2004). TIR images have approximately 30 km width and >100 km length covering the entire martian global surface. This global coverage enables researchers to study Mars at a regional scale. Nighttime TIR images are used to calculate thermal inertia whereas daytime images are used for calculating albedo of the martian surface. Since THEMIS has a higher spatial resolution (~100 m/pixel) than the TES pixels (3 km/pixel), the THEMIS data are more useful for the local and regional scale analysis compared to TES data (Quantin-Nataf et al., 2018). THEMIS dataset has a global coverage that allows a regional and planetary scale study at a higher resolution. THEMIS TIR captures high spatial resolution for the investigation of important surface characteristics including morphological, thermophysical, and composition properties of the planet (Christensen et al., 2004).

2.5.4: Mars Global Surveyor (MGS)

2.5.4.1: Thermal Emission Spectrometer (TES)

Mars Global Surveyor (MGS) onboard the Thermal Emission Spectrometer (TES) is an infrared (5.8- to 50-μm) interferometric spectrometer (Christensen et al., 2001). The instrument also includes a broadband thermal (5.1 μm to 150 μm) radiometer and a visible/near-IR (0.3 μm to 2.9 μm) radiometer (Christensen et al., 2001). TES investigations are broadly used in analyzing different characteristics of martian surfaces, for instance; surface composition (minerals, rocks, and ices), characteristics of the polar region, and surface thermophysical characteristics (Christensen et al., 2001). Besides, the TES investigation is used to characterize the atmospheric properties of Mars such as temperature changes and dynamics of the atmosphere and the properties of the martian atmospheric aerosols and clouds (Christensen et al., 2001). The TES measures radiance from both the atmosphere and surface of the Mars roughly in 3x6 km^2 spatial scale. The TES records

hyperspectral data over 142 channels (Christensen et al., 2001). The data are recorded between 1651 cm^{-1} and 201 cm^{-1} (6.1 μm–49.7 μm) with a sampling interval of 10 cm^{-1} and 5 cm^{-1} (Christensen et al., 2001). However, to ensure the highest quality of data used, one should subset data considering a few parameters as described in Rogers and Bandfield (2009) and Salvatore et al. (2018). TES spectra are selected based on in the early mapping orbit phase (orbital clock keeper: ock 1- 5317) with higher surface temperatures (≥260 K), low emission angle (<30°), low total ice (≤0.04), low lambert albedo (<0.14), and low total dust (≤0.15) (e.g., Salvatore et al., 2018). MGS onboard the Thermal Emission Spectrometer (TES) instrument measures emitted infrared (IR) energy (Christensen et al., 2001). The brightness and surface kinetic temperature (surface temperature) are inferred from this measured infrared energy (Christensen et al., 2001). With the determination of brightness (and surface) temperature and thermal inertia, one can map the surface physical properties of the planet to understand the spatial distribution and transport of surface materials (e.g., Kieffer et al., 1977; Palluconi and Kieffer, 1981). TIR data from TES are used to detect bulk-mineralogy through employing spectral deconvolution analysis with selected laboratory mineral endmember spectra.

2.5.4.2: Mars Orbiter Laser Altimeter (MOLA)

The Mars Orbiter Laser Altimeter (MOLA) instrument is onboard the Mars Global Surveyor (MGS) spacecraft. The MOLA investigations measure topography, surface roughness, 1.064 μm reflectivity of the planet, and volatile and dust clouds heights (Smith et al., 2001). The instrument measures the overall time for a laser pulse takes to reach its target (both from the martian surface or atmospheric layers) and return to the spacecraft to calculate elevation. The MOLA points are collected at an interval of 300 m along their tracks and separated from other tracks by 4 km (Smith et al., 2001). Though the original data are point shot laser altimeter or elevation data, planetary data systems (PDS) processed gridded data from MOLA observation that are available on orbital data

explorer (ODE) website. The gridded data are available as Mission Experiment Gridded Data Record (MEGDR) with a spatial resolution of 128/64/32/16/4 pixels per degree (ppd). The MOLA point shot data are also in processing DEMs of HiRISE, CTX, and HRSC from stereo pair of these high-resolution sensors.

2.6: Conclusion

Mars is the planet of human's most curiosity since it has alike characteristics of the earth such as eccentricity, orbital inclination, seasonality and similar kind of landform (e.g., Faure 2007; Carr 1980; Barlow 2008). Studying Mars adds to the knowledge about the earlier history of the solar system. The surface of Mars is the blueprint of its earlier history. Therefore, the study of Mars demands details on thermophysical, morphological and stratigraphic, and mineralogical characterization. Accumulation of this information allows ascertaining characteristics of landforms and climates of early Mars. Orbital data are the reconnaissance information for the future manned mission or rover mission (e.g., Mars 2020) to the surface of Mars. There are many areas, for instance, NW Isidis and NE Sytris of Mars, that are major areas interest for the planetary exploration of the diverse history of mineralogy, morphology, and stratigraphic architecture. This study aimed at identifying thermophysical, morphological, stratigraphic, and mineralogical characteristics of different parts of Mars. The study solely uses orbital remote sensing imagery of visible (VIS), near-infrared (NIR), shortwave infrared (SWIR), and thermal infrared (TIR) data of the sensors the HiRISE, CTX, HRSC, CRISM, THEMIS, TES, MOC, and MOLA. The study expects that the outcomes from this orbital data characterization of the study area would augment scientific knowledge in deciding future rover and lander *in-situ* exploration on the surface of Mars.

References

Bandfield, Joshua L., Deanne Rogers, Michael D. Smith, and Philip R. Christensen, 2004. Atmospheric Correction and Surface Spectral Unit Mapping Using Thermal Emission Imaging System Data. Journal of Geophysical Research: Planets 109 (E10):E10008. https://doi.org/10.1029/2004JE002289.

Barlow, N., 2008. Mars: An Introduction to its Interior, Surface and Atmosphere. Cambridge University Press, Cambridge: UK. ISBN 978-0-521-85226-5

Beyer, R.A., O. Alexandrov, and Z. Moratto., 2014. Aligning terrain model and laser altimeter point clouds with the Ames Stereo Pipeline. Lunar Planet. Sci., 45. Abstract 2902. https://www.hou.usra.edu/meetings/lpsc2014/pdf/2902.pdf

Bibring, J.-P., A. Soufflot, M. Berthé, Y. Langevin, B. Gondet, P. Drossart, M. Bouyé, et al., 2004. OMEGA: Observatoire Pour La Minéralogie, l'Eau, Les Glaces et l'Activité. In Mars Express - The Scientific Payload, European Space Agency Special Publication, SP-1240, edited, pp. 37-49, ESA. http://adsabs.harvard.edu/abs/2004ESASP1240...37B.

Blair, Terence C., and John G. McPherson., 1994. Alluvial Fans and Their Natural Distinction from Rivers Based on Morphology, Hydraulic Processes, Sedimentary Processes, and Facies Assemblages. Journal of Sedimentary Research 64 (3a):450–89. https://doi.org/10.1306/D4267DDE-2B26-11D7-8648000102C1865D.

Bramble, Michael S., John F. Mustard, and Mark R. Salvatore., 2017. The Geological History of Northeast Syrtis Major, Mars. Icarus 293 (Supplement C):66–93. https://doi.org/10.1016/j.icarus.2017.03.030.

Broxton, M.J., and L.J. Edwards., 2008. The Ames Stereo Pipeline: automated 3D surface reconstruction from orbital imagery. Lunar Planet. Sci., 39, Abstract 2419 http://adsabs.harvard.edu/abs/2008LPI....39.2419B.

Canup, R.M. and C.B. Agnor., 2000. Accretion of the terrestrial planets and the Earth–Moon system. In Origin of the Earth and Moon, edt. R.M. Canup and K. Righter. Tucson, AZ: University of Arizona Press.

Carr, M.H., 1980. The Morphology of the Martian Surface. Space Science Review 25 (3): 231-284 https://doi.org/10.1007/BF00221929

Carr, M.H., 2007. The Surface of Mars. Cambridge University Press.

Carr, M.H., 2012. The fluvial history of Mars. Philosophical Transactions of the Royal Society of London Series A 370, 2193–2215. https://doi.org/10.1098/rsta.2011.0500

Carr, M.H., Head, J.W., 2010. Geologic history of Mars. Earth and Planetary Science Letters, Mars Express after 6 Years in Orbit: Mars Geology from Three-Dimensional Mapping by the High Resolution Stereo Camera (HRSC) Experiment 294, 185–203. https://doi.org/10.1016/j.epsl.2009.06.042

Carr, M.H., Head, J.W., 2010. Geologic history of Mars. Earth and Planetary Science Letters, Mars Express after 6 Years in Orbit: Mars Geology from Three-Dimensional Mapping by the High Resolution Stereo Camera (HRSC) Experiment 294, 185–203. https://doi.org/10.1016/j.epsl.2009.06.042

Chambers, John E., 2004. Planetary Accretion in the Inner Solar System. Earth and Planetary Science Letters 223 (3):241–52. https://doi.org/10.1016/j.epsl.2004.04.031.

Christensen, P. R., J. L. Bandfield, V. E. Hamilton, S. W. Ruff, H. H. Kieffer, T. N. Titus, M. C. Malin, et al., 2001. Mars Global Surveyor Thermal Emission Spectrometer Experiment:

Investigation Description and Surface Science Results. Journal of Geophysical Research: Planets 106 (E10):23823–71. https://doi.org/10.1029/2000JE001370.

Christensen, P.R., Bandfield, J.L., Hamilton, V.E., Ruff, S.W., Kieffer, H.H., Titus, T.N., Malin, M.C., Morris, R.V., Lane, M.D., Clark, R.L., Jakosky, B.M., Mellon, M.T., Pearl, J.C., Conrath, B.J., Smith, M.D., Clancy, R.T., Kuzmin, R.O., Roush, T., Mehall, G.L., Gorelick, N., Bender, K., Murray, K., Dason, S., Greene, E., Silverman, S., Greenfield, M., 2001. Mars Global Surveyor Thermal Emission Spectrometer experiment: Investigation description and surface science results. Journal of Geophysical Research: Planets 106, 23823–23871. https://doi.org/10.1029/2000JE001370

Christensen, P.R., Jakosky, B.M., Kieffer, H.H., Malin, M.C., McSween, H.Y., Nealson, K., Mehall, G.L., Silverman, S.H., Ferry, S., Caplinger, M., Ravine, M., 2004. The Thermal Emission Imaging System (THEMIS) for the Mars 2001 Odyssey Mission. Space Science Reviews 110, 85–130. https://doi.org/10.1023/B:SPAC.0000021008.16305.94

Christensen, Philip R. 1988. Global Albedo Variations on Mars: Implications for Active Aeolian Transport, Deposition, and Erosion. Journal of Geophysical Research: Solid Earth 93 (B7):7611–24. https://doi.org/10.1029/JB093iB07p07611.

Christensen, Philip R., 1998. Variations in Martian Surface Composition and Cloud Occurrence Determined from Thermal Infrared Spectroscopy: Analysis of Viking and Mariner 9 Data. Journal of Geophysical Research: Planets 103 (E1):1733–46. https://doi.org/10.1029/97JE02114.

Christensen, Philip R., Bruce M. Jakosky, Hugh H. Kieffer, Michael C. Malin, Harry Y. Mcsween Jr, Kenneth Nealson, Greg L. Mehall, et al., 2004. The Thermal Emission Imaging System (Themis) for the Mars 2001 Odyssey Mission. In 2001 Mars Odyssey, 85–130. Springer, Dordrecht. https://doi.org/10.1007/978-0-306-48600-5_3.

Christensen, Philip R., Joshua L. Bandfield, James F. Bell III, Noel Gorelick, Victoria E. Hamilton, Anton Ivanov, Bruce M. Jakosky, et al., 2003. Morphology and Composition of the Surface of Mars: Mars Odyssey THEMIS Results. Science 300 (5628):2056–61. https://doi.org/10.1126/science.1080885.

Delamere, W. Alan, Livio L. Tornabene, Alfred S. McEwen, Kris Becker, James W. Bergstrom, Nathan T. Bridges, Eric M. Eliason, et al., 2010. Color Imaging of Mars by the High Resolution Imaging Science Experiment (HiRISE). Icarus, MRO/HiRISE Studies of Mars, 205 (1): 38–52. https://doi.org/10.1016/j.icarus.2009.03.012.

Dinwiddie, Robert, Philip Eales, David Hughes, Iain Nicolson, Ian Ridpath, Robin Scagell, Giles Sparrow, Pam Spence, Carole Stott, and Kevin Tildsley., 2012. In Universe. edt. Martin Rees. Revised, Updated ed. edition. New York: DK.

Edgett, K.S., Christensen, P.R., 1991. The particle size of Martian aeolian dunes. Journal of Geophysical Research: Planets 96, 22765–22776. https://doi.org/10.1029/91JE02412

Edwards, C. S., K. J. Nowicki, P. R. Christensen, J. Hill, N. Gorelick, and K. Murray., 2011. Mosaicking of Global Planetary Image Datasets: 1. Techniques and Data Processing for Thermal Emission Imaging System (THEMIS) Multi-Spectral Data. Journal of Geophysical Research: Planets 116 (E10):E10008. https://doi.org/10.1029/2010JE003755.

Ehlmann, B.L., Edwards, C.S., 2014. Mineralogy of the Martian Surface. Annual Review of Earth and Planetary Sciences 42, 291–315. https://doi.org/10.1146/annurev-earth-060313-055024

Ehlmann, Bethany L., and John F. Mustard., 2012., An In-Situ Record of Major Environmental Transitions on Early Mars at Northeast Syrtis Major. Geophysical Research Letters 39 (11):L11202. https://doi.org/10.1029/2012GL051594

Ehlmann, Bethany L., John F. Mustard, Caleb I. Fassett, Samuel C. Schon, James W. Head III, David J. Des Marais, John A. Grant, and Scott L. Murchie., 2008. Clay Minerals in Delta

Deposits and Organic Preservation Potential on Mars. Nature Geoscience 1 (6):ngeo207. https://doi.org/10.1038/ngeo207.

Ehlmann, Bethany L., John F. Mustard, Gregg A. Swayze, Roger N. Clark, Janice L. Bishop, Francois Poulet, David J. Des Marais, et al., 2009. Identification of Hydrated Silicate Minerals on Mars Using MRO-CRISM: Geologic Context near Nili Fossae and Implications for Aqueous Alteration. Journal of Geophysical Research: Planets 114 (E2):E00D08. https://doi.org/10.1029/2009JE003339.

Fassett, Caleb I., and James W. Head., 2005. Fluvial Sedimentary Deposits on Mars: Ancient Deltas in a Crater Lake in the Nili Fossae Region. Geophysical Research Letters 32 (14):L14201. https://doi.org/10.1029/2005GL023456.

Faure, G and T.M. Mensing., 2008. Introduction to Planetary Science: The Geological Prspective. Springer Netherlands. doi 10.1007/978-1-4020-5544-7

Gillespie, Alan R., 1992. Enhancement of Multispectral Thermal Infrared Images: Decorrelation Contrast Stretching. Remote Sensing of Environment 42 (2):147–55. https://doi.org/10.1016/0034-4257(92)90098-5.

Goudge, T. A., B. L. Ehlmann, C. I. Fassett, J. W. Head, J. F. Mustard, N. Mangold, S. Gupta, R. E. Milliken,and A. J., 2017b. Jezero Crater, Mars, as a Compelling Site for Future In Situ Exploration. In 48th Lunar and Planetary Science Conference, 20-24 Mar. 2017. The Woodlands, TX; United States. https://ntrs.nasa.gov/search.jsp?R=20170002464.

Goudge, T.A., Milliken, R.E., Head, J.W., Mustard, J.F., Fassett, C.I., 2017. Sedimentological evidence for a deltaic origin of the western fan deposit in Jezero crater, Mars and implications for future exploration. Earth and Planetary Science Letters 458, 357–365. https://doi.org/10.1016/j.epsl.2016.10.056

Goudge, Timothy A., John F. Mustard, James W. Head, Caleb I. Fassett, and Sandra M. Wiseman., 2015b. Assessing the Mineralogy of the Watershed and Fan Deposits of the Jezero Crater Paleolake System, Mars. Journal of Geophysical Research: Planets 120 (4):2014JE004782. https://doi.org/10.1002/2014JE004782.

Goudge, Timothy A., John F. Mustard, James W. Head, Mark R. Salvatore, and Sandra M. Wiseman., 2015a. Integrating CRISM and TES Hyperspectral Data to Characterize a Halloysite-Bearing Deposit in Kashira Crater, Mars. Icarus 250 (Supplement C):165–87. https://doi.org/10.1016/j.icarus.2014.11.034.

Goudge, Timothy A., Ralph E. Milliken, James W. Head, John F. Mustard, and Caleb I. Fassett., 2017a. Sedimentological Evidence for a Deltaic Origin of the Western Fan Deposit in Jezero Crater, Mars and Implications for Future Exploration. Earth and Planetary Science Letters 458 (Supplement C):357–65. https://doi.org/10.1016/j.epsl.2016.10.056.

Gupta, R.P., 1991. Remote Sensing Geology. Springer-Verlag, Berlin Heidelberg.

Gwinner, K., R. Jaumann, E. Hauber, H. Hoffmann, C. Heipke, J. Oberst, G. Neukum, et al., 2016. The High Resolution Stereo Camera (HRSC) of Mars Express and Its Approach to Science Analysis and Mapping for Mars and Its Satellites. Planetary and Space Science 126 (July): 93–138. https://doi.org/10.1016/j.pss.2016.02.014.

Haberle, Robert M., and Bruce M. Jakosky., 1991. Atmospheric Effects on the Remote Determination of Thermal Inertia on Mars. Icarus 90 (2):187–204. https://doi.org/10.1016/0019-1035(91)90100-8.

Hartmann, W.K., Neukum, G., 2001. Cratering Chronology and the Evolution of Mars. Space Science Reviews 96, 165–194. https://doi.org/10.1023/A:1011945222010

Hayashi, Joan N., Bruce M. Jakosky, and Robert M. Haberle., 1995. Atmospheric Effects on the Mapping of Martian Thermal Inertia and Thermally Derived Albedo. Journal of Geophysical Research: Planets 100 (E3):5277–84. https://doi.org/10.1029/94JE02449.

Hayward, R.K., Fenton, L., Titus, T.N., 2014. Mars Global Digital Dune Database (MGD3): Global dune distribution and wind pattern observations. Icarus 230, 9. https://doi.org/10.1016/j.icarus.2013.04.011

Hayward, R.K., Mullins, K.F., Fenton, L.K., Hare, T.M., Titus, T.N., Bourke, M.C., Colaprete, A., Christensen, P.R., 2007. Mars global digital dune database and initial science results. Journal of Geophysical Research E: Planets 112. https://doi.org/10.1029/2007JE002943

Howard, Alan D., Jeffrey M. Moore, and Rossman P. Irwin., 2005. An Intense Terminal Epoch of Widespread Fluvial Activity on Early Mars: 1. Valley Network Incision and Associated Deposits. Journal of Geophysical Research: Planets 110 (E12):E12S14. https://doi.org/10.1029/2005JE002459.

Hoyt, W.G., Wesley, W.G., 1977. Lowell and Mars. American Journal of Physics 45, 316–317. https://doi.org/10.1119/1.10630

Hynek, B.M., Phillips, R.J., 2003. New data reveal mature, integrated drainage systems on Mars indicative of past precipitation. Geology 31, 757–760. https://doi.org/10.1130/G19607.1

Irwin, Rossman P., Alan D. Howard, Robert A. Craddock, and Jeffrey M. Moore., 2005. An Intense Terminal Epoch of Widespread Fluvial Activity on Early Mars: 2. Increased Runoff and Paleolake Development. Journal of Geophysical Research: Planets 110 (E12):E12S15. https://doi.org/10.1029/2005JE002460.

Jakosky, Bruce M., 1986. On the Thermal Properties of Martian Fines. Icarus 66 (1):117–24. https://doi.org/10.1016/0019-1035(86)90011-4.

Jakosky, Bruce M., Michael T. Mellon, Hugh H. Kieffer, Philip R. Christensen, E. Stacy Varnes, and Steven W. Lee., 2000. The Thermal Inertia of Mars from the Mars Global Surveyor Thermal Emission Spectrometer. Journal of Geophysical Research: Planets 105 (E4):9643–52. https://doi.org/10.1029/1999JE001088.

Jarell, Elizabeth M., 2015. Using Curiosity to Search for Life. Mars Daily. Last Accessed October 25, 2017. http://www.marsdaily.com/reports/Using_Curiosity_to_Search_for_Life_

Jaumann, R., G. Neukum, T. Behnke, T. C. Duxbury, K. Eichentopf, J. Flohrer, S. v. Gasselt, et al., 2007. The High-Resolution Stereo Camera (HRSC) Experiment on Mars Express: Instrument Aspects and Experiment Conduct from Interplanetary Cruise through the Nominal Mission. Planetary and Space Science 55 (7): 928–52. https://doi.org/10.1016/j.pss.2006.12.003.

Jaumann, R., Tirsch, D., Hauber, E., Ansan, V., Di Achille, G., Erkeling, G., Fueten, F., Head, J., Kleinhans, M.G., Mangold, N., Michael, G.G., Neukum, G., Pacifici, A., Platz, T., Pondrelli, M., Raack, J., Reiss, D., Williams, D.A., Adeli, S., Baratoux, D., de Villiers, G., Foing, B., Gupta, S., Gwinner, K., Hiesinger, H., Hoffmann, H., Deit, L.L., Marinangeli, L., Matz, K.-D., Mertens, V., Muller, J.P., Pasckert, J.H., Roatsch, T., Rossi, A.P., Scholten, F., Sowe, M., Voigt, J., Warner, N., 2015. Quantifying geological processes on Mars—Results of the high resolution stereo camera (HRSC) on Mars express. Planetary and Space Science 112, 53–97. https://doi.org/10.1016/j.pss.2014.11.029

Kieffer, H. H., S. C. Chase, E. Miner, G. Münch, and G. Neugebauer., 1973. Preliminary Report on Infrared Radiometric Measurements from the Mariner 9 Spacecraft. Journal of Geophysical Research 78 (20):4291–4312. https://doi.org/10.1029/JB078i020p04291.

Kieffer, Hugh H., T. Z. Martin, Alan R. Peterfreund, Bruce M. Jakosky, Ellis D. Miner, and Frank Don Palluconi., 1977. Thermal and Albedo Mapping of Mars during the Viking Primary

Mission. Journal of Geophysical Research 82 (28):4249–91. https://doi.org/10.1029/JS082i028p04249.
Kirk, R. L., E. Howington-Kraus, M. R. Rosiek, J. A. Anderson, B. A. Archinal, K. J. Becker, D. A. Cook, et al., 2008. Ultrahigh Resolution Topographic Mapping of Mars with MRO HiRISE Stereo Images: Meter-Scale Slopes of Candidate Phoenix Landing Sites. Journal of Geophysical Research: Planets 113 (E3): E00A24. https://doi.org/10.1029/2007JE003000.
Lewis, Kevin W., and Oded Aharonson., 2006. Stratigraphic Analysis of the Distributary Fan in Eberswalde Crater Using Stereo Imagery. Journal of Geophysical Research: Planets 111 (E6):E06001. https://doi.org/10.1029/2005JE002558.
Malin, Michael C., and Kenneth S. Edgett., 2003. Evidence for Persistent Flow and Aqueous Sedimentation on Early Mars. Science 302 (5652):1931–34. https://doi.org/10.1126/science.1090544.
Malin, Michael C., James F. Bell, Bruce A. Cantor, Michael A. Caplinger, Wendy M. Calvin, R. Todd Clancy, Kenneth S. Edgett, et al., 2007. Context Camera Investigation on Board the Mars Reconnaissance Orbiter. Journal of Geophysical Research: Planets 112 (E5):E05S04. https://doi.org/10.1029/2006JE002808.
Mangold, N., F. Poulet, J. F. Mustard, J.-P. Bibring, B. Gondet, Y. Langevin, V. Ansan, et al., 2007. Mineralogy of the Nili Fossae Region with OMEGA/Mars Express Data: 2. Aqueous Alteration of the Crust. Journal of Geophysical Research: Planets 112 (E8):E08S04. https://doi.org/10.1029/2006JE002835.
Mangold, N., Poulet, F., Mustard, J.F., Bibring, J.-P., Gondet, B., Langevin, Y., Ansan, V., Masson, P., Fassett, C., Head, J.W., Hoffmann, H., Neukum, G., 2007. Mineralogy of the Nili Fossae region with OMEGA/Mars Express data: 2. Aqueous alteration of the crust. Journal of Geophysical Research: Planets 112. https://doi.org/10.1029/2006JE002835
McEwen, A.S., Eliason, E.M., Bergstrom, J.W., Bridges, N.T., Hansen, C.J., Delamere, W.A., Grant, J.A., Gulick, V.C., Herkenhoff, K.E., Keszthelyi, L., Kirk, R.L., Mellon, M.T., Squyres, S.W., Thomas, N., Weitz, C.M., 2007. Mars Reconnaissance Orbiter's High Resolution Imaging Science Experiment (HiRISE). Journal of Geophysical Research: Planets 112. https://doi.org/10.1029/2005JE002605
Mellon, M.T., Jakosky, B.M., Kieffer, H.H., Christensen, P.R., 2000. High-Resolution Thermal Inertia Mapping from the Mars Global Surveyor Thermal Emission Spectrometer. Icarus 148, 437–455. https://doi.org/10.1006/icar.2000.6503
Mellon, Michael T., and Bruce M. Jakosky., 1993. Geographic Variations in the Thermal and Diffusive Stability of Ground Ice on Mars. Journal of Geophysical Research: Planets 98 (E2):3345–64. https://doi.org/10.1029/92JE02355.
MER., 2013. The Mars Exploration Rover Mission. NASA Report. November 2013, 20. Last Accessed October 25, 2017. https://mars.nasa.gov/mer/home/resources/MERLithograph.pdf
Michalski, J.R., Bleacher, J.E., 2013. Supervolcanoes within an ancient volcanic province in Arabia Terra, Mars. Nature 502, 47–52. https://doi.org/10.1038/nature12482
Moratto, Z.M., M.J. Broxton, R.A. Beyer, M. Lundy, K., 2010. HusmannAmes Stereo Pipeline, NASA's open source automated stereogrammetry software. Lunar Planet. Sci., 41, Article Abstract 2364. http://adsabs.harvard.edu/abs/2010LPI....41.2364M
Murchie, S., Arvidson, R., Bedini, P., Beisser, K., Bibring, J.-P., Bishop, J., Boldt, J., Cavender, P., Choo, T., Clancy, R.T., Darlington, E.H., Marais, D.D., Espiritu, R., Fort, D., Green, R., Guinness, E., Hayes, J., Hash, C., Heffernan, K., Hemmler, J., Heyler, G., Humm, D., Hutcheson, J., Izenberg, N., Lee, R., Lees, J., Lohr, D., Malaret, E., Martin, T., McGovern, J.A., McGuire, P., Morris, R., Mustard, J., Pelkey, S., Rhodes, E., Robinson, M., Roush, T.,

Schaefer, E., Seagrave, G., Seelos, F., Silverglate, P., Slavney, S., Smith, M., Shyong, W.-J., Strohbehn, K., Taylor, H., Thompson, P., Tossman, B., Wirzburger, M., Wolff, M., 2007. Compact Reconnaissance Imaging Spectrometer for Mars (CRISM) on Mars Reconnaissance Orbiter (MRO). Journal of Geophysical Research: Planets 112. https://doi.org/10.1029/2006JE002682

Murphy, N. W., B. M. Jakosky, S. C. R. Rafkin, K. Larsen, N. E. Putzig, and M. T. Mellon., 2005. Thermophysical Properties of the Surface of Isidis Basin, Mars. Lunar Planet. Sci., 2005. Abstract 2218. https://www.lpi.usra.edu/meetings/lpsc2005/pdf/2218.pdf

Murphy, Nathaniel W., Bruce M. Jakosky, Scot C. Rafkin, Kristopher W. Larsen, Nathaniel E. Putzig, and Michael T. Mellon., 2007. Thermophysical Properties of the Isidis Basin, Mars. Journal of Geophysical Research: Planets 112 (E5):E05004. https://doi.org/10.1029/2005JE002586.

Mustard, J. F., B. L. Ehlmann, S. L. Murchie, F. Poulet, N. Mangold, J. W. Head, J.-P. Bibring, and L. H. Roach., 2009. Composition, Morphology, and Stratigraphy of Noachian Crust around the Isidis Basin. Journal of Geophysical Research: Planets 114 (E2):E00D12. https://doi.org/10.1029/2009JE003349.

Neukum, G., R. Jaumann, HRSC Co-Investigator and Experiment Team., 2004. HRSC: The High-Resolution Stereo Camera of Mars Express. In A. Wilson (Ed.), Mars Express: The Scientific Payload, ESA, Noordwijk, The Netherlands (2004), pp. 17-35

Nimmo, F., Tanaka, K., 2005. Early Crustal Evolution of Mars. Annual Review of Earth and Planetary Sciences 33, 133–161. https://doi.org/10.1146/annurev.earth.33.092203.122637

Ori, Gian Gabriele, Lucia Marinangeli, and Antonio Baliva., 2000. Terraces and Gilbert-Type Deltas in Crater Lakes in Ismenius Lacus and Memnonia (Mars). Journal of Geophysical Research: Planets 105 (E7):17629–41. https://doi.org/10.1029/1999JE001219.

Palluconi, Frank Don, and Hugh H. Kieffer., 1981. Thermal Inertia Mapping of Mars from 60°S to 60°N. Icarus 45 (2):415–26. https://doi.org/10.1016/0019-1035(81)90044-0.

Pelkey, S. M., J. F. Mustard, S. Murchie, R. T. Clancy, M. Wolff, M. Smith, R. Milliken, et al., 2007. CRISM Multispectral Summary Products: Parameterizing Mineral Diversity on Mars from Reflectance. Journal of Geophysical Research: Planets 112 (E8):E08S14. https://doi.org/10.1029/2006JE002831.

Pelkey, Shannon M, Bruce M Jakosky, and Philip R Christensen., 2003. Surficial Properties in Melas Chasma, Mars, from Mars Odyssey THEMIS Data. Icarus 165 (1):68–89. https://doi.org/10.1016/S0019-1035(03)00152-0.

Putzig, N.E., Barratt, E.M., Mellon, M.T., Michaels, T.I., 2013. MARSTHERM: A Web-based System Providing Thermophysical Analysis Tools for Mars Research Abstract P43C-2023. Poster presented at the AGU Fall Meeting in San Frnacisco, Decemeber 12. http://nathaniel.putzig.com/research/agu2013/Putzig_et_al_2013_AGU_abstract.pdf

Putzig, Nathaniel E., and Michael T. Mellon., 2007. Apparent Thermal Inertia and the Surface Heterogeneity of Mars. Icarus 191 (1):68–94. https://doi.org/10.1016/j.icarus.2007.05.013.

Putzig, Nathaniel E., Michael T. Mellon, Katherine A. Kretke, and Raymond E. Arvidson., 2005. Global Thermal Inertia and Surface Properties of Mars from the MGS Mapping Mission. Icarus 173 (2):325–41. https://doi.org/10.1016/j.icarus.2004.08.017.

Putzig, Nathaniel E., Michael T. Mellon, Kenneth E. Herkenhoff, Roger J. Phillips, Brian J. Davis, Kenneth J. Ewer, and Lauren M. Bowers., 2014. Thermal Behavior and Ice-Table Depth within the North Polar Erg of Mars. Icarus, Third Planetary Dunes Systems, 230 (Supplement C):64–76. https://doi.org/10.1016/j.icarus.2013.07.010.

Quantin-Nataf, C., L. Lozac'h, P. Thollot, D. Loizeau, B. Bultel, J. Fernando, P. Allemand, et al., 2018. MarsSI: Martian Surface Data Processing Information System. Planetary and Space

Science, Enabling Open and Interoperable Access to Planetary Science and Heliophysics Databases and Tools, 150 (January): 157–70. https://doi.org/10.1016/j.pss.2017.09.014.

Quinn, D. P., and B. L. Ehlmann., 2014. Structural Constraints on the Origin of the Sulfate-Bearing Unit at Northeast Syrtis Major. In 8th International Conference on Mars, held July 14-18, 2014 in Pasadena, California. LPI Contribution No. 1791 (1437). http://adsabs.harvard.edu/abs/2014LPICo1791.1437Q.

Ramirez, R.M., Kopparapu, R., Zugger, M.E., Robinson, T.D., Freedman, R., Kasting, J.F., 2014. Warming early Mars with CO_2 and H_2. Nature Geoscience 7, 59–63. https://doi.org/10.1038/ngeo2000

Rangarajan, V.G., Bharti, R., Mondal, S.K., Pradhan, C., Dutta, S., 2018. Remote Sensing for Martian Studies: Inferences from Syrtis Major. J Indian Soc Remote Sens 46, 1537–1551. https://doi.org/10.1007/s12524-018-0826-7

Rogers, A. Deanne, and Joshua L. Bandfield. 2009. Mineralogical Characterization of Mars Science Laboratory Candidate Landing Sites from THEMIS and TES Data. Icarus 2 (203):437–53. https://doi.org/10.1016/j.icarus.2009.04.020.

Salvatore, M.R., Goudge, T.A., Bramble, M.S., Edwards, C.S., Bandfield, J.L., Amador, E.S., Mustard, J.F., Christensen, P.R., 2018. Bulk mineralogy of the NE Syrtis and Jezero crater regions of Mars derived through thermal infrared spectral analyses. Icarus 301, 76–96. https://doi.org/10.1016/j.icarus.2017.09.019

Schon, Samuel C., James W. Head, and Caleb I. Fassett., 2012. An Overfilled Lacustrine System and Progradational Delta in Jezero Crater, Mars: Implications for Noachian Climate. Planetary and Space Science 67 (1):28–45. https://doi.org/10.1016/j.pss.2012.02.003.

Schultz, Richard A., and Herbert V. Frey., 1990. A New Survey of Multiring Impact Basins on Mars. Journal of Geophysical Research: Solid Earth 95 (B9):14175–89. https://doi.org/10.1029/JB095iB09p14175.

Schultz, Richard A., and Herbert V. Frey., 1990. A New Survey of Multiring Impact Basins on Mars. Journal of Geophysical Research: Solid Earth 95 (B9):14175–89.

Smith, David E., Maria T. Zuber, Herbert V. Frey, James B. Garvin, James W. Head, Duane O. Muhleman, Gordon H. Pettengill, et al., 2001. Mars Orbiter Laser Altimeter: Experiment Summary after the First Year of Global Mapping of Mars. Journal of Geophysical Research: Planets 106 (E10): 23689–722. https://doi.org/10.1029/2000JE001364.

Tanaka, K.L., Skinner, J.A., Jr., Dohm, J.M., Irwin, R.P., III, Kolb, E.J., Fortezzo, C.M., Platz, T., Michael, G.G., and Hare, T.M., 2014, Geologic map of Mars: U.S. Geological Survey Scientific Investigations Map 3292, scale 1:20,000,000, pamphlet 43 p., https://dx.doi.org/10.3133/sim3292.

THEMIS User Guide, 2006. Thermal Emission Imaging System 2001 Mars Odyssey: Themis Geometric Processing User's Guide. Last Accessed May 23, 2019. Available at https://static.mars.asu.edu/pds/ODTGEO_v2/document/geometry.pdf

Viviano-Beck, C. E., S. L. Murchie, A. W. Beck, and J. M. Dohm., 2017. Compositional and Structural Constraints on the Geologic History of Eastern Tharsis Rise, Mars. Icarus 284 (Supplement C):43–58. https://doi.org/10.1016/j.icarus.2016.09.005.

Viviano-Beck, Christina E., Frank P. Seelos, Scott L. Murchie, Eliezer G. Kahn, Kimberley D. Seelos, Howard W. Taylor, Kelly Taylor, et al., 2014. Revised CRISM Spectral Parameters and Summary Products Based on the Currently Detected Mineral Diversity on Mars. Journal of Geophysical Research: Planets 119 (6):2014JE004627. https://doi.org/10.1002/2014JE004627.

Wenk, H.-R., Bulakh, A., 2016. Minerals: Their Constitution and Origin, 2 edition. ed. Cambridge University Press, Cambridge.

Wichman, R. W., and P. H. Schultz., 1989. Sequence and Mechanisms of Deformation around the Hellas and Isidis Impact Basins on Mars. Journal of Geophysical Research: Solid Earth 94 (B12):17333–57. https://doi.org/10.1029/JB094iB12p17333.

Zubrin, Robert, and Richard Wagner., 1997. The Case for Mars: The Plan to Settle the Red Planet and Why We Must. New York: Touchstone.

Zurek, Richard W., and Suzanne E. Smrekar., 2007. An Overview of the Mars Reconnaissance Orbiter (MRO) Science Mission. Journal of Geophysical Research: Planets 112 (E5): E05S01. https://doi.org/10.1029/2006JE002701.

Chapter 3: Semi-Automated Identification and Thermal Infrared (TIR) Response of the Dunes at Hargraves Crater, Mars

Abstract

This paper aims to identify individual dunes from a semi-automated object-based image analysis technique and the thermal infrared response of dune materials at Hargraves crater, Mars. The existing Mars digital dune database (MGD[3]) were mapped manually through visual photo-interpretation from the lower resolution the Thermal Emission Imaging System (THEMIS; 100 m/pixel) images that would benefit to be updated for an improved understanding of the martian surface and its atmospheric mechanisms at the local scale. An object-based image-analysis technique was applied here to the Context Camera (CTX; 6m/pixel) dataset to extract dune data in a relatively quick, reliable, and accurate fashion. This study is a test case in validating a remote sensing method that has wide applicability to the entire martian surface for updating the dune database at a higher resolution than the existing database. An average thermal inertia value of 243±23 $Jm^{-2}K^{-1}s^{-0.5}$ was found for the dune materials, indicating a surface composed of an effective grain-size of ~230 μm, suggesting a fine sand size at the surface and moderately indurated areas with small granules or unconsolidated materials. The compositional analysis specifies that the dune materials are composed of a mixture of feldspar, olivine, and pyroxene having a relatively lower bulk-silica content. The wind movement inside the crater (inferred based on the dune slipface orientation) indicates that the prevailing wind direction inside the crater is flowing to the west-northwest. The dunes are labeled as active (stability index of 2) and do not appear to have been influenced by subsurface water ice or volatiles. The study emphasizes that with the accurate dune identification based on semi-automated method, coupled with the compositional and thermophysical characteristics for individual martian dune fields, would provide an important addition to the MGD[3] providing a better understanding of surface and atmospheric behavior of Mars at the local scale.

Keywords: Dune, Hargraves crater, Mars, Thermal infrared, and Object-based image analysis

1. Introduction

Despite a variety of environments involved, dune fields provide an important insight into aeolian transport regimes (both past and present) of terrestrial planets like Earth, Mars, and Venus (e.g., Greeley and Iversen, 1987; Kocurek and Ewing, 2005; Beveridge et al., 2006), as well as transport regimes extant on some icy satellites such as Titan (e.g., Lorenz et al., 2006; Yu et al., 2018) and Triton (Smith et al., 1989), and on the dwarf planet Pluto (Telfer et al., 2018). The surface of Mars is home to aeolian dune fields in a variety of locations including the circum-north polar region (e.g., Edgett and Christensen, 1991; Bandeira et al., 2010). Dune materials and aeolian processes pave the way to understanding the interactions between the surface and atmosphere of the planet, as well as the weather, climate, and climatic evolution during martian history (e.g., Greeley et al., 2001; Wilson and Zimbelman, 2004). On Earth, where field observations are possible, dune fields have been studied in conjunction with satellite remote sensing in order to understand the evolution of aeolian sand dunes (Elbelrhiti et al., 2008; Hugenholtz et al., 2012). This integration of remote sensing and advanced quantitative investigation allows an understanding of the relationship between patterns of atmospheric circulation and transport of regional sediments (e.g., Pont et al., 2014; Fenton et al., 2014). However, in the instance of Mars, direct field observation of dunes, wind velocities, and atmospheric circulation trends are not available in quantity so far, even though the relationship between bedform and atmospheric circulation are of critical interest (Vaz et al., 2015). Over the past decades, studies had been done to better understand martian surface processes and global scale atmospheric dynamics from analysis of various aeolian processes and wind-related features (e.g., Ward et al., 1985; Fenton et al., 2005; Hayward et al., 2009; Silvestro et al., 2010; Gardin et al., 2012; Sefton-Nash et al., 2014).

Though regional scale dunes (and dune fields) were first detected on Mars during the early 1970s on Mariner 9 images (Sagan et al., 1972), more dunes were detected from high-resolution orbital images of Mars Global Surveyor (MGS) during the late 1990s (Edgett and Malin, 2000) and thus was found to have similarities with dunes of Earth (Bandeira et al., 2010). Recently, a more complete catalogue for the martian dune fields was created by a group of planetary scientists and is called the Mars Global Digital Dune Database (MGD^3) (Hayward et al., 2007; Hayward et al., 2014). MGD^3 database contains locations and characteristics of dune fields (regional or landscape scale; >1 km^2) as well as other parameters, including intracrater dune-field centroids, crater centroids, dune slipface orientations, and inferred wind directions (e.g., Gullikson et al., 2018). This compiled database has a nearly global view, encompassing the area from latitude 65°N to 65°S (the equatorial region), from 60°N to 90°N (the north polar region), and from 60° to 90°S (the south polar region), facilitating understanding in relationships between the martian global atmospheric circulation and sediment dynamics (Hayward et al., 2007; Hayward et al., 2014).

The delineation of dune fields in MGD^3 was prepared manually through visual photo-interpretation from the 2001 Mars Odyssey's onboard Thermal Emission Imaging System (THEMIS; Christensen et al., 2004), which yielded specific imagery at 100 meters per pixel spatial resolution (Hayward et al., 2007; Hayward et al., 2014). The database contains information of regional to planetary scale dunes and dune fields (>1 km^2), including classification of dune morphologies, the digitized dune parameters, and mapped dune slipface orientations (Gullikson et al., 2018; Vaz et al., 2015). The trends of the prevailing surface winds are estimated from the measured dune slipface orientation and gross dune morphology. However, manual digitizing of the dune parameters from the lower spatial resolution THEMIS images is a very arduous, labor-intensive, and time-consuming task. That is why, a semi-automated method from high spatial resolution images, e.g., the Context Camera

(CTX; Malin et al., 2007) are more efficient at maximizing the extraction of significant surface morphological information about martian dune fields (Bandeira et al., 2010; Vaz et al., 2015). CTX sensor onboard the Mars Reconnaissance Orbiter (MRO) spacecraft has a spatial resolution of ~6 m/pixel which provides a more comprehensive understanding of the martian dune fields compared to the MGD[3] information constructed from THEMIS images.

Many studies on martian dune fields have been conducted over the past few decades (e.g., Vaz and Silvestro, 2014; Vaz et al., 2015; Bandeira et al., 2010; Emran et al., 2019), and of those studies, some used traditional manual digitizing of dune parameters and other geomorphic characteristics using satellite images (e.g., Greeley and Thompson, 2003; Silvestro et al., 2010; Fenton et al., 2014a; 2014b). Extracting dune parameters from orbital datasets is not only cumbersome but also involves some degree of user bias such as identifying patterns of aeolian dune analysis (Hugenholtz et al., 2012) that renders an obstacle in terms of integration and standardization of observation (Vaz et al., 2015). Recently, a few studies applied automated detection of dune characteristics through the object-based image identifications (e.g., Vaz and Silvestro, 2014; Vaz et al., 2015; Bandeira et al., 2010; Sholes et al., 2013; Bandeira et al., 2011; Silvestro et al., 2013). The study of Vaz et al. (2015) used an object-based image classification for mapping and pattern characterization of dunes in Ganges Chasma and Gale crater, Mars from CTX images. Sholes et al. (2013) developed a rule set in eCognition software for object-based classifications and showed the validity of the method for use in extraplanetary remote sensing. Vaz and Silvestro (2014) introduced a new set of object-based approaches for simple and quick mapping of dunes and characterization of local-scale aeolian bedforms at the Mars Science Laboratory (MSL) landing site in Gale Crater. Bandeira et al., (2011) used Mars Orbiter Camera (MOC) data of the Mars Global Surveyor (MGS) probe through an automated method based on the extraction of local information from images for detection and delineation of dune fields on Mars. Most of these

studies identified linear dune features (longitudinal, transverse, reverse, and star dunes) which can be easily recognized because of their easily identifiable linear slipface structure through an automated method. In contrast, identification of small barchan and barchanoids are occasionally very difficult to detect from remote sensing image analysis techniques (Vaz et al., 2015). Because of this higher level of difficulty to identify slipfaces of small barchan and barchanoids dunes, the present study uses a semi-automated method for improved accuracy in identification of non-linear dunes at a local scale.

This study employs a semi-automated object-based image-analysis approach for mapping and characterization of intracrater dune field at Hargraves craters, Mars. The delineation of the MGD[3] for Hargraves is not accurate for the study area because the outline of the dune field does not cover all the dunes present (Fig. 3.1a). The objective of this work in identifying individual dunes at Hargraves is to correct the anomaly in the dune-field delineation of MGD[3] at Hargraves. A semi-automated method from higher resolution CTX data was employed to identify the individual dunes as opposed to the manual pixel-based photo-interpretation technique in delineating the entire dune field from the comparatively lower spatial resolution THEMIS data. The method uses the generic algorithms of object-based image analysis (OBIA) technique. Having many advantages over the pixel-based photo interpretation, OBIA can produce more robust, efficient, and accurate results in detecting dunes on Mars using higher resolution images. The study, indeed, is a test case and if proven reliable then the method can be applied to other martian surfaces with the goal to make a higher resolution dune database, which will be an updated version of the existing database.

Besides identifying dunes themselves, an attempt was made to analyze the thermal infrared (TIR) responses of constituent dune materials based on multispectral THEMIS and hyperspectral Thermal Emission Spectrometer (TES; Christensen et al., 2001) datasets. Those analyses include surface grain-

size distribution and compositional (e.g., mineral abundances and bulk-silica content) characteristics of the dune materials. Analysis of grain-size distributions is important in classifying sedimentary environments and understanding the sediment transport dynamics. Sediment grain-size provides important information about shear stress applied by the medium of transport in order to initiate and to sustain the movement of particles, and is regulated by characteristics of transport medium, distance traveled, nature of source materials, and surface topography (Abuodha, 2003). On Mars, grain-size distribution has a direct relationship with the thermophysical characteristic or more specifically thermal inertia (Kieffer et al., 1977; Haberle and Jakosky, 1991). Therefore, in this study, thermal inertia is calculated from the nighttime TIR image of THEMIS. Characterizing thermal inertia and local dune morphology variation provides insight into the near-surface composition and local to regional climate (Courville et al., 2016); for instance, the presence of subsurface ice or volatiles. In addition to thermal inertia, the High-Resolution Imaging Science Experiment (HiRISE; McEwen et al. 2007) images were used as a visual survey tool for analyzing the grain-size distribution and local variability of the dune field. Compositional analysis of dune materials is crucial for a better understanding of the martian dune studies. The dunes' bulk-composition can reveal the extent of compositional similarities (and dissimilarities) between aeolian sands and the surrounding surfaces, the provenance (or sources) of dune materials, transport behavior of the aeolian medium, and alteration (if any) of the aeolian sands versus their source materials (e.g., Fenton et al., 2019). This study compared the bulk mineral assemblage of dune materials to the surrounding inferred source materials from the TES data. Additionally, the study determines the stability (modification) of the dunes inferred from the apparent presence or absence of specific feature(s) identified higher resolution CTX and HiRISE data. Gullikson et al. (2018) recently attempted a similar study to expand the existing MGD[3] and in so doing characterized dune fields through compositional analysis, stability, and thermal inertia. However, their work was confined to dune fields of 300 km^2 or larger in the equatorial and south

polar region. Gullikson et al. (2018) identified the mineralogy of dune fields but did not compare the dune composition to the corresponding source materials or provenance. Moreover, the work of Gullikson et al., (2018) did not focus updating the existing dune fields' geometric parameters (e.g., area) from the available higher resolution images, rather they only focused on the compositional and thermal behavior of existing larger dune fields of ≥300 km^2 area. The present study focuses on more detailed dune identification, as well as compositional and thermophysical behavior of dune materials on a local scale and compares dune materials to their inferred source materials.

1.1. Object-based image analysis (OBIA)

Traditional pixel-based image classifications have been widely applied in remote sensing image classification and feature extraction since the earlier era of satellite remote sensing. Such pixel-based classification, for instance, maximum likelihood, has been regarded as a well-accepted paradigm in many remote sensing environmental applications (Strahler et al., 1986; Castilla and Hay, 2008). However, having many limitations such as difficulties in processing high-resolution images due to 'salt-and-pepper' effects and inability to distinguish child objects from their parents (e.g., shadow effects) such pixel-based remote-sensing analysis results sometimes yielded unreliable findings (e.g., Sholes et al., 2013; Blaschke et al., 2014). Thus, pixel-based image classification has garnered some criticism during the past twenty years (Fisher, 1997; Blaschke and Strobl, 2002; Burnett and Blaschke, 2003). Due to the limitations of pixel-based methods for high-resolution image analysis, a new paradigm of object-based image analysis (OBIA) also known as geographic object-based image analysis (GeOBIA), has gained considerable attention among remote sensing applications (e.g., Castilla and Hay, 2008; Baatz et al., 2008; Blaschke et al., 2014; Tzotsos and Argialas, 2008; Blaschke, 2010; Hay and Castilla, 2008). The ongoing studies based on object-based image classification showed a successful paradigm shift toward OBIA from tradition pixels-based image analysis. Object-based rule

sets can successfully account homogeneity, shape, texture, position, and other conditions besides traditionally looking into multi-band level spectral analysis from high-resolution data (Sholes et al., 2013). This study, therefore, employs a set of semi-automated object-based rule sets for identifying the individual dunes at Hargraves crater, Mars to employ full advantages of object-based image classification techniques.

2. Study area and geologic settings

The Nili Fossae is a suite of concentric grabens in the northwest of the Isidis basin and north of Syrtis Major of Mars (Goudge et al., 2015). The area is hypothesized to has formed due to crustal flexure resulting from the formation and subsequence infilling of the Isidis basin (Wichman and Schultz, 1989; Ryan et al., 2016; Ryan et al., 2017). Approximately 50 km to the east of the eastern wall Nili Fossae Trough (NFT) is the 65 km diameter Hargraves crater (Fig. 3.1a), which formed during the late Noachian or early Hesperian Period (Ivanov et al., 2012). The crater is considered as a part of the Jezero crater watershed (Goudge et al., 2015) and its location is centered on 75.75^0 E and 20.75^0 N. The impact event that created the Hargraves crater involved diverse bedrock lithologies of ancient Mars and the excavated minerals are exposed even in the distal parts of impact ejecta that have been sourced from upper few hundreds of meters crust (Mangold et al., 2007; Cannon et al., 2015; Goudge et al., 2015). The ballistic component of Hargraves ejecta may be derived from the upper 3 km depth of target materials, while any melt-component in the ejecta may have originated from deeper in the target (up to 7.2 km) (Osinski et al., 2011; cited in Ryan et al., 2016). Though a lot of interest has been paid to the nearby Jezero crater and Nili Fossae, relatively little attention has been paid to Hargraves crater. Based on tone, texture, and morphological characteristics, Goudge et al. (2015) identified few major morphologic units inside the Hargraves crater such as alluvial fan (AF), crater

central peak (Ccp), crater floor materials (Cfm), crater ejecta (Ce), and surficial debris cover (Ac); described in figure 3.1(b). The crater is home to the visible dune field at CTX resolution (Fig. 3.1a). The dune field is labeled as surficial debris cover (Ac), which is characterized by aggregates of dunes (Goudge et al., 2015). Just northwest of the dune field there is a depositional alluvial fan on the northwestern interior wall of the crater that was emplaced by the fluvial activities along the crater rim (Mangold et al., 2007). The MGD[3] outlines that the dune field has barchan (B) and barchanoid (Bd) dune types based on the dune classification method of McKee et al. (1979). McKee et al. (1979) define the barchan (B) as a crescent in plain view with single slipface that indicates a wind movement towards one predominant direction. On the other hand, barchanoids (Bd) have a row of connected crescents in plain view (connected dunes are merged together) with a single slipface (McKee et al., 1979; Hayward et al., 2007). The MGD[3] indicates absence of linear, star, and transverse dunes at Hargraves. Though the existing database did not find sand sheets in the study area, the visible CTX images show a thin sand apron present on the western part of the dune field. This study aimed at identifying individual barchans and barchanoids dunes in the crater using higher resolution images along with analysis of the grain-size distribution, mineral abundances, and bulk silica content of dune materials. In addition, the geology of the crater is interpreted using the existing data of the dune field database e.g., dune centroid, slipface, wind vectors, etc.

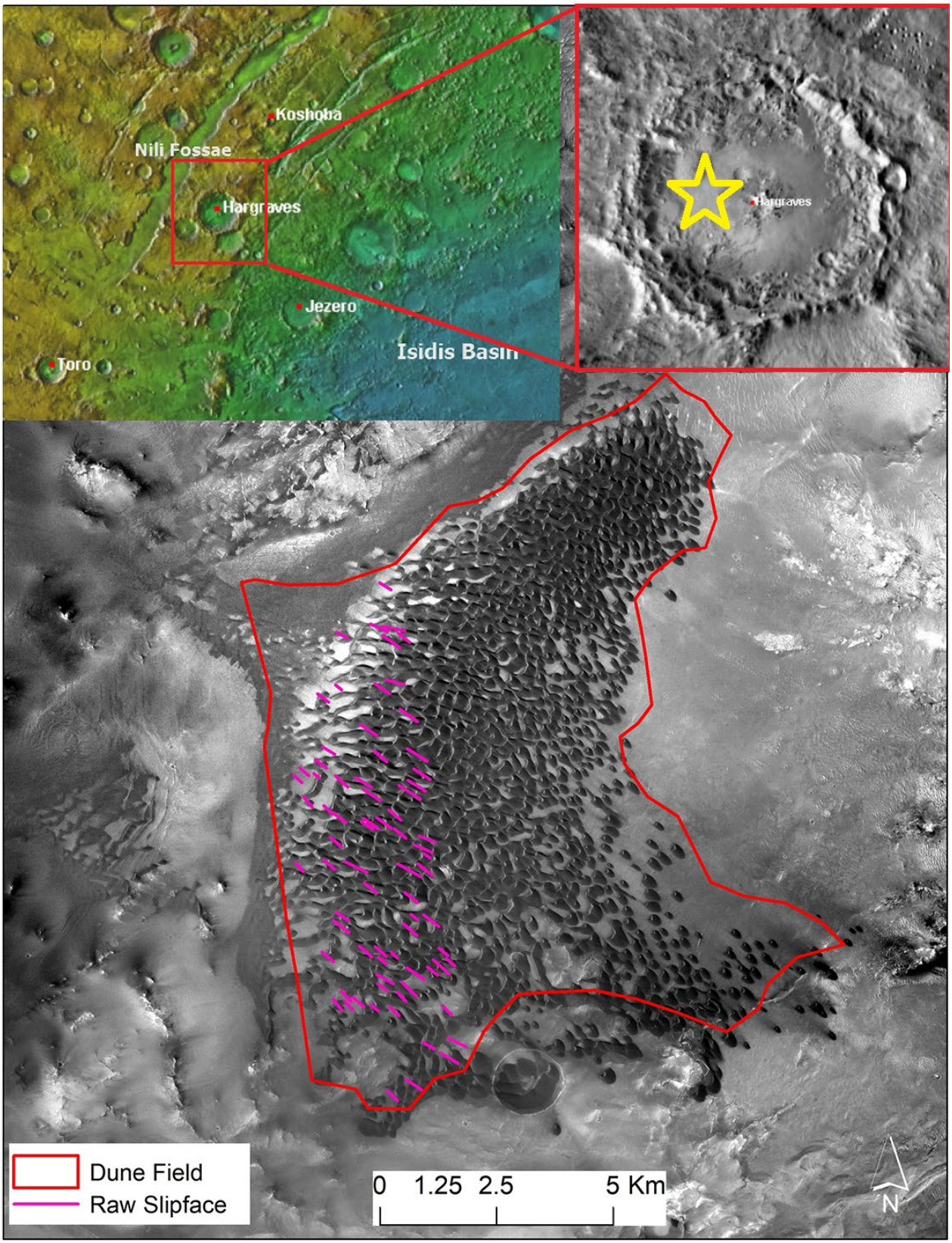
Koshoba
Nili Fossae
Hargraves
Jezero
Isidis Basin
Toro
Hargraves
Dune Field
Raw Slipface
0 1.25 2.5 5 Km
N

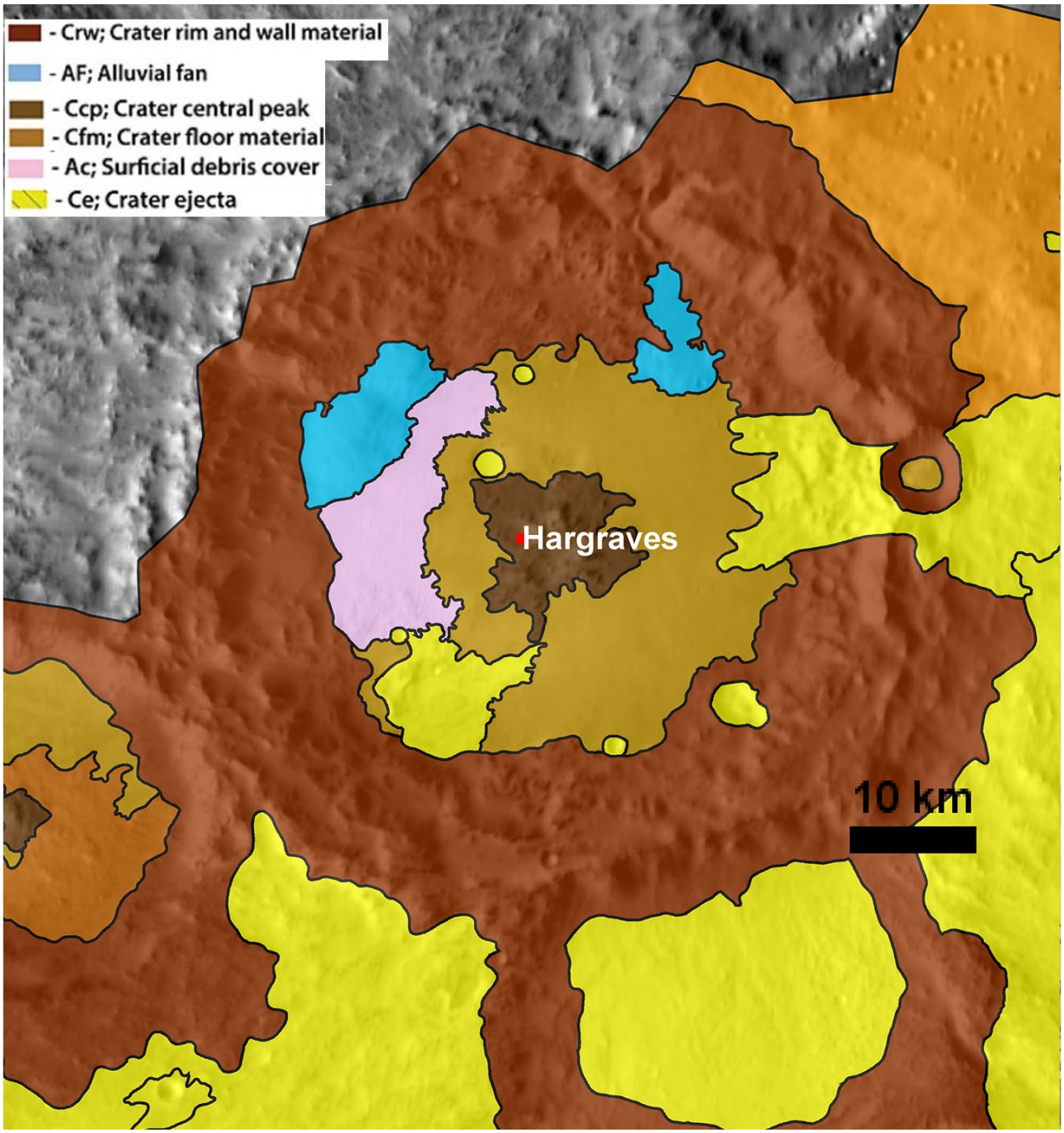

Fig. 3.1: The location of the Hargraves crater is on the east side of the Nili Fossae Trough (NFT) and northwest of the Isidis Basin. a) The dune field in CTX image resolution, inset is the reference map (the yellow star is the location of dune inside the crater). The red outline is the dune field boundary and magenta transect are the raw slipface as defined by MGD[3]. b) The geological units inside the Hargraves; crater ejecta (Ce), crater crater floor materials (Cfm), crater central peak (Ccp), and rim and wall materials (Crw; Goudge et al., 2015), and Dune materials (Du; under the surficial debris cover or Ac unit as described in Goudge et al., 2015).

3. Data and methods

This section describes the data and the associated methods used to attain the objectives of the present study. CTX visible image data and their stereo-pair derived outputs (e.g., DEM, slope, shaded relief, etc.) were used to identify the individual dunes (barchan and barchanoids) at the study areas. A detailed methodology of the semi-automated object-based image analysis techniques, including the image processing routine for CTX data, used to derive the dunes were then thoroughly described. A description of the hyperspectral TES sensor and the method of deriving bulk mineralogy using a non-negative spectral deconvolution method were thoroughly labeled subsequently. Though a quantitative bulk mineralogical analysis is derived from the hyperspectral TES data; however, having a lower spatial resolution thermal infrared TES sensor data compelled this study to take the advantages of using the comparatively higher spatial resolution multi-spectral thermal infrared THEMIS data as well for an additional proxy of compositional analysis. Thermal infrared data of THEMIS images are used to calculate nighttime thermal inertia, decorrelation stretch (DCS), and weighted absorption center (WAC) for analyzing the grain-size distribution, a proxy of compositional characteristics, and bulk silicate content analysis, respectively, for the dune materials. The detailed method of deriving this information from THEMIS images was described with an overview of the sensor characteristics.

3.1. Context Camera (CTX)

The Context Camera (CTX) instrument onboard the Mars Reconnaissance Orbiter (MRO) is a push-broom visible-image camera. CTX acquires grayscale images at a spatial resolution of ~6 meters/pixel and has a swath width of 30 km (Malin et al., 2007). CTX makes an observation for analyzing critical science targets such as observed features of interest to exploration initiative in addition to providing a wider context for the more higher resolution HiRISE investigation and mineralogy search by CRISM observations (Malin et al. 2007). Stereo-pair images are captured by

CTX, which are used to produce high-resolution digital elevation models (DEMs) for topographic and morphologic mapping of the martian surface (Malin et al., 2007). CTX stereo-pairs D14_032860_2009 and D15_033071_2009 were used as input layers in this study. Calibration, projection, and production of the DEM from CTX stereo-pairs were all done using USGS's Integrated Software for Imagers and Spectrometers (ISIS3) pipelines and NASA Ames Stereo Pipeline (ASP) stereogrammetry software (Broxton and Edwards 2008; Moratto et al. 2010; Beyer et al. 2014; Quantin-Nataf et al., 2018). The CTX derived point cloud DEM was tied to the Precision Experiment Data Record (PEDR) point shot data of the Mars Orbiter Laser Altimeter (MOLA) instrument (Smith et al., 2001) using the *pc_align* function (Beyer et al. 2014) to account for the error of regional scale topography (Goudge et al., 2017). The final DEM was co-registered with other datasets such as THEMIS, HiRISE, and CTX grayscale images; rendered in eCognition, ArcGIS, and JMARS for further analyses.

3.1.1. Semi-automated object-based dune identification

The semi-automated object-based dune identification methodology consists of an application of image segmentation into a set of image objects whose parameters were then used to classify dunes from the non-dune object using eCognition software. The map projected CTX panchromatic image ("pan") of D15_033071_2009 and the digital elevation model (DEM; derived from CTX stereo-pair) were used as the input layers. The ancillary data layers, e.g., slope, roughness index, and shaded relief were produced from the DEM using ESRI's ArcMap GIS software and were integrated into the process tree for better segmentation and subsequent outputs. The goal in the semi-automated object-based algorithm in this project was to extract the dune objects from the non-dune objects in the study area. The multi-resolution segmentation algorithm was used where weights of the layers were given as 1:4 to DEM and "pan" layers, respectively. The multi-resolution segmentation uses a bottom-up

region-merging algorithm, which considers each pixel of the scene as an individual object (Darwish et al., 2003). The merging decisions are taken considering local homogeneity of the image objects based on a user-defined threshold criterion known as scale parameter (Darwish et al., 2003). The higher the scale parameter the higher the likelihood of more merging to bigger objects. The homogeneity criteria used in multi-resolution segmentation consist of a combination of color (or spectral value) and shape parameters (splits into two additional parameters i.e., smoothness and compactness). Using the different combination of homogeneity parameters (e.g., scale and shape parameters) based on a trial-and-error routine, a user creates a hierarchical network of image objects (Darwish et al., 2003). In this study, the scale[a] parameter was set as 40 whereas shape[b] (or smoothness) was fixed to 0.6 and compactness[c] was set as 0.5. Those parameters for the multi-resolution segmentation were used to come up with the best segmentation routine of the dune objects (Fig. 3.2a). CTX panchromatic ("pan") data layer was given more weight than the DEM data layer in the segmentation algorithm since dune features are clearly visible in the panchromatic layer and the appropriate parameter values were determined from the results based on trial-and-error. After the segmentation of image objects, a set of rules (e.g., object thresholding) were applied to the image objects to differentiate dunes from non-dune objects (Fig. 3.2b). Object thresholding can separate the dune features from the non-dune image objects using, for instance, a mean value at the image object level (in layer properties of image object) of the CTX grayscale image and DEM. In addition to using the "pan" and DEM layers, the slope, roughness index, and shaded relief layers (at object level) were also examined to distinguish

[a] Affects by determining size of resultant image objects and controls the amount of spectral variation within image objects.
[b] Optimizes for spectral and spatial homogeneity or weighting between the objects shape and its spectral color (demines the degree of smoothness).
[c] A weighting for representing the compactness of the objects formed during the segmentation.

[For more information about the multi-resolution segmentation algorithm, the readers are suggested to read the document at http://www.ecognition.com/sites/default/files/405_baatz_fp_12.pdf

dune objects from non-dune objects. Because the study only uses gray-scale, single-band CTX images and the derived DEM for the object-based analysis, automated rule sets could not entirely distinguish all individual dunes in the study area. Lastly, the identified dune objects were carefully examined, and then slightly modified (and the few unclassified dunes were merged to the automatically extracted dune objects). After dunes object extraction and classification, the spatially separated individual barchan dunes and/or mixed dunes (barchanoids) were exported as polygon features. The features were later exported from the classification scheme as a vector layer file. Each vector layer represents the individual dunes including all the geospatial information (e.g., coordinate, shape, geometry, length, area, etc.). The connected dunes were then merged as barchanoids. The vector files were then ready for analysis in ESRI's ArcGIS software and merged into a single dune field vector layer. The dune polygon vector layers were then further processed and converted to an ESRI's ArcGIS geodatabase format for the ease of further analysis and additional uses. Note here that like the existing database, only barchans and barchanoids dune types were identified as defined by MGD[3] and ignored the thin sand apron in classification scheme in this study. Finally, the present study assessed the accuracy of the classified dune objects considering 500 simple random points in the study area.

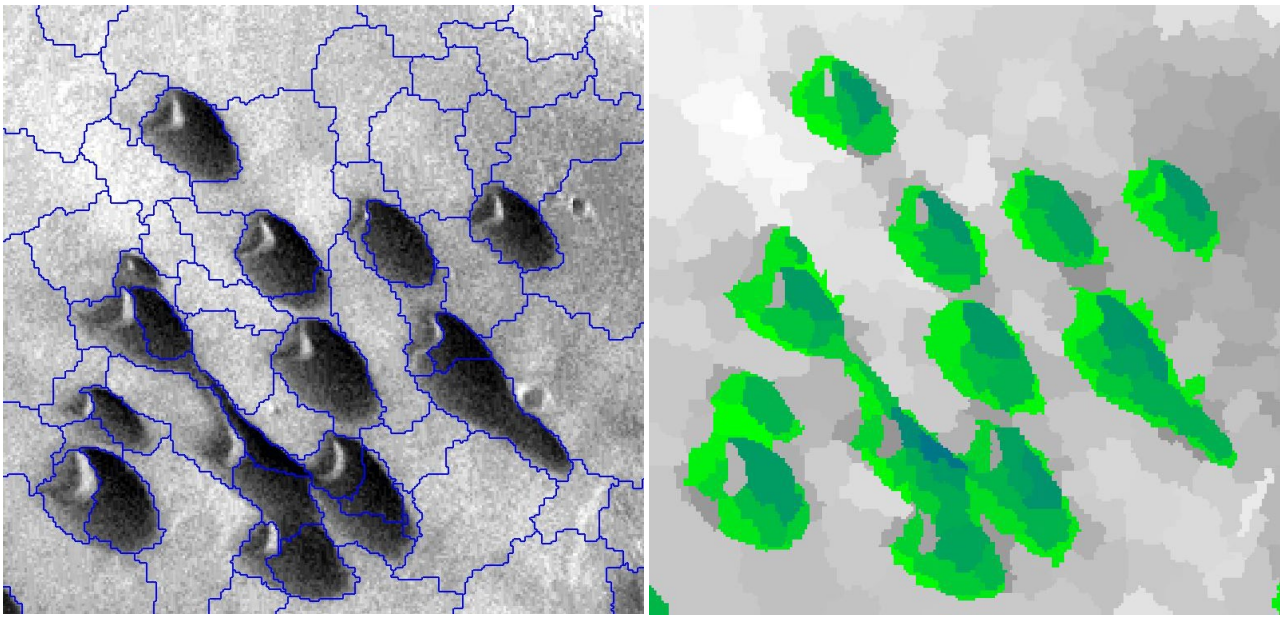

Fig. 3.2. Semi-automated dune identification in eCognition software. a) a subset of image segmentation using multi-resolution segmentation algorithm. The individual polygons are the distinct object considered in the object-based classification. b) object thresholding and classification of the desired object using a mean value at object level method. The green objects are the classified dune fields derived from thresholding.

3.2. High Resolution Imaging Science Experiment (HiRISE)

The High Resolution Imaging Science Experiment (HiRISE) onboard MRO is a push-broom visible and near-infrared imager used for detailed analysis of surfaces at a nominal spatial resolution of ~25 cm/pixel (McEwen et al. 2007; Zurek and Smrekar, 2007; Delamere et al., 2010). HiRISE uses an array of 14 charge-coupled devices (CCDs) of 3 different color filters e.g., ten red (RED) detectors centered at 0.694 μm, two blue-green (BG) detectors centered at 0.536 μm, and two near-infrared (NIR) detectors centered at 0.874 μm (McEwen et al., 2007). The martian surface composition and albedo heterogeneities are derived from HiRISE color images which are directly correlated to the results obtained from other orbital images e.g., CTX and THEMIS (Zurek and Smrekar, 2007; Quantin-Nataf et al., 2018). In this study, HiRISE images were used as supplementary dataset coupled

with CTX images to interpret the fine scale textural variation for dune fields in the study area. HiRISE datasets were used as a visual survey tool for the grain-size distribution and local variability of the dune field. The HiRISE data were also used to visually identify the non-aeolian features in analyzing dune stability (modification) of the dune field (discussed in detail later).

3.2.1. Dune modification and stability

Fenton and Hayward (2010) mapped and categorized the martian dune fields into six morphological classes. Their classification scheme was based on an inferred dune stability scale constructed upon the apparent presence or lack of superposed non-aeolian features as well as the apparent level of degradation (or modification) by non-aeolian processes (Banks et al., 2018). A stability index (SI) value (1 through 6, where a higher number indicates increasing evidence of stability or modification) was also assigned to the dune classes. The stability index is an inferred metric, which is measured from the degree of influences of non-aeolian processes (e.g., mass wasting) to the surface morphology of dune fields (Fenton and Hayward, 2010; Gullikson et al., 2018). Determining appropriate stability index value is a subjective procedure based on the presence or absence of specific features (Fenton and Hayward, 2010). The dunes with lower SIs ($\leq$3) are thought to be active and those that have higher SI values are considered as inactive dunes (e.g., Fenton and Hayward, 2010; Gullikson et al., 2018; Banks et al., 2018). Higher resolution CTX and HiRISE datasets were used to identify the presence or absence of several non-aeolian features, besides determining SI, to the dune field. The presence or absence of features like gullies, small pits, and mass-wasting features from high-resolution images can give insight into recent aeolian activities (Gullikson et al., 2018). The stability index was determined based on the prevalence and magnitude of stabilization features (e.g., rounded dune brinks, presence of a sharp-edged sand apron around the dune field, a dissected surface, etc.) for

the ease of dune-type identification (Gullikson et al., 2018; Fenton et al., 2019). Noted here that the presence or lack of these feature(s) are interpreted as the indication of aeolian activities or stability of dunes. The presence of these features is consistent with aeolian inactivity or paucity of sand transport allowing the influence of other erosional or depositional processes to dominate dune morphology (Gullikson et al., 2018).

3.3. Thermal Emission Spectrometer (TES)

The Thermal Emission Spectrometer (TES) onboard Mars Global Surveyor (MGS) spacecraft is an infrared (5.8 to 50 μm) interferometric spectrometer (Christensen et al., 2001). The instrument also includes a broadband thermal (5.1 μm to 150 μm) radiometer and a visible/near-infrared (0.3 μm to 2.9-μm) radiometer (Christensen et al., 2001). This study used TES data that were recorded between the wavelengths of 1651 cm^{-1} and 201 cm^{-1} with a sampling interval of 10 cm^{-1} resulting in 143 channels (Christensen et al., 2001). To ensure the best possible or highest quality of data used in this study, a subset of the data was made considering several parameters described in Rogers and Bandfield (2009) and Salvatore et al. (2018). TES spectra were extracted from early in the mapping orbit phase (orbits 1- 5317) that belong to high surface temperatures (≥260 K), low total ice (≤0.04), and low total dust cover (≤0.15). This quality control practice has successfully been applied in previous studies such as Rogers and Christensen (2007), Rogers et al. (2007), Salvatore et al. (2014), and Salvatore et al. (2016) and this control ensured the true spectral characteristics of the surface of the planet (Salvatore et al., 2018). The spectral data were collected only from the spectra that are over the dune field, hereafter called dune unit (Du). For the compositional comparison to inferred provenance, spectra were also collected over the crater floor materials (Cfm), crater ejecta (Ce), crater central peak (Ccp), and crater rim and wall materials (Crw) units as identified by the work of Goudge et al. (2015), mentioned in figure 3.1(b). Note here that the floor material unit in Salvatore et al. (2018) consists of the

combination of crater floor materials (Cfm) and crater central peak (Ccp) units in Goudge et al. (2015). However, in this study, each individual unit was considered and retained the central peak (Ccp) as a separate unit. The spectra for all units (e.g., Du, Cp, Ce, CFM, and Crw) were collected very carefully so that only the spectra fall inside the units. Since the alluvial fan (AF) unit is in front of the dune unit (Du) this study did not consider the fan unit as a potential source of dune materials.

Prior to averaging the spectra for each representative morphologic unit, an atmospheric correction algorithm is run to each orbital group (orbit counter keeper; ocks) spectra to remove the atmospheric effects using the spectral deconvolution algorithm of Smith et al. (2000). The study chooses a non-negative least square minimization routine (Lawson and Hanson, 1995; Seelos and Arvidson, 2003; Rogers and Aharonson, 2008; Salvatore et al., 2014, Salvatore et al., 2016) between 230 cm^{-1} and 1305 cm^{-1}. The used algorithm is different from the technique of Ramsey and Christensen (1998) (Salvatore et al., 2018). These unmixing algorithms (Ramsey and Christensen, 1998; Rogers and Aharonson, 2008) use a library of atmospheric end-members (Bandfield et al., 2000b) and a library of surface end-member spectra (Rogers and Fergason, 2011; Ahrens and Titus, 2014) listed in Table 3.1. Each of the spectra was treated individually for atmospheric correction that involves extracting surface emissivity through subtracting the atmospheric contributions from the measure emissivity spectra (Salvatore et al., 2018). The surface emissivity spectra for each representative morphologic unit were then averaged following the atmospheric correction. Average surface composition and mineral assemblage (Bandfield et al., 2000) were extracted using a non-negative least square fitting routine (spectral unmixing) by the chosen mineral endmember library (Rogers and Fergason, 2011; Ahrens and Titus, 2014). Using the spectral unmixing the study generated a mineral group assemblage consisting of 8 mineral groups (Rogers and Fergason, 2011; Ahrens and Titus, 2014) for each unit with a higher accuracy and detection threshold (Feely and Christensen, 1999; Christensen et al., 2000;

Bandfield, 2002; Rogers et al., 2007). The output of spectral unmixing includes modeled abundance and model error for each mineral group (and individual minerals as well).

Table 3.1: The list of thermal infrared spectral endmembers (both a library of atmospheric end-members and a library of surface end-member spectra) used for unmixing TES data in this study.

Mineral Group	Spectrum/endmember name	Mineral ID	Reference
Quartz	Quartz	BUR-4120	[1]
Alkali feldspar	Microcline	BUR-3460	[1]
Plagioclase	Albite	WAR-0235	[1]
	Oligoclase	BUR-060D	[1]
	Andesine	WAR-0024	[1]
	Labradorite	BUR-3080A	[1]
	Bytownite	WAR-1384	[1]
	Anorthite	BUR-340	[1]
	Shocked anorthosite	None	[2]
	at 17 GPa		
	at 21 GPa		
	at 25.5 GPa		
	at 27 GPa		
	at 38 GPa		
	at 56.3 GPa		
Orthopyroxene	Bronzite	NMNH-93527	[1]
	Enstatite	HS-9.4B	[1]
	Hypersthene	NMNH-B18247	[1]
Low-Ca clinopyroxene	Average Lindsley pigeonite	None	[3]
High-Ca clinopyroxene	Diopside	WAR-6474	[1]
	Augite	NMNH-9780	[1]
	Augite	NMHN-122302	[1]
	Hedenbergite manganoan	DSM-HED01	[1]
Olivine	Forsterite	BUR-3720A	[1]
	Fayalite	WAR-RGFAY01	[1]
	Olivine Fo_{60}	KI 3362	[4]
	Olivine Fo_{68}	KI 3115	[4]
	Olivine Fo_{35}	KI 3373	[4]
	Olivine Fo_{10}	KI 3008	[4]
Phyllosilicates	Illite Imt-1 < 0.2 μm (pellet)	Imt-1	[5]
	Ca-montmorillonite solid	STx-1	[1]
	Saponite (Eb-1) < 0.2 μm (pellet)	None	[6]
	SWy-1 < 0.2 microns (pellet)	None	[5]
Glass	K-rich glass	None	[3]
	SiO2 glass	None	[3]
Amorphous silica	Opal-A	01–011	[7]
	Al-Opal	None	[8]
Oxide	Average Meridiani and Aram Hematite (TT derived)	None	[9]
Sulfate	Anhydrite	ML-S9	[1]
	Gypsum	ML-S6	[1]
Carbonate	Kieserite	None	[10]
	Calcite	C40	[1]
Zeolite	Dolomite	C20	[1]
	Crystalline heulandite	None	[11]
	Crystalline stilbite	None	[11]
Atmosphere	Low-opacity dust	None	[12]

High-opacity dust	None	[12]
Water ice (small)	None	[12]
Water ice (large)	None	[12]
Synthetic CO_2	None	[12]
Synthetic water vapor	None	[12]

[1] Christensen et al. (2000); [2] Johnson et al. (2002); [3] Wyatt et al. (2001) [4] Koeppen and Hamilton (2008); [5] Michalski et al. (2006); [6] Michalski et al. (2005); [7] Michalski et al. (2003); [8] provided by M. D. Kraft/cited in Rogers and Fergason (2011) [9] Glotch et al. (2004); [10] Baldridge (2007); [11] Ruff (2004); [12] Bandfield et al. (2000).

3.4. Thermal Emission Imaging System (THEMIS)

The Thermal Emission Imaging System (THEMIS) consists of two multispectral imagers onboard 2001 Mars Odyssey (ODY) spacecraft enabling useful analysis on the morphology, thermophysical properties, composition, bulk mineralogy, and physical properties of the martian surface (Christensen et al, 2004; Edwards and Ehlmann, 2015; Huang et al., 2013). THEMIS sensor consists of visible (VIS), near-infrared (NIR), and thermal-infrared (TIR) imager. The thermal infrared sensor has 10 channels ranging from 6.78 μm to 14.88 μm, whereas visible sensor has 5 channels from 0.42 μm to 0.86 μm (Christensen et al., 2004). The spatial resolution for THEMIS images differs for the data types: both daytime and nighttime thermal infrared data are acquired at a 100 m/pixel whereas visible data are acquired at 18 to 35 m/pixel (Christensen et al. 2004). In this study, THEMIS daytime images were used to analyze surface composition (e.g., bulk-silica content) and nighttime images were used to analyze the thermophysical characteristics or thermal inertia (e.g., grain-size distribution). The surface compositional and thermal inertia data can be extracted from the representative surface units through overlapping THEMIS daytime and nighttime IR images that allow an assessment of the relationship between the material composition and grain-size distribution (Bandfield et al., 2011). THEMIS daytime radiance data are atmospherically corrected, calibrated, and converted to surface emissivity using the methods described in Christensen et al. (2004), Bandfield et al. (2004a), and Edwards et al. (2011). The images were selected considering highest possible quality having surface

temperature >250 K, dust opacity <0.15, and image quality ≥5 (as per THEMIS website the image ratings 3 to 6 are acceptable for scientific studies).

3.4.1. Thermal inertia and grain-size measurement

The thermal inertia (TI) of a material (I) can be defined as $I = \sqrt{(kpc)}$, where k means the thermal conductivity, p is the density, and c represents the specific heat (e.g., Edgett and Christensen, 1991). On Mars, thermal inertia is considered as a primary physical property measuring the resistance of materials to a temperature change and can be used as an indicator of surface geological characteristics for the upper few centimeters (e.g., Edgett and Christensen, 1991; Jakosky et al., 2000; Mellon et al., 2000; Putzig et al., 2005). Thermal inertia is influenced by surface materials' thermal conductivity and physical structure, e.g., particle grain-size, induration, porosity, rock abundance, bedrock exposure, and compaction (e.g., Kieffer et al., 1977; Jakosky, 1986; Putzig et al., 2005; Fergason et al., 2006; Edwards et al., 2009). Surface bulk thermal conductivity, however, mostly influences thermal inertia characteristics of the martian surface (e.g., Jakosky, 1986). Ideally, a higher value of bulk thermal conductivity or thermal inertia values is associated with compacted rock and/or larger particle-size materials (Williams et al., 2018) corresponding to a mechanically strong surface such as well-indurated (cemented) rock. On the other hand, weakly lithified rocks and/or unconsolidated (weakly indurated) materials are associated with lower thermal inertia values (Williams et al., 2018). Thus, a lower thermal inertia represents loose, fine surface dust or fine particles, and very few rocks whereas a higher thermal inertia indicates a combination of coarse sand, dune sand, strongly-crusted materials, abundant rocks, and/or scattered bedrock (e.g., Kieffer et al., 1977; Mellon et al., 2000; Jakosky et al., 2000; Putzig et al., 2005; Fergason et al., 2006; Edwards et al., 2009). However, a mixture of particles or presence of duricrust can produce moderate thermal inertia values that require examination of higher resolution images (e.g., HiRISE) to determine true surface characteristics (Rogers and Fergason, 2011). HiRISE

datasets were used for a more detailed examination of the surface materials at Hargraves. Besides thermal inertia, nighttime temperature also highlights the variation in the surface physical properties such as a colder nighttime temperature represents unconsolidated fine-grained materials whereas a warmer surface indicates lithified rock materials (Salvatore et al., 2016). The present study used a subset of quantitative thermal inertia data extracted from the global thermal inertia map that was produced by using the method of Fergason et al. (2006) (Christensen and Fergason, 2013). The relative accuracy of THEMIS derived thermal inertia is around ±20% (Fergason et al., 2006). Additionally, to examine further in the local variations of thermal inertia, apparent thermal inertia was calculated from a particular THEMIS scene using MARSTHERM, a thermophysical analysis tool (Putzig et al., 2013), using the method developed by Putzig et al. (2014). Using this technique, the study extracted apparent thermal inertia values in the dune field and compares it to other nearby morphologic units.

3.4.2. Decorrelation stretch (DCS) and spectral unit

As a qualitative investigation of surface composition, the study used DCS images (Gillespie et al., 1986; Edwards et al., 2011) derived as a standard THEMIS IR product (Bandfield et al., 2004b). The standard DCS images can be rendered in band combinations such as 8-7-5, 9-6-4, or 6-4-2 displayed in red, green, and blue channels, respectively. Yellow in DCS stretches of bands 8-7-5 and 9-6-4, and magenta in band 6-4-2 tend to correspond with elevated bulk-silica content (Amador and Bandfield, 2016). DCS images also demonstrate absorption features that illustrate olivine-bearing basalts (Edwards et al., 2011) such that high olivine content regions appear purple, purple, cyan in the band combinations of 8-7-5, 9-6-4, and 6-4-2 DCS stretches, respectively (e.g., Bandfield et al., 2011; Amador and Bandfield, 2016; Salvatore et al., 2016). In this study, DCS stretch images are specifically emphasized using bands 8 (11.79 μm), 7 (11.04 μm) and 5 (9.35 μm) in red, greed, and blue channels, respectively, to highlight the spectral and compositional variability present on the dune field and

surrounding areas (Salvatore et al., 2018). The color of DCS image is scene-specific; that is the spectral variability of DCS within a particular scene should be interpreted for that specific scene only and cannot be used as a proxy of similar composition for the all martian regions (Rogers and Fergason, 2011). Though temperature variation may affect the color representation to ambiguous interpretation, DCS images are a good proxy for the surface composition within the scene.

3.4.3. Weighted absorption center (WAC) and bulk-silica content

The corrected THEMIS emissivity data are used to measure the bulk-silica content using a method called "weighted absorption center" (Smith et al., 2013). This method rapidly identifies units with elevated bulk-silica compositions from THEMIS emissivity images (Amador and Bandfield, 2016; Salvatore et al., 2016). Amador and Bandfield (2016) introduced a new approach that is a renamed version of the "center of gravity" method developed by Smith et al. (2013). Having the diagnostic reststrahlen Si–O asymmetric stretch absorption bands, THEMIS emissivity data are sensitive to bulk-silica abundance if a surface contains silicate minerals (Amador and Bandfield, 2016; Salvatore et al., 2016; Salvatore et al., 2018). For the detailed methods of the WAC calculation, the readers are referred to Amador and Bandfield (2016). Though the calculation renders results in numeric values, it should be visually interpreted and analyzed regardless of the actual numeric values (Salvatore et al., 2016) such that the higher values correspond to lower silica content while lower values consistent to elevated silica content (Salvatore et al., 2018). Although the sensitivity of non-silicate phases (e.g., sulfate) to WAC can lead to a vague interpretation sometimes (Amador and Bandfield, 2016), the WAC tool gives a fast overview of bulk-silica content. WAC is calculated from the same THEMIS image used for DCS calculation. The bulk silica content of the dune field is compared with the other morphologic units described by Goudge et al. (2015). The result is also simultaneously analyzed with the mineral assemblage from hyperspectral TES data.

4. Results and discussion

This section first describes the result of the employed semi-automated object-based image analysis technique for identifying the individual barchans and barchanoids in Hargraves crater. A delineated output map of the dunes was prepared, described in terms of the dune geometry (e.g., area, average elevation), and then compared with the existing Mars dune database (MGD^3). The accuracy of the employed classification for the segregation of the dunes from the non-dune objects was, subsequently, described qualitatively through visual interpretation of the reference map and quantitatively using statistical analyses e.g., error matrix, overall accuracy, and kappa coefficient. Followed by the dune identification, the result of grain-size distribution for the delineated dunes materials are outlined. A comparative grain-size analysis for the dune field and surrounding units were analyzed based on the result of nighttime thermal inertia. Due to the uncertainties involved in thermal inertia, the result from nighttime and daytime infrared (IR) global map in JMARS was analyzed as another indicator of grain-size distribution. The result of bulk mineralogy of the dune materials and the putative provenances calculated from the hyperspectral TES data were listed, compared and explained. Since TES hyperspectral has a lower spatial resolution, the result from the higher resolution THEMIS analysis were also considered for the discussion. The result of bulk mineralogy from TES analysis was revisited with the multi-spectral THEMIS analysis of DCS and WAC result and, then, compared in association with the bulk mineralogy. Finally, an analysis from the result for dune modification (stability) was reported and explained for the dune field in Hargraves crater.

4.1. Dune identification

A vector (ESRI .shp) file was produced for the dunes i.e., barchans and barchanoids at the study area. The dunes vector data were then analyzed qualitatively (e.g., visual interpretation) and quantitatively (e.g., accuracy assessment). The MGD^3 maps dune field of Hargraves as a single dune

field entity (though it does not correctly delineate appropriate dune field outline as shown in the figure 3.1a) but the dune database prepared in this project includes individual dunes and their geometric information (e.g., length, perimeter, area, etc.). It should be noted that having a linear structure in longitudinal, transverse, reverse, and star dunes make them easily identified whereas the identification of small barchan or barchanoids are sometimes very difficult to identify (Vaz et al., 2015). Therefore, the method and dune identification are validated both qualitatively through visual interpretation and quantitatively through descriptive statistics. Average elevation was calculated for the dunes at Hargraves as -1870 meters with reference to the Mars datum whereas the MGD[3] defined elevation for the entire dune field as -1851 meters. The study calculated the average elevation from the CTX stereo-derived DEM whereas the MGD[3] calculates the average elevation from the MOLA gridded topography raster. The differences between elevation data used in this study and the MGD[3] is the reason why there is a slight discrepancy in the elevation measurements. Since the digital elevation data from CTX stereo-pair were used, which has a higher spatial resolution than the MOLA gridded topography data, the result of this study is likely more reliable. The MGD[3] identified a total area of ~99 sq. km of dune field at the study area whereas this study found a total of ~73 sq. km of dune areas. This discrepancy between the estimations is likely due to semi-automated verses manual identification methods as well as this study only calculated dune areas from the individual dunes excluding the outlined surrounding areas used for the MGD[3]. Qualitative validation results show an almost perfect match with the dune distribution as assessed through visual photo inspection from the projected CTX data (Fig. 3.3).

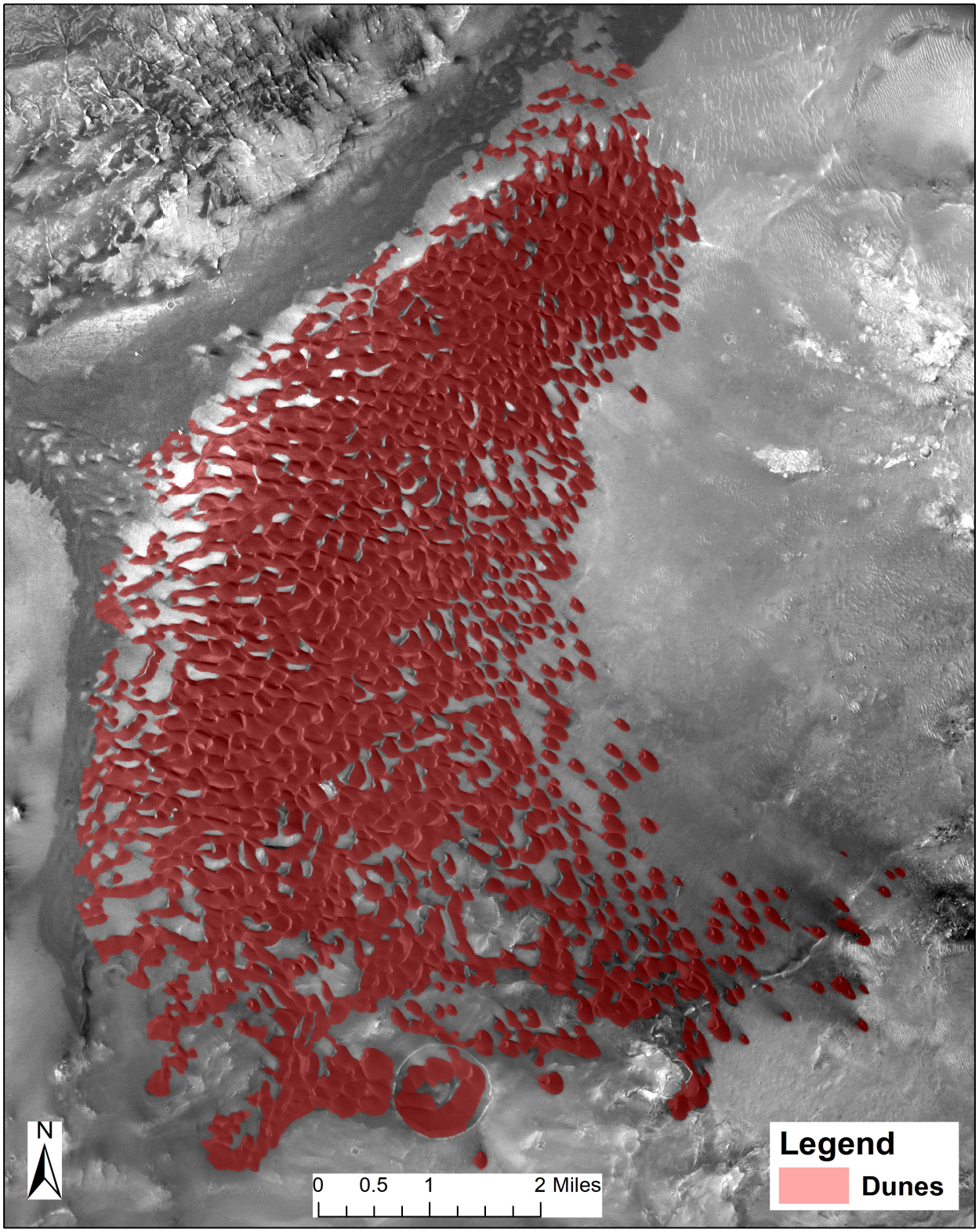

Fig. 3.3: The final delineated dunes at Hargraves crater. The prepared dune vector (ESRI .shp) file overlain on CTX images. The red polygon indicates dune shapes. Visual photo inspection shows an appropriately perfect match with the dune distribution from background CTX image.

The accuracy of the dune classification (i.e., quantitative validation) was conducted through a statistical assessment in this study. The projected CTX images were used as the reference dataset to evaluate the accuracy of the classified dunes. Exactly 500 random points were considered within the dune outline using ESRI's ArcGIS "create random points" tool. Each of the points was carefully assessed with the reference projected CTX image. An error matrix was used to evaluate the accuracy of the classification through assessing overall accuracy (OA) and kappa coefficient (kappa) statistics (Foody, 2002). The error matrix calculates the producer and user accuracy of the classification (Table 3.2). The higher OA and kappa values indicate a higher level of accuracy of the classification. Overall accuracy indicates what proportion were classified correctly and expressed as percent (%). On the other hand, kappa evaluates how well the classification performed as compared to just randomly assigning values. The producer and user accuracy were assessed for the dune classification and were 88% and 98%, respectively (Table 3.2). The overall accuracy and the kappa coefficient were 91% and 82%, respectively (Table 3.3). Having provided results showing that the higher accuracy and validated method are better in this incidence, it is argued that OBIA technique can be applied to the entire martian surface for an updated dune database. However, the study does point out that the ruleset likely will have to be modified for different regions.

Table 3.2: Details of the error matrix of the classification. The producer accuracy and user accuracy are listed in the table.

Producer Accuracy

	Accurate	Reference	Percentage
Non-Dune	166	171	97.08
Dune	291	329	88.45

User Accuracy

	Accurate	Total Points	Percentage
Non-Dune	166	204	81.37
Dune	291	296	98.31

Table 3.3: Details of the final accuracy assessment result of the classification. The overall accuracy and kappa ko-efficient are listed in the table below.

Accuracy	User (%)	Producer (%)
Dune	98.31	88.45
Non-dune	81.37	97.08
Overall accuracy (OA)	0.91 or 91%	
Kappa coefficient (*kappa*)	0.82 or 82%	

4.2. Grain-size distribution

Grain-size distribution of the dune materials was inferred from the nighttime thermal infrared products of THEMIS instrument. Though the nighttime thermal inertia indicates the grain-size distribution, nighttime surface temperature information and the global nighttime and daytime IR mosaics from THEMIS IR band 9 (12.57μm) radiance images (Hill and Christensen, 2017; Hill et al., 2014; Edwards et al., 2001; Edwards et al., 2014) were used as supplementary data. The quantitative thermal inertia values were extracted for the dune area that was measured through the semi-automated dunes identification methods (Fig. 3.4a). The calculated average thermal inertias for the dune materials at Hargraves is 243±23 $Jm^{-2}K^{-1}s^{-0.5}$ and indicates a surface composed of effective grain-size of ~230 μm (Presley and Christensen, 1997; Piqueux and Christensen, 2011). The average thermal inertia values are extracted from the thermal inertia global map of Christensen and Fergason (2013). The study then also extracted the apparent thermal inertia values for the dune materials from the thermal inertia calculated from the THEMIS I05459012 using the method developed by Putzig et al. (2014). In this case, the average apparent thermal inertia of dune materials from the THEMIS I05459012 scene was ~280±40 $Jm^{-2}K^{-1}s^{-0.5}$ which is also consistent with the grain-size indicated before. It should be noted here that this range of thermal inertia (~220 to 320 $Jm^{-2}K^{-1}s^{-0.5}$) suggest a surface that is moderately indurated and likely has some rock or unconsolidated materials (Rogers and Fergason, 2011). Figure

3.4(a) shows that the thermal inertia follows the outline of the dunes at Hargraves. Over the dunes and the associated sand aprons, there is comparatively lower thermal inertia than over the surrounding alluvial fan, crater floor, and crater central peak. This indicates that the dune materials are composed of relatively fine grain materials rather than other higher thermal inertia units. A relative comparison of grain-sizes of the dunes to the surrounding units (or source units) can be analyzed from nighttime temperature and colorized day IR and night IR mosaics. The nighttime surface temperature was examined which also follows the thermal inertia trend i.e., colder temperature over the dune materials than the surrounding units. The surface with warmest nighttime temperature had higher thermal inertia values. Due to uncertainties in thermal inertia calculation, the colorized nighttime and daytime infrared (IR) global map was examined as the supplementary of thermal inertia values. This nighttime and daytime IR global data eventually can be used as another survey tool for surface grain size distribution (Hill and Christensen, 2017; Edwards et al., 2001). This mosaic can provide qualitative information about the thermophysical or compositional information for the surface (Edwards et al., 2001) showing green tones indicating lower thermal inertia compared to red-toned higher thermal inertia values (Fig. 3.4b). The tonal variation of the dune materials was inspected from HiRISE data and indicated that the dunes have a darker tone than the surrounding materials (easily distinguishable). The results from the thermal inertia values and local variation from HiRISE images lead to a hypothesis that the dunes are less degraded and active in nature since active dunes have lower apparent thermal inertia because of finer grained material along the crest (Courville et al., 2016). Moreover, being located in the equatorial region, distinct identifiable crests that are visible in high resolution images (e.g., CTX and HiRISE), along with absence of dune-field stability features (Gullikson et al., 2018; Fenton et al., 2019) and thermal inertia values, the present study hypotheses that unlike the southern-high latitude dune fields, the dunes at Hargraves are not affected by subsurface ice or volatiles.

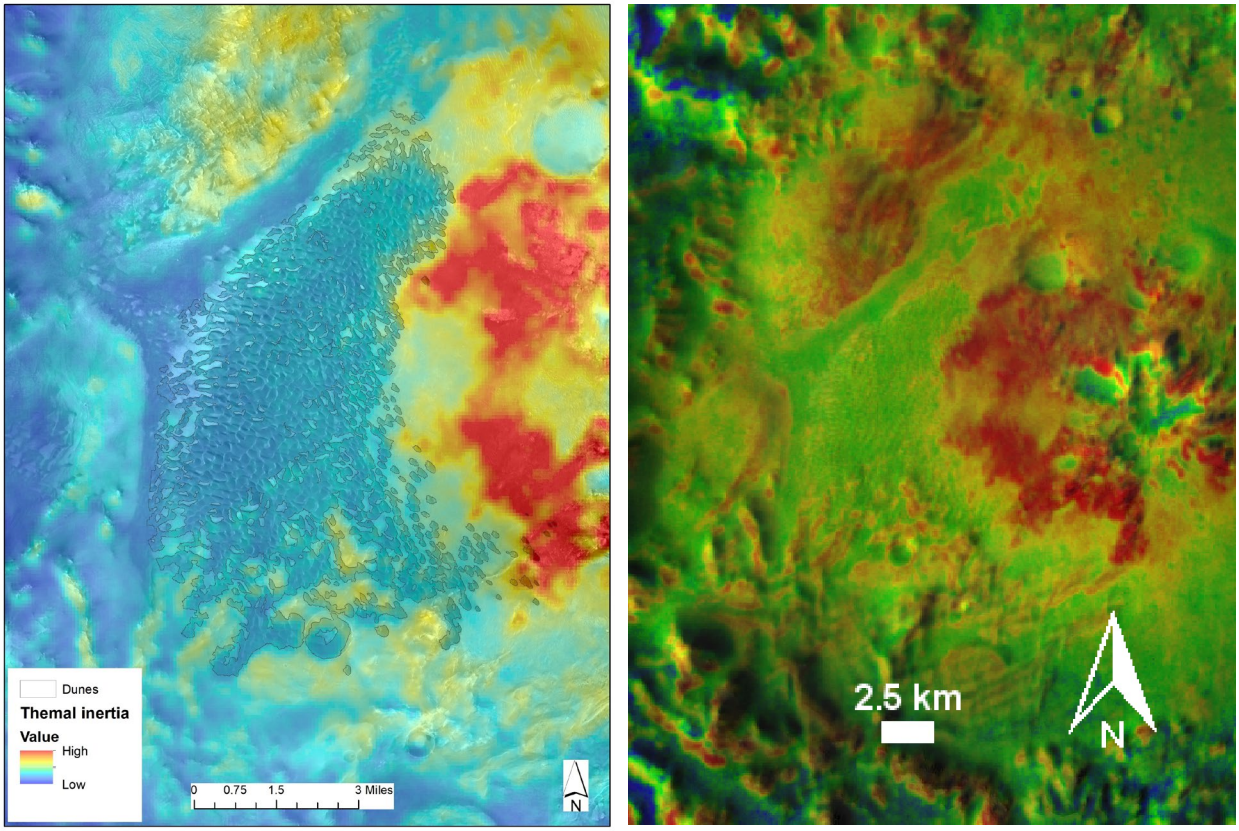

Fig. 3.4: Thermophysical characteristics of the dunes and surrounding materials derived from nighttime thermal inferred data overlain on CTX mosaics. a) nighttime thermal inertia that follows the outline of the dunes. Over the dunes and the associated sand aprons, there is comparatively lower thermal inertia than over the surrounding areas. b) colorized daytime and nighttime IR mosaic shows green tones indicating lower thermal inertia compared to red toned higher thermal inertia values.

4.3. Composition of dunes materials

The study analyzed the bulk mineralogy of dune materials and compared the composition with inferred provenances (source units). The crater floor materials (CFM), crater ejecta (Ce), central peak (Cp), and crater rim and wall (Crw) unit were considered as the putative provenances of dune materials. Because the alluvial fan (AF) unit is situated in a downwind direction from the dunes, the unit was not considered as a potential source for dune materials. The mineral abundance analyzed consists of 8 mineral groups (Rogers and Fergason, 2011; Ahrens and Titus, 2014) based on non-negative least

square spectral unmixing analysis of TES emissivity data. The mineral groups include feldspar (both plagioclase and alkali feldspar), pyroxene (both high-Ca clinopyroxene [HCP] and low-Ca clinopyroxene [LCP]), high-silica phase (HSP; including amorphous silica and phyllosilicates), sulfate, olivine, hematite, carbonate, and quartz. Table 3.4 shows the interpreted dune mineral assemblage. Table 3.3 shows that dune materials are enriched in a mixture of feldspar, pyroxene, olivine, and other silicate minerals. Even though dune materials (Du) have a higher concentration of olivine than any of the other units, the concentration of high-silica phase minerals is lower than all other units except crater ejecta unit (Ce). The average mineral abundance of the dune materials indicates that the surface of dune materials is composed of a mixture of feldspar, pyroxene, olivine, and a high-silica phase (mineral or mineraloid). The crater ejecta (Ce) unit has the highest concentration of feldspar but has the lowest abundance of olivine. The high-silica phases are reported in the crater floor and central peak unit followed by rim and wall materials. The average surface emissivity spectra and modeled spectra for the five geomorphic units in the crater are shown in Figure 3.5.

Based on the mineralogy of the dune materials, it is suggested that they were derived from physical weathering, especially aeolian erosion, of a mixture of the crater floor, central peak, and crater rim and wall lithologies. The erosion and transport process typically modify the percentages of constituent grains. In this instance, olivine is apparently enriched in the dunes. The higher concentration of olivine in the dunes versus provenance sites cannot be attributed only to the density of the olivine grains, which is slightly less than the companion pyroxene grains (Lapotre et al., 2017; 2018). Another factor must be involved, and Lapotre et al. (2017) have suggested grain size and/or grain shape as mitigating factors in understanding compositional analysis of other martian dunes. One of these two factors likely cause olivine grains to be preferentially left behind as a lag deposit, particularly on the windward side of dunes such as those in the study area and in the interdune areas (Greeley et al., 1999; 2002;

Jerolmack et al., 2006; Mangold et al., 2011; Hooper et al., 2012). Rather than being a pervasive lag deposit, the olivine particles may be sequestered specifically in small coarse-grained ripples and other fine-scale bedforms of the windward sides and interdunes, which are very common in dune areas of Mars (Hooper et al., 2012; Lapotre et al., 2017; 2018). The grain shapes of olivine cannot be assessed directly, but the lack of cleavage in olivine and the pervasive presence of strong cleavage in pyroxenes may result in more angular and more equidimensional grains as fundamental characteristics of the olivine grain population. Wind-drag across coarse-grained martian ripples has been interpreted to cause the infiltration of finer, less equidimensional grains (i.e., pyroxenes) (Hooper et al., 2012). These factors, combined with the slight tendency for olivine grains to be slightly larger than companion pyroxenes in Mars aeolian systems (Lapotre et al., 2017; 2018), suggests that olivine may comprise a disproportionate amount of surficial grains in the dune-mantling ripple deposits envisioned here.

Table 3.4: The result of spectral unmixing procedure on TES data in the dune (Du), crater floor materials (CFM), central peak (Cp), and crater rim and wall (Crw) unit as defined by Goudge et al. (2015). Reported are the average areal abundances of each mineral group (in percentage) along with the calculated model error.

Mineral group	Dune materials (Du)	Floor material (CFM)	Crater ejecta (Ce)	Central peak (Ccp)	Rim and wall (Crw)
Feldspar	35.87±7.32	24.32±5.50	38.60±4.25	27.04±6.32	36.24±6.65
Pyroxene	22.01±5.92	29.48±4.57	29.08±3.93	21.20±5.40	20.52±4.55
Olivine	12.26±4.51	7.32±5.05	2.64±2.18	8.10±3.51	7.29±3.15
High-silica phase	16.23±6.96	22.71±4.85	15.15±3.82	22.41±5.68	20.52±4.55
Carbonate	4.98±0.87	2.55±0.66	3.65±0.46	4.11±0.73	3.05±0.61
Sulfate	3.06±1.84	9.88±1.36	7.09±1.44	11.57±2.83	8.65±2.43
Hematite	4.24±1.44	3.74±1.44	3.81±0.91	5.56±1.61	5.94±1.31
Quartz	1.34±1.78	0±0	0±0	0±0	1.08±0.98
Blackbody	0.3999±3.21	0.3892±2.22	0.1977±2.51	0.4256±2.63	0.5412±2.32
RMSE	0.25	0.22	0.28	0.26	0.17

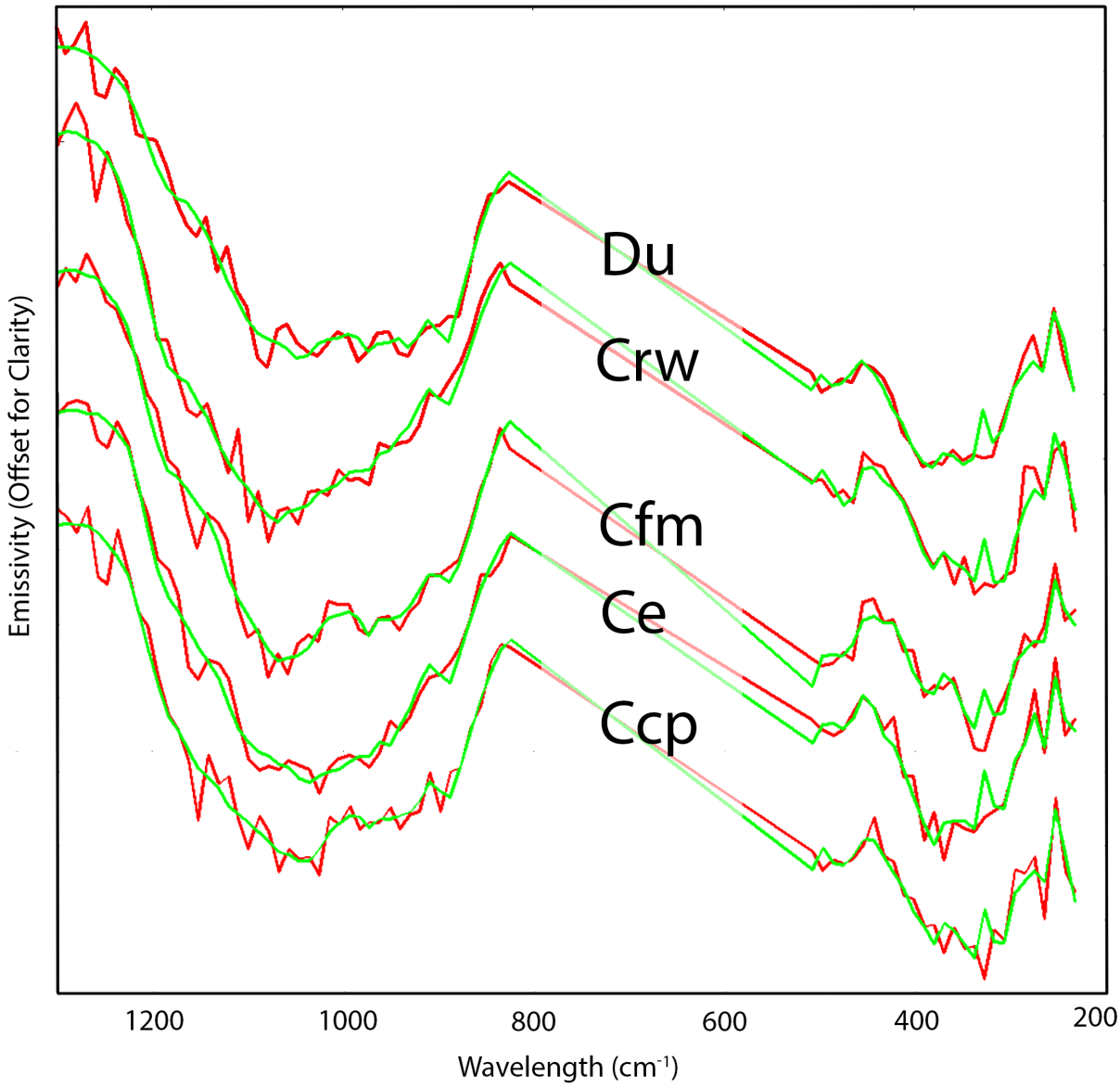

Fig. 3.5: Average atmospherically corrected TES emissivity spectra (red) for each of the investigated morphologic units in Hargraves crater, with the best-fit model spectra (green) derived from the non-linear unmixing procedures. (For interpretation of the references to color in this figure legend, the reader is referred to the web version of this article.)

The composition of the dune materials was qualitatively analyzed from decorrelation stretch (DCS) image of different band combination from THEMIS daytime IR image (Fig. 3.6) because it can be used as a proxy tool for olivine-bearing basalt and bulk silica content of the surface materials (Edwards et al., 2011; Amador and Bandfield, 2016). The dune field does not show a distinctive

(homogeneous) spectral feature in DCS combinations. DCS bands 8-7-5 indicates a mixture of purple, magenta, and yellow colors over the dune materials suggesting a composition of a mixture of olivine, pyroxene, and Fe/Mg-smectite which are very typical of the Nili Fossae area (Goudge et al., 2015 and the references therein). Having a paucity of high-resolution e.g., full resolution targeted (FRT) observation of visible-near infrared CRISM data for dune materials individually (and other units as a whole), the present study could not analyze reflectance spectra for the surface mineralogy. However, in the latter part of the article, the bulk-silica content of dune materials and nearby units from higher spatial resolution images, as available THEMIS data permits, were separately compared. A previous study of the mineralogy of the crater floor unit in VNIR spectroscopy indicates a lacking significant abundance of altered phase but exhibits the presence of olivine and high calcium pyroxene (Salvatore et al., 2018). The bulk mineralogy from the TES data by Salvatore et al. (2018) indicates that crater floor unit (combing Cfm and Ccp units of Goudge et al. [2015]) has a comparable phyllosilicate and amorphous component (PAC) than nearby Syrtis basalt and contains comparable amounts of plagioclase, pyroxene (both high and low calcium), and olivine. The slight discrepancies in bulk mineralogy of crater floor materials in the result of Salvatore et al. (2018) with this study is likely because Salvatore et al. (2018) averaged the spectra from central peak and crater floor units of Goudge et al. (2015) into a single crater floor unit while this study consider individual unit as a separate entity. DCS band combinations (9-6-4 and 6-4-2) are also consistent with the interpretation of the band combination of 8-7-5. Alluvial fan unit appears more yellowish indicating inferred higher bulk-silica content than the dune materials, though this study did not concern alluvial fan unit. Due to the scarcity of the CRISM-VNIR data over the dune field, it cannot be assured about local scale individual mineral distributions of the units independently. However, the product of the DCS images at different combinations and the result from bulk mineralogy of TES data, provide an impression about the constituent materials of the dune and its surrounding morphologic units.

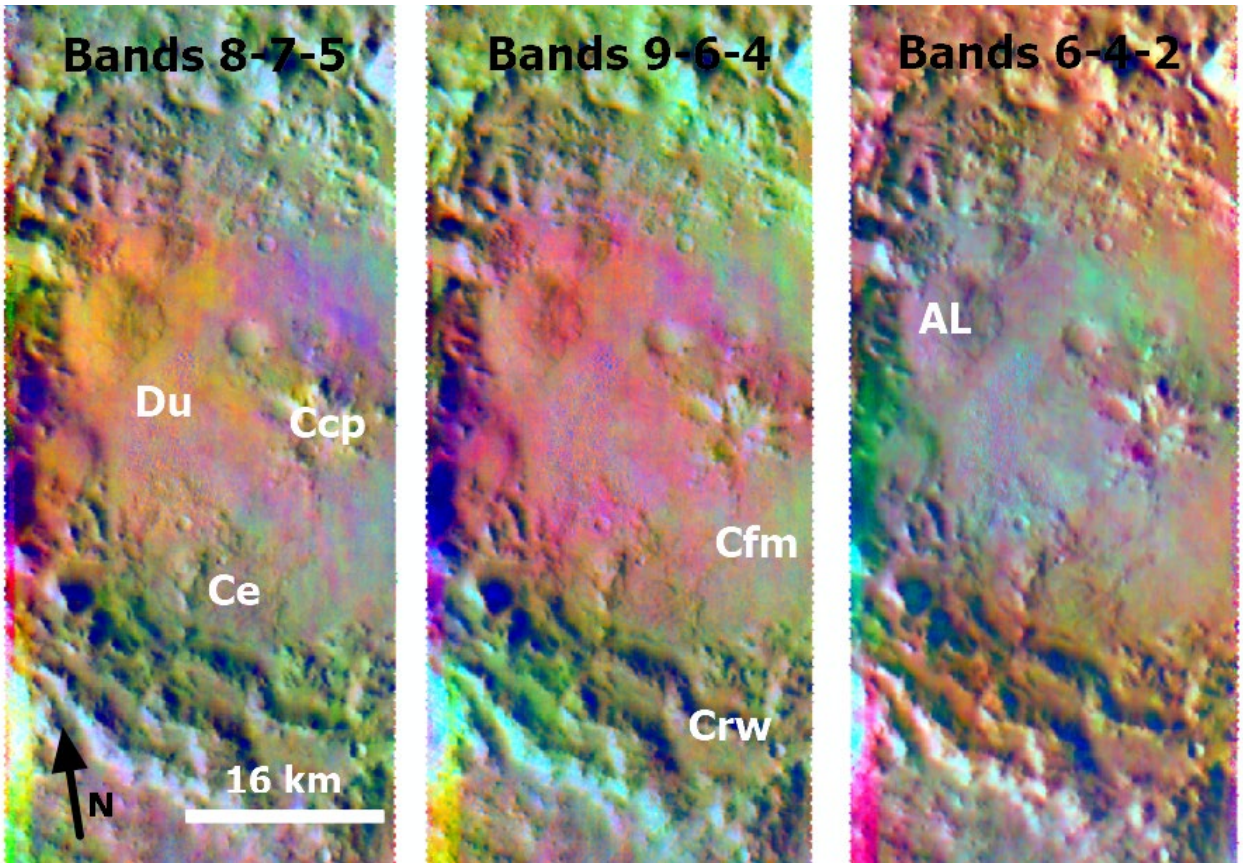

Fig. 3.6: 3-panel decorrelation stretch (DCS) for the THEMIS image I47821006 overlain on the radiance image of the same scene. The geomorphic units are labeled on the DCS images: dune (Du), central peak (Ccp), floor materials (Cfm), crater ejecta (Ce), and rim and wall materials (Crw) in the color combination across all three stretches.

THEMIS average emissivity spectra (bands 3 through 9) were collected for each of the morphologic units (Fig. 3.7). In THEMIS multispectral data, the dune (Du) materials are distinguished from other units by a strong absorption at band 7 (~11 μm) which is consistent with higher olivine enrichment. To determine a qualitative measurement of bulk-silica content on the dune materials and other units, the "weighted absorption center (WAC)" was calculated from the same THEMIS image I47821006. The result shows that the THEMIS emissivity image has WAC values ranging ~9.6 through 10.2 μm within a specified area (Fig. 3.8). Noteworthy here, regardless of the actual WAC wavelength values, the higher values correspond to lower silica content while lower values consistent

to elevated bulk-silica content (Amador and Bandfield, 2016; Salvatore et al., 2018). The figure indicates that the dune material has comparatively higher WAC values meaning band minimum shifts to longer wavelengths consistent to the decrease in bulk silica abundances (Vincent and Thomson, 1972; Walter and Salisbury, 1989). The result from WAC is consistent with the result from the TES mineralogy and DCS indicating comparatively lower silica content in the dune materials. In contrast, the central peak, rim and wall, and floor material units show lower values meaning band minimum shifts to shorter wavelengths consistent with the increase in bulk silica abundances, consistent with TES mineralogy. It is posited that the higher silica content in the alluvial fan than the dune materials are attributed to the geologic processes and sources involved for the alluvial fan materials. The materials of the alluvial fan likely came from the crater rim or outside the crater through fluvial activities. In contrast, the dune materials are the product of the aeolian process sourced mostly from inside the crater materials (e.g., crater floor, central peak, and rim).

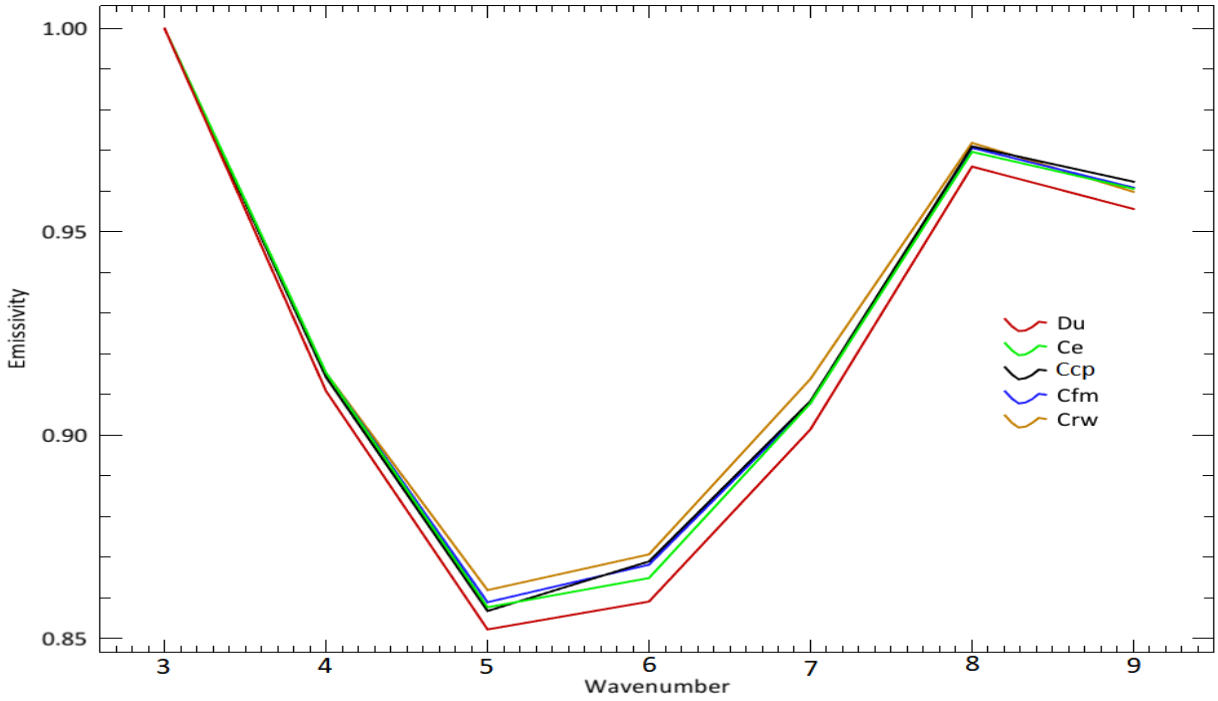

Fig. 3.7: TMEMIS emissivity spectra (bands 3 through 9; offset for clarity) THEMIS image I47821006 for morphologic units; dune (Du), central peak (Ccp), floor materials (Cfm), crater ejecta (Ce), and rim and wall materials (Crw).

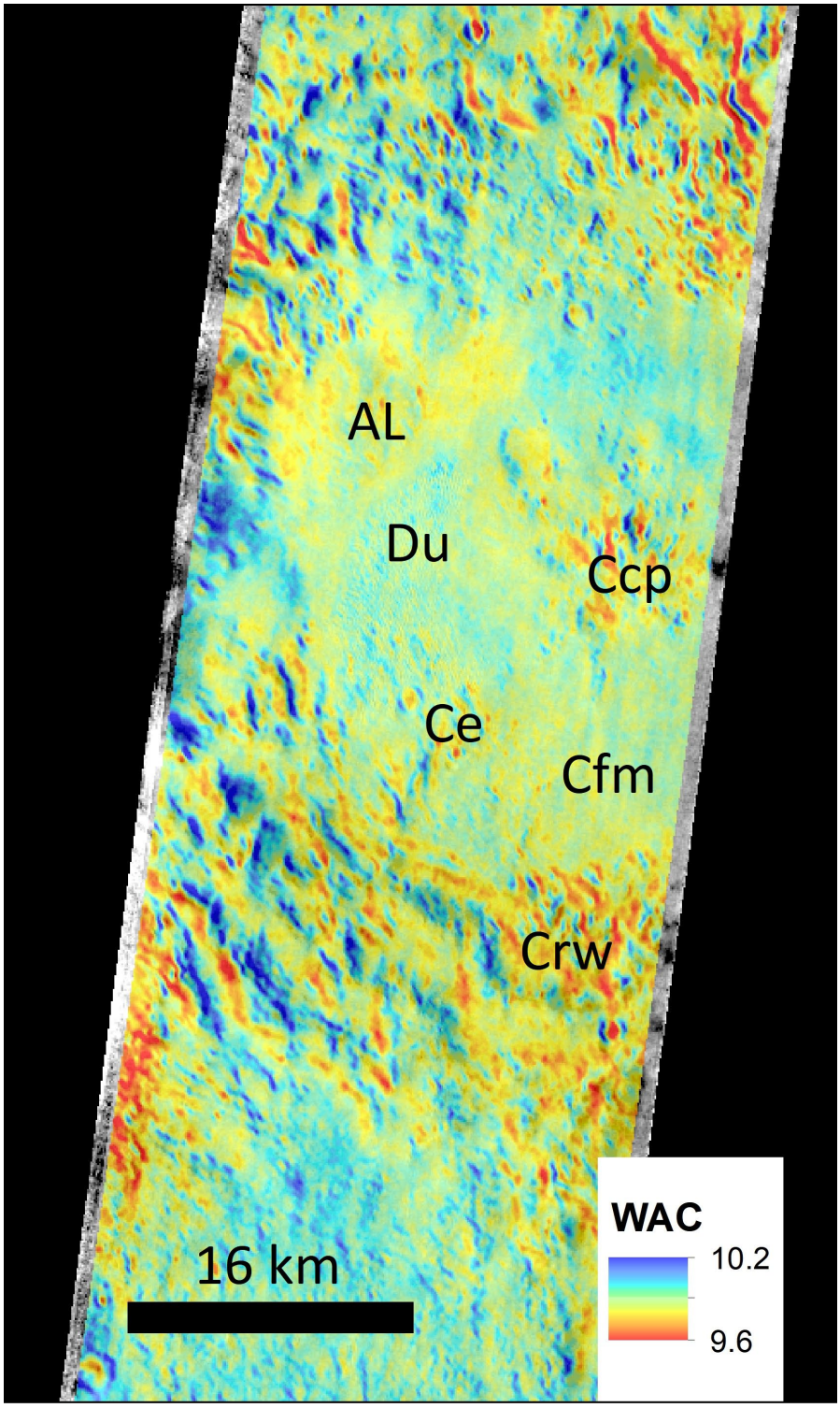

Fig. 3.8: Weighted absorption center (WAC) for the THEMIS image I02781003 overlain on the radiance image of the same scene. North is up on the map. The geomorphic units are labeled on the DCS images: dune (Du), central peak (Ccp), floor materials (Cfm), crater ejecta (Ce), and rim and wall materials (Crw). The higher values in WAC corresponds to lower silica content while lower values consistent with elevated bulk-silica content.

4.4. Slipface, wind movement, and dune mobility

The raw slipfaces of the dunes were analyzed to interpret the wind movement inside the crater as was prepared by the MGD[3]. A total of 77 raw slipfaces were prepared from the Mars Orbiter Camera's narrow-angle (MOC-NA; Malin et al., 1992) observations and THEMIS visible camera images (Hayward et al., 2007). For the Hargraves crater, MOC-NA R1102034 and THEMIS-VIS V02781004, V09634019, and V13016004 images were used to verify the location of, to classify, or to measure slipfaces of dunes. MOC-NA has a higher spatial resolution like the CTX image does, therefore, the study did not prepare a separate raw slipfaces data for the dunes; rather, it used the existing raw slipface prepared by the MGD[3]. The slipfaces were derived from gross dune morphology in Hargraves crater. The slipfaces indicate the prevailing wind direction of significant dune modification at the last time (Hayward et al., 2007). The work of Hayward et al. (2007) shows that slipface orientations for the dune fields within craters are less correlated with the martian wind general circulation model (GCM); rather, the dune orientation is predominantly influenced by the effect of the local topography. That is why this project also hypothesize that the local topography within the Hargraves crater determines the wind direction, slipface orientation, and eventually the shape of the dunes. The calculated raw slipface azimuth of the dunes has a minimum value of 281.13^0 to 321.55^0 with an average slipface value of 306.46^0. The primary wind direction was recorded, in this study, by an estimated average of the individual slipface azimuths discernible from gross dune morphology of different dune types (i.e., barchans and barchanoids) that were shaped by unidirectional winds. Thus, the study asserts that the prevailing wind movement direction inside the crater is around 300^0. Though the temporal movement of the dunes at the crater does not belong to the scope of the present study, it is presumed that the dunes in the present study area are active or mobile. The reason for this hypothesis roots into the global latitudinal dune field stability (Gullikson et al., 2018; Fenton et al., 2019). The study of Gullikson et al. (2018) found that the dune field from the high northern latitude to mid-southern latitude

(including the present study area) has no features associated with dune-field stability and thus inferred to be active. This project inferred that the dunes at the carter are also active (albeit the annual rate of movement is unknown until now) with a wind movement towards west-northwest (300^0 azimuths).

To confirm the interpretations on dune mobility and modification, the stability index was used for the dunes at Hargraves crater. With the CTX and HiRISE data, the study looked for finding the presence of superposed non-aeolian features and to apprehend the apparent level of dune degradation (or modification) by non-aeolian processes. The project searched for some specific feature like gullies, small pits, and mass wasting features from high-resolution images (e.g., CTX and HiRISE) at the dune field. The study did not find any of these non-aeolian features; however, there is a thin sand apron present on the western part of the dune field. Based on visual inspection it is posited that the dune field has a stability index of 2; the dunes are partially surrounded by crisp-edged sandy aprons that do not completely merge with those of neighboring dunes. In addition, the study suggests that unlike the dunes at the southern-high latitude, the dunes at Hargraves crater are not modified or influenced by the subsurface water ice or other volatiles.

5. Conclusion

The delineation of dune fields in MGD^3 was prepared manually through visual photo-interpretation from the THEMIS imagery at 100 m/pixel spatial resolution, including the digitized dune parameters and mapped dune slipface orientations. However, the manual digitizing of the dune parameters from the lower resolution THEMIS images is a tedious and time-consuming task. Thus, a semi-automated method from higher resolution images e.g., CTX at ~6 m/pixel can be used more efficiently to extract significant morphological information about the martian dune fields. This study employed a semi-automated object-based image analysis technique to extract dunes at Hargraves carter

as a test case of OBIA application. The validated and relatively accurate results indicate the applicability of the OBIA method for dune mapping for the entire surface of Mars.

The project then analyzed the thermal infrared response of the dune materials to identify the grain-size distribution and surface mineral composition of the dune field. The study found average thermal inertia for the dune materials is 243±23 $Jm^{-2}K^{-1}s^{-0.5}$, indicating a surface composed of effective grain-size of ~230 μm (i.e., fine sand grain materials). The result from the bulk mineralogy, decorrelation stretch (DCS), and weighted absorption center (WAC) analysis showed that the dune materials are composed of a mixture of feldspar, olivine, pyroxene, and with a relatively lower bulk-silica content. The wind movement was analyzed inside the crater from the dune slipface orientation which indicates the prevailing wind direction inside the crater towards the west-northwest. The dune field was identified as having active dunes with a stability index of 2.

Acknowledgments

The authors would like to thank the team members of 2001 Mars Odyssey, Mars Global Surveyor (MGS), and Mars Reconnaissance Orbiter (MRO) spacecraft missions for targeting, collecting, and archiving THEMIS, TES, CTX, and HiRISE datasets. JMARS, ISIS3, Ames Stereo Pipelines (ASP), Davinci, THMPROC, MARSTHERM, and ArcGIS software/tools were used for data processing and analysis. Special thanks to the team of Arizona State University's Mars Space Flight Facility. The author would also like to thank the anonymous reviewer(s) for the critical review of this paper.

References

Abuodha, J.O.Z., 2003. Grain size distribution and composition of modern dune and beach sediments, Malindi Bay coast, Kenya. Journal of African Earth Sciences 36, 41–54. https://doi.org/10.1016/S0899-5362(03)00016-2

Ahrens, C.J., Titus, T.N., 2014. An Assessment of the Reliability of Mineral Abundance Estimates Derived from TES Data over Dune Sites. Presented at the Eighth International Conference on Mars, p. 1012.

Amador, E.S., Bandfield, J.L., 2016. Elevated bulk-silica exposures and evidence for multiple aqueous alteration episodes in Nili Fossae, Mars. Icarus 276, 39–51. https://doi.org/10.1016/j.icarus.2016.04.015

Baatz, M., Hoffmann, C., Willhauck, G., 2008. Progressing from object-based to object-oriented image analysis, in: Object-Based Image Analysis, Lecture Notes in Geoinformation and Cartography. Springer, Berlin, Heidelberg, pp. 29–42. https://doi.org/10.1007/978-3-540-77058-9_2

Baldridge, A. M., 2007. Thermal infrared spectral studies of sulfates and chlorides: Applications to salts on the Martian surface. Thesis, Ariz. State Univ., Tempe. Pp, 204.

Bandeira, L., Marques, J.S., Saraiva, J., Pina, P., 2010. Automated Detection of Sand Dunes on Mars, in: Image Analysis and Recognition, Lecture Notes in Computer Science. Presented at the International Conference Image Analysis and Recognition, Springer, Berlin, Heidelberg, pp. 306–315. https://doi.org/10.1007/978-3-642-13775-4_31

Bandeira, L., Marques, J.S., Saraiva, J., Pina, P., 2011. Automated Detection of Martian Dune Fields. IEEE Geoscience and Remote Sensing Letters 8, 626–630. https://doi.org/10.1109/LGRS.2010.2098390

Bandfield, J.L., 2002. Global mineral distributions on Mars. Journal of Geophysical Research: Planets 107, 9-1-9–20. https://doi.org/10.1029/2001JE001510

Bandfield, J.L., Christensen, P.R., Smith, M.D., 2000b. Spectral data set factor analysis and end-member recovery: Application to analysis of Martian atmospheric particulates. Journal of Geophysical Research: Planets 105, 9573–9587. https://doi.org/10.1029/1999JE001094

Bandfield, J.L., Deanne Rogers, A., Edwards, C.S., 2011. The role of aqueous alteration in the formation of martian soils. Icarus 211, 157–171. https://doi.org/10.1016/j.icarus.2010.08.028

Bandfield, J.L., Hamilton, V.E., Christensen, P.R., 2000a. A Global View of Martian Surface Compositions from MGS-TES. Science 287, 1626–1630. https://doi.org/10.1126/science.287.5458.1626

Bandfield, J.L., Hamilton, V.E., Christensen, P.R., McSween, H.Y., 2004a. Identification of quartzofeldspathic materials on Mars. Journal of Geophysical Research: Planets 109. https://doi.org/10.1029/2004JE002290

Bandfield, J.L., Rogers, D., Smith, M.D., Christensen, P.R., 2004b. Atmospheric correction and surface spectral unit mapping using Thermal Emission Imaging System data. Journal of Geophysical Research: Planets 109. https://doi.org/10.1029/2004JE002289

Banks, M.E., Fenton, L.K., Bridges, N.T., Geissler, P.E., Chojnacki, M., Runyon, K.D., Silvestro, S., Zimbelman, J.R., 2018. Patterns in Mobility and Modification of Middle- and High-Latitude Southern Hemisphere Dunes on Mars. Journal of Geophysical Research: Planets 123, 3205–3219. https://doi.org/10.1029/2018JE005747

Beveridge, C., Kocurek, G., Ewing, R.C., Lancaster, N., Morthekai, P., Singhvi, A.K., Mahan, S.A., 2006. Development of spatially diverse and complex dune-field patterns: Gran Desierto Dune Field, Sonora, Mexico. Sedimentology 53, 19. https://doi.org/10.1111/j.1365-3091.2006.00814.x

Beyer, R.A., Alexandrov, O., Moratto, Z.M., 2014. Aligning Terrain Model and Laser Altimeter Point Clouds with the Ames Stereo Pipeline. Presented at the Lunar and Planetary Science Conference, p. 2902.

Blaschke, T., 2010. Object based image analysis for remote sensing. ISPRS Journal of Photogrammetry and Remote Sensing 65, 2–16. https://doi.org/10.1016/j.isprsjprs.2009.06.004

Blaschke, T., Hay, G.J., Kelly, M., Lang, S., Hofmann, P., Addink, E., Queiroz Feitosa, R., van der Meer, F., van der Werff, H., van Coillie, F., Tiede, D., 2014. Geographic Object-Based Image Analysis – Towards a new paradigm. ISPRS Journal of Photogrammetry and Remote Sensing 87, 180–191. https://doi.org/10.1016/j.isprsjprs.2013.09.014

Blaschke, T., Strobl, J., 2002. What's wrong with pixels? Some recent developments interfacing remote sensing and GIS. GIS–Zeitschrift für Geoinformationssysteme, 14 (6), 12-17

Broxton, M.J., Edwards, L.J., 2008. The Ames Stereo Pipeline: Automated 3D Surface Reconstruction from Orbital Imagery. Presented at the Lunar and Planetary Science Conference, p. 2419.

Burnett, C., Blaschke, T., 2003. A multi-scale segmentation/object relationship modelling methodology for landscape analysis. Ecological Modelling, Landscape Theory and Landscape Modelling 168, 233–249. https://doi.org/10.1016/S0304-3800(03)00139-X

Cannon, K., Mustard, J., Osinski, G., Tornabene, L., Parman, S., Amador, E., Brown, A., Viviano-Beck, C., Ehlmann, B., Sapers, H., Pontefract, A., Marais, D.D., Mangold, N., Wiseman, S., 2015. An Ancient Crustal Stratigraphy in the Nili Fossae Troug Clays, Carbonates, Impacts and Volcanics. In 2nd Mars 2020 Landing Site Workshop.

Castilla, G., Hay, G.J., 2008. Image objects and geographic objects, in: Object-Based Image Analysis, Lecture Notes in Geoinformation and Cartography. Springer, Berlin, Heidelberg, pp. 91–110. https://doi.org/10.1007/978-3-540-77058-9_5

Christensen, P.R., Bandfield, J.L., Hamilton, V.E., Howard, D.A., Lane, M.D., Piatek, J.L., Ruff, S.W., Stefanov, W.L., 2000. A thermal emission spectral library of rock-forming minerals. Journal of Geophysical Research: Planets 105, 9735–9739. https://doi.org/10.1029/1998JE000624

Christensen, P.R., Bandfield, J.L., Hamilton, V.E., Ruff, S.W., Kieffer, H.H., Titus, T.N., Malin, M.C., Morris, R.V., Lane, M.D., Clark, R.L., Jakosky, B.M., Mellon, M.T., Pearl, J.C., Conrath, B.J., Smith, M.D., Clancy, R.T., Kuzmin, R.O., Roush, T., Mehall, G.L., Gorelick, N., Bender, K., Murray, K., Dason, S., Greene, E., Silverman, S., Greenfield, M., 2001. Mars Global Surveyor Thermal Emission Spectrometer experiment: Investigation description and surface science results. Journal of Geophysical Research: Planets 106, 23823–23871. https://doi.org/10.1029/2000JE001370

Christensen, P.R., Engle, E., Anwar, S., Dickenshied, S., Noss, D., Gorelick, N., Weiss-Malik, M., 2009. JMARS - A Planetary GIS. AGU Fall Meeting Abstracts 22, IN22A-06.

Christensen, P.R., Fergason, R.L., Edwards, C.S., Hill, J., 2013. THEMIS-Derived Thermal Inertia Mosaic of Mars: Product Description and Science Results. Presented at the Lunar and Planetary Science Conference, p. 2822.

Christensen, P.R., Jakosky, B.M., Kieffer, H.H., Malin, M.C., McSween, H.Y., Nealson, K., Mehall, G.L., Silverman, S.H., Ferry, S., Caplinger, M., Ravine, M., 2004. The Thermal Emission Imaging System (THEMIS) for the Mars 2001 Odyssey Mission. Space Science Reviews 110, 85–130. https://doi.org/10.1023/B:SPAC.0000021008.16305.94

Courville, S.W., Putzig, N.E., Hoover, R., Fenton, L.K., 2016. Thermophysical Variation within Dune Fields in the Southern Hemisphere of Mars. AGU Fall Meeting Abstracts 21, P21A-2073.

Darwish, A., Leukert, K., Reinhardt, W., 2003. Image segmentation for the purpose of object-based classification, in: IGARSS 2003. 2003 IEEE International Geoscience and Remote Sensing Symposium. Proceedings (IEEE Cat. No.03CH37477). Presented at the IGARSS 2003. 2003

IEEE International Geoscience and Remote Sensing Symposium. Proceedings (IEEE Cat. No.03CH37477), pp. 2039–2041. https://doi.org/10.1109/IGARSS.2003.1294332

Delamere, W.A., Tornabene, L.L., McEwen, A.S., Becker, K., Bergstrom, J.W., Bridges, N.T., Eliason, E.M., Gallagher, D., Herkenhoff, K.E., Keszthelyi, L., Mattson, S., McArthur, G.K., Mellon, M.T., Milazzo, M., Russell, P.S., Thomas, N., 2010. Color imaging of Mars by the High Resolution Imaging Science Experiment (HiRISE). Icarus, MRO/HiRISE Studies of Mars 205, 38–52. https://doi.org/10.1016/j.icarus.2009.03.012

Edgett, K.S., Christensen, P.R., 1991. The particle size of Martian aeolian dunes. Journal of Geophysical Research: Planets 96, 22765–22776. https://doi.org/10.1029/91JE02412

Edgett, K.S., Malin, M.C., 2000. New views of Mars eolian activity, materials, and surface properties: Three vignettes from the Mars Global Surveyor Mars Orbiter Camera. Journal of Geophysical Research: Planets 105, 1623–1650. https://doi.org/10.1029/1999JE001152

Edwards, C.S., Ehlmann, B.L., 2015. Carbon sequestration on Mars. Geology 43, 863–866. https://doi.org/10.1130/G36983.1

Edwards, C.S., Nowicki, K.J., Christensen, P.R., Hill, J., Gorelick, N., Murray, K., 2011. Mosaicking of global planetary image datasets: 1. Techniques and data processing for Thermal Emission Imaging System (THEMIS) multi-spectral data. Journal of Geophysical Research: Planets 116. https://doi.org/10.1029/2010JE003755

Ehlmann, B.L., Mustard, J.F., Swayze, G.A., Clark, R.N., Bishop, J.L., Poulet, F., Marais, D.J.D., Roach, L.H., Milliken, R.E., Wray, J.J., Barnouin-Jha, O., Murchie, S.L., 2009. Identification of hydrated silicate minerals on Mars using MRO-CRISM: Geologic context near Nili Fossae and implications for aqueous alteration. Journal of Geophysical Research: Planets 114. https://doi.org/10.1029/2009JE003339

Elbelrhiti, H., Andreotti, B., Claudin, P., 2008. Barchan dune corridors: Field characterization and investigation of control parameters. Journal of Geophysical Research: Earth Surface 113 (F2). https://doi.org/10.1029/2007JF000767

Emran, A., Marzen, L.J., King, D.T., 2019. Automated Object-Based Identification of Dunes at Hargraves Crater, Mars. Presented at the Lunar and Planetary Science Conference, p. 1157.

Ewing, R.C., Kocurek, G., Lake, L.W., 2006. Pattern analysis of dune-field parameters. Earth Surface Processes and Landforms 31, 1176–1191. https://doi.org/10.1002/esp.1312

Feely, K.C., Christensen, P.R., 1999. Quantitative compositional analysis using thermal emission spectroscopy: Application to igneous and metamorphic rocks. Journal of Geophysical Research: Planets 104, 24195–24210. https://doi.org/10.1029/1999JE001034

Fenton, L. K., Gullikson, A. L., Hayward, R. K., Charles, H., Titus, T. N., 2019. The Mars Global Digital Dune Database (MGD^3): Composition and Stability. Presented at the Lunar and Planetary Science Conference, p. 1115.

Fenton, L.K., Hayward, R.K., 2010. Southern high latitude dune fields on Mars: Morphology, aeolian inactivity, and climate change. Geomorphology, Planetary Dune Systems 121, 98–121. https://doi.org/10.1016/j.geomorph.2009.11.006

Fenton, L.K., Michaels, T.I., Beyer, R.A., 2014a. Inverse maximum gross bedform-normal transport 1: How to determine a dune-constructing wind regime using only imagery. Icarus, Third Planetary Dunes Systems 230, 5–14. https://doi.org/10.1016/j.icarus.2013.04.001

Fenton, L.K., Michaels, T.I., Chojnacki, M., Beyer, R.A., 2014b. Inverse maximum gross bedform-normal transport 2: Application to a dune field in Ganges Chasma, Mars and comparison with HiRISE repeat imagery and MRAMS. Icarus, Third Planetary Dunes Systems 230, 47–63. https://doi.org/10.1016/j.icarus.2013.07.009

Fenton, L.K., Toigo, A.D., Richardson, M.I., 2005. Aeolian processes in Proctor Crater on Mars: Mesoscale modeling of dune-forming winds. Journal of Geophysical Research (Planets) 110, E06005. https://doi.org/10.1029/2004JE002309

Fergason, R.L., Christensen, P.R., Kieffer, H.H., 2006. High-resolution thermal inertia derived from the Thermal Emission Imaging System (THEMIS): Thermal model and applications. Journal of Geophysical Research: Planets 111. https://doi.org/10.1029/2006JE002735

Fisher, P., 1997. The pixel: A snare and a delusion. International Journal of Remote Sensing 18, 679–685. https://doi.org/10.1080/014311697219015

Foody, G.M., 2002. Status of land cover classification accuracy assessment. Remote Sensing of Environment 80, 185–201. https://doi.org/10.1016/S0034-4257(01)00295-4

Gardin, E., Allemand, P., Quantin, C., Silvestro, S., Delacourt, C., 2012. Dune fields on Mars: Recorders of a climate change? Planetary and Space Science, Titan Through Time: A Workshop on Titan's Formation, Evolution and Fate 60, 314–321. https://doi.org/10.1016/j.pss.2011.10.004

Glotch, T.D., Morris, R.V., Christensen, P.R., Sharp, T.G., 2004. Effect of precursor mineralogy on the thermal infrared emission spectra of hematite: Application to Martian hematite mineralization. Journal of Geophysical Research: Planets 109. https://doi.org/10.1029/2003JE002224

Goudge, T.A., Milliken, R.E., Head, J.W., Mustard, J.F., Fassett, C.I., 2017. Sedimentological evidence for a deltaic origin of the western fan deposit in Jezero crater, Mars and implications for future exploration. Earth and Planetary Science Letters 458, 357–365. https://doi.org/10.1016/j.epsl.2016.10.056

Goudge, T.A., Mustard, J.F., Head, J.W., Fassett, C.I., Wiseman, S.M., 2015. Assessing the mineralogy of the watershed and fan deposits of the Jezero crater paleolake system, Mars. Journal of Geophysical Research: Planets 120, 775–808. https://doi.org/10.1002/2014JE004782

Greeley, R., Bridges, N.T., Kuzmin, R.O., Laity, J.E., 2002. Terrestrial analogs to wind-related features at the Viking and Pathfinder landing sites on Mars. Journal of Geophysical Research: Planets 107, 5-1-5–22. https://doi.org/10.1029/2000JE001481

Greeley, R., Iversen, J.D., 1987. Wind as a Geological Process: On Earth, Mars, Venus and Titan. Cambridge University Press, Cambridge.

Greeley, R., Kraft, M., Sullivan, R., Wilson, G., Bridges, N., Herkenhoff, K., Kuzmin, R.O., Malin, M., Ward, W., 1999. Aeolian features and processes at the Mars Pathfinder landing site. Journal of Geophysical Research: Planets 104, 8573–8584. https://doi.org/10.1029/98JE02553

Greeley, R., Kuzmin, R.O., Haberle, R.M., 2001. Aeolian Processes and their Effects on Understanding the Chronology of Mars. Space Science Reviews 96, 393–404. https://doi.org/10.1023/A:1011917910624

Greeley, R., Thompson, S.D., 2003. Mars: Aeolian features and wind predictions at the Terra Meridiani and Isidis Planitia potential Mars Exploration Rover landing sites. Journal of Geophysical Research (Planets) 108, 8093. https://doi.org/10.1029/2003JE002110

Gullikson, A.L., Hayward, R.K., Titus, T.N., Charles, H., Fenton, L.K., Hoover, R.H., Putzig, N.E., 2018. Mars global digital dune database (MGD3)—Composition, stability, and thermal inertia (USGS Numbered Series No. 2018–1164), Open-File Report. U.S. Geological Survey, Reston, VA.

Haberle, R.M., Jakosky, B.M., 1991. Atmospheric effects on the remote determination of thermal inertia on mars. Icarus 90, 187–204. https://doi.org/10.1016/0019-1035(91)90100-8

Hay, G.J., Castilla, G., 2008. Geographic Object-Based Image Analysis (GEOBIA): A new name for a new discipline, in: Object-Based Image Analysis, Lecture Notes in Geoinformation and

Cartography. Springer, Berlin, Heidelberg, pp. 75–89. https://doi.org/10.1007/978-3-540-77058-9_4

Hayward, R.K., Fenton, L., Titus, T.N., 2014. Mars Global Digital Dune Database (MGD3): Global dune distribution and wind pattern observations. Icarus 230, 9. https://doi.org/10.1016/j.icarus.2013.04.011

Hayward, R.K., Mullins, K.F., Fenton, L.K., Hare, T.M., Titus, T.N., Bourke, M.C., Colaprete, A., Christensen, P.R., 2007. Mars global digital dune database and initial science results. Journal of Geophysical Research E: Planets 112. https://doi.org/10.1029/2007JE002943

Hayward, R.K., Titus, T.N., Michaels, T.I., Fenton, L.K., Colaprete, A., Christensen, P.R., 2009. Aeolian dunes as ground truth for atmospheric modeling on Mars. Journal of Geophysical Research E: Planets 114. https://doi.org/10.1029/2009JE003428

Hooper, D.M., McGinnis, R.N., Necsoiu, M., 2012. Volcaniclastic aeolian deposits at Sunset Crater, Arizona: terrestrial analogs for Martian dune forms. Earth Surface Processes and Landforms 37, 1090–1105. https://doi.org/10.1002/esp.3238

Huang, J., Edwards, C.S., Ruff, S.W., Christensen, P.R., Xiao, L., 2013. A new method for the semiquantitative determination of major rock-forming minerals with thermal infrared multispectral data: Application to THEMIS infrared data. Journal of Geophysical Research: Planets 118, 2146–2152. https://doi.org/10.1002/jgre.20160

Hugenholtz, C.H., Levin, N., Barchyn, T.E., Baddock, M.C., 2012. Remote sensing and spatial analysis of aeolian sand dunes: A review and outlook. Earth-Science Reviews 111, 319–334. https://doi.org/10.1016/j.earscirev.2011.11.006

Hugenholtz, C.H., Levin, N., Barchyn, T.E., Baddock, M.C., 2012. Remote sensing and spatial analysis of aeolian sand dunes: A review and outlook. Earth-Science Reviews 111, 319–334. https://doi.org/10.1016/j.earscirev.2011.11.006

Ivanov, M.A., Hiesinger, H., Erkeling, G., Hielscher, F.J., Reiss, D., 2012. Major episodes of geologic history of Isidis Planitia on Mars. Icarus 218, 24–46. https://doi.org/10.1016/j.icarus.2011.11.029

Jerolmack, D.J., Mohrig, D., Grotzinger, J.P., Fike, D.A., Watters, W.A., 2006. Spatial grain size sorting in eolian ripples and estimation of wind conditions on planetary surfaces: Application to Meridiani Planum, Mars. Journal of Geophysical Research: Planets 111. https://doi.org/10.1029/2005JE002544

Johnson, J.R., Hörz, F., Lucey, P.G., Christensen, P.R., 2002. Thermal infrared spectroscopy of experimentally shocked anorthosite and pyroxenite: Implications for remote sensing of Mars. Journal of Geophysical Research: Planets 107, 3-1-3–14. https://doi.org/10.1029/2001JE001517

Kieffer, H.H., Martin, T.Z., Peterfreund, A.R., Jakosky, B.M., Miner, E.D., Palluconi, F.D., 1977. Thermal and albedo mapping of Mars during the Viking primary mission. Journal of Geophysical Research 82, 4249–4291. https://doi.org/10.1029/JS082i028p04249

Kocurek, G., Ewing, R.C., 2005. Aeolian dune field self-organization – implications for the formation of simple versus complex dune-field patterns. Geomorphology 72, 94–105. https://doi.org/10.1016/j.geomorph.2005.05.005

Koeppen, W.C., Hamilton, V.E., 2008. Global distribution, composition, and abundance of olivine on the surface of Mars from thermal infrared data. Journal of Geophysical Research: Planets 113. https://doi.org/10.1029/2007JE002984

Lapotre, M.G.A., Ehlmann, B.L., Minson, S.E., Arvidson, R.E., Ayoub, F., Fraeman, A.A., Ewing, R.C., Bridges, N.T., 2017. Compositional variations in sands of the Bagnold Dunes, Gale crater, Mars, from visible-shortwave infrared spectroscopy and comparison with ground truth

from the Curiosity rover. Journal of Geophysical Research: Planets 122, 2489–2509. https://doi.org/10.1002/2016JE005133

Lapotre, M.G.A., Ewing, R.C., Weitz, C.M., Lewis, K.W., Lamb, M.P., Ehlmann, B.L., Rubin, D.M., 2018. Morphologic Diversity of Martian Ripples: Implications for Large-Ripple Formation. Geophysical Research Letters 45, 10,229-10,239. https://doi.org/10.1029/2018GL079029

Lawson, C.L., Hanson, R.J., 1995. Solving Least Squares Problems. Prentice-Hall, Englewood Cliffs, NJ, pp 340.

Lorenz, R.D., Wall, S., Radebaugh, J., Boubin, G., Reffet, E., Janssen, M., Stofan, E., Lopes, R., Kirk, R., Elachi, C., Lunine, J., Mitchell, K., Paganelli, F., Soderblom, L., Wood, C., Wye, L., Zebker, H., Anderson, Y., Ostro, S., Allison, M., Boehmer, R., Callahan, P., Encrenaz, P., Ori, G.G., Francescetti, G., Gim, Y., Hamilton, G., Hensley, S., Johnson, W., Kelleher, K., Muhleman, D., Picardi, G., Posa, F., Roth, L., Seu, R., Shaffer, S., Stiles, B., Vetrella, S., Flamini, E., West, R., 2006. The Sand Seas of Titan: Cassini RADAR Observations of Longitudinal Dunes. Science 312, 724–727. https://doi.org/10.1126/science.1123257

Malin, M.C., Bell, J.F., Cantor, B.A., Caplinger, M.A., Calvin, W.M., Clancy, R.T., Edgett, K.S., Edwards, L., Haberle, R.M., James, P.B., Lee, S.W., Ravine, M.A., Thomas, P.C., Wolff, M.J., 2007. Context Camera Investigation on board the Mars Reconnaissance Orbiter. Journal of Geophysical Research (Planets) 112, E05S04. https://doi.org/10.1029/2006JE002808

Malin, M.C., Danielson, G.E., Ingersoll, A.P., Masursky, H., Veverka, J., Ravine, M.A., Soulanille, T.A., 1992. Mars Observer camera. Journal of Geophysical Research: Planets 97, 7699–7718. https://doi.org/10.1029/92JE00340

Mangold, N., Baratoux, D., Arnalds, O., Bardintzeff, J.-M., Platevoet, B., Grégoire, M., Pinet, P., 2011. Segregation of olivine grains in volcanic sands in Iceland and implications for Mars. Earth and Planetary Science Letters 310, 233–243. https://doi.org/10.1016/j.epsl.2011.07.025

Mangold, N., Poulet, F., Mustard, J.F., Bibring, J.-P., Gondet, B., Langevin, Y., Ansan, V., Masson, P., Fassett, C., Head, J.W., Hoffmann, H., Neukum, G., 2007. Mineralogy of the Nili Fossae region with OMEGA/Mars Express data: 2. Aqueous alteration of the crust. Journal of Geophysical Research: Planets 112. https://doi.org/10.1029/2006JE002835

McEwen, A.S., Eliason, E.M., Bergstrom, J.W., Bridges, N.T., Hansen, C.J., Delamere, W.A., Grant, J.A., Gulick, V.C., Herkenhoff, K.E., Keszthelyi, L., Kirk, R.L., Mellon, M.T., Squyres, S.W., Thomas, N., Weitz, C.M., 2007. Mars reconnaissance orbiter's high resolution imaging science experiment (HiRISE). Journal of Geophysical Research E: Planets 112. https://doi.org/10.1029/2005JE002605

McGuire, P.C., Bishop, J.L., Brown, A.J., Fraeman, A.A., Marzo, G.A., Frank Morgan, M., Murchie, S.L., Mustard, J.F., Parente, M., Pelkey, S.M., Roush, T.L., Seelos, F.P., Smith, M.D., Wendt, L., Wolff, M.J., 2009. An improvement to the volcano-scan algorithm for atmospheric correction of CRISM and OMEGA spectral data. Planetary and Space Science 57, 809–815. https://doi.org/10.1016/j.pss.2009.03.007

Michalski, J.R., Kraft, M.D., Diedrich, T., Sharp, T.G., Christensen, P.R., 2003. Thermal emission spectroscopy of the silica polymorphs and considerations for remote sensing of Mars. Geophysical Research Letters 30. https://doi.org/10.1029/2003GL018354

Michalski, J.R., Kraft, M.D., Sharp, T.G., Williams, L.B., Christensen, P.R., 2006. Emission spectroscopy of clay minerals and evidence for poorly crystalline aluminosilicates on Mars from Thermal Emission Spectrometer data. Journal of Geophysical Research: Planets 111. https://doi.org/10.1029/2005JE002438

Michalski, J.R., Kraft, M.D., Sharp, T.G., Williams, L.B., Christensen, P.R., 2005. Mineralogical constraints on the high-silica martian surface component observed by TES. Icarus 174, 161–177. https://doi.org/10.1016/j.icarus.2004.10.022

Moratto, Z.M., Broxton, M.J., Beyer, R.A., Lundy, M., Husmann, K., 2010. Ames Stereo Pipeline, NASA's Open Source Automated Stereogrammetry Software. Presented at the Lunar and Planetary Science Conference, p. 2364.

Murchie, S., Arvidson, R., Bedini, P., Beisser, K., Bibring, J.-P., Bishop, J., Boldt, J., Cavender, P., Choo, T., Clancy, R.T., Darlington, E.H., Des Marais, D., Espiritu, R., Fort, D., Green, R., Guinness, E., Hayes, J., Hash, C., Heffernan, K., Hemmler, J., Heyler, G., Humm, D., Hutcheson, J., Izenberg, N., Lee, R., Lees, J., Lohr, D., Malaret, E., Martin, T., McGovern, J.A., McGuire, P., Morris, R., Mustard, J., Pelkey, S., Rhodes, E., Robinson, M., Roush, T., Schaefer, E., Seagrave, G., Seelos, F., Silverglate, P., Slavney, S., Smith, M., Shyong, W.-J., Strohbehn, K., Taylor, H., Thompson, P., Tossman, B., Wirzburger, M., Wolff, M., 2007. Compact Reconnaissance Imaging Spectrometer for Mars (CRISM) on Mars Reconnaissance Orbiter (MRO). Journal of Geophysical Research (Planets) 112, E05S03. https://doi.org/10.1029/2006JE002682

Murphy, N.W., Jakosky, B.M., Rafkin, S.C., Larsen, K.W., Putzig, N.E., Mellon, M.T., 2007. Thermophysical properties of the Isidis basin, Mars. Journal of Geophysical Research: Planets 112. https://doi.org/10.1029/2005JE002586

Osinski, G.R., Tornabene, L.L., Grieve, R.A.F., 2011. Impact ejecta emplacement on terrestrial planets. Earth and Planetary Science Letters 310, 167–181. https://doi.org/10.1016/j.epsl.2011.08.012

Pelkey, S.M., Mustard, J.F., Murchie, S., Clancy, R.T., Wolff, M., Smith, M., Milliken, R., Bibring, J.-P., Gendrin, A., Poulet, F., Langevin, Y., Gondet, B., 2007. CRISM multispectral summary products: Parameterizing mineral diversity on Mars from reflectance. Journal of Geophysical Research: Planets 112. https://doi.org/10.1029/2006JE002831

Piqueux, S., Christensen, P.R., 2011. Temperature-dependent thermal inertia of homogeneous Martian regolith. Journal of Geophysical Research: Planets 116. https://doi.org/10.1029/2011JE003805

Pont, S.C. du, Narteau, C., Gao, X., 2014. Two modes for dune orientation. Geology 42, 743–746. https://doi.org/10.1130/G35657.1

Presley, M.A., Christensen, P.R., 1997. Thermal conductivity measurements of particulate materials 1. A review. Journal of Geophysical Research: Planets 102, 6535–6549. https://doi.org/10.1029/96JE03302

Putzig, N.E., Barratt, E.M., Mellon, M.T., Michaels, T.I., 2013. MARSTHERM: A Web-based System Providing Thermophysical Analysis Tools for Mars Research. AGU Fall Meeting Abstracts 43, P43C-2023.

Putzig, N.E., Mellon, M.T., Herkenhoff, K.E., Phillips, R.J., Davis, B.J., Ewer, K.J., Bowers, L.M., 2014. Thermal behavior and ice-table depth within the north polar erg of Mars. Icarus, Third Planetary Dunes Systems 230, 64–76. https://doi.org/10.1016/j.icarus.2013.07.010

Quantin-Nataf, C., Lozac'h, L., Thollot, P., Loizeau, D., Bultel, B., Fernando, J., Allemand, P., Dubuffet, F., Poulet, F., Ody, A., Clenet, H., Leyrat, C., Harrisson, S., 2018. MarsSI: Martian surface data processing information system. Planetary and Space Science, Enabling Open and Interoperable Access to Planetary Science and Heliophysics Databases and Tools 150, 157–170. https://doi.org/10.1016/j.pss.2017.09.014

Ramsey, M.S., Christensen, P.R., 1998. Mineral abundance determination: Quantitative deconvolution of thermal emission spectra. Journal of Geophysical Research: Solid Earth 103, 577–596. https://doi.org/10.1029/97JB02784

Rogers, A.D., Aharonson, O., 2008. Mineralogical composition of sands in Meridiani Planum determined from Mars Exploration Rover data and comparison to orbital measurements. Journal of Geophysical Research: Planets 113. https://doi.org/10.1029/2007JE002995

Rogers, A.D., Bandfield, J.L., Christensen, P.R., 2007. Global spectral classification of Martian low-albedo regions with Mars Global Surveyor Thermal Emission Spectrometer (MGS-TES) data. Journal of Geophysical Research: Planets 112. https://doi.org/10.1029/2006JE002726

Rogers, A.D., Christensen, P.R., 2007. Surface mineralogy of Martian low-albedo regions from MGS-TES data: Implications for upper crustal evolution and surface alteration. Journal of Geophysical Research: Planets 112. https://doi.org/10.1029/2006JE002727

Rogers, A.D., Fergason, R.L., 2011. Regional-scale stratigraphy of surface units in Tyrrhena and Iapygia Terrae, Mars: Insights into highland crustal evolution and alteration history. Journal of Geophysical Research: Planets 116. https://doi.org/10.1029/2010JE003772

Ruff, S.W., 2004. Spectral evidence for zeolite in the dust on Mars. Icarus 168, 131–143. https://doi.org/10.1016/j.icarus.2003.11.003

Ryan, C.H., Tornabene, L.L., Cannon, K.M., Mustard, J.F., Sapers, H.M., Osinski, G.R., 2017. Geomorphological Mapping of Hargraves Ejecta in the Nili Fossae Trough: Insight into Impact Processes at Potential Mars 2020 Landing Site. Presented at the Lunar and Planetary Science Conference, p. 2861.

Ryan, C.H., Tornabene, L.L., Osinski, G.R., Cannon, K.M., Mustard, J.F., MacRae, R.A., Corney, R., Sapers, H.M., 2016. Geomorphological Mapping of the Hargraves Ejecta and Polygonal Terrain Associated with the Candidate Mars 2020 Landing Site, Nili Fossae Trough. Presented at the Lunar and Planetary Science Conference, p. 2524.

Sagan, C., Veverka, J., Fox, P., Dubisch, R., Lederberg, J., Levinthal, E., Quam, L., Tucker, R., Pollack, J.B., Smith, B.A., 1972. Variable features on Mars: Preliminary mariner 9 television results. Icarus 17, 346–372. https://doi.org/10.1016/0019-1035(72)90005-X

Salvatore, M.R., Goudge, T.A., Bramble, M.S., Edwards, C.S., Bandfield, J.L., Amador, E.S., Mustard, J.F., Christensen, P.R., 2018. Bulk mineralogy of the NE Syrtis and Jezero crater regions of Mars derived through thermal infrared spectral analyses. Icarus 301, 76–96. https://doi.org/10.1016/j.icarus.2017.09.019

Salvatore, M.R., Kraft, M.D., Edwards, C.S., Christensen, P.R., 2016. The geologic history of Margaritifer basin, Mars. Journal of Geophysical Research: Planets 121, 273–295. https://doi.org/10.1002/2015JE004938

Salvatore, M.R., Mustard, J.F., Head, J.W., Rogers, A.D., Cooper, R.F., 2014. The dominance of cold and dry alteration processes on recent Mars, as revealed through pan-spectral orbital analyses. Earth and Planetary Science Letters 404, 261–272. https://doi.org/10.1016/j.epsl.2014.08.006

Salvatore, M.R., Mustard, J.F., Wyatt, M.B., Murchie, S.L., 2010. Definitive evidence of Hesperian basalt in Acidalia and Chryse planitiae. Journal of Geophysical Research: Planets 115. https://doi.org/10.1029/2009JE003519

Seelos, F.P., IV, Arvidson, R.E., 2003. Bounded Variable Least Squares -- Application of a Constrained Optimization Algorithm to the Analysis of TES Emissivity Spectra. Presented at the Lunar and Planetary Science Conference.

Sefton-Nash, E., Teanby, N.A., Newman, C., Clancy, R.A., Richardson, M.I., 2014. Constraints on Mars' recent equatorial wind regimes from layered deposits and comparison with general circulation model results. Icarus, Third Planetary Dunes Systems 230, 81–95. https://doi.org/10.1016/j.icarus.2013.11.014

Sholes, S.F., Chevrier, V.F., Tullis, J.A., 2013. Object based image analysis for remote sensing of planetary surfaces. 44th Lunar and Planetary Science Conference, Houston, Texas.

Silvestro, S., Di Achille, G., Ori, G.G., 2010. Dune morphology, sand transport pathways and possible source areas in east Thaumasia Region (Mars). Geomorphology, Planetary Dune Systems 121, 84–97. https://doi.org/10.1016/j.geomorph.2009.07.019

Silvestro, S., Vaz, D.A., Ewing, R.C., Rossi, A.P., Fenton, L.K., Michaels, T.I., Flahaut, J., Geissler, P.E., 2013. Pervasive aeolian activity along rover Curiosity's traverse in Gale Crater, Mars. Geology 41, 483–486. https://doi.org/10.1130/G34162.1

Smith, B.A., Soderblom, L.A., Banfield, D., Barnet, C., Basilevsky, A.T., Beebe, R.F., Bollinger, K., Boyce, J.M., Brahic, A., Briggs, G.A., Brown, R.H., Chyba, C., Collins, s A., Colvin, T., Cook, A.F., Crisp, D., Croft, S.K., Cruikshank, D., Cuzzi, J.N., Danielson, G.E., Davies, M.E., Jong, E.D., Dones, L., Godfrey, D., Goguen, J., Grenier, I., Haemmerle, V.R., Hammel, H., Hansen, c J., Helfenstein, c P., Howell, C., Hunt, G.E., Ingersoll, A.P., Johnson, T.V., Kargel, J., Kirk, R., Kuehn, D.I., Limaye, S., Masursky, H., McEwen, A., Morrison, D., Owen, T., Owen, W., Pollack, J.B., Porco, C.C., Rages, K., Rogers, P., Rudy, D., Sagan, C., Schwartz, J., Shoemaker, E.M., Showalter, M., Sicardy, B., Simonelli, D., Spencer, J., Sromovsky, L.A., Stoker, C., Strom, R.G., Suomi, V.E., Synott, S.P., Terrile, R.J., Thomas, P., Thompson, W.R., Verbiscer, A., Veverka, J., 1989. Voyager 2 at Neptune: Imaging Science Results. Science 246, 1422–1449. https://doi.org/10.1126/science.246.4936.1422

Smith, D.E., Zuber, M.T., Frey, H.V., Garvin, J.B., Head, J.W., Muhleman, D.O., Pettengill, G.H., Phillips, R.J., Solomon, S.C., Zwally, H.J., Banerdt, W.B., Duxbury, T.C., Golombek, M.P., Lemoine, F.G., Neumann, G.A., Rowlands, D.D., Aharonson, O., Ford, P.G., Ivanov, A.B., Johnson, C.L., McGovern, P.J., Abshire, J.B., Afzal, R.S., Sun, X., 2001. Mars Orbiter Laser Altimeter: Experiment summary after the first year of global mapping of Mars. Journal of Geophysical Research 106, 23689–23722. https://doi.org/10.1029/2000JE001364

Smith, M.D., Bandfield, J.L., Christensen, P.R., 2000. Separation of atmospheric and surface spectral features in Mars Global Surveyor Thermal Emission Spectrometer (TES) spectra. Journal of Geophysical Research: Planets 105, 9589–9607. https://doi.org/10.1029/1999JE001105

Strahler, A.H., Woodcock, C.E., Smith, J.A., 1986. On the nature of models in remote sensing. Remote Sensing of Environment 20, 121–139. https://doi.org/10.1016/0034-4257(86)90018-0

Telfer, M.W., Parteli, E.J.R., Radebaugh, J., Beyer, R.A., Bertrand, T., Forget, F., Nimmo, F., Grundy, W.M., Moore, J.M., Stern, S.A., Spencer, J., Lauer, T.R., Earle, A.M., Binzel, R.P., Weaver, H.A., Olkin, C.B., Young, L.A., Ennico, K., Runyon, K., The New Horizons Geology, G. and I.S.T.T., 2018. Dunes on Pluto. Science 360, 992–997. https://doi.org/10.1126/science.aao2975

Tzotsos, A., Argialas, D., 2008. Support Vector Machine Classification for Object-Based Image Analysis, in: Object-Based Image Analysis, Lecture Notes in Geoinformation and Cartography. Springer, Berlin, Heidelberg, pp. 663–677. https://doi.org/10.1007/978-3-540-77058-9_36

Vaz, D.A., Sarmento, P.T.K., Barata, M.T., Fenton, L.K., Michaels, T.I., 2015. Object-based Dune Analysis: Automated dune mapping and pattern characterization for Ganges Chasma and Gale crater, Mars. Geomorphology 250, 128–139. https://doi.org/10.1016/j.geomorph.2015.08.021

Vaz, D.A., Silvestro, S., 2014. Mapping and characterization of small-scale aeolian structures on Mars: An example from the MSL landing site in Gale Crater. Icarus, Third Planetary Dunes Systems 230, 151–161. https://doi.org/10.1016/j.icarus.2013.08.007

Viviano-Beck, C.E., Murchie, S.L., Beck, A.W., Dohm, J.M., 2017. Compositional and structural constraints on the geologic history of eastern Tharsis Rise, Mars. Icarus 284, 43–58. https://doi.org/10.1016/j.icarus.2016.09.005

Viviano-Beck, C.E., Seelos, F.P., Murchie, S.L., Kahn, E.G., Seelos, K.D., Taylor, H.W., Taylor, K., Ehlmann, B.L., Wiseman, S.M., Mustard, J.F., Morgan, M.F., 2014. Revised CRISM spectral parameters and summary products based on the currently detected mineral diversity on Mars.

Journal of Geophysical Research: Planets 119, 1403–1431. https://doi.org/10.1002/2014JE004627

Ward, A.W., Doyle, K.B., Helm, P.J., Weisman, M.K., Witbeck, N.E., 1985. Global map of eolian features on Mars. Journal of Geophysical Research 90, 19.

Wichman, R.W., Schultz, P.H., 1989. Sequence and mechanisms of deformation around the Hellas and Isidis Impact Basins on Mars. Journal of Geophysical Research 94, 17333. https://doi.org/10.1029/JB094iB12p17333

Wilson, S.A., Zimbelman, J.R., 2004. Latitude-dependent nature and physical characteristics of transverse aeolian ridges on Mars. Journal of Geophysical Research: Planets 109, E10. https://doi.org/10.1029/2004JE002247

Wyatt, M.B., Hamilton, V.E., McSween, H.Y., Christensen, P.R., Taylor, L.A., 2001. Analysis of terrestrial and Martian volcanic compositions using thermal emission spectroscopy: 1. Determination of mineralogy, chemistry, and classification strategies. Journal of Geophysical Research: Planets 106, 14711–14732. https://doi.org/10.1029/2000JE001356

Yu, X., Hörst, S.M., He, C., McGuiggan, P., Crawford, B., 2018. Where Does Titan Sand Come From: Insight From Mechanical Properties of Titan Sand Candidates. Journal of Geophysical Research: Planets 123, 2310–2321. https://doi.org/10.1029/2018JE005651

Zurek, R.W., Smrekar, S.E., 2007. An overview of the Mars Reconnaissance Orbiter (MRO) science mission. Journal of Geophysical Research: Planets 112. https://doi.org/10.1029/2006JE002701

Chapter 4: NIR-TIR Spectral Investigations of Siloe Patera in Arabia Terra, Mars

Abstract

Having a debated geologic history of the late Noachian to early Hesperian Siloe Patera in Arabia Terra, this study aimed at resolving the possible origin of the feature. Available high-resolution images were used to analyze the morphology and thermal inertia in testing its impact crater verses supervolcanic origin hypothesis. Local geologic features were interpreted from the Thermal Emission Imaging System (THEMIS), the Context Camera (CTX), and the High Resolution Imaging Science Experiment (HiRISE) sensors data. Thermal inertia was derived from the nighttime thermal infrared data of the THEMIS images. Mineralogy of olivine, phyllosilicate, and hydrated silicates phases was identified using the Compact Reconnaissance Imaging Spectrometer for Mars (CRISM) visible near infrared (VNIR) data. The study interprets that Siloe Patera has experienced multiple geologic processes; initially formed as an impact crater, followed by subsequent modification by the Noachian (or early Hesperian) fluvial activities and/or periglacial reworking and, then, followed by a major collapse event due to primarily of cryospheric subsurface ice-removal resulting in melting of accumulated subsurface snow and ice deposits that formed boomerang lake and fresh shallow valley (FSV) system in conjunction with possible effusive lava flow and volcanic heating during the Hesperian - Amazonian period. Later, the depression has experienced with glacial reworking during the late Amazonian epoch and recent aeolian modification. Though the study does not rule out the presence of bedded and friable deposits that are of supervolcanic origin in the area, Siloe Patera is not a source of these supervolcanic deposits i.e., not a volcanic caldera.

Keywords: Siloe Patera, Arabia Terra, Mars, THEMIS, CTX, HiRISE

1. Introduction

Arabia Terra is a heavily cratered region lying on the margins of the southern highland of Mars (Tanaka et al., 2003) which dates back to the middle to late Noachian period (Tanaka et al., 2014) of approximately ~3.7-3.9 Ga (Michael, 2013). The region has an area of roughly ~12×10^6 sq. km extending about 20° - 280° W and 50° N to the equator (e.g., Anguita et al., 1997) with a regional slope of around 0.0016° that featuring only gradual elevation changes (Carr, 2007). The area was thought to have formed from the northern plain basement through the processes of uplift, resurfacing, and exposure (Zuber, 2001) during before about 3.7 Ga (Hartmann and Neukum, 2001). In contrast, Hynek and Phillips (2001) interpret that Arabia Terra is a part of southern highlands based on observations of widespread denudation, superposition relations, and crater counts (Brugman, 2014). The regional morphology of the area is attributed by heavily degraded and incised landscape with numerous inliers, rugged craters with adjacent smooth topographic lowers, and linear ridges within the intra-crater plains (e.g., McGill, 2000; Hynek and Phillips, 2001). Widespread valley networks truncated upon entering Arabia Terra suggesting large scale resurfacing of the highlands that resulted in aggregate sediment deposition (and transportation) of ~4.5×10^6 km^3 on the northern plains (Hynek and Phillips, 2001). The linear ridges, known as wrinkle ridges, in this region have been interpreted to represent tectonic deformation of the surface (e.g., Watters, 1988; Raitala, 1990; Watters, 1993). The development of the fretted and chaotic terrains along the dichotomy boundary in the region are thought to have formed from the removal of ground ice, subsurface magma, or liquid water-related geologic activities (Sharp, 1973). Inverted channels with anabranching geometry and tributary junction all indicate the paleo-fluvial systems present in Arabia Terra (Davis et al., 2016). Evidence of high albedo and low thermal inertia values are interpreted as the result of dust mantling (thickness of few centimeters to a meter) in Arabia Terra region (e.g., Fergason and Christensen, 2008).

The martian surface is composed mostly of basaltic composition as revealed by satellite orbital data (e.g., Bandfield, 2002), martian meteorites (e.g., McSween, 1985), and lander and rover data (e.g., Baird et al., 1976; Ruff et al., 2006). The abundant layered crater morphologies or multiple layer ejecta (MLE) in Arabia Terra are proposed to have originated from subsurface water (Zuber, 2001; Dohm et al., 2007). The presence of fine-grained layered deposits (etched terrain or mantled unit) in the region have been interpreted to be sourced from aeolian, air dust fall or loess deposits (e.g., Schultz and Lutz, 1988; Grant and Schultz, 1990; Fergason and Christensen, 2008), airborne and pyroclastic tuff deposits (Moore, 1990), oceanic sediment deposits (Edgett and Parker, 1997; Achille and Hynek, 2010), deposition by dust and ice (Tanaka, 2000), and intrusion of volcanic sills (Wilhelms and Baldwin, 1988). Mars also favors explosive volcanism (Carr, 2007) and some previous literature asserts that the layered deposits of friable materials in Arabia Terra may have sourced from explosive volcanism, i.e., volcanic ash falls and pyroclastic deposits (e.g., Moore, 1990; Hynek et al., 2003; Fassett and Head, 2007; Kerber et al., 2012; Michalski and Bleacher, 2013). The terrestrial explosive volcanism is attributed by higher-silica content and higher viscosity (e.g., Self, 2006) in contrast to the martian basaltic lower-silica content surface. The martian volcanic features are mostly effusive in nature that have been characterized as shield volcanoes, flood lavas, and fields of small vents (e.g., Carr, 1973; Greeley and Spudis, 1981; Francis and Wood, 1982; Robinson et al., 1993). However, lack of nearby source vents for the repeated eruptions that would be required to create these layered deposits in Arabia Terra (Moore, 1990; Kerber et al., 2012) leads to an alternative explanation, e.g., possible supervolcano complexes in the region (Michalski and Bleacher, 2013). Based on observations of crater morphologies and morphometry, Michalski and Bleacher (2013) have proposed a new type of irregularly shaped volcanic construct, labeled as "plains-style caldera complexes", within the region.

Supervolcano calderas in the region are characterized by low topographic relief, collapsed features (possibly of nested depressions), association with ridge plain, ring fractures and faults, the occurrence of friable deposits, interior slum blocks, and lava lakes and lava deposits (Michalski and Bleacher, 2013; 2014). The caldera structures in Arabia Terra lack evidence of a clear raised rim, possess evidence of extensive ejecta alternation compared to impact craters of similar size, and higher depth diameter (d/D) ratio compared to impact craters of similar size and age to its immediate vicinity (Michalski and Bleacher, 2013). These calderas are reported to have formed from the subduction of the volatile-rich crust beneath the region during the early plate tectonic episode (Sleep, 1994). A total of seven collapsed depressions within northwestern Arabia Terra have been proposed to be volcanic caldera including Eden Patera, Ismenia Patera, Euphrates Patera, etc. (Fig. 4.1). One such feature is Siloe Patera in Arabia Terra which consists of a nested set of depressions likely have formed due to collapse event that was previously reported as the possible impact craters (e.g., Salamunićcar et al., 2011; Robbins and Hynek, 2012a Robbins and Hynek, 2012b). Based on its identified geology, lack of typical impact crater characteristics and structure, Siloe Patera has been interpreted likely to belong in the plains-style caldera complex category although the influence of subsurface ice and thermokarsts formation mechanism has not been completely ruled out by the work of Michalski and Bleacher (2013). Previous literature has reported the feature as a potential impact crater with the highest level of confidence (e.g., Salamunićcar et al., 2011; Robbins and Hynek, 2012a). Using the new algorithms of terrain models (Robbins and Hynek, 2013), the study of Brugman (2014) processed the martian crater database (Robbins and Hynek, 2012a) and casts doubt on the supervolcanic origin hypothesis of the proposed calderas in the northern Arabia Terra including Siloe Patera. Moreover, based on crater morphometry, thermophysical properties, and comparing its morphology with other craters and calderas on Mars, the recent work of Garcia (2018)

rules out its origin as supervolcano caldera and once again reemphasized its origin as an impact crater and subsequent modification by dewatering processes and periglacial reworking.

Amid the debated geological history, the objective of the study is interpreting surficial geology, including possible geologic history, of Siloe Patera at Arabia Terra. The present study revisited the feature with available high-resolution data; however, in some cases, the study summarizes the results of previous literature and critically analyzed and assessed the previous findings. All possible formation mechanisms e.g., supervolcanic (and effusive lava flow), impact cratering, dewatering, and subsurface ice removal and resulting thermokarst structure were considered to test the most appropriate formation hypothesis of Siloe Patera. The study uses the High Resolution Imaging Science Experiment (HiRISE; McEwen et al., 2007) and the Context Camera (CTX; Malin et al., 2007) onboard the Mars Reconnaissance Orbiter (MRO) spacecraft and the 2001 Mars Odyssey aboard the Thermal Emission Imaging System (THEMIS; Christensen et al., 2004) instrument data to analyze the surface morphologic features visible in these sensors resolutions. The surficial geology of the study area was analyzed by combining investigation of spectral units, inferred bulk-silica content, colorized nighttime IR overlain daytime IR mosaic, and thermal inertia characteristics derived from thermal-infrared (TIR) data from the Thermal Emission Imaging System (THEMIS; Christensen et al., 2004) and mineral index map from near-infrared (NIR) data from the Compact Reconnaissance Imaging Spectrometer for Mars (CRISM; Murchie et al., 2007) instrument. The collective wavelength coverage (NIR and TIR) from THEMIS and CRISM images allow investigation of both bulk surface compositions of the study area as well as secondary alteration products identification (e.g., Amador and Bandfield, 2016). However, the focus of this study is primarily on the 2001 Mars Odyssey onboard THEMIS IR spectral data to determine various surficial characteristics in the areas of interest.

The chapter first describes in detail of the spectral units identified from THEMIS thermal infrared images within and around Siloe Patera. The units were identified based on the decorrelation stretch (DCS) 8-7-5 bands combination. Thermal inertia, bulk-silica content, and spectral shape of the identified units were then thoroughly described. Mineralogy of olivine, phyllosilicates, and hydrated phyllosilicates have been investigated within the THEMIS identified spectral units. In the later section, the study investigated morphology, morphometry, and crater database to constrain the geological history of Siloe Patera.

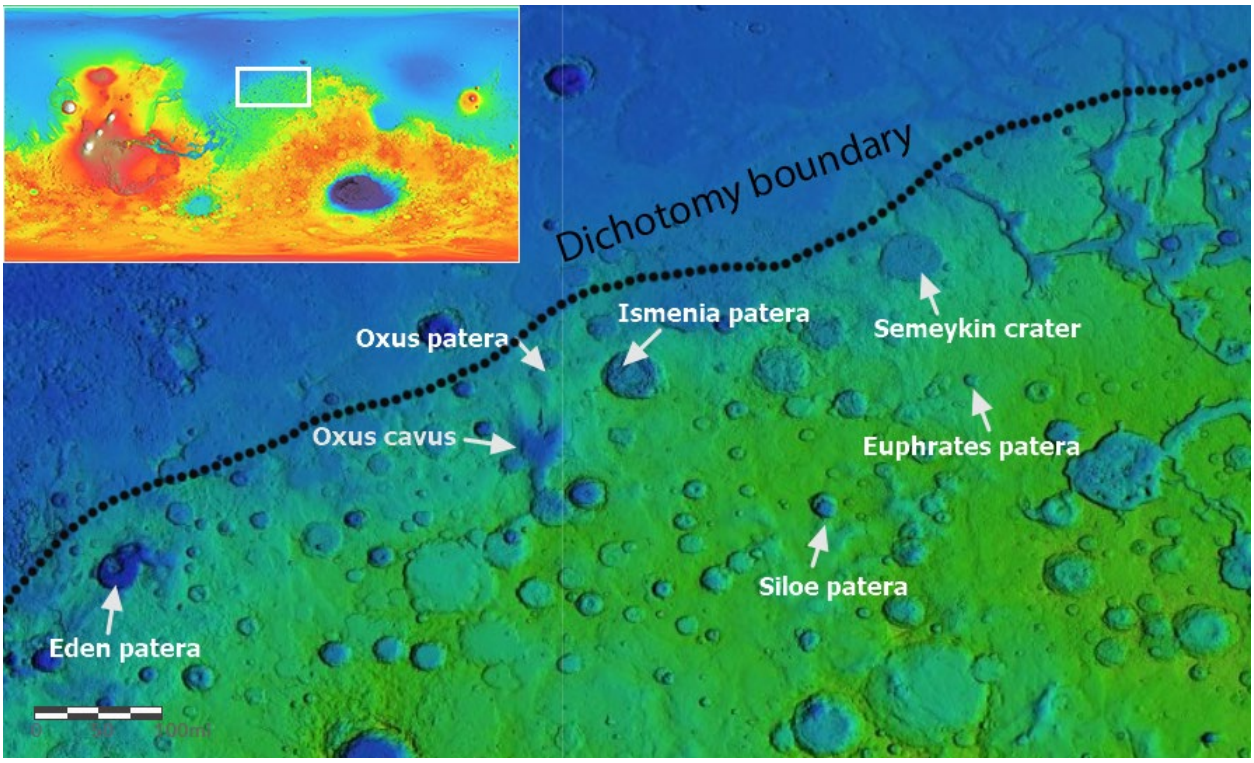

Fig. 4.1: Context map of HRSC colorized elevation overlain on THEMIS daytime IR image mosaic showing seven calderas in northwestern Arabia Terra, Mars. Inset is the MOLA colorized global elevation map of Mars showing the context of the northern Arabia Terra indicated in a white rectangular box. The seven calderas, namely Eden Patera, Oxus Patera, Oxus Cavus, Ismenia Patera, Siloe Patera, Euphrates Patera, and Semeykin crater, are indicated by the white arrows. The dichotomy boundary is outlined as a black dashed line that separates northern lowland to the southern highland.

1.1. Geology of Siloe Patera

Siloe Patera, located in Arabia Terra (6.60 E, 35.20 N), has been identified as a nested deep depression - a collapsed feature with possible volcanic activities (Michalski and Bleacher, 2013). Siloe Patera has a diameter of approximately 40 km (north-south) by 30 km (west-east) with a set of nested craters with the deepest point that reaches a depth approximately ~ 1,750 m below the surrounding plains (Fig. 4.2; Michalski and Bleacher, 2013; 2014). Although the precise age has not been determined, Siloe Patera has been interpreted likely to be early Hesperian or older and has possibly experienced with the modifications due to the regional history of erosion and deposition in Arabia Terra (McGill, 2000; Fergason and Christensen, 2008). Siloe Patera has been characterized as steep-walled nested deep depressions with arcuate scarps and faults akin to nearby Eden Patera in the region (Michalski and Bleacher, 2013). The primary structure of the feature is sub-circular in shape and has a unique higher depth-to-diameter ratio distinguishes it from impact craters in the immediate vicinity (Garcia, 2018). Prior literature investigated morphology, morphometry, and topography that identified a subtle northeast-southwest-trending depression attached to the primary collapse structure (e.g., Michalski and Bleacher, 2013; Wilkes et al., 2013; Wilkes, 2014; Emran et al., 2018a; Emran et al., 2018b; Garcia, 2018). This subtle northeast-southwest-trending depression of ~700 m depth in the southern part (Michalski and Bleacher, 2013) has been interpreted as evidence for sagging due to the demagmatization of crust, thus indicating possible magma chamber at shallow depth (Michalski and Bleacher, 2013; Morschhauser et al., 2014; Michalski and Bleacher, 2014). Siloe Patera lacks direct evidence of fresh impact ejecta around its structure, and also lacking is an impact-induced central uplift or peak, or a raised or overturned rim, which are the typical characteristics of impact craters (e.g., Michalski and Bleacher, 2013; Wilkes et al., 2013; Wilkes, 2014; Emran et al., 2018b; Garcia, 2018). Siloe Patera's single set of southeastern-emanating lobate flows has been interpreted as a set of lava or pyroclastic flows that reach around 60 km from the souther-eastern

rim (Michalski and Bleacher, 2013). Inside the nested crater, the irregular mount of friable materials is thought to be pyroclastic from a volcano or as younger deposits of unknown origin (Michalski and Bleacher, 2013; 2014).

Another possible interpretation of the origin of Siloe Patera is an impact crater and can be considered as a degraded crater. Noting here that the martian impact craters (e.g., Barlow and Bradley, 1990) are classified into four distinct classes (1 through 4) based on morphology and level of crater preservation, degradation, and modification (e.g., Robbins and Hynek, 2012a; Robbins and Hynek, 2012b). Class 4 is considered as a pristine (fresh) or least degraded crater possessing a sharply-raised rim, visible ejecta deposits, and a central peak; whereas class 1 represent the most degraded craters lacking discernable ejecta, missing or poorly defined rim, and generally flat floor (e.g., Craddock and Maxwell, 2012; Robbins and Hynek, 2012a; Robbins and Hynek, 2012b). To discount possible impact crater origin, Michalski and Bleacher (2013) assessed the morphology in terms of depth-to-diameter ratios of three proposed calderas in Arabia Terra e.g., Siloe, Euphrates, and Eden Patera with other martian the craters. Based on their result, they interpret that the calderas in Arabia Terra can be considered as class 2 type impact craters which should have some preserved crater morphological signatures e.g., crater raised rim and ejecta deposit. Lack of these morphological signatures goes against their impact induced origin. With a comparison of these calderas to terrestrial supervolcanoes, thermokarsts, and some martian scalloped terrains, Michalski and Bleacher (2013) showed that the dimensions of these calderas are consistent with terrestrial supervolcanoes. As an alternative formation theory, they also tested a possibility of these collapsed features to formed from the excavation of surface ice and ruled out the ice-related process as a sole formation factor.

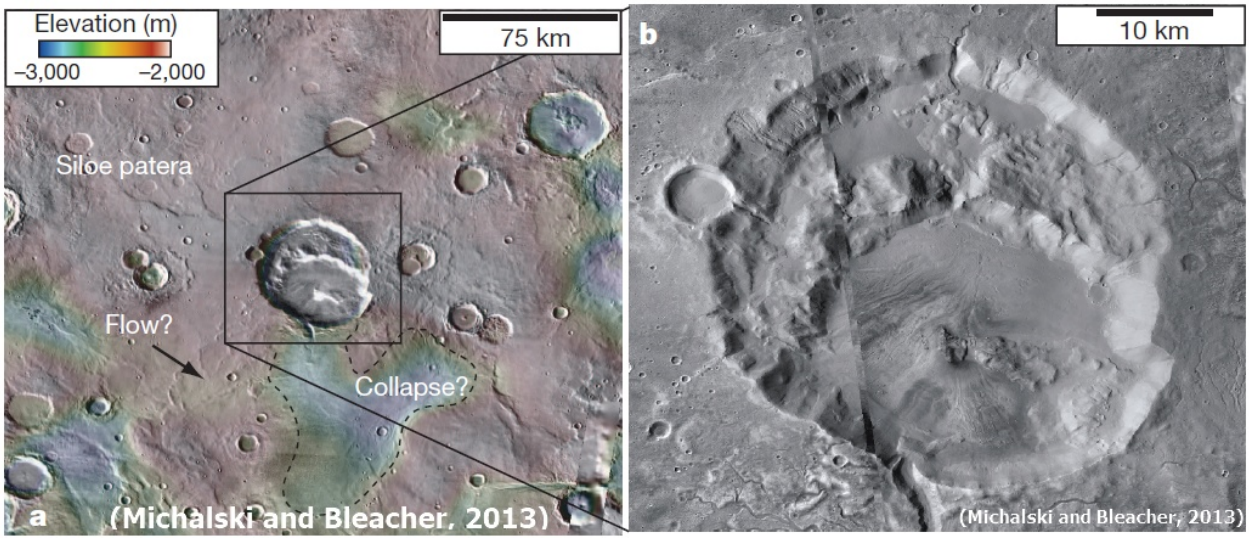

Fig. 4.2: Context map showing the morphology of Siloe Patera, adopted from Michalski and Bleacher (2013). a) MOLA topographic data overlain on CTX images showing the morphologies. The black rectangle outlines the area of interest. b) Mosaic produced using of CTX grayscale observations, corresponding to the black rectangle in (a), also adopted from Michalski and Bleacher (2013).

2. Data and methods

The information about the martian surface (up to upper tens of microns) mineral composition can be derived from the spectroscopic measurements obtained by orbital spacecraft (e.g., Ehlmann and Edwards, 2014; Amador and Bandfield, 2016). This information on mineralogy can then be used to constrain the geologic and environmental history of the planet (e.g., Bandfield et al., 2004a; Ehlmann and Edwards, 2014; Williams et al., 2018). Having specific sensitivities of near-infrared (NIR; wavelength range ~1.0–3.0 μm) and thermal-infrared (TIR; wavelength range ~5.0–50.0 μm) spectral datasets (e.g., Amador and Bandfield, 2016), the study used both NIR and TIR data in determining the surficial characteristics of Siloe Patera. For instance, TIR spectra are sensitive to major mineral phases and bulk-rock composition (e.g., Thomson and Salisbury, 1993; Ramsey and Christensen, 1998; Smith et al., 2013), whereas hydrated and Fe-bearing phases are sensitive to NIR spectral wavelengths (e.g., Hunt, 1977). Using either dataset may not render the complete scenario

of the martian surface and, therefore, demands an in-depth simultaneous/combined investigation of both NIR and TIR wavelength regions (e.g., Mustard and Cooper, 2005; Amador and Bandfield, 2016). In this study, the TIR wavelength of THEMIS dataset and NIR wavelength of CRISM data sets were used to constrain the in-depth surficial geology of Siloe Patera including thermophysical characteristics and mineral composition.

2.1. The Thermal Emission Imaging System (THEMIS)

THEMIS onboard the 2001 Mars Odyssey spacecraft is a multispectral imager. THEMIS data provide insight into the understanding of morphology, bulk mineralogic composition, and physical properties of the martian surface (Christensen et al, 2004; Huang et al., 2013; Edwards and Ehlmann, 2015). TIR dataset of THEMIS is analyzed with different techniques to determine the surficial properties. First, as a preliminary survey tool, the study used the standard decorrelation stretch (DCS) image product of THEMIS data for a preliminary overview of the surface compositional variability in the study area (Bandfield et al., 2004; Amador and Bandfield, 2016). Then, the study obtained variability of bulk-silica content of the surface from the colorized index mapping tool named as the "weighted absorption center (WAC)", alternatively known as the "center of gravity" (e.g., Smith et al., 2013) through the analysis of THEMIS infrared emissivity information (Amador and Bandfield, 2016). Lastly, surface thermal inertia was derived from nighttime THEMIS-TIR images and colorized nighttime IR overlay on daytime IR mosaics (Edwards et al., 2001; Hill et al., 2014; Edwards et al., 2014; Hill and Christensen, 2017) for understanding the nature and grain-size distribution of the surficial materials (e.g., Jakosky et al., 2000; Mellon et al., 2000; Putzig et al., 2005).

2.1.1. Introduction to data and atmospheric corrections

The THEMIS multi-spectral instrument includes visible (VIS) and thermal infrared (TIR) sensors (Christensen et al, 2004). The instrument has 10 bands in the TIR channels between 6.78 μm and 14.88 μm (Table 4.1) and 5 bands in the visible channels between 0.42 μm through 0.86 μm (Christensen et al. 2004). THEMIS infrared is a push broom imager that has a spatial resolution of 100 m/pixel that acquires data both in the day and nighttime. In contrast, the visible bands have a spatial resolution from 18 to 35 m/pixel (Christensen et al. 2004). THEMIS acquires images in all 10 bands in the daytime while nighttime images are acquired typically in 3 bands e.g., band 4 (8.56 μm), band 9 (12.57 μm), and band 10 (14.88 μm). TIR images have global coverage of the planet with a swath width of approximately 32 km. The global coverage of the THEMIS dataset allows for regional investigation at a relatively high resolution to analyze the martian surface characteristics including compositional, morphological, and thermophysical properties (Christensen et al., 2004). THEMIS IR radiance images are calibrated, atmospherically corrected, and then converted to surface emissivity using the methods described by Christensen et al. (2004), Bandfield et al. (2004a), and Edwards et al. (2011). In this study, the best quality daytime and nighttime images available were used for Siloe Patera (Table 4.2). THEMIS images were selected considering few criteria, e.g., higher surface temperature, lower water-ice, and dust opacities, and as possible as higher image quality index. THEMIS daytime images were used to produce decorrelated stretch (DCS) images and calculating weighted absorption center (WAC) while the nighttime images were used to identify the thermal inertia (TI).

Table 4.1: THEMIS TIR spectral bands.

Band number	Center wavelength (μm)	Band number	Center wavelength (μm)
1	6.78	6	10.21
2	6.78	7	11.04
3	7.93	8	11.79
4	8.56	9	12.57
5	9.35	10	14.88

2.1.2. THEMIS data selection

THEMIS daytime infrared images (a total of 21) were surveyed for the area of interest to cover entire study area based on a visual inspection and image metadata e.g., average surface temperature, water-ice or dust opacity, and image quality. The study only considered the best THEMIS daytime images available which had surface temperature >230 K, dust opacity <0.15, and image quality ≥4 (as per THEMIS website the image ratings 3 to 6 are acceptable for scientific studies). Therefore, the study had chosen I45489019, I04656002, and I53118012 for the final daytime THEMIS images to be used for analysis. The Thermal Emission Spectrometer (TES; Christensen et al., 2001) instrument onboard the Mars Global Surveyor (MGS) measures nighttime thermal emission which is used to derive thermal inertia of martian surface (Murphy et al., 2007). The same derivation technique used for TES can be applied to THEMIS (Putzig et al., 2014) and, therefore, the study considered THEMIS nighttime images for high-resolution thermal inertia calculation. For that, the present study surveyed THEMIS nighttime images over the area of interest and selected the best images (e.g., I27002020 and I35449015) to cover the study area. The selected images had the following characteristics: surface temperature >167 K, average dust opacity 0, and image quality ≥4 (best available image satisfying certain criterion). Moreover, the study selected the aforementioned THEMIS nighttime images since these images produce the highest pixel quality ratios, within the

area of interest, in calculating thermal inertia using the MARSTHERM processing tool (Putzig et al., 2013). The selected THEMIS daytime images were examined using DCS stretched images. In DCS band combinations of 8-7-5, a region with higher olivine content appears purple/magenta and the surface with elevated silica content appears yellow/amber (e.g., Amador and Bandfield, 2016). The selected daytime images were then calibrated, atmospherically corrected, and converted to surface emissivity (Christensen et al., 2004; Bandfield et al., 2004a; Edwards et al., 2011) using THMPROC, a THEMIS image processing web interface developed by Arizona State University (ASU). The emissivity images were used for the analysis of WAC indices and maps. The spectrally district units identified from DCS 8-7-5 were also described for other analysis techniques.

2.1.3. Decorrelation stretch (DCS)

DCS images (Gillespie et al., 1986; Edwards et al., 2011), derived as a standard THEMIS IR product, are useful to identify spectrally district units in the individuals THEMIS image (Bandfield et al., 2004b). DCS images are displayed in a band combination of 8-7-5, 9-6-4, or 6-4-2 in red, green, and blue channels, respectively. Typically, a region with elevated bulk-silica content has shorter wavelength absorptions in THEMIS wavelength and appears yellow in bands 8-7-5 and 9-6-4, and appears magenta in band 6-4-2 DCS stretches (e.g., Amador and Bandfield, 2016). The decorrelation stretch (DCS) images demonstrate to the surface materials of absorption features associated with olivine-bearing basalts (Edwards et al., 2011). For example, a region with high olivine content appears purple, purple, cyan in the band combinations of 8-7-5, 9-6-4, and 6-4-2 DCS stretches, respectively, consistent with long wavelength emissivity absorptions (Amador and Bandfield, 2016). DCS stretch image using bands 8 (11.79 μm), 7 (11.04 μm) and 5 (9.35 μm) was used to highlight the spectral variability throughout the individual scene in the area of interest (Salvatore et al., 2018). One

of the major shortcomings of DCS images is that, though THEMIS DCS renders a quick overview of the spectrally unique surface on an individual image, the temperature variation may affect the color representation of DCS which may lead to ambiguous interpretation (Amador and Bandfield, 2016). Therefore, DCS is not sufficient for in-depth interpretation rather in-depth understanding demands further spectral analysis.

2.1.4. Weighted absorption center (WAC)

Amador and Bandfield (2016) introduced a new approach for rapid identification of surface unit that composed of elevated bulk-silica content using THEMIS emissivity images. The tool was labeled as "weighted absorption center (WAC)" index map (Vincent and Thomson, 1972; Smith et al., 2013). This new approach of WAC offers a more accurate investigation of the bulk-silica content of the martian surface (Amador and Bandfield, 2016), which is a renamed version of "center of gravity" method developed by Smith et al. (2013). THEMIS infrared wavelengths (8-12 μm) include the diagnostic reststrahlen Si–O asymmetric stretch absorption band and, therefore, THEMIS emissivity data are highly sensitive to the bulk-silica enriched surfaces (e.g., Amador and Bandfield, 2016). Determining bulk-silica content suggest the presence of silicate materials on the surface or bedrock materials. A shifting of the reststrahlen absorption band minimum to shorter wavelengths is consistent with the increase in bulk-silica abundances (Vincent and Thomson, 1972; Walter and Salisbury, 1989). WAC is calculated from the atmospherically corrected THEMIS emissivity spectra of bands 3 through 9. Although WAC calculation results in numeric values, however, regardless of the actual numeric values, the higher values in WAC wavelength correspond to lower silica content while lower values in WAC wavelength corresponds to elevated silica content (Amador and Bandfield, 2016; Salvatore et al., 2018). The detail method of the WAC calculation is described in

Amador and Bandfield (2016). WAC index has a shortcoming because of its sensitivity to the non-silicate phases such as sulfate since sulfate minerals have a band-minima to the shorter wavelength range in THEMIS spectra (Amador and Bandfield, 2016). NIR spectra of CRISM data, therefore, were used to ensure the correct detection of minerals. Having limitations of both DCS and WAC the study used a combined approach to ensure and confidentially determine the surficial unit properties of Siloe Patera.

2.1.5. Thermal inertia

On Mars, thermal inertia (TI) is considered as the primary physical property that is a measure of resistance of the materials to a temperature change and can be used as an indicator of surface geological characteristics for the upper few centimeters (e.g., Jakosky et al., 2000; Mellon et al., 2000; Putzig et al., 2005). TI is related to the thermal conductivity and physical structure (e.g., particle size, porosity, and compaction) of top few decimeters of surficial materials (e.g., Kieffer et al. 1977; Jakosky, 1986; Putzig et al. 2005; Fergason et al., 2006; Edwards et al., 2009). However, the thermal inertia of martian surfaces is mostly influenced by the bulk thermal conductivity of materials (e.g., Jakosky, 1986). A compacted rock and/or larger particle size materials are associated with higher values of bulk thermal conductivity and, therefore, higher TI values (Williams et al., 2018). A mechanically strong surface such as well indurated (cemented) rock has demonstrated higher thermal inertia while lower thermal inertia corresponds to weakly lithified rocks and/or unconsolidated materials (Williams et al., 2018). In general, a lower thermal inertia represents a loose, fine surface dust particles with very few rocks (mechanically weak surface); a medium/moderate thermal inertia means a combination of coarser loose particles, crusted fine-grained materials, a reasonable amount of scattered rocks; whereas a higher thermal inertia indicates a combination of mechanically strong

coarse-grained sand (dune sand), strongly-crusted or indurated fines with abundant rocks, and/or scattered bedrocks (e.g., Kieffer et al., 1977; Palluconi and Kieffer, 1981; Jakosky et al., 2000; Mellon et al., 2000; Putzig et al., 2005). A thermal inertia value of <100 $Jm^{-2}K^{-1}s^{-1/2}$ corresponds fine, loosely consolidated material whereas a value of >350 $Jm^{-2}K^{-1}s^{-1/2}$ and >1200 $Jm^{-2}K^{-1}s^{-1/2}$ are representative of well-cemented sedimentary rock and crystalline igneous rocks, respectively (e.g., Edwards et al., 2009; Fraeman et al., 2016). TI is determined remotely from measurements of the thermal emission at a point on the surface by comparing the measured temperature with the temperature inferred from a thermal model (Jakosky et al., 2000; Putzig et al., 2005). THEMIS nighttime infrared (IR) images (I27002020 and I35449015) were used to calculate the surficial thermal inertia of the study area. The study uses MARSTHERM, a thermophysical analysis tool (Putzig et al., 2013) developed by Mars researchers at the Planetary Science Institute in Tucson, Arizona, to derive thermal inertia using the method developed by Putzig et al. (2014). The study has used higher spatial resolution (100 m/pixel) THEMIS data (Christensen et al., 2004) which has more detailed spatial coverage than the Thermal Emission Spectrometer (TES; Christensen et al., 2001) (~3 km per pixel). This advantage of using THEMIS enables to quantify of the surface physical properties observed in other high-resolution images e.g., HiRISE and CTX. Thermal inertia is often consistent to surface morphologic features (and nature of surface material) as identified from the high-resolution images (e.g., CTX and HiRISE) and the integration of thermal inertia enables to attain more robust conclusions (Kieffer et al., 1977; Palluconi and Kieffer, 1981; Jakosky et al., 2000; Mellon et al., 2000; Putzig et al., 2005). However, the surfaces of Mars are typically composed of mixtures of materials and uncertainty of THEMIS image calibrations, a straight forward interpretation of thermal inertia may lead to ambiguous interpretation (Williams et al., 2018). Therefore, as a supplementary interpretation of thermal inertia, the study used global nighttime and daytime IR mosaics of THEMIS IR band 9 as a proxy to thermophysical characteristics of the surface materials.

2.1.6. THEMIS daytime and colorized nighttime IR mosaics

The global nighttime and daytime IR mosaics have been generated from THEMIS IR band 9 (12.57μm) radiance images (Hill and Christensen, 2017; Hill et al., 2014; Edwards et al., 2001; Edwards et al., 2014). Daytime and nighttime IR mosaics are done using band 9 with high surface emissivity, lower atmospheric opacity, and higher surface-atmosphere temperature variation since THEMIS band 9 has the highest signal-to-noise ratio both for day and nighttime images (Edwards et al., 2001). The version of Hill et al. (2014) for THEMIS daytime IR global mosaic was leveled as version 12.0 while the version of Hill et al. (2017) for THEMIS nighttime IR global mosaic was leveled as version 14.0. THEMIS daytime and nighttime global mosaics were then produced to emphasize the relationship between surface morphology and thermophysical characteristics of surface materials (Hill and Christensen, 2017; Edwards et al., 2001). The details of these procedures for the mosaic generation has been described in Hill and Christensen (2017). Nighttime IR global mosaics are colorized using an algorithm binning the data in a digital number (DN) format ranging from 1 to 255 into six equally sized DN bins (Hill and Christensen 2017). Each bin has been assigned a different color in visible wavelengths where violet is allocated for the low values while red corresponds to higher values. In general, the blue tones correspond to the lower thermal inertia values or dustier surface materials while the red tones correspond to the higher thermal inertia or rockier materials/bedrock. The colorized THEMIS nighttime temperature data overlain on daytime temperature mosaic provides, therefore, the morphological context for thermophysical characteristics (Edwards et al., 2001). The thermophysical characteristics are expressed as the variations in the THEMIS nighttime surface temperature while the morphology is expressed primarily as the variations in daytime surface temperature derived from THEMIS band 9 radiance images (Hill and Christensen, 2017). The surface with warmest nighttime temperature will have, thus, higher thermal inertia values. The case study used in Edwards et al. (2001) showed that the

warmest nighttime temperature or higher thermal inertia are concentrated on the steep slopes e.g., cliffs and crater walls of exposed rocky materials, a layered region of past lava flow from the volcano, and fracture regions of the caldera. THEMIS daytime IR with the colorized Night IR global map is used as a proxy for the thermal inertia characteristics which ultimately can be used as a preliminary survey tool for surface grain size distribution (Hill and Christensen, 2017; Edwards et al., 2001). Though global nighttime and daytime IR mosaics can be used as an extremely useful method of primary reconnaissance tool, however, this mosaic can only be used as a piece of qualitative information about the thermophysical or surface compositional information (Edwards et al., 2001). THEMIS daytime and colorized nighttime IR 100 meter per pixel global mosaics are publicly available in Java Mission-planning and Analysis for Remote Sensing (JMARS) program, a geospatial information system (GIS) developed by ASU's Mars Space Flight Facility (Christensen et al., 2009) software package.

2.2. Compact Reconnaissance Imaging Spectrometer for Mars (CRISM)

The Compact Reconnaissance Imaging Spectrometer for Mars (CRISM) onboard Mars Reconnaissance Orbiters (MRO) spacecraft is a hyperspectral imager capable of gathering mineralogic information around ~20 m/pixel at the highest spatial resolution (Murchie et al., 2007). The hyperspectral instrument covers visible to near-infrared wavelengths and has multiple data acquisition modes at different spatial and spectral sampling e.g. targeted hyperspectral and mapped multi-spectral (Murchie et al., 2007). The hyperspectral targeted mode tracks the targets with 544 bands (~0.4 to 4.0 μm at a spectral sampling of 6.55 nm/channel) whereas multispectral untargeted mode with 72 bands (chosen over the 544 spectral bands) to identify principal minerals (Murchie et al., 2007). CRISM multi-spectral survey products (MSP) images were used in this study (a list of

images used are given in Table 4.2). Though MSP has 72 spectral bands with a spatial resolution of 200 meters/pixel, the study relied on MSP data since it covers areas of interest, otherwise unavailable with hyperspectral targeted datasets, and detect major mineral phases. CRISM data are processed through a set of standard spectral corrections routine (e.g. atmospheric and photometric correction) and spatial transforms (e.g. geometric correction) (Pelkey et al., 2007; McGuire et al., 2009; Viviano-Beck et al., 2014 and 2017). The atmospheric correction is relied on scaling atmospheric gas absorption over the Olympus Mons volcano also known as volcanic scan correction (McGuire et al., 2009; Ehlmann et al., 2009). Spectral index maps from CRISM data are derived as the method described in the Pelkey et al. (2007) and Viviano-Beck et al. (2014). These index maps are used for rapid analysis of the diversity of mineral phase presence based on specific spectral feature presence in CRISM wavelength (Pelkey et al., 2007; Ehlmann et al., 2009; Salvatore et al., 2010; Viviano-Beck et al., 2014; Amador and Bandfield, 2016). The present study used the CRISM spectral index map produced by Arizona State University available at JMARS software program (Christensen et al., 2009).

2.3. Context Camera (CTX)

The Context Camera (CTX) onboard MRO is a camera acquiring grayscale images at ~6 m/pixel scale spatial resolution over a swath width of 30 km (Malin et al., 2007). CTX provides context images for the HiRISE and CRISM observations and used in analyzing critical science targets such as observe features of interest to exploration initiative (Malin et al., 2007). Spatially co-registered CTX images were used to investigate the morphology, stratigraphy, and texture of surface units. CTX acquires stereo pairs of selected areas that are used to produce digital elevation models (DEMs) for topographic and morphologic mapping (Malin et al., 2007). The USGS's Integrated Software for Imagers and Spectrometers (ISIS3) pipelines and NASA Ames Stereo Pipeline (ASP)

stereogrammetry software (Broxton and Edwards 2008; Moratto et al. 2010; Beyer et al. 2014) were used for the calibration, projection, and producing the DEMs from CTX stereo pair (Quantin-Nataf et al., 2018). CTX derived stereo pairs of D15_033113_2155 & D15_033258_2155 and F23_044902_2157 & J03_045891_2151 are used to produce DEM of Siloe Patera (Table 4.2). The CTX derived DEM was tied to the Precision Experiment Data Record (PEDR) point shot data of the Mars Orbiter Laser Altimeter (MOLA) instrument (Smith et al., 2001) using *pc_align* function (Beyer et al. 2014) account for the error of regional scale topography (Goudge et al., 2017). The final DEM was co-registered with THEMIS and CTX images, rendered in JMARS. Terrain profiles were extracted from the selected location along the casted transects.

2.4. High Resolution Imaging Science Experiment (HiRISE)

The High Resolution Imaging Science Experiment (HiRISE) onboard MRO is a telescope of the visible and near-infrared wavelengths (McEwen et al. 2007; Zurek and Smrekar, 2007; Delamere et al., 2010). HiRISE images are used for analyzing surface in detail at a spatial resolution of 1m size or 0.25-1.3 m/pixel (McEwen et al., 2007). The camera has a total of 14 charged coupled device (CCD) of 3 different color filters e.g. red (RED; 570-830 nm), blue-green (BG; <580 nm), and near-infrared (NIR; >790 nm) (McEwen et al., 2007). HiRISE color images enable in distinguishing the surface composition and albedo heterogeneities directly correlated to the results obtained from other orbital images e.g. CTX and THEMIS (Zurek and Smrekar, 2007; Quantin-Nataf et al., 2018). HiRISE images coupled with CTX were used to interpret the fine local morphology and textural variation in spectral units (a list of images used are given in Table 4.2).

2.5. HRSC MOLA blended global DEM

Local and regional scale elevation information, in this study, was derived from the High-Resolution Stereo Camera (HRSC; Neukum et al., 2004) and the Mars Orbiter Laser Altimeter (MOLA; Smith et al., 2001) to produce blended global digital elevation models (DEM) data products at 200m version 2 (Fergason et al., 2018). The product was downloaded from the USGS astrogeology data server. The data were prepared in support of thermal modeling of the planet and product creation of Mars (e.g., Laura and Fergason, 2016; Fergason et al., 2017). The MOLA investigations measure topography, surface roughness, 1.064 μm reflectivity of the planet, and volatile and dust clouds heights (Smith et al., 2001). The instrument measures the overall time for a laser pulse takes to reach its target (both from the martian surface or atmospheric layers) and return to the spacecraft to calculate elevation. The data product used more than 600 million MOLA point shot measurements acquired between the years of 1999 and 2001 with an average horizontal accuracy for each point of ~100 m and at least ±3 m total elevation uncertainty (Smith et al., 2001; Fergason et al., 2018). HRSC is a multi-channel stereo color push-broom camera onboard the European Space Agency (ESA)'s Mars Express (MEx) spacecraft mission. HRSC captures global imagery of martian surface in both panchromatic and color images which paved the way to produce stereo-imagery for DEM production (Neukum et al., 2004).

2.6. Collapse volume calculation

The study calculates the amount of collapse volume that occurred at Siloe Patera to test the amount of magma involved in the igneous volcanic process and/or the amount of cryospheric ice underneath the feature involved in thermokarsts process. HRSC MOLA blended DEM at 200m data was used to calculate the volume of the collapse. The digital elevation model data were contoured

and draped onto the hillshade (calculated from same DEM) and CTX image mosaic data. With the help of contoured information, THEMIS daytime infrared product, and CTX data, the study fitted a plane of maximum allowable elevation level that corresponds to the closest approximation of the collapses and was fixed as the elevation value of -2400 meters. The study has calculated the depth of each pixel about the fitted plane (-2400 m contour line), followed by calculating the volume of each pixel, and then summed up all pixels' volume to get the total volume of the collapsed beneath the reference plane. One caveat of this volume estimation is that the study assumes that the topography of Siloe Patera (including interior depressions and nearby sagging collapse feature in fig. 4.3) has not changed since the formation of these features. Since the study used the current elevation data to estimate the volume of the collapse, which is presumed not to be, it is considered as a limitation of the current technique used. Another potential limitation of this technique is that the presence of younger impact craters that superimposed on the feature that complicated the volume calculation in terms of overestimation of volume. However, every effort has been made to calculate an approximate volume of the collapse feature with a very careful fashion to avoid possible overestimation of total volume by offsetting the effects of younger impact craters. In the present study, therefore, the fitted reference plane was set slightly below the rim of the depression, considering the discernable elevation changes visible in THEMIS and CTX image resolutions. The technique also has another loophole resulting from the underestimation of volume due to the fill deposits onto the interior floor. The fill deposits materials may have been sourced from the rim (walls) or depressions themselves and there is no way to identify the underlying original depression floor since the deposit materials overlain the original terrain. However, if these deposits have been sourced from the depression itself (rim and floor materials) then the underestimation was partially offset by the fact that the study considers the eroded portion of the depression as well in the total volume calculation. Therefore, the total calculated volume is an approximation of the total collapse

volume (with a very marginal error that does not vary in total volume appreciably) during the original formation of the depressions.

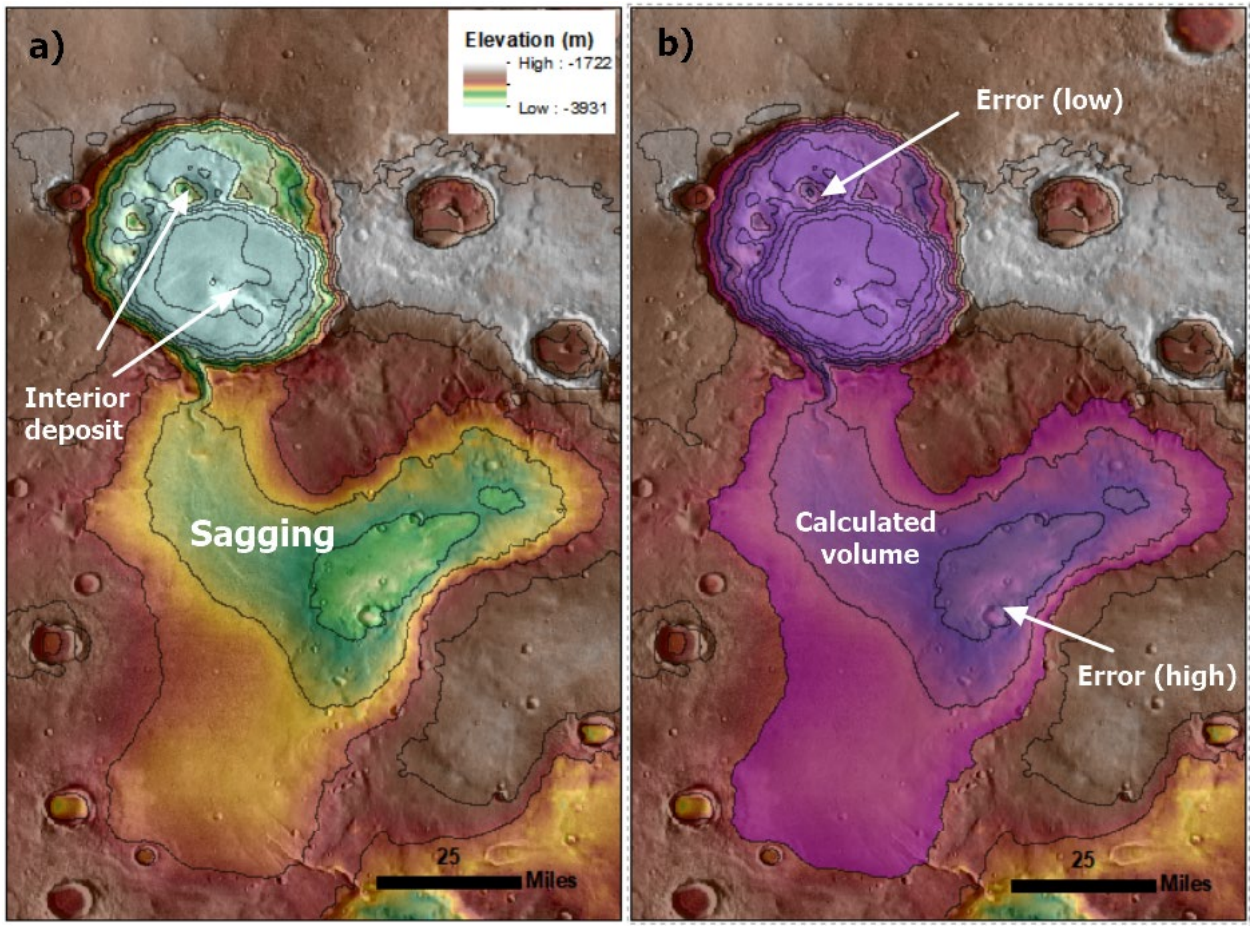

Fig 4.3: Volume calculations at Siloe Patera from HRSC MOLA blended 200m DEM overlain on THEMIS daytime infrared image mosaic (a-b). The study calculated the total volume of collapse within the marked purple line (below a fitted plane of a specific contour line) that corresponds to the amount of void space above modern topographic information from the HRSC MOLA blended 200 m resolution data. The two types of estimation errors are also marked as underestimation errors (leveled as low) and overestimation errors (leveled as high). The figure was recreated after Michalski and Bleacher (2013).

2.7. Porosity and volume of subsurface ice calculation

The martian subsurface is a reservoir of perennially frozen-ice known as the cryosphere (Clifford et al., 2010) that is believed to contains nearly ~90 to 95% of the total remaining water of the planet (e.g., Carr, 1986). The study tests the possibility of collapse formation due to the removal of subsurface ice since a catastrophically melted subsurface ice can form a collapse feature like in Siloe Patera. The study calculated the possible total volume or amount of subsurface (cryospheric) ice underneath the delineated area of the depression (Fig. 4.3) and then compared it with the volume of collapse to test the subsurface ice removal formation hypothesis. The latitudinal distribution and amount of cryospheric ice have been calculated using models (e.g., Clifford, 1993; Clifford and Parker, 2001; Clifford et al., 2010) that state the amount of cryospheric ice depends on the accessible pore volume (alternatively called porosity) of the subsurface. The total amount of subsurface pore space or porosity can potentially be filled with the cryospheric ice underneath the delineated depression. Cryospheric or subsurface porosity is a function of depth and the variation of porosity is measured using an exponential decay with depth relationship as calculated from the following equation (Clifford, 1993):

$$\phi(z) = \phi(0).\exp(-\frac{z}{D})$$

where ϕ (0) = the surface porosity (which is a value of 0.35), z = the depth (in km), and D = the gravitationally scaled porosity decay constant which is estimated to be ~2.82 km for Mars (Clifford, 1993). Therefore, this implies that at ~10 km underneath the surface the cryospheric porosity decay is nearly zero. Noting here that, porosity for both consolidated volcanic dense rock (as vesicles and fractures) and unconsolidated, porous volcanic or sedimentary rock (as intergranular porosity) are

considered the same in cryospheric modeling (e.g., Clifford et al., 2010). The total volume of subsurface porosity (correspond to potential cryospheric ice) underneath the delineated collapsed area was calculated considering a certain number of equal depth stake layers or unit volumes (i.e., 100) from the surface up to the depth of 10 km. Though using a certain number of stake layers in calculating the volume of the porosity may result in a very slightly inaccurate result, this technique is less computationally demanding and renders an approximate result. Using more stake layers does not substantially differ the total amount and therefore the present study ignored the computationally demanding method. The latitudinal cryospheric modeling of Clifford et al. (2010) considering many dynamic factors (e.g., three groundwater frizzing temperatures, two values of mean global heat flow, and two values of desiccated regolith thermal conductivity) showed that the cryosphere spans around 10 km deep at ±40° latitude; Siloe Patera is located at 35.20° N. This result supports the calculation used in this study for the total volume of porosity up to 10 km depth.

Table 4.2: Summary of the list of images used in the study.

Sensor	Image Type	Image ID
THEMIS	Daytime	I45489019; I04656002; I53118012
	Nighttime	I27002020; I35449015
CRISM	MSP	MSP000046DB; MSP000283AE; MSP00004EC5; MSP000329D0; MSP00005393; MSP00019753
CTX	Stereopair/RDR	D15_033113_2155 & D15_033258_2155; F23_044902_2157 & J03_045891_2151
HiRISE	ESP	ESP_030344_2155; ESP_033258_2160; ESP_036726_2155; ESP_037082_2155; ESP_041223_2155; ESP_047236_2155; ESP_047592_2155; ESP_052563_2160; ESP_052774_2160

3. Results and discussion

3.1. THEMIS TIR spectral results

3.1.1. Spectral units from DCS 8-7-5 stretch

Within the area of interest, THEMIS DCS stretched images show different distinct and mixed spectral units. Four different units were identified based on color composition: the purple unit, fuchsia/magenta unit, yellow/amber unit, and pale-brown or green unit (Fig. 4.4). The pale-brown or green unit consistent, indeed, to unremarkable terrain, generally of a washed out across the areas of interest and is referred hereafter as "typical terrain"; similarly, as defined in Amador and Bandfield (2016). The purple unit exposures are extensive in eastern and north-eastern rims and scarps of the headwall. Whereas the fuchsia unit is evident in the south-western rim and scarp and adjacent floor, the yellow/amber unit is on the floor of southern depression near the south-central highland/spire, and the pale-brown/green unit (typical terrain) on most of the floor surface and north-western rim and scarp of the patera. Though most of the previous literature used DCS 8-7-5 stretched image in determining spectral units, the THEMIS-TIR defined spectral units can also be identified from DCS stretched images in other band combinations (e.g., Amador and Bandfield, 2016; Salvatore et al., 2018). For instance, the purple unit may appear magenta and cyan in DCS 8-7-5 band combinations whereas the yellow/amber may display a yellow and magenta in DCS 9-6-4 and 6-4-2 band combinations, respectively (Amador and Bandfield, 2016).

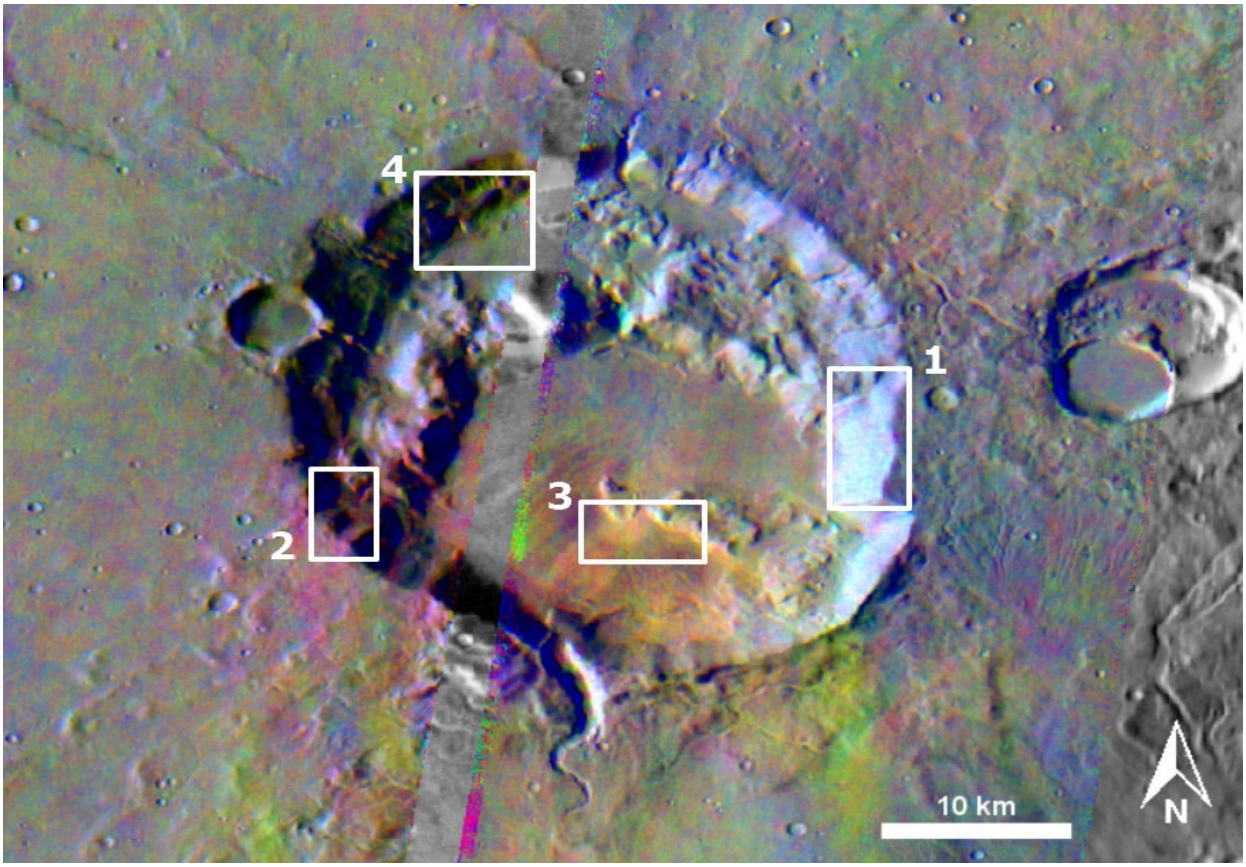

Fig. 4.4: Decorrelation stretches (DCS) for THEMIS image I45489019 and I04656002 in the band combinations of 8-7-5 in red, green, and blue channels, respectively, overlain on a mosaic of daytime THEMIS grayscale images. DCS stretched images show four spectral units (indicated by rectangular boxes) identified based on color composition: the purple unit (1), fuchsia/magenta unit (2), yellow/amber unit (3), and pale-brown/green or typical terrain unit (4).

3.1.2. Weighted absorption center (WAC) images

The WAC map was produced from the THEMIS I53118012 and I45489019 emissivity images (Fig. 4.5). THEMIS image within the Siloe Patera has WAC values ranges from ~9.27 μm to 11.60 μm. Noteworthy here, regardless of the actual WAC values, the higher values in WAC wavelength correspond to lower silica content while lower values in WAC wavelength corresponds to elevated silica content (Amador and Bandfield, 2016; Salvatore et al., 2018). At a glance, the purple unit appears higher WAC values whereas the yellow/amber and typical terrain appear lower WAC values,

however, the fuchsia unit appears mixed in high and low WAC values. The average WAC values, including a standard deviation (SD) value, from the representative spectral units defined by DCS 8-7-5 stretched THEMIS images (localities are given in Fig. 4.4) was collected using ENVI's region of interest (ROI) tool (Table 4.3). The purple unit, identified from DCS 8-7-5 stretched images, has the highest WAC values with a mean ~10.40 μm and a standard deviation value of 0.050, but the WAC value can be as high as 11.60 μm. While the yellow/amber unit shows a mean ~10.20 μm and a standard deviation value of 0.054, the typical terrain has a mean value of ~10.29 μm and a standard deviation value of 0.045, respectively. Lastly, the fuchsia unit has a mean WAC value of ~10.12 μm and a standard deviation value of 0.086 (the highest standard deviation among the spectral unit; this is likely due to mixed pixel values within the fuchsia unit). In summary, the purple unit has the highest mean WAC values followed by typical terrain, yellow/amber unit, and fuchsia unit. However, even though the fuchsia unit has the lowest mean values among the spectral unit, the yellow/amber unit contains the lowest min. WAC values. The lowest WAC values (~9.27 μm) are not clustered into a single spectral unit (not correspond to the single unit) rather these values are single isolated pixels or very small clustered of pixels within the THEMIS image. However, the study does point out that these WAC values can likely be affected by the surface slopes.

Table 4.3: THEMIS TIR defined unit and its corresponding CRISM NIR identifications

DCS 8-7-5 defined spectral unit	WAC values (mean plus minus standard deviation or SD)	Thermal Inertia (relative)	CRISM NIR identification
Purple	~10.40 μm (up to 11.60 μm)	Higher values	Olivine-rich
Yellow/Amber	~10.20 μm (lowest as ~9.27 μm)	Highest values	-
Fuchsia	~10.12 μm (highest SD and mixed pixel)	Higher values	Olivine-rich
Typical Terrain	~10.29 μm	Lowest values	Fe/Mg-silicates

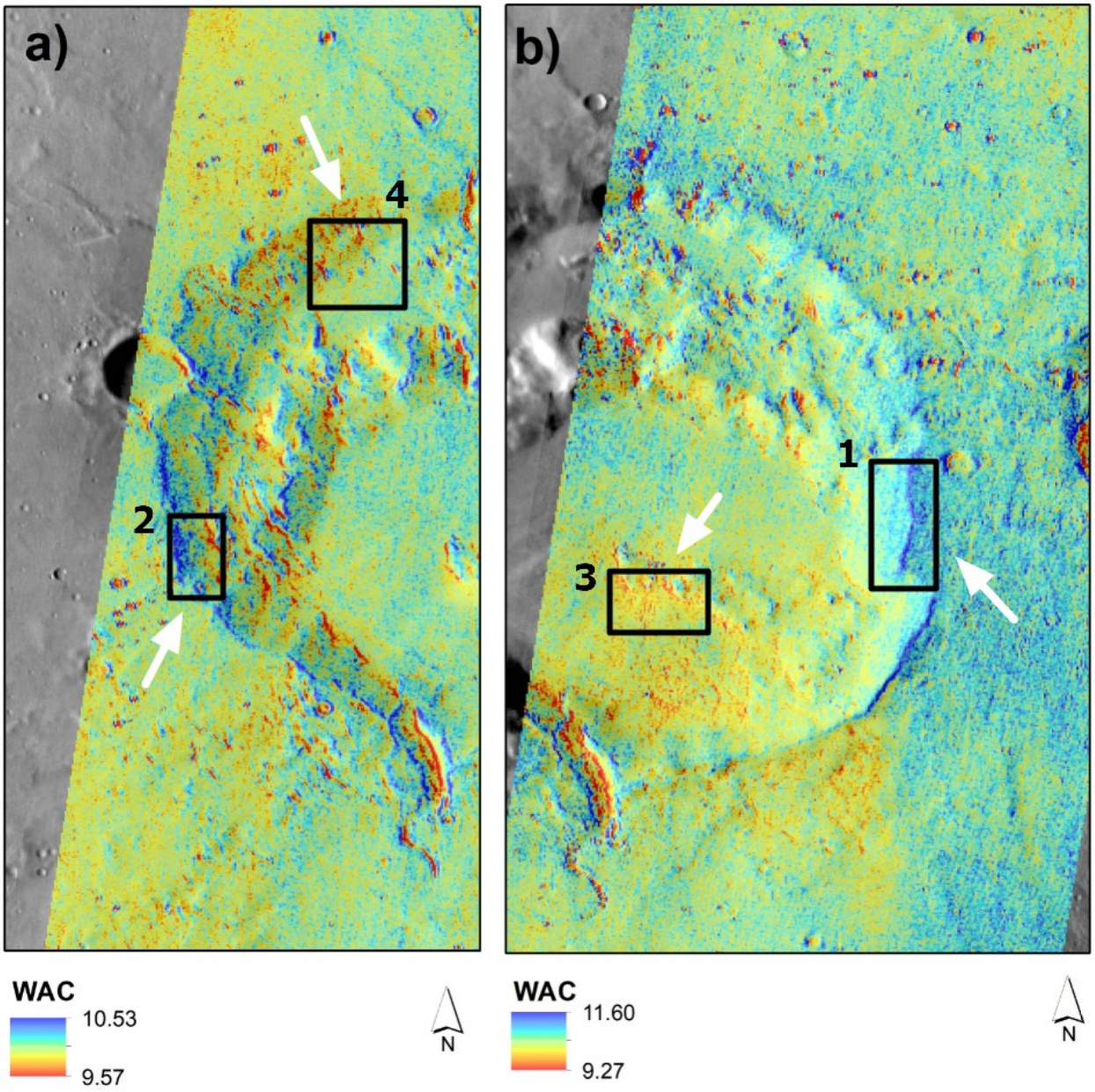

Fig. 4.5: THEMIS weighted absorption center (WAC) map for THEMIS image I53118012 (a) and I45489019 (b) overlain on a mosaic of THEMIS daytime images. THEMIS images within the Siloe Patera have WAC values ranges from ~9.27 to 11.60 μm. The higher values of WAC correspond to lower silica content whereas a lower value in WAC indicates elevated bulk-silica content. WAC values were compared to a spectral unit of THEMIS DCS 8-7-5 stretched images outline as rectangular box (indicated by white arrows): purple unit (2), fuchsia/magenta unit (3), yellow/amber unit (1), and typical terrain unit (4). The purple unit has the highest mean WAC values followed by a typical terrain unit, yellow/amber unit, and fuchsia unit. However, though the fuchsia unit has the lowest mean values among the spectral unit, the yellow/amber unit contains the lowest min WAC values.

3.1.3. Spectral shapes

The surface emissivity information was collected from the atmospherically corrected THEMIS emissivity image I53118012 and I45489019. The mean surface emissivity values were extracted from the representative spectral units of THEMIS-TIR defined DCS 8-7-5 stretches using ENVI's region of interest (ROI) tool (Fig. 4.6). The mean emissivity spectra for these four spectral units show distinct shapes corresponding to the identified surface units in DCS images as well as WAC index map. The purple unit shows lower spectral contrast, absorption weighted toward longer wavelength, and emissivity minima occur in band 6 (central wavelength at 10.21 μm). The lower spectral contrast means the homogeneous surface materials within the purple unit and the spectral shape of this unit is consistent with the higher WAC values calculated for the purple unit. The fuchsia unit has the highest spectral contrast including the lowest band depth at 9.35 μm and 10.21 μm (Fig. 4.6), consistent to the lowest WAC mean with a highest standard deviation corresponding alternative mixed pixel characteristics of high and low WAC values, and the emissivity minima occurring in band 5 (central wavelength at 9.35 μm). Emissivity spectra for yellow/amber and typical terrain show a similar shape, however, there is subtle differences between these spectral shapes. Though both yellow/amber and typical terrain have their emissivity minima occurring in band 6, the former has higher spectral contrast than the latter one. The higher spectral contrast in yellow/amber than pale-brown/green is consistent with the mean WAC values of these units, while the yellow/amber unit has the lowest WAC value as low as ~9.27 μm. Based on the result of DCS, WAC, and spectral shape analysis it can be presumed that the purple unit is composed of basaltic olivine-bearing surface (as purple in DCS 8-7-5 indicates olivine-rich materials) with lower silica content, the fuchsia unit also, indeed, rich in olivine phase minerals with some other possible mixed phase. The yellow/amber and typical terrain unit both have higher silica contents. However, a misleading or ambiguous conclusion may be constrained based on these two findings since DCS is influenced by

temperature variation and surficial composition while WAC is affected by dust cover and false detection of silicate minerals (Amador and Bandfield, 2016). Considering these shortcomings of DCS and WAC the study relied on other analysis from THEMIS-TIR data, e.g., thermal inertia and mineralogy identified from CRISM-NIR data. As the supplementary information, the study used local scale morphology identified from the higher resolutions CTX and HiRISE dataset.

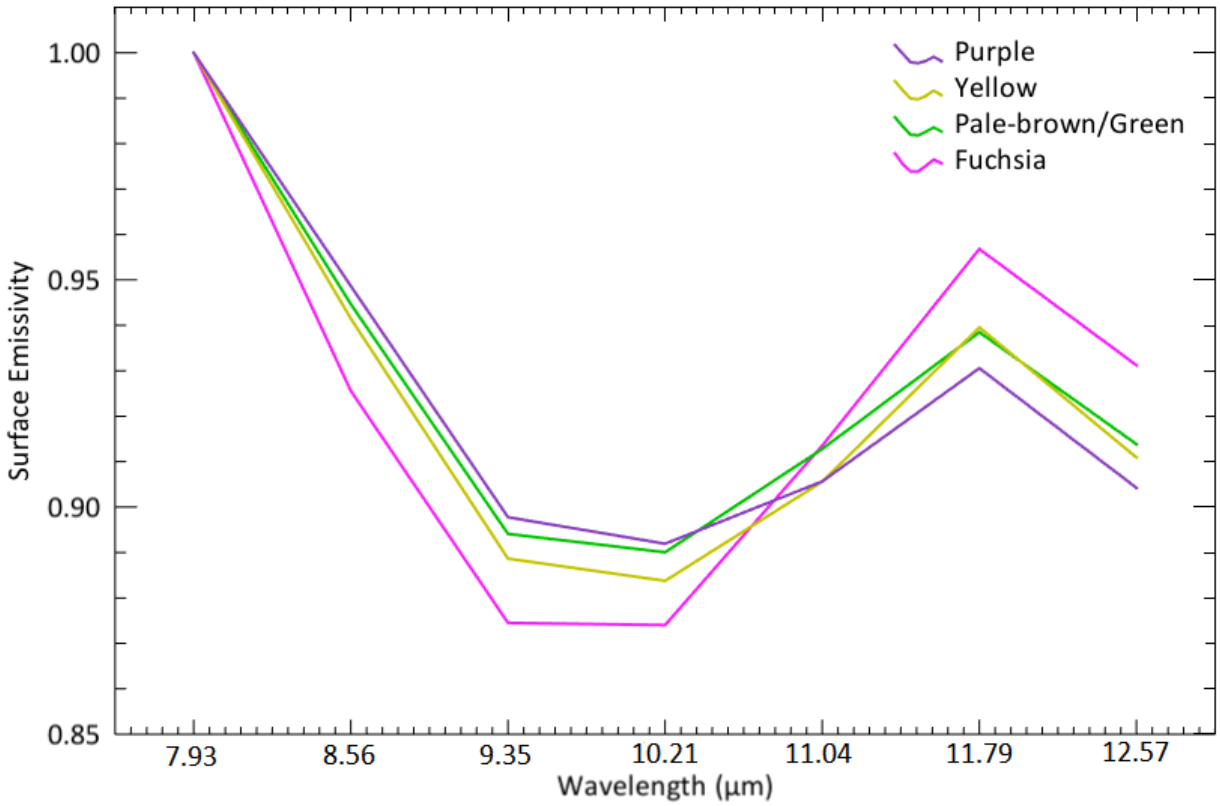

Fig. 4.6: THEMIS surface emissivity data from 7.93 μm through 12.57 μm. Spectral data for the four THEMIS-TIR defined spectral units: the purple unit, fuchsia/magenta unit, yellow/amber unit, and pale-brown/green (typical terrain) unit.

3.1.4. Thermal inertia and colorized nighttime and daytime IR mosaics

Thermal inertia values in Siloe Patera have a minimum of 10 $Jm^{-2}K^{-1}s^{-1/2}$ to maximum 337 $Jm^{-2}K^{-1}s^{-1/2}$ (Fig. 4.7) which are consistently lower values like the other volcanic features on Mars e.g., Apollinaris Mons (Garcia, 2018). The thermal inertia was calculated from a single measurement of THEMIS images. Some complex factors, e.g., uncertainties in instrument calibration, may not result in actual quantitative thermal inertia values (Putzig et al., 2013). Since the entire study area has a consistent lower thermal inertia (<600 $Jm^{-2}K^{-1}s^{-1/2}$), the study posits that the surface is composed of weakly-consolidated loose fine-grain particulate matters. Having consistent lower values and uncertainties in deriving thermal inertia, the study emphasizes that the thermal inertia map presented here can be interpreted qualitatively to show the local variations in surficial materials in the areas of interest. The study interprets that a comparative lower apparent thermal inertia values in the study area likely represent mechanically weak fine particles primarily composed of dust, silt, or fine sand whereas relatively "higher" apparent thermal inertia surfaces in the study area may consist of weakly indurated sand, surface crusts, rock fragments, or a combination of these materials (Mellon et al., 2000; Putzig et al., 2005). The thermal inertia from the surficial materials shows distinct characteristics which follows elevation and local topography. The comparatively higher thermal inertia on the headwall scrap, unlike the floor materials, suggest that the collapsed block in southeastern interior floor (tilted toward the collapsed center) materials are different from the scarp and were resulted from the landslide or slumping of the interior block (Michalski and Bleacher, 2013). The thermal inertia values (in $Jm^{-2}K^{-1}s^{-1/2}$) were collected from the representative spectral units of THEMIS-TIR defied DCS 8-7-5 stretches images (Fig. 4.4) using ENVI's region of interest (ROI) tool. The pattern of thermal inertia distribution for these four spectral units shows consistency to the surface units of DCS images (Fig. 4.4) and WAC index map (Fig. 4.5). The purple unit has a comparatively higher thermal inertia value (than other units) with a mean ~170 $Jm^{-2}K^{-1}s^{-}$

$^{1/2}$, which can be up to ~300 $Jm^{-2}K^{-1}s^{-1/2}$. This relatively higher thermal inertia (compared to the other units) in the purple unit may represent olivine-bearing weakly-consolidated materials. While the yellow/amber unit shows highest (among all units) thermal inertia mean value of ~217 $Jm^{-2}K^{-1}s^{-1/2}$ and may be composed of combinations of weakly indurated fine sand, surface crusts, and/or rock fragments. The "typical terrain" unit has the lowest thermal inertia values, but the thermal inertia value can be as low as 10 $Jm^{-2}K^{-1}s^{-1/2}$. This lowest thermal inertia values of typical terrain unit may be representative of surface materials of homogeneous dust, silt, or fine sand materials. Lastly, the fuchsia unit in the area of interest has a mean thermal inertia value of ~190 $Jm^{-2}K^{-1}s^{-1/2}$, may be the representative of the surface materials like the purple unit. Since thermal inertia may lead to ambiguous interpretations, the study surveyed colorized nighttime IR overlain daytime IR in JMARS software interface as a proxy for thermal inertia. The colorized image shows similar results from the THEMIS thermal inertia used in this study (Fig. 4.6c). The blue tones are the regions with lower nighttime temperatures or lower thermal inertia values composed primarily of dustier materials while the red tones are the regions with warmest nighttime temperature or higher thermal inertia composed primarily of mechanically weak materials. The warmest nighttime temperatures are concentrated on steep clips or wall of the Siloe Patera, representing exposed surface materials. The higher thermal inertia value on the steep slopes may be an indicator of possible fracture region of the patera. Additionally, perhaps weakly indurated materials (e.g., warmest nighttime temperature) are also concentrated on some parts the floor of the study area. This relatively higher thermal inertia values on the floor might be the evidence of weakly consolidated materials.

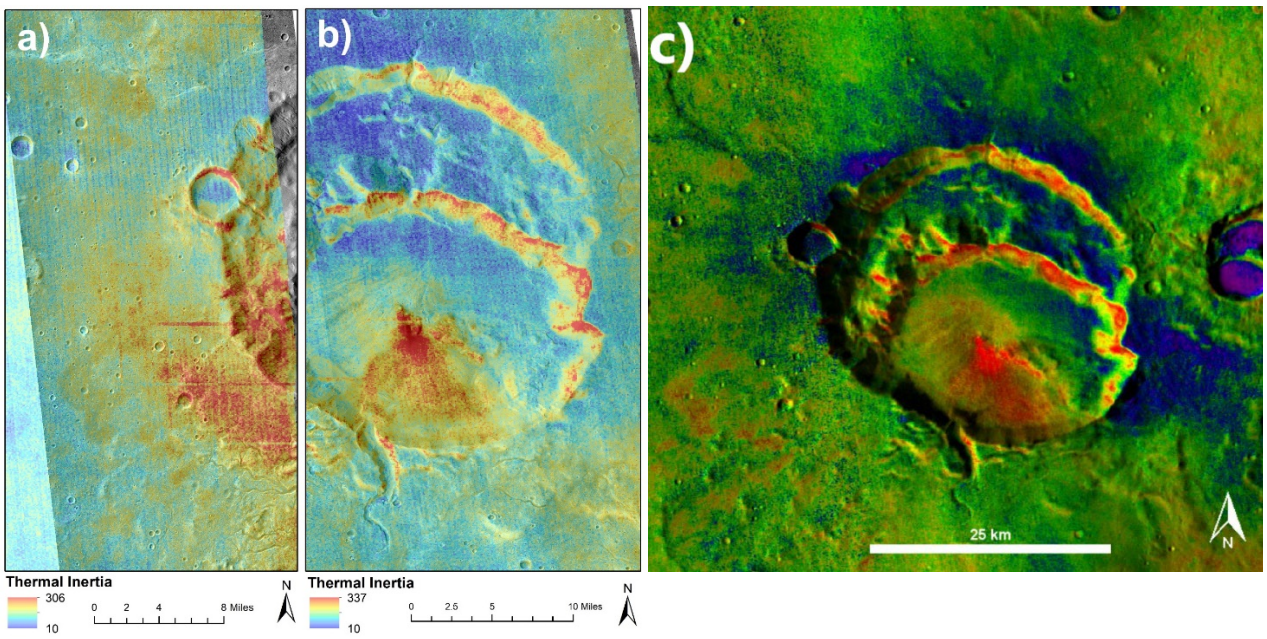

Fig. 4.7: Nighttime thermal inertia map for THEMIS image I35449015 (a) and I27002020 (b) overlain on CTX grayscale image. THEMIS nighttime image within the area of interest has thermal inertia values ranges from 10 $Jm^{-2}K^{-1}s^{-1/2}$ to maximum 337 $Jm^{-2}K^{-1}s^{-1/2}$. The thermal inertia from the surficial materials show distinct characteristics which follows elevation and local topography as the scarps of headwall have relatively "higher" thermal inertia values compared to the most floor materials. (c) Colorized nighttime IR overlain on daytime IR mosaics shows similar results to the THEMIS thermal inertia. The blue tones are the regions with lower nighttime temperature or lower thermal inertia values composed primarily of dustier materials, while the red tones are the regions with warm nighttime temperatures or higher thermal inertia composed primarily of mechanically weakly indurated materials.

3.2. CRISM-NIR spectral analysis

3.2.1. Index maps

NIR spectral index map of CRISM produced by Arizona State University, which is available at JMARS, were surveyed in areas of interest defined by THEMIS-TIR data (Fig. 4.4). Arabia Terra is thought to have fine-grained, phyllosilicate-bearing materials within an extensive Noachian fluvial system (e.g., Michalski and Bleacher, 2013; Davis et al., 2016). Moreover, Siloe Patera shows numerous channels and gully networks, as well as some likely phyllosilicate mineral phases,

therefore, the study searched mineral phases associated with aqueous altered basaltic rock, including phyllosilicates and hydrated silica phases. To ensure the sufficient quality of CRISM multi-spectral survey products (MSP) data, the study first surveyed OLINDEX3 (i.e., sensitive to the broad olivine absorption at or near 1.0 μm; Pelkey et al., 2007, Viviano-Beck et al., 2014; Amador and Bandfield, 2016) in the area where the olivine-rich basaltic rocks are to be expected based on THEMIS-TIR analyses. The study only used MSP images that showed sufficient olivine absorption in the areas where olivine was expected based on THEMIS-TIR analysis, e.g., DCS and WAC. A total of three spectral indices, e.g., OLINDEX3, D2300, and DB1900_2 were surveyed from the selected MSP images, covering four spectral units defined in THEMIS-TIR analysis. The spectral indices used in this study are given in Table 4.4.

Table 4.4: CRISM spectral indices[a] used in the study.

INDEX	PARAMETER	FORMULATION	RATIONALE
OLINDEX3	Board absorption at 1 μm	*RB*1210*0.1+*RB*1250*0.1+*RB*1263*0.2+ *RB*1276*0.2+*RB*1300*0.4	Olivine will be strongly >0
D2300	2.3 μm drop-off	1-(((*R*2290/*RC*2290) +(*R*2320/*RC*2320) +(*R*2330/*RC*2330))/((*R*2120/*RC*2120) +(*R*2170/*RC*2170) +(*R*2210/*RC*2100)))	Sensitive to hydroxylated Fe/Mg-silicates
BD1900_2	1.9 μm H_2O band depth	0.5*(1-(*R*1930/a*1850+b*2067)) + (1-(*R*1985/a**R*1850+b**R*2067))	Sensitive to bound and/or absorbed H_2O molecule

[a]Note: *R* indicates reflectance of the particular wavelength(s), *RC* indicates reflectance at center wavelength, *RB* indicates band depth, and a&b can be solved using the equation: a=1-b. For more details, the readers are referred to Pelkey et al. (2007) and Viviano-Beck et al. (2014).

The indices map thus produced were based on individually stretched CRISM MSP index images. The stretching was applied to each individual image to emphasize the highest or best possible realistic index values. OLINDEX3 index shows a broad absorption within the THEMIS-TIR defined purple and fuchsia units (Fig. 4.8). This positive absorption feature of OLINDEX3 within

the purple and fuchsia units confirm olivine-rich surface materials in these areas. In some instances of scattered distributions, the fuchsia unit that was adjacent or interlocked (mixed with) to yellow/amber and typical terrain also appears positive for the detection of OLINDEX3 index. However, the olivine index shows broad absorption spatially co-located extensively with the purple and fuchsia units. CRISM-NIR spectral index D2300 appears to be variable in distribution on Siloe Patera as the higher index values incorporate mostly with the typical terrain unit but few in the yellow/amber and purple units or mixed TIR unit (Fig. 4.9). In other words, the distribution of phyllosilicate D2300 absorption, indicating the occurrence of a Fe/Mg-smectite, is present on the floor surface. Some locations of the yellow/amber and fuchsia units where WAC has comparatively lower values, consistent with elevated bulk-silica content, appears moderately highlighted in D2300 index. However, D2300 index does not show sufficient positive detection in the THEMIS-TIR defined the purple and fuchsia units in this study. BD1900_2 hydration index values are spatially very limited in distribution inside the study area. Positive detection of BD1900_2 occurs inside the patera area, which is spatially co-located with the fuchsia and typical terrain, as well in some areas of the mixed unit, where there is a network of channels and gully present. The study found a few elevated BD1900_2 index values that are associated with the high D2300 index values, thus indicating the presence of hydrated-phyllosilicate phase, but also showing lower values in WAC that are consistent with elevated bulk-silica content (Fig. 4.9). The areas with both high index values of D2300 and BD1900_2, therefore, are likely the areas having a presence of hydrated phyllosilicate phase, morphologically adjacent to the channels and gully networks. In cases of some mixed pixels, where the yellow/amber color coexists with typical terrain, D2300 index appears higher values but weakly or not even highlighted in BD1900_2 index represent phyllosilicates with limited abundance or no hydrated phase. Noteworthy here is that THEMIS-TIR-defined the yellow/amber or typical terrain may not consistent with a higher concentration of D2300 index. However, this non-detection

of D2300 index in these areas does not necessarily mean these areas are devoid of key mineral phases (Amador and Bandfield, 2016). To ensure on positive detection of mineral phase identified by MSP spectral index map, care should be taken to examine individual I/F spectra.

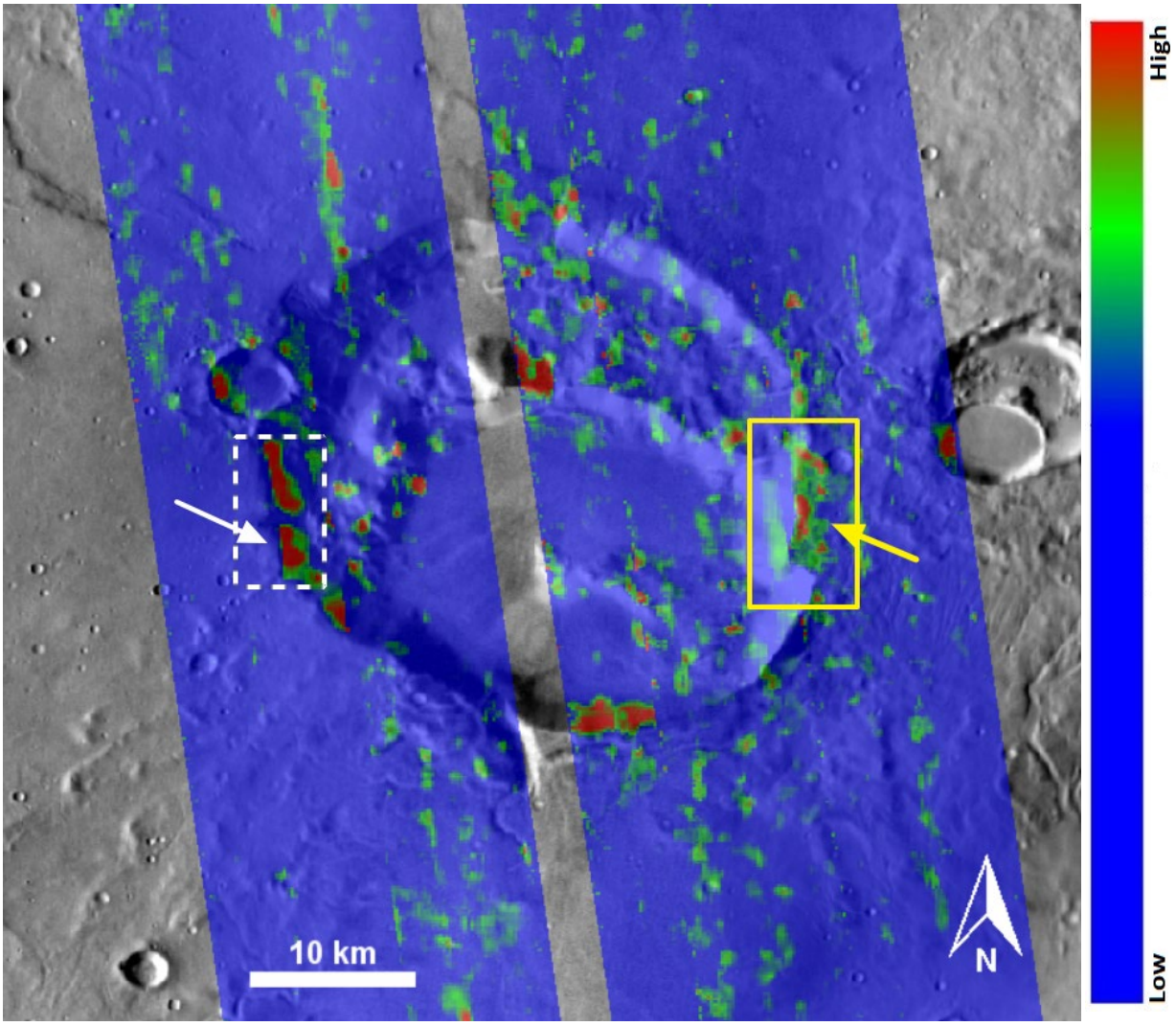

Fig. 4.8: CRISM MSP OLIDEX3 olivine index map using individually stretched images in Siloe Patera. The white box and arrow inside indicate the location of fuchsia unit suggesting positive absorption in OLINDEX3 olivine index. The yellow box and arrow inside indicate the location of the purple unit suggesting board absorption in OLINDEX3 olivine index.

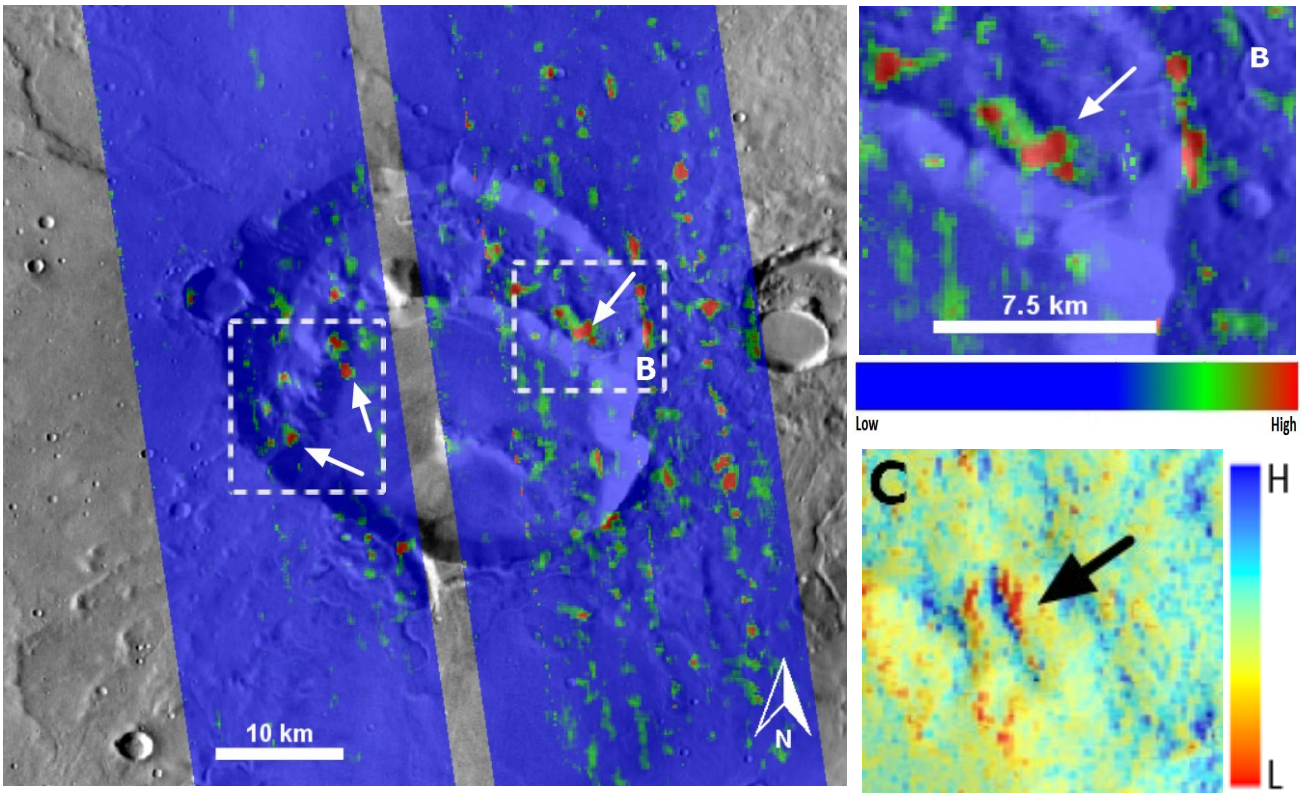

Fig. 4.9: CRISM MSP D2300 phyllosilicate index map using individually stretched images in Siloe Patera (a). The white dashed boxes and arrows inside indicate the location of positive absorption in both D2300 and BD1900_2 indices suggesting signature of hydrated, phyllosilicate-bearing mineral phases. b) Dashed polygons indicate the location of enlarged from (a). c) WAC map in the same location in b) indicated by black arrow suggestion a lower value in WAC consistent with elevated bulk silica content.

3.2.2. Reflectance I/F spectra

CRISM MSP00019753_01 image was selected to extract ratio I/F spectra for analysis of spectral absorption features. The image was corrected for standard spectral corrections (e.g., atmospheric correction, volcanic scan correction, etc.) (Pelkey et al., 2007; McGuire et al., 2009; Viviano-Beck et al., 2014 and 2017) using CRISM Analysis Toolkit (CAT v7.4) extension in ENVI. The spectra were collected for average (mean) of 3x3 pixels from the areas where the indices had the best absorption signature. The spectra were extracted from the regions with high OLINDEX3 (sensitive to broad

olivine absorption at around ~1 μm; Amador and Bandfield, 2016) from the area with sufficient high absorption. OLINDEX3 spectra for 3x3 pixel indicates broad absorption ~1 μm and the long wavelength shoulder (Fig. 4.10). This broad absorption ~1 μm indicates the presence of an olivine phase in the area. The study then extracted spectra (3x3 pixels) from the area showing sufficient absorption in both D2300 (sensitive to a 2.3 μm drop-off that is diagnostic characteristics of phyllosilicate; Pelkey et al., 2007; Viviano-Beck et al., 2014; Amador and Bandfield, 2016) and BD1900_2 (sensitive to bound and/or absorbed H_2O molecules; Pelkey et al., 2007; Viviano-Beck et al., 2014; Amador and Bandfield, 2016). The spectra for these D2300 and BD1900_2 indicates absorption near ~1.4, 1.9, and 2.3 μm (Fig. 4.10). The characteristic absorption features at ~1.4, 1.9, and 2.3 μm indicate co-existence or occurrence of hydrated phyllosilicate phases. The spectra for D2300 and BD1900_2 shows absorption near ~1 μm as well, consistent with the existence of olivine in the spectral shape, this may be subpixel contribution from the neighboring olive bearing phase (Amador and Bandfield, 2016).

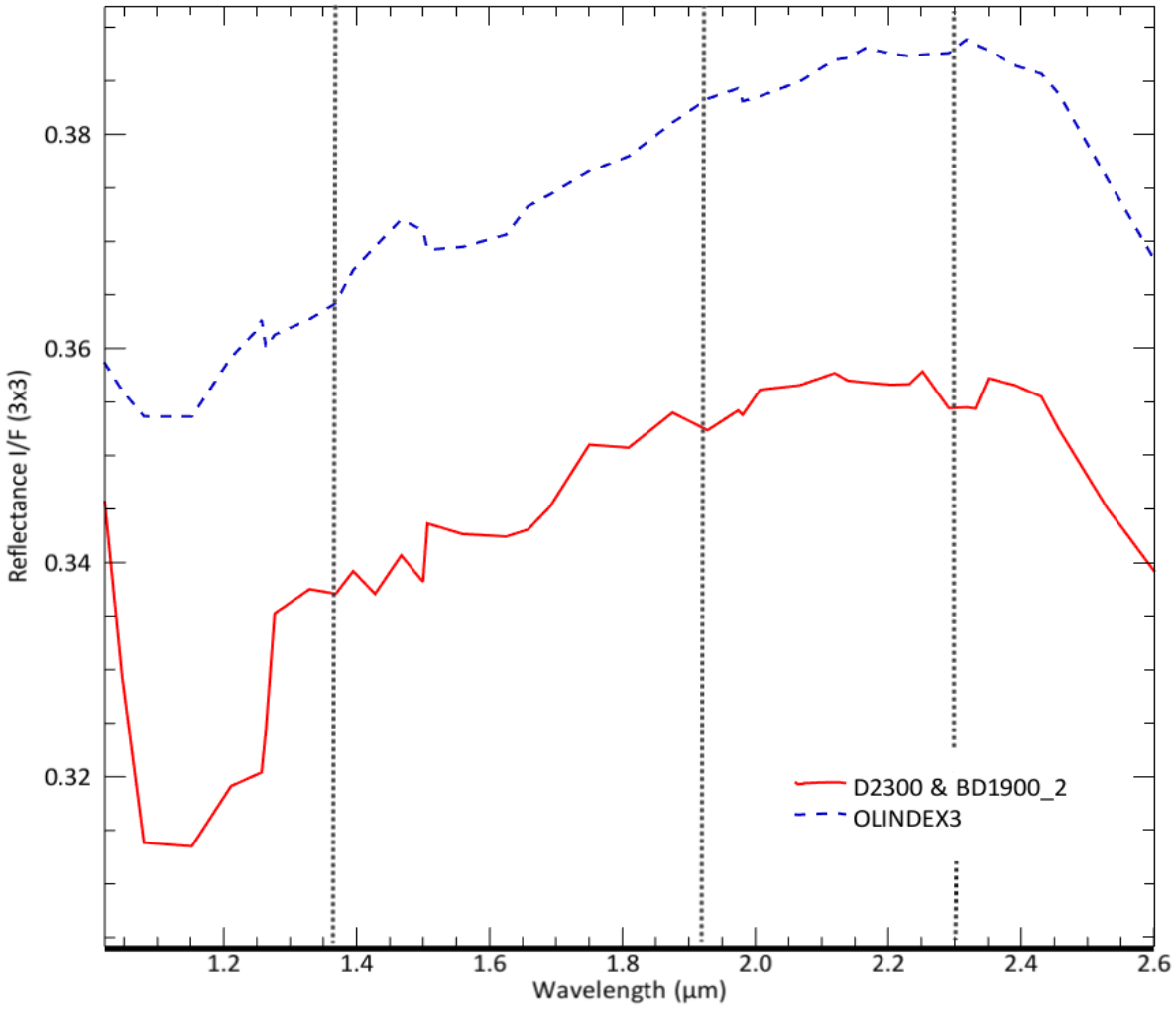

Fig. 4.10: CRISM MSP spectra collected at 3x3 pixels for OLINDEX3, D2300, and BD1900_2 indices from ratio I/F spectra of MSP00019753_01 image. OLINDEX3 spectra show broad absorption ~1 μm indicating the presence of olivine phase while D2300 and BD1900_2 spectra have absorptions near ~1.4, 1.9, and 2.3 μm indicating the presence of hydrated phyllosilicate phases.

3.3. Unit texture

The texture of spectral units defined by THEMIS-TIR analysis was assessed using a mosaic of CTX datasets (Fig. 4.11). Among the spectral units, the yellow/amber unit lies mostly near to the highland area or spire near the southern depression's center. The unit appears relatively homogeneous, dark-toned in texture relative to the surrounding surfaces, and relatively smooth in

local scale, however, this unit contains superimposed ripples (described in the following section in detail), and a very few numbers of small impact craters. The fuchsia unit is composed of light-toned materials and mostly lies on the southwestern rim and scarp area. In contrast, the pale-brown/green (typical terrain) unit shows variably-toned materials, and in some areas (beyond the southern rim) it has a mixed texture of dark- and light-toned materials, whereas in most instances this unit is composed of moderately homogeneous light-toned materials of smooth surface at local scale, home to few craters, and contains some ripples in some places. Lastly, the purple unit has moderately dark-toned materials in the rim and scarp areas.

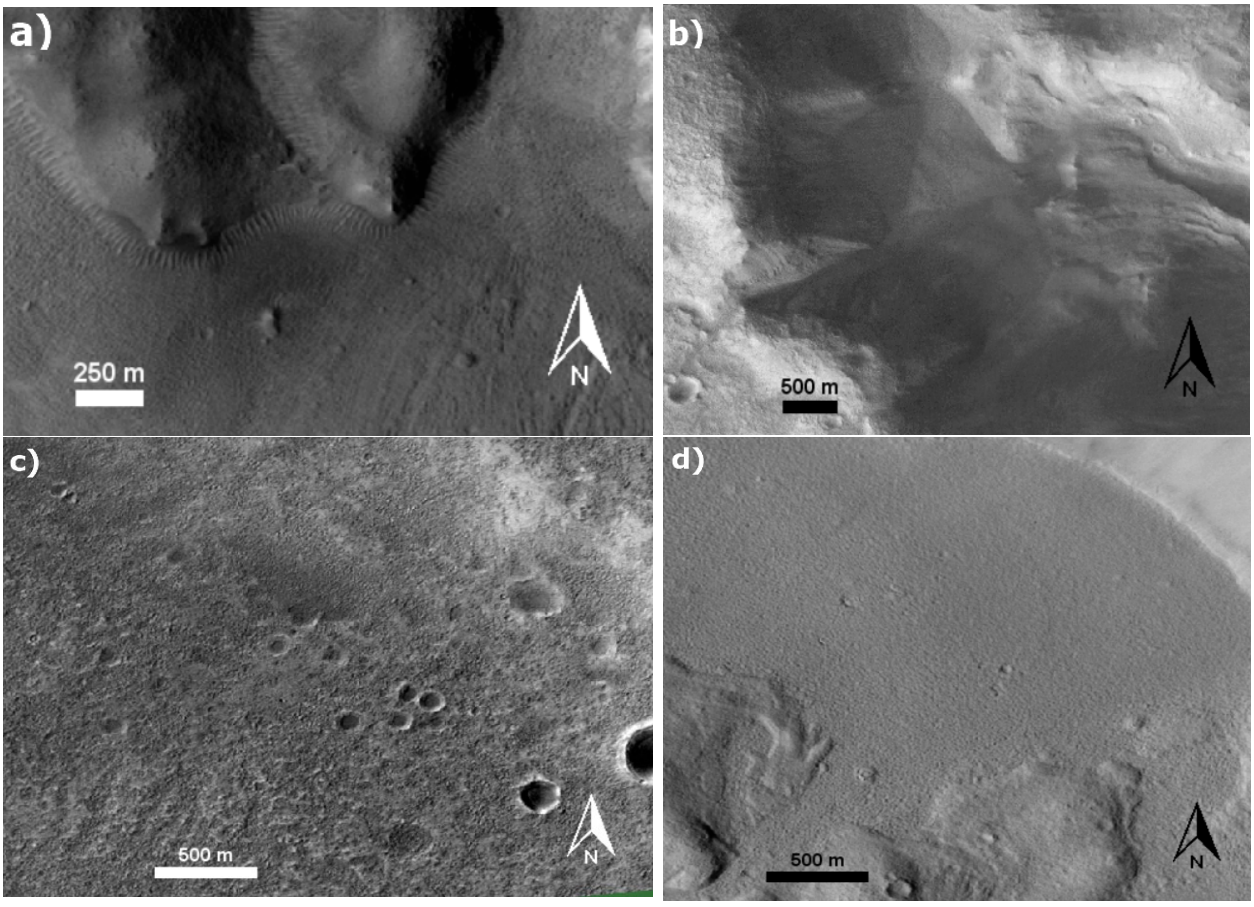

Fig. 4.11: Unit texture as derived from a mosaic of CTX images. a) yellow/amber unit shows dark-toned materials, b) fuchsia unit appears in light-toned texture, whereas the pale-brown/green (typical) terrain shows a mixture of the dark- and light-toned materials beyond the southern rim (c) and homogeneous light-toned materials elsewhere (d).

3.4. Morphology

Surface morphology was analyzed to constrain the local geology of Siloe Patera considering notable geological features using THEMIS, CTX, and HiRISE datasets (Fig. 4.12). Higher resolution images show a prominent valley-like feature in the foreground that cuts into the main depression. Many nearly parallel channels and gullies are identified in southwestern, east and southeastern, and east and northeastern rims, which cut into the walls and are partly flowing into the depression (Fig. 4.12b). Valley and small channels/gullies appear to cut through a material (called lobate flow) to the lower left of the craters. This lobate flow feature has been interpreted as a volcanic flow or pyroclastic deposit (Michalski and Bleacher, 2013); however, this feature can also be impact ejecta.

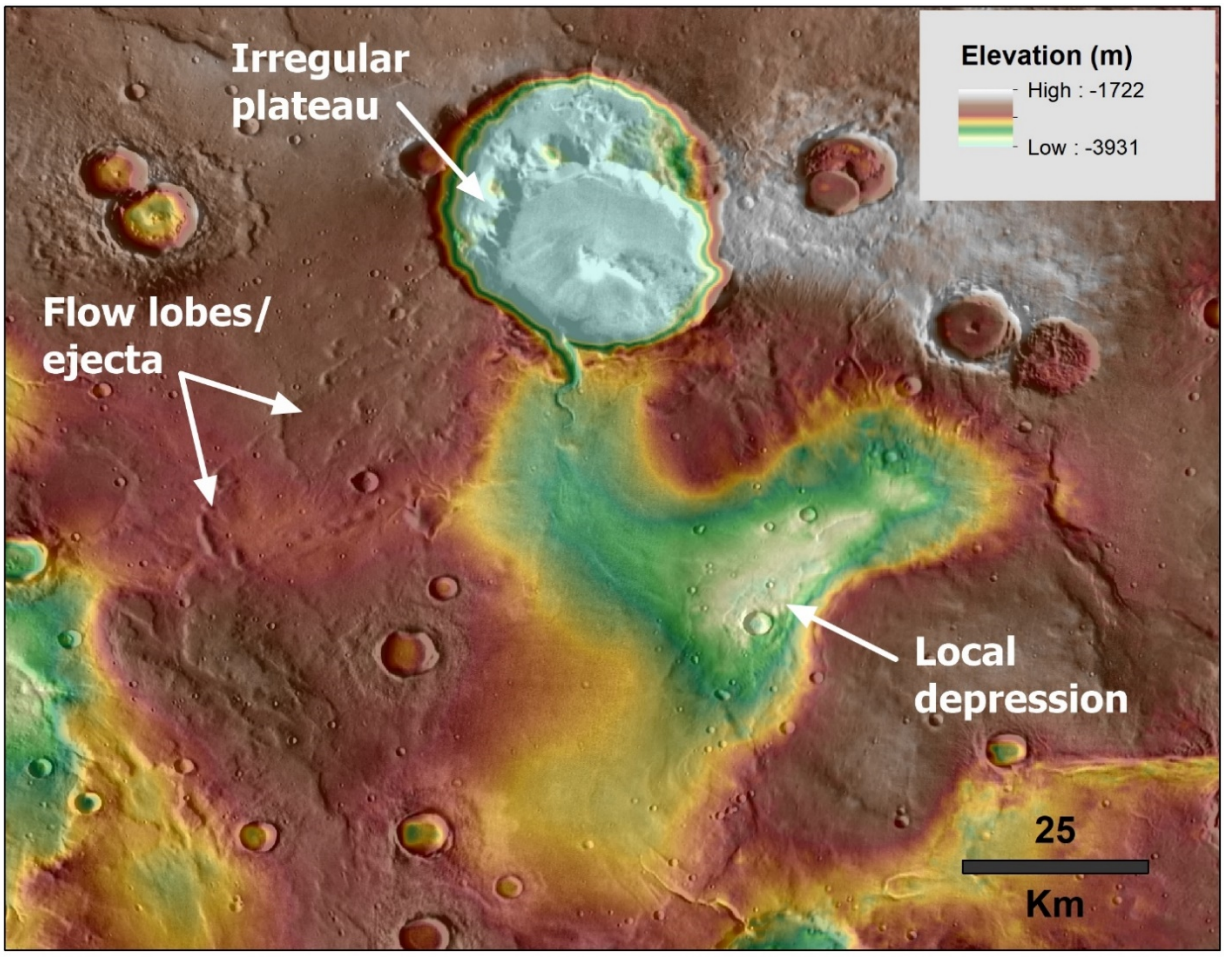

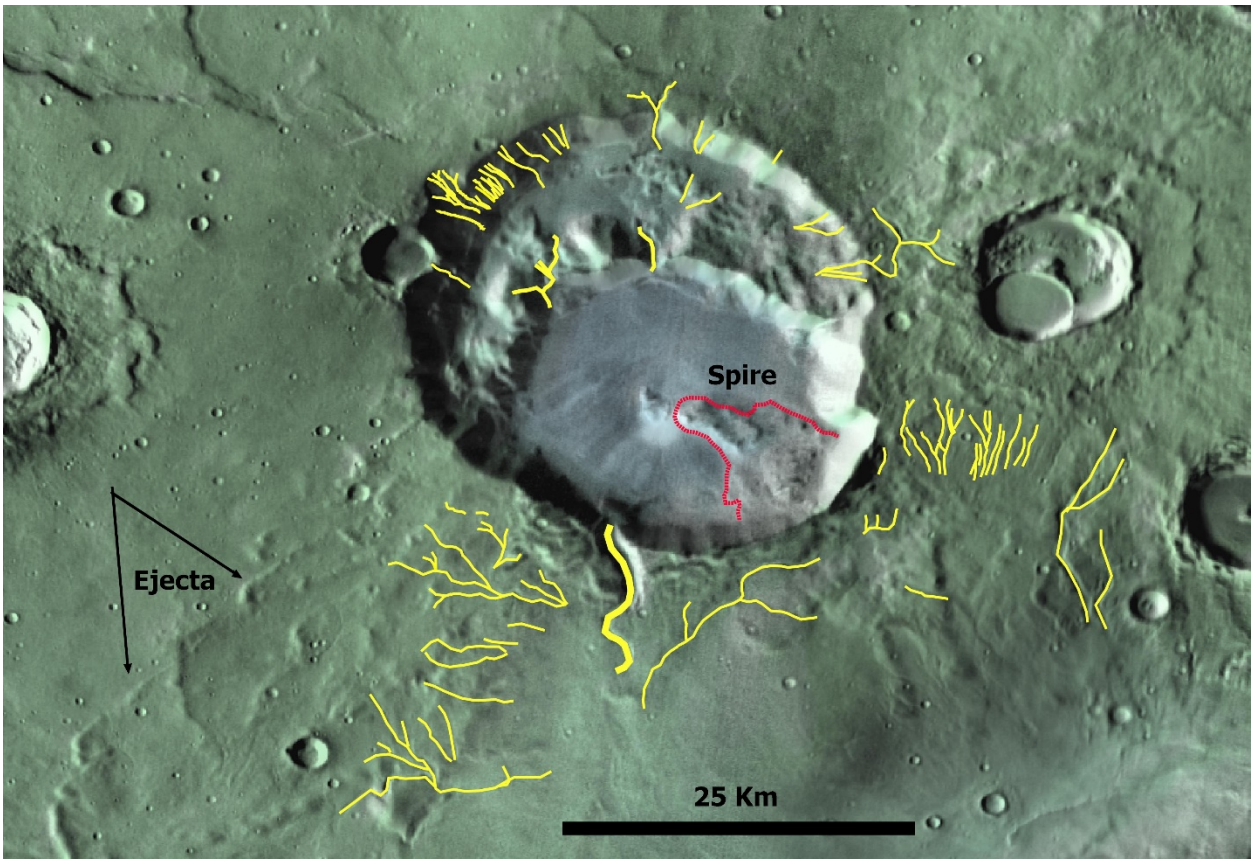

Fig. 4.12: Local geologic features of Siloe Patera shown as MOLA colorized elevation data overlain on daytime THEMIS global mosaics. a) The lobate feature is interpreted as lava flow and irregular mount on the northern plateau are considered as friable materials (Michalski and Bleacher, 2013). b) Geological map including sinuous valley features within and around Siloe Patera are represented by yellow lines. The spire is outlined in red and possible impact ejecta is indicated by the black arrows.

The crater dataset of Robbins and Hynek (2012a) indicates Siloe Patera as having multiple craters: the northern and southern. The northern crater has a modeled circular diameter of ~35 km while southern crater has a circular diameter of 26.6 km based on MOLA topographic information (Robbins and Hynek, 2012a). The average height of the rims of northern and southern craters was measured as 110 and 330 meters, respectively, as calculated from the average height of rim minus the average height of the surrounding areas. The present study also extracted elevation profile of rim (across the depression) in different sides from the HRSC MOLA blended 200m DEM. The

elevation profile cross sections show that the rim of depression has a height values of ~100's of meters from the sounding topography (Fig. 4.13).

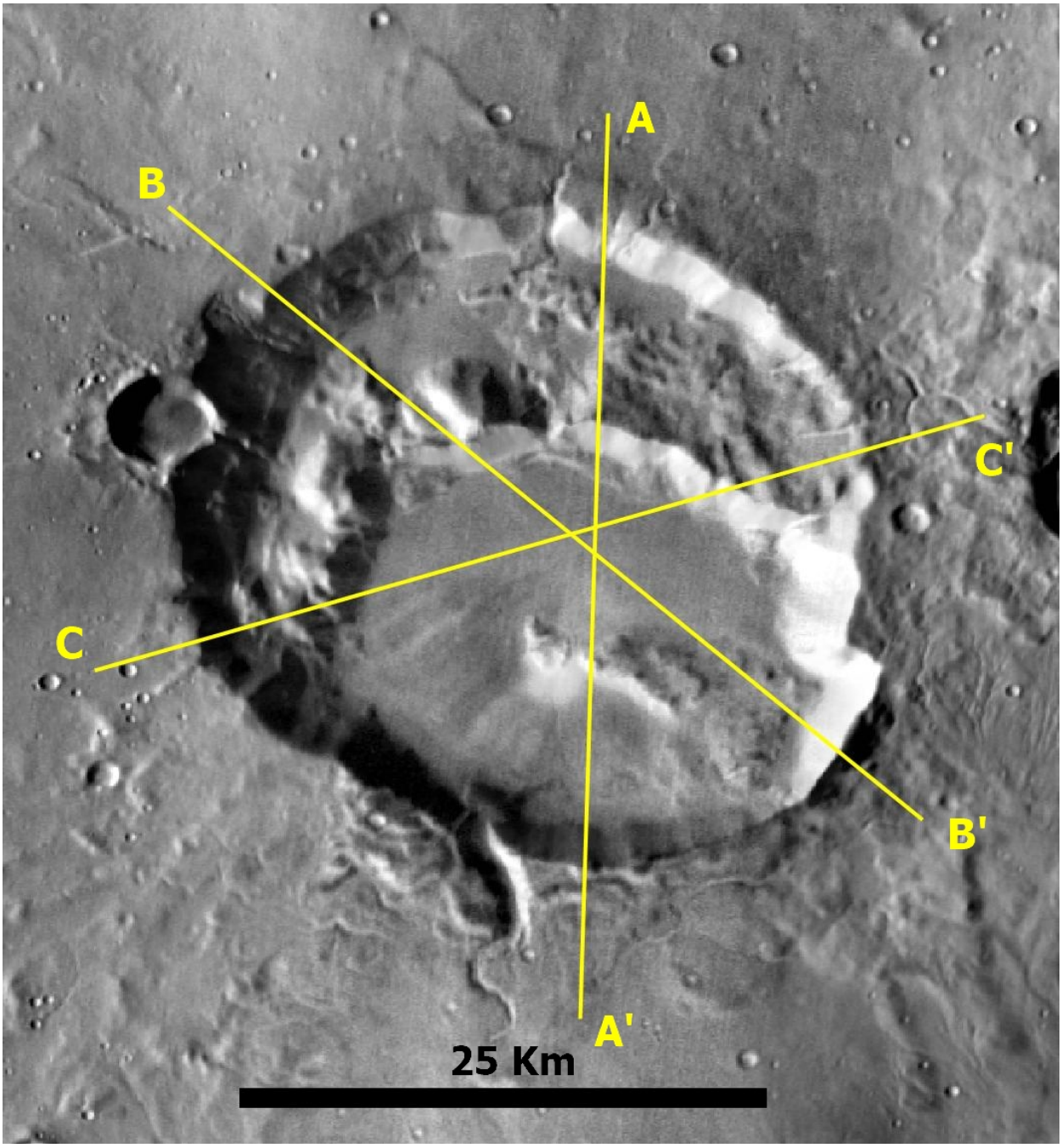

Fig. 4.13: a) Elevation profile of the rim (across the depression) in different sides from the HRSC MOLA blended 200m DEM overlain on THEMIS daytime IR images. Three elongated transects (AA', BB', and CC') were drawn along Siloe Patera to extract the cross-section elevation profile of the rim. North is up on the map.

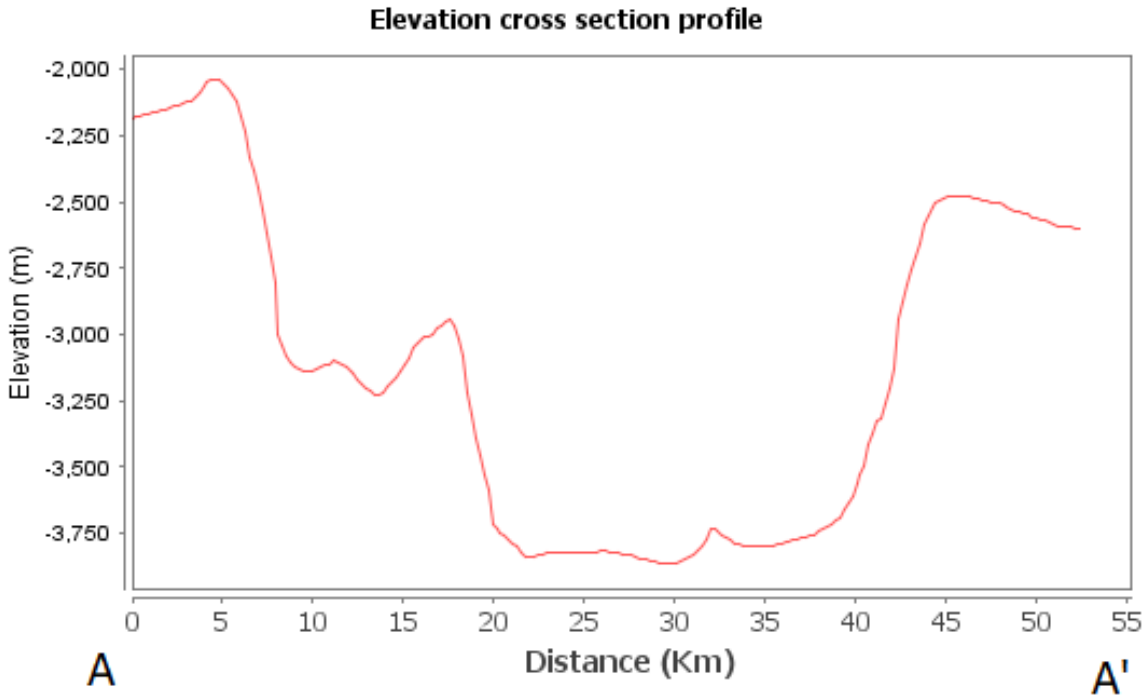
Elevation cross section profile
-2,000
-2,250
-2,500
-2,750
-3,000
-3,250
-3,500
-3,750
Elevation (m)
0
5
10
15
20
25
30
35
40
45
50
55
Distance (Km)
A
A'

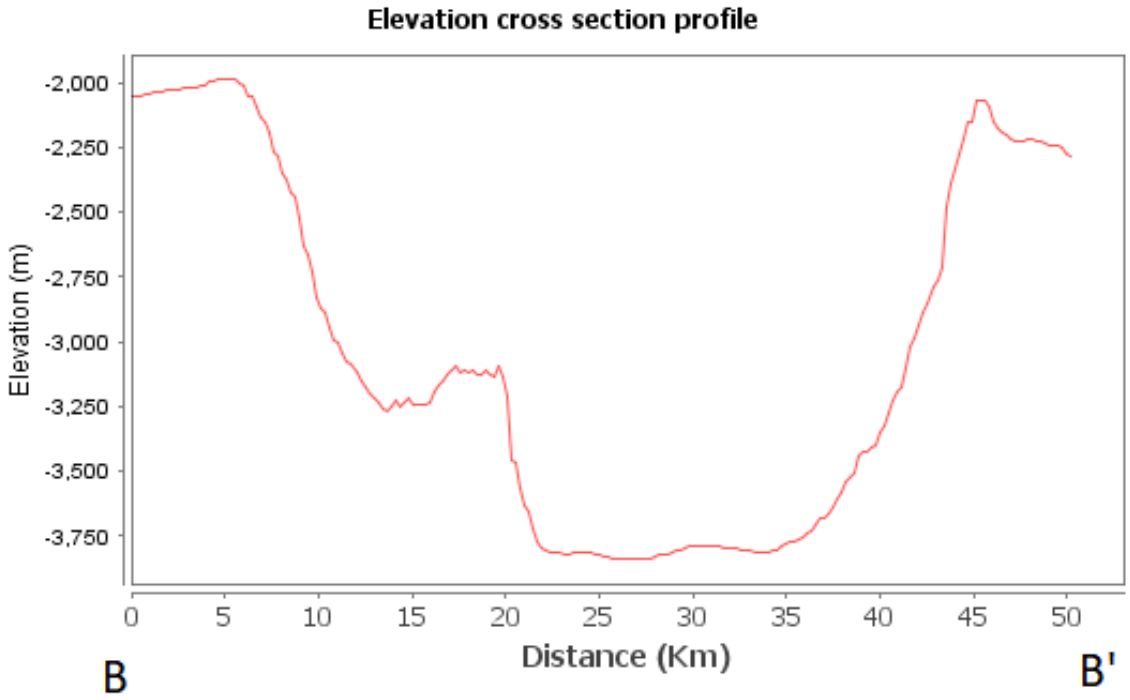
Elevation cross section profile
-2,000
-2,250
-2,500
-2,750
-3,000
-3,250
-3,500
-3,750
Elevation (m)
0
5
10
15
20
25
30
35
40
45
50
Distance (Km)
B
B'

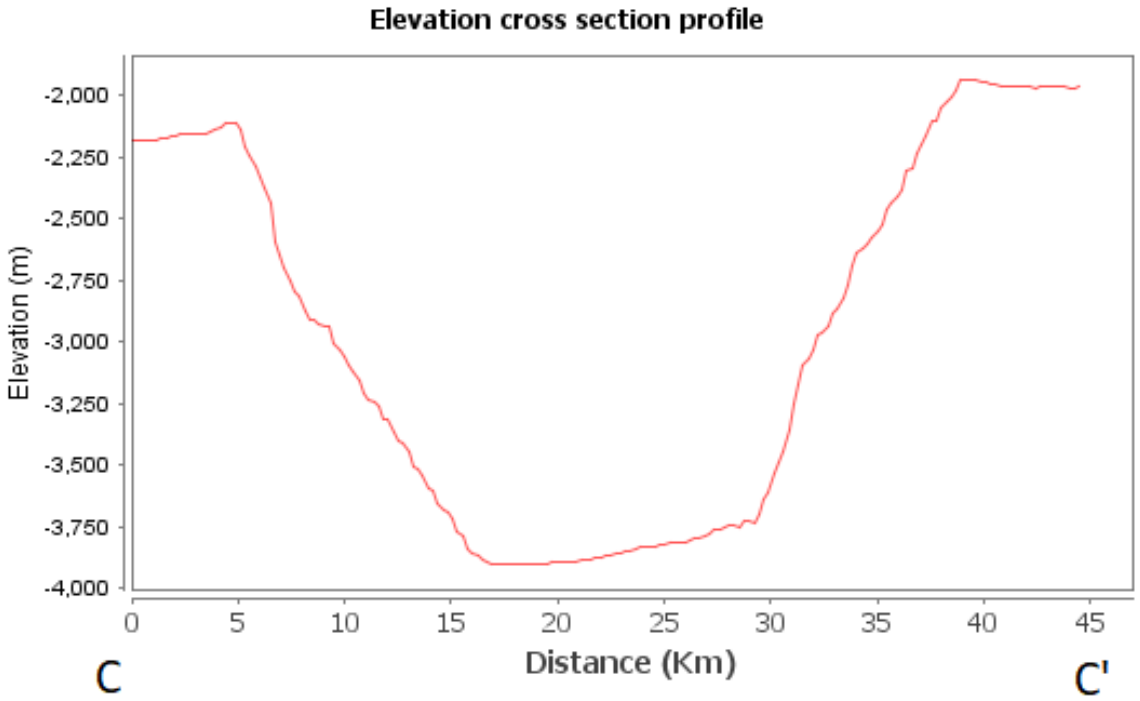

Fig. 4.13: b-d) Elevation profile of rim (across the depression) in different sides from the HRSC MOLA blended 200m DEM. The elevation profile cross sections show that the rim of depression has a height values of ~100's of meters from the sounding topography.

The wall slopes, derived from HRSC MOLA blended 200 m DEM, of Siloe Patera varies from 10° to 25° with the steepest slope in the eastern wall. Interior of Siloe Patera contains a plateau (or bench) along the northern wall or rim. The mosaic of CTX images show few irregularly raised mounds along the scarp line of the bench (can have possible faulting) and along the north-eastern portion. In general, the plateau has an irregular topography interpreted as flat and hummocky terrain with irregular mounts that are thought to have been formed from the pyroclastic deposits (Michalski and Bleacher, 2013) dissected by a series of valleys emaciated from the northern wall. On the plateau, the low elevation surface shows a smooth surface with a discontinuous linear to curvilinear ridges in HiRISE images, details are described in the subsequent section (Fig. 4.14). The southern depression has a deeper floor of an area of ~530 sq. km (area = πr^2, where r is the radius = d/2, d is

the diameter) and subtle distinct textured than the surface of the northern plateau in CTX and HiRISE images (Fig. 4.14). The southern floor surface shows rougher surface than plateau surface with linear to curvilinear ridges, fractures, and linear shallow valley-like features. This subtle difference in the surface texture of the northern and southern floor materials is described in the subsequent section in detail.

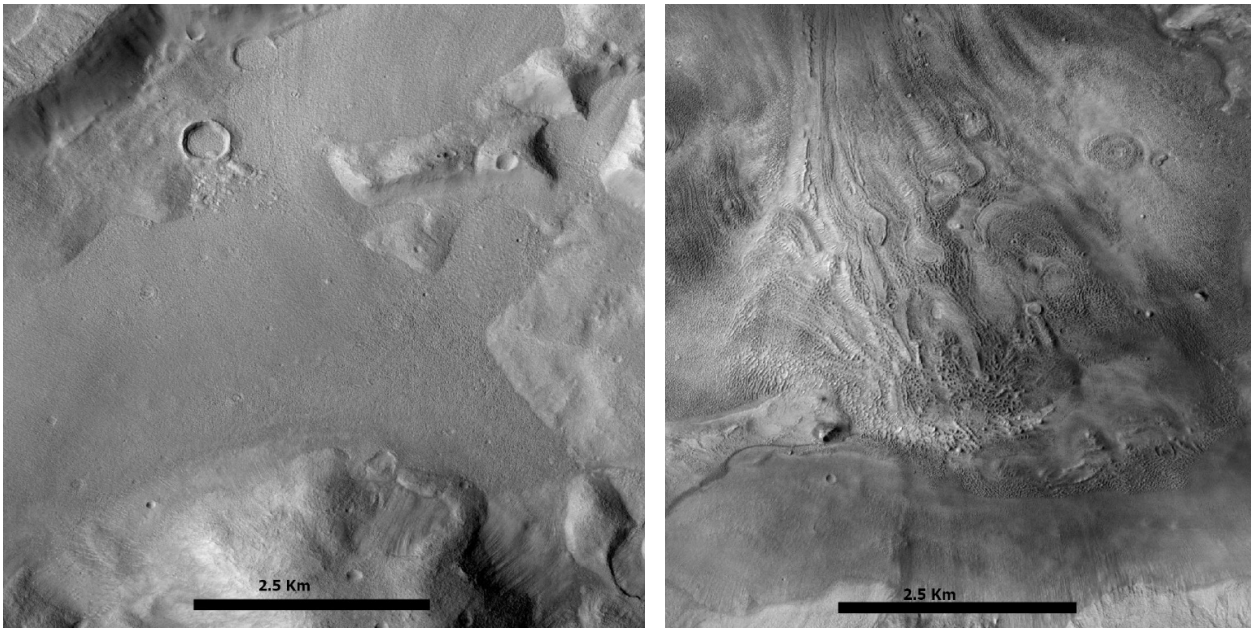

Fig. 4.14: The floors of the Siloe Patera in CTX image mosaic. a) The texture of the northern depression on the plateau area shows a relatively smooth surface whereas b) the surface of the southern floor materials shows a distinct rough surface.

An elongated mound on the floor of southern depression, the study referred here as a spire, dips toward the southern depression center. On the northern plateau, the irregular mounds along the fault scarp with clear individual peaks in CTX DEM data are thought to be divided by channels. It is suspected that a series of concentric exposures along the right side of the northern bench could be ring faults which might be degraded and likely covered by layers of dust or ash fall, leaving little room for rock exposure (Wilkes, 2014). The spire located on the floor of southern depression is

broken into multiple parts; one isolated mound and another elongated mound. They extend and grade up in elevation until they connect to the southeastern headwall of Siloe Patera. CTX DEM elevation data shows that it is higher than the surrounding floor with elevations that rise toward the rim. Though central peaks and isolated mounds on the floor are common of many impact craters (e.g., Smith, 1976), Siloe Patera, in contrast, lacks many other clearly discernable pieces of evidence of impact cratering (Michalski and Bleacher, 2013; Wilkes, 2014). In the study of Wilkes (2014), this spire was interpreted to be a primary igneous feature, possibly an eroded cone or dike, rather than a clastic sedimentary deposit. The spire is connected to the southern rim and the two appear to have pretty similar characteristics of THEMIS-TIR higher thermal inertia values. For example, the spire could be a slumping of headwall or could be covered by rim-derived scattered rock and/or generally abundant with rocks. Also, the peak appears like mechanically relatively weakly indurated materials in high-resolution image CTX and HiRISE images. Based on these characteristics, the study interprets the spire most possibly resulting from the slumping of rim materials, but it is also difficult to rule out it as the vent of a smaller volcano that might have been degraded or obscured by surficial materials. However, local slope, derived from CTX DEM, does not support the spire to be a volcanic vent but rather the result of deposits or slumping of rim materials. The study hypothesizes the formation the spire as slumping of the crater wall, not as a landslide or mass-wasting since landslide and mass-wasting produce 'fan style' deposits or concentrating materials on the base of the rim or wall (Craddock et al., 2018). The spire present in Siloe Patera does not look like a fan, therefore, the study presumes this spire is formed as slumping of the wall materials. Beddings are found on the rim wall (eastern and northern) of the Siloe Patera from HiRISE images (Fig. 4.15) and no boulders within or below the bedding. The eastern rim shows three distinct bedded layers with few boulders found at the base of the wall (Garcia, 2018). Besides the above-discussed features, the

study also investigated other local geologic features from HiRISE images that have not been previously identified in Siloe Patera.

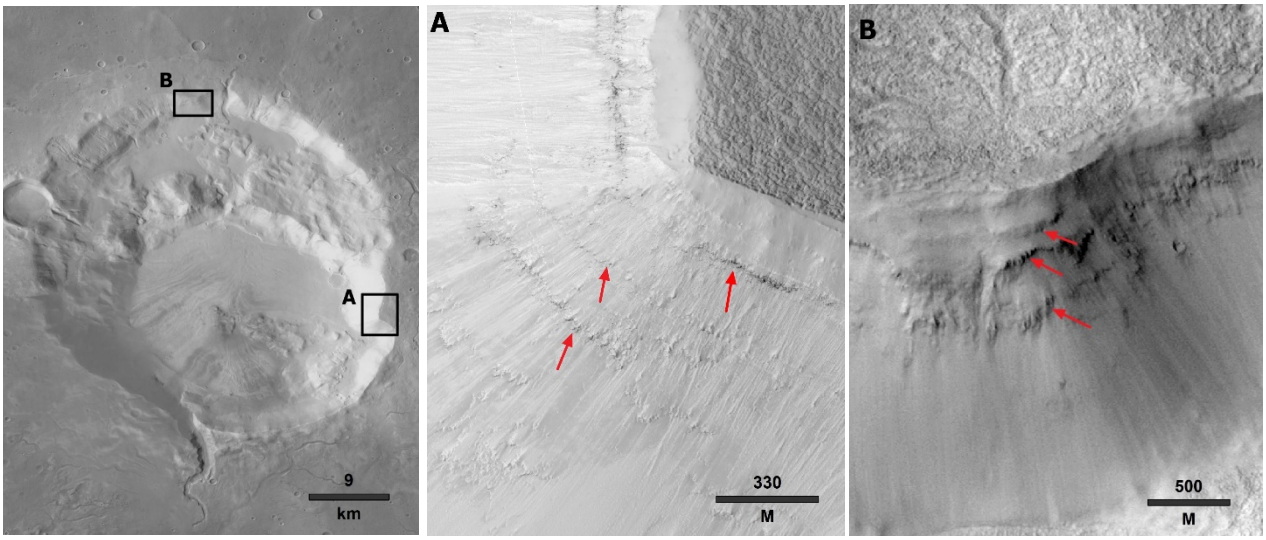

Fig. 4.15: Bedding found in the eastern wall of the Siloe Patera as shown from HiRISE data overlain on CTX global mosaic. No boulder within or below the bedding. The eastern rim shows three distinct bedded layers with few boulders are found at the base of the wall.

3.4.1. Possible flow features on the floor

CTX data for the floor of the southern depression are consistent with a feature more likely seems a distinct pattern of flow and block materials (Fig. 4.16). The study interprets these features could be large effusive lava flows. The stratigraphy of floor materials indicates that these lava flows occurred *after* the surface collapse (or impact) event and, therefore, these are post-collapse volcanic flows on the caldera floor. The flow features appear as light-toned areas that are outlined by dark-toned materials, as compared to surrounding surfaces. The terrain profile extracted from the CTX DEM indicates flow features as alternate uneven profiles (Fig. 4.16b). THEMIS-TIR-derived analysis in these lava-flow features showed that the image DCS 8-7-5 shows a mixture of most of the purple and limited fuchsia, as well as a concentration of limited yellow/amber unit, WAC

analysis shows absorption to comparatively higher wavelengths, which corresponds to comparatively lower silica content, and thermal inertia indicates moderately high values. The eruption style of terrestrial volcanism i.e., effusive verses explosive eruption (e.g., Self, 2006) depends on the composition of magma and volatile content (e.g., Francis, 1993). Mafic magmas with lower silica content tend to be less viscous (e.g., Hulme, 1974). These mafic magmas can contain volatiles which is readily escaped and results in a more effusive style of volcanic lava eruption (Vergniolle and Jaupart, 1986). The comparatively lower silica content present in the lava flow (than the surrounding areas) may suggest that the lava flow on the southern depression is an effusive style volcanic eruption and composed of mafic (basaltic) magma. This interpretation is also consistent with the observation that most of the martian surface is composed of basaltic materials or mafic in composition. The slope and shape of the flow features suggest that the lava flowed from the southwestern portion then downslope into the northeastern area. This flow direction is consistent with the interpretation of Michalski and Bleacher (2013) that the subtle northeast-southwest-trending depression can be evidence of sagging due to demagmatization at shallow depth. However, thermal inertia value does not completely comply with the flow feature and block materials to be a volcanic lava flow. Since volcanic lava flows are composed of competent or higher strength rock of higher thermal inertia ($\geq\sim$ 600 $Jm^{-2}K^{-1}s^{-1/2}$), the flow feature identified here has a comparatively lower thermal inertia. One potential reason for having this lower thermal inertia can be subsequent surface mantling by glacial rework, fluvial modification, and/or the dust mantling which buried the competent lava materials. However, if it is considered as a volcanic lava flow then it must be interpreted an effusive flow feature.

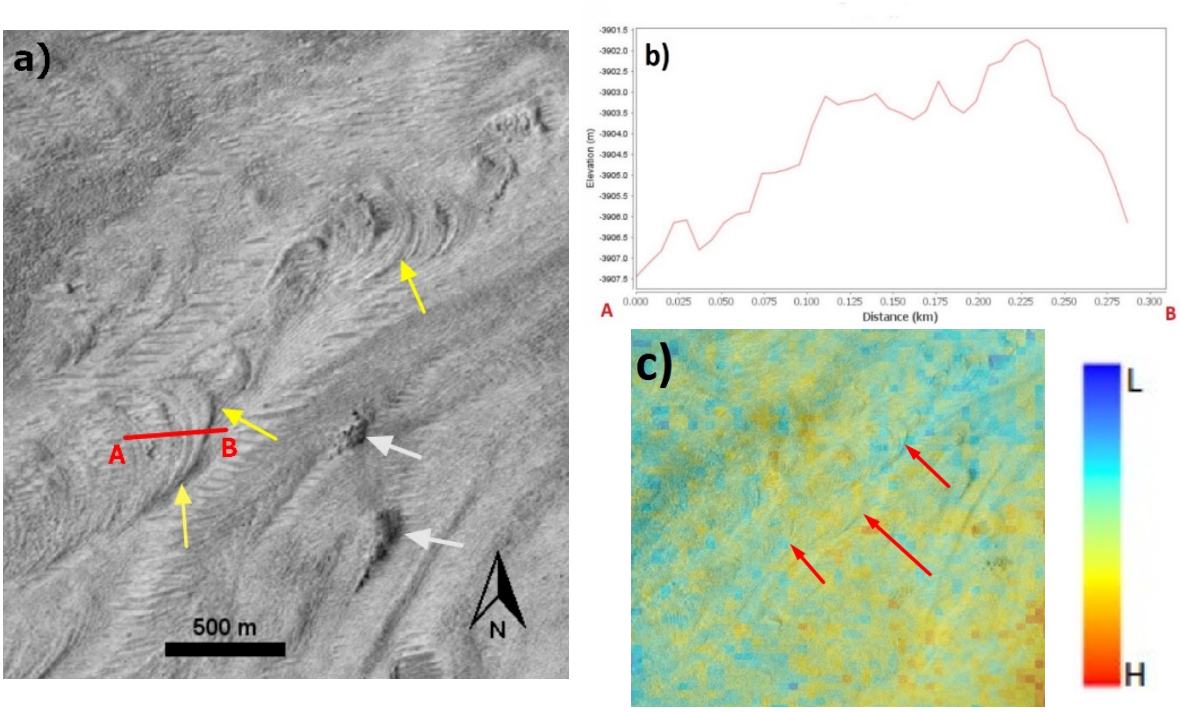

Fig. 4.16: Volcanic lava flows feature identified from a mosaic of CTX images. a) The yellow arrows indicate the flow pattern, white arrows are putative block materials, and the red is transect placed (from left to right) to extract terrain profile across the flow features. b) The terrain profile (from left to right) for the transect on a), shows that changes of elevation along the transect. c) Thermal inertia distribution on flow feature; moderately high values and the red arrows in indicating the flow pattern.

3.4.3. Boomerang lake and fresh shallow valley

The subtle northeast-southwest broadly curved depression adjacent in the southern part (named earlier as collapsed due to sagging; see the Fig 4.3) has been interpreted as "boomerang lake" with heavily dissected fresh shallow valley (FSV) system (see the figure 4.17) in the recent study of Wilson et al. (2016). They interpreted the boomerang lake and FSV to be a result of post-Noachian cold-wet environmental processes during the Hesperian-Amazonian era that has been thought active in the northern Arabia Terra region. To the north, this lake has breached the southern rim of the Siloe Patera and deposited a steep front delta (Fig. 4.17). Likewise, the boomerang lake flowed into another unnamed depression to the south and formed another small delta (Fig. 4.17d). The delta on

the Siloe Patera floor is ~1 km long from its apex to toe and possesses a steep front visible in HiRISE resolution indicating subtle layering and the delta formation implies deposition into a deep standing water body (Fig. 4.17c; Wilson et al., 2016). The depression basin itself might have held water for some time as indicated by many sinuous inflow channels cut on the southern and northern wall. Based on hydrologic models, Wilson et al. (2016) found that water filled Siloe Patera to a depth over 850 m by an overflow of the boomerang lake that incised the southern rim of the crater through a fresh shallow valley. There are variety of mechanism hypotheses proposed for the formation FSV, source of water, and related water activities including snowpack melting from volcanic heating (e.g., Fassett and Head, 2006), volcanic hydrothermal circulation (e.g., Gulick, 2001), glacio-fluvial activities (Fassett et al., 2010), and melting of snow and ice (e.g., Adeli et al., 2016; Wilson et al., 2016 and references therein). The discharge from the hundreds of meters accumulated basal ice and snow melting at the base might have triggered the formation and excavation of the FSV system in boomerang lake (Carr and Head, 2003). The formation of the valley can also be linked to impact cratering, directly or indirectly, as prior literature suggests (Wilson et al., 2016 and references therein). The impact cratering produces heating that melts the cryospheric accumulated snow and ice underneath the ejecta (e.g., Segura et al., 2002; Morgan and Head, 2009; Toon et al., 2010; Jones et al., 2011; Mangold, 2012). The formation of FSV due to groundwater seeping is less likely (Wilson et al., 2016) since thick cryospheric ice had accumulated in the Hesperian and Amazonian period (Clifford et al., 2010) that makes groundwater source to be discounted.

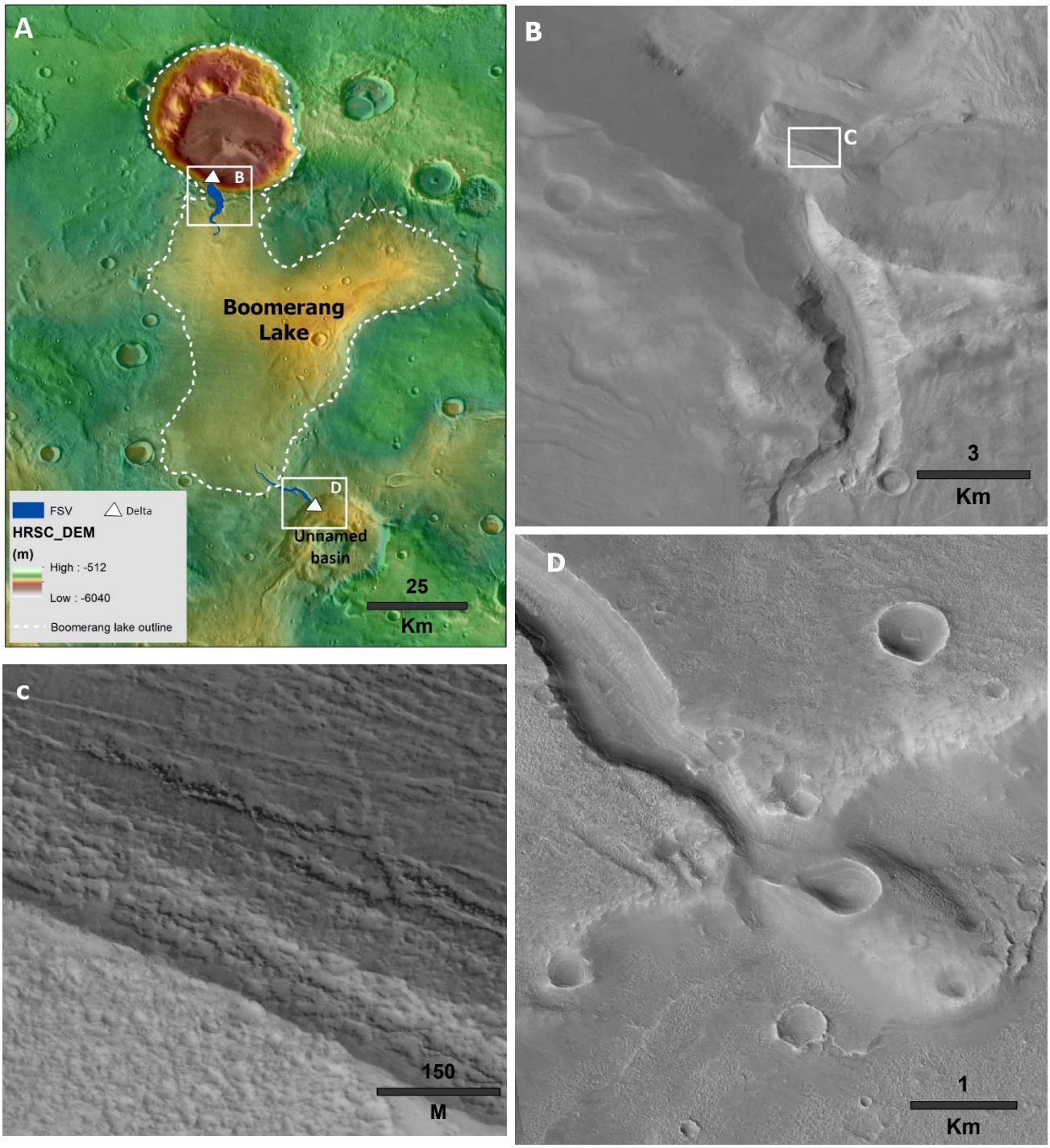

Fig. 4.17: Boomerang lake and fresh shallow valley (FSV) in the Siloe Patera area (a) in HRSC digital elevation model overlain on THEMIS daytime IR image mosaic. The boomerang lake area has a very high concentration of valley network (also see fig. 4.12b) and outflow channel (blue line) that breached into the basin of Siloe Patera in the north and into an unnamed basin in the south. The white dashed line indicates the outline of water in peak overflow of boomerang lake during the more humid condition (Wilson et al., 2016). (b) The inflowing FSV and delta deposit on the basin floor of Siloe Patera in CTX image resolution and (c) the visible subtle layers and blocks in delta front shown

in HiRISE image resolution. (d) the FSV and delta deposit are due to overflow into an unnamed basin in the south of the boomerang lake. The figure was recreated after Wilson et al. (2016).

3.4.3. Sedimentary outwash, brain terrain, and glacier landforms

Near the delta deposit, presumably emanating from the southern rim, the outwash and sedimentary plains present a gently sloping surface that is marked by numerous closely spaced rills and ridges, which appear to be water-formed features (Fig. 4.18). This sedimentary wedge has a non-distinct composition and appears to be a homogenous mixture of materials derived mainly from the southern rim feature of the southern caldera. The base of this unit has a relatively sharp contact with the caldera floor features. Some unusual textured landforms have been observed on the interior floor of Siloe Patera including concentric crater fill (CCF), lineated valley fill (LVF), and lobate debris aprons (LDA) which are collectively called brain terrains [BT] (e.g., Levy et al., 2009a; Levy et al., 2009b; Levy et al., 2010; Levy et al., 2014). These brain terrains resemble a complex morphology of small, discrete surface, like the cell of human brain structure (Fig. 4.18). Although there are few formation theories of this concentric crater fill features such as aeolian modification (Zimbelman et al., 1989) and rock-glacial process (Mangold and Allemand, 2001), these features were confidently interpreted as glacial landforms based on presence of their lineated structure and debris aprons (e.g., Levy et al., 2009b; Levy et al., 2010; Levy et al., 2014). Both closed cell (arcuate mounded cell with a flat and rounded top) and open cell (cuspate cell demarcated by ridges of the convex-up boundary) brain terrain (e.g., Levy et al., 2009b) are found in the southern depression floor. Lineated valley fill (LVF) has also seen on the southern floor along the linear to a curvilinear fault and fracture lines. Mantling from debris and dust were also seen on the floor. The northern depression floor, on the other hand, displays very smooth glacial landform surface mostly of lobate debris apron (LDA). Boulders-sized clasts on the southern depression floor indicate the rock-fall entrained on an ice-rich

zone of the rim that has been transported by glacial flow (e.g., Marchant et al., 2002; Marchant and Head, 2007; Levy et al., 2009b). These type of glacial landform features have been identified in the mid-to-high latitude martian surface and have been interpreted that the glacial processes were dominated during the late Amazonian period (e.g., Levy et al., 2014). Therefore, it is evident that recent (late Amazonian) glacial working and medication has shaped the floor of the depressions.

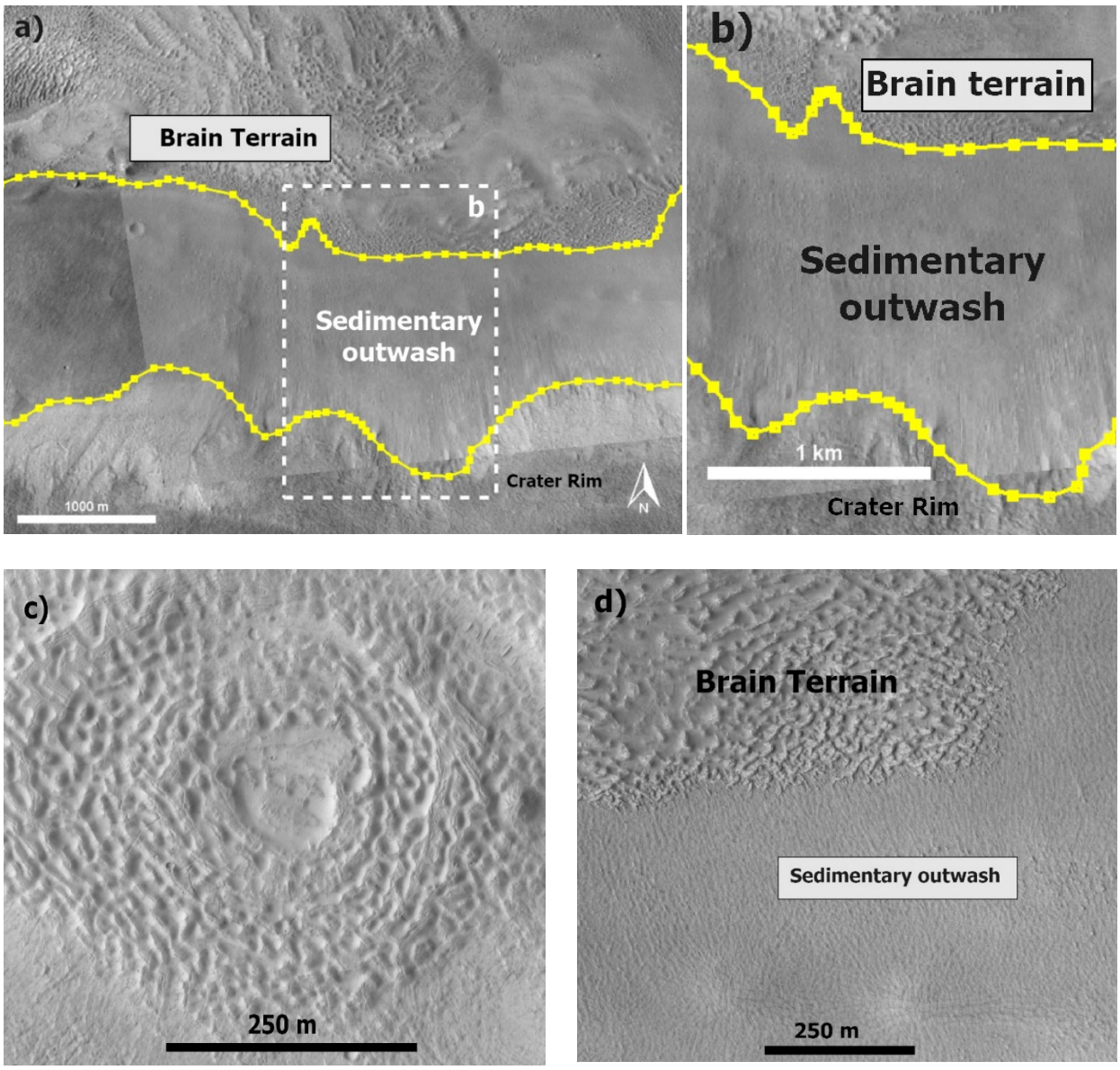

Fig. 4.18: A typical view of the sedimentary outwash feature in the southern basin depression. The feature is bounded between the crater rim and brain terrain features showed outlined with yellow

lines (a). (b) The white dashed polygons indicate the location of enlarged from (a). The feature has a gently sloping surface that is marked by numerous closely spaced rills and ridges, which appear to be sedimentary outwash features. c) The typical view of brain terrain as resembling human brain-pattern and d) shows the transition of the sedimentary outwash and the brain terrain.

3.4.3. Fractures and fault lines

Prior literature cites faults that occur in Siloe Patera along arcuate scarps (Michalski and Bleacher, 2013; Wilkes, 2014). Further, several fractures and fault lines were found on the floor or collapsed block inside the patera from HiRISE images (Fig. 4.19). The fracture/fault lines are parallel and rectilinear in some instances, and in some places, are circular. Such structures are to be expected in a caldera where there is differential subsidence of geological materials of different densities and ages, uplift and subsidence attendant with magma movements, and potential small seismic disturbances associated with volcanic activity. The morphology of all the fractures and faults suggests gravity-dominated, or normal fault movements and none suggests tectonic reverse or thrust movements, or the low-angle normal and reverse faults commonly associated with impacts. The fractures are present along with the glacier landforms e.g., brain terrain mostly on the southern depression floor. These fractures on crater fill materials are interpreted to have been formed from the brittle deformation of surface glacial ice due to gravitational stress coupled with seasonal repeated heating and cooling derived thermal stress (Mellon, 1997) as like as similar features seen on terrestrial debris cover in glacial landforms (Levy et al., 2006). Although the faults and fracture are visible in the southern depression floor, the study did not find any visible fractures or faults on the northern bench of the study area. This potentially means that the faults or fractures, if any, on northern plateau floor materials are somehow buried or mantled by debris apron. Although the rectilinear and circular faults or fractures are found on the floor of Siloe Patera, the comparative

study conducted by Garcia (2018) showed that these fractures are not consistent with the other martian volcanic features e.g., Apollinaris Mons or terrestrial calderas on Earth.

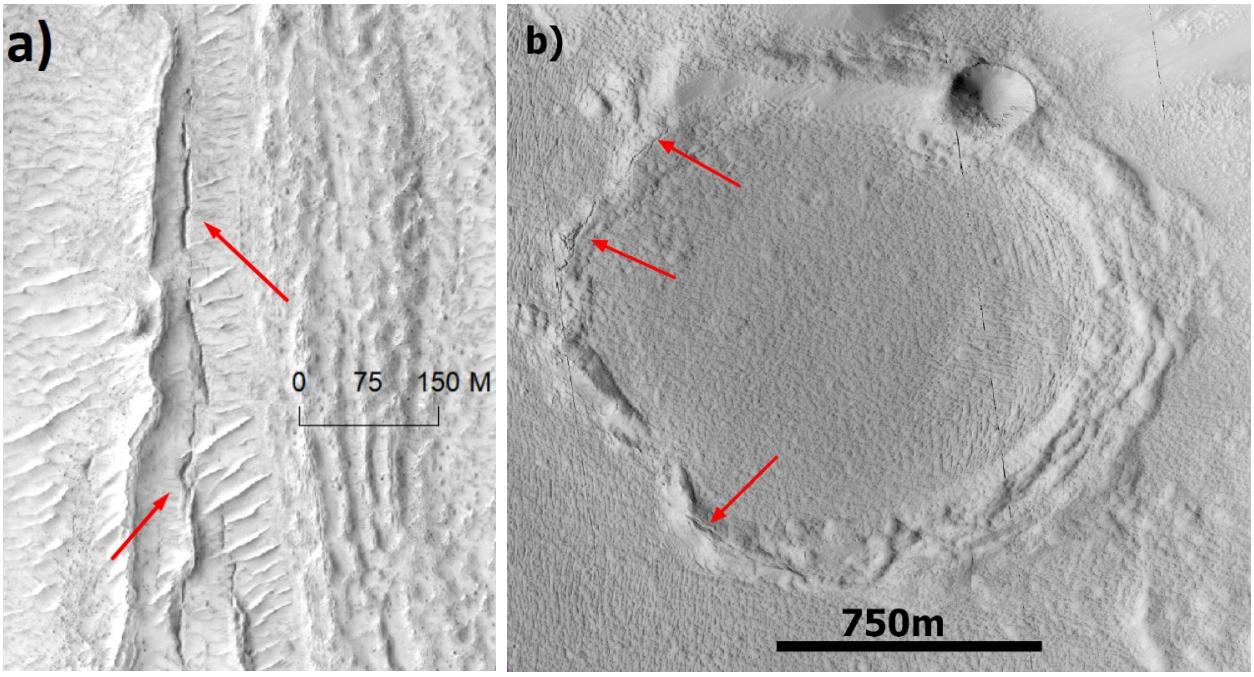

Fig. 4.19: Fractures and fault-lines as derived from a mosaic of HiRISE images. a) The red arrow indicates the parallel (a) and circular (b) traces of these fractures and faults on the caldera floor. The parallel fractures are also associated with the lineated valley fill as described in the above section.

3.4.4. Sand ripples and aeolian rework

HiRISE dataset shows numerous aeolian sand ripples on the southern edge of the spire (Fig. 4.20). These sand ripples show parallel features in meter scale, which is visible in CTX resolution (~6 m/pixel) but may be obscured in THEMIS resolution (100 m/pixel). Generally, however, it is impossible to identify these ripples from the low-resolution images. Sand ripples show dark-toned materials on CTX mosaics. DCS 8-7-5 analysis indicates ripples belong predominantly to the yellow/amber unit. WAC investigation indicates shorter wavelength absorption-consistent with

elevated silica content whereas thermal inertia indicates higher values suggesting that these sand ripples are composed possibly of fine or coarse-grained sand or dune sand materials. CRISM-NIR derived phyllosilicate D2300 appears as a weak positive signature suggesting a limited abundance of the phyllosilicates phase. The ripple profile or cross-section was extracted from surface cross-section transect across a sand ripple (Fig. 4.20b). The terrain profile shows that there are sharp changes of elevation (steep slope) along one side of the transect while the other side is gentler. The cross-section of the ripple (Fig. 4.20b) confirmed the ripple being a transverse sand ripple.

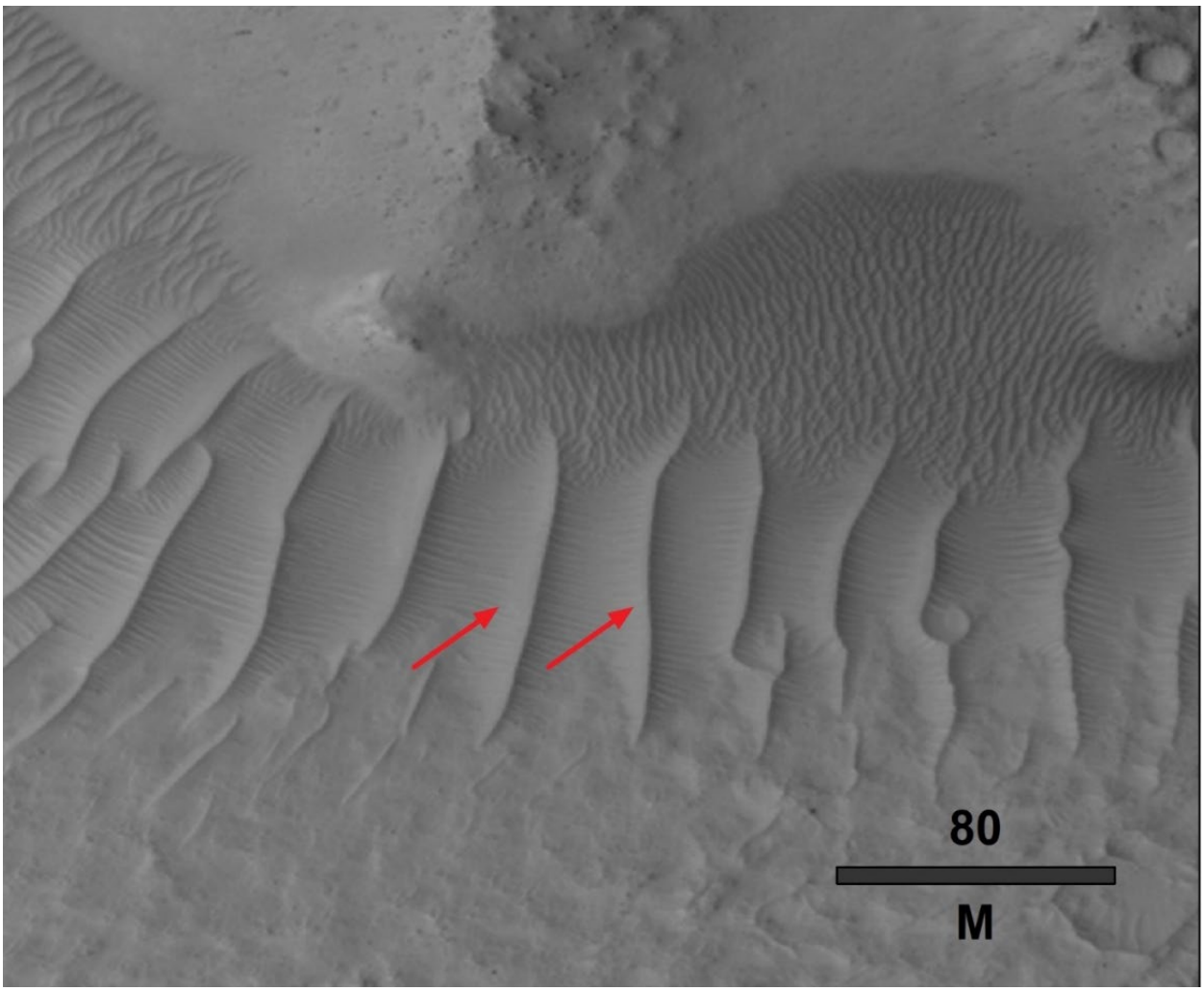

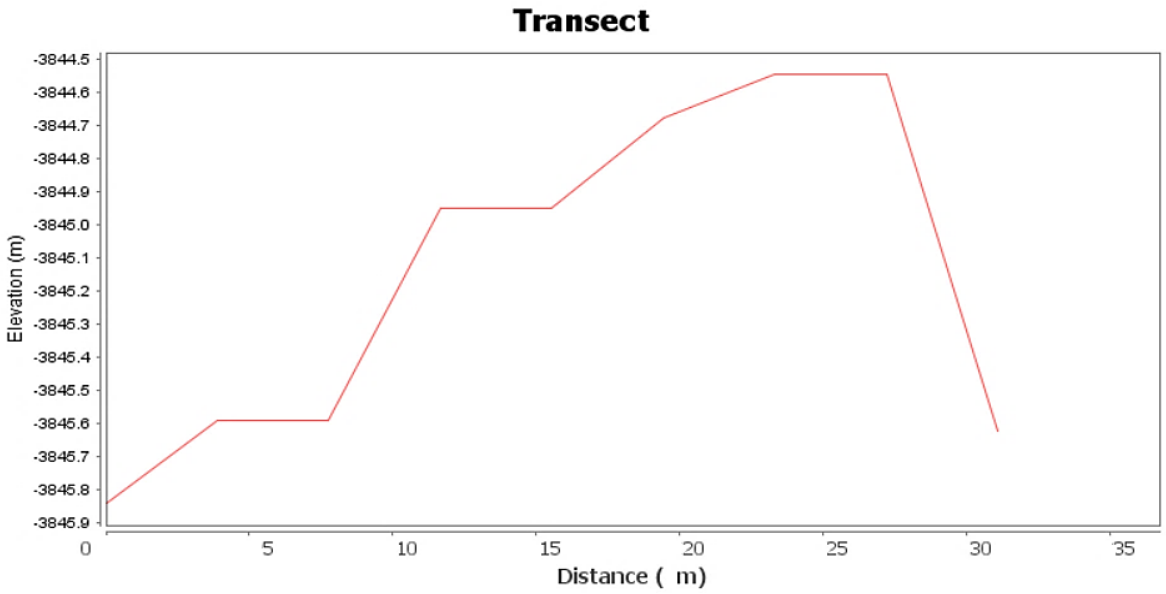

Fig. 4.20: Sand ripples at the southern floor of the basin of Siloe Patera as derived from a mosaic of HiRISE image. a) The red arrow indicates the parallel transverse ripples. b) An individual sand ripple terrain profile for the transect derived from the CTX stereo pair digital elevation models shows that changes of elevation along the transect.

4. Geological history

While the presence of wrinkle ridges in Arabia Terra, lack of typical impact signature, and size consistency with terrestrial caldera lead Siloe Patera to be a possible volcanic construct (Michalski and Bleacher, 2013), these characteristics are not unique to volcanic calderas solely (Garcia, 2018). Wrinkle ridges are a common physiographic feature found in a variety of terrestrial features e.g., faulted layered materials resulting from the deformation of shallow thrust fault (e.g., Plescia and Golombek, 1986) and identified to be in many similar sized i.e., depth-to-diameter ratios impact craters in Arabia Terra region (Garcia, 2018). Moreover, the lack of discernable volcanic edifice and presence of other similar collapsed features e.g., chaos terrains and concentric fracturing feature in Arabia Terra region question the Siloe Patera to be a supervolcanic origin. The lobate feature emaciating from the southwestern rim which was thought to be lava flow or pyroclastic deposits (Michalski and Bleacher, 2013), alternatively this feature can be altered impact ejecta. The study

posits that this lobate flow is the impact crater ejecta of Siloe Patera (Fig. 4.11). This feature spreads in a single direction and interpreted as multiple layered, rampart, and sinuous ejecta (MLERS; Robbins and Hynek, 2012a). Like Siloe Patera, many of other designated impact craters in Arabia Terra do not also have impact crater related preserved morphological signatures of the well preserved raised rim, central peak, and/or ejecta blanket. Although the comparatively lower thermal inertia values are consistent with the lower thermal inertia characteristics of the other volcanic feature on Mars e.g., Apollinaris Mons (Garcia, 2018), the same level topography including shallow rim height of Siloe Patera to the surrounding areas and lack of a positive visible edifice disagree it to be a supervolcanic explosive caldera. A concentric ring fracture is thought to be an ideal characteristic feature (although not unique for volcanic caldera but present around some of the proposed caldera in Arabia Terra), Siloe Patera does not have any of such concentric ring fractures visible in either of THEMIS, CTX, or HiRISE data. This lack of concentric ring fracture also goes against Siloe Patera to be originated as a supervolcanic feature. In denying being a potential thermokarst like other well-known martian thermokarsts (Soare et al., 2008), Siloe Patera has been interpreted resemble as terrestrial supervolcano of similar scale and morphology (Michalski and Bleacher, 2013). However, the well-known martian explosive volcanoes preserve edifice structure (e.g., Hynek and Phillips, 2001) as many terrestrial supervolcanoes do (e.g., Tizzani et al., 2007; Chesner, 2012; Delgado and Pavez, 2015), Siloe Patera lacks discernable edifice in its structure. Consequently, it is reasonable to suspect that Siloe Patera may initially have formed as an impact crater undergone with subsequent collapse and modification i.e., resurfacing and denudation to be considered it as a degraded impact crater. The rationale behind degraded impact crater hypothesis is that early Mars had a humid environment with significant surface runoff (e.g., Hynek and Phillips, 2001; Zabrusky et al., 2012; Davis et al., 2016) which can modify an impact crater at substantial levels that typical crater rims and peaks can be eroded, ejecta signature can be erased, and ultimately

the crater landform can be infilled by deposition (e.g., Craddock et al., 1997; Craddock et al., 2018). A morphometric comparison (diameter verses rim-floor depth) between the caldera constructs of Arabia Terra (including Siloe Patera), other modified martian craters, and martian dewatering style depressions were performed by Garcia (2018; see the original literature for detail). Her study shows that the anomaly of higher depth-to-diameter ratios for Siloe Patera caldera can be resulting from post-impact collapse and found that Siloe Patera (along with other proposed calderas in Arabia Terra) has likely the morphologies of modified impact craters. Moreover, the higher depth-to-diameter of Siloe Patera is consistent with the results of Robbins and Hynek (2012b). Their study was based on the global crater database for martian impact craters with D ≥1 km (Robbins and Hynek, 2012a) and showed that both fresh (class type 4) and modified craters (class type 1 through 3) of Mars display high depth-to-diameter ratios. Although the caldera does not have a discernable raised rim; the crater database study of Robbins and Hynek (2012a) identified a set of nested impact craters having a level of 100's of meters of rim height. The present study also extracted elevation profile of rim (across the depression) on different sides. The elevation profile cross-sections extracted from HRSC MOLA blended 200m DEM show that the rim of depression has height values of ~100's meters from the sounding topography (Fig. 4.13) consistent to degraded craters. Although Michalski and Bleacher (2013) hypothesized that Siloe Patera should lack a rim to designate it as a supervolcanic caldera, the result of this study does not agree since the present study did find a shallow rim of the feature. Moreover, a recent study (Brugman, 2014) comparing the rim-floor depth to diameter of similar-sized craters showed that the depth of Siloe Patera is not consistently deeper than the other craters and found inconsistent with the caldera hypothesis of Michalski and Bleacher (2013). Noting here, a morphometric analysis of 264 fresh and 186 modified impact carters (from the highland) of ~3 to 76 km in diameters were mapped by Craddock et al. (1997) using photoclinometric algorithm of Davis and Soderblom (1984). The crater profiles

extracted by Craddock et al. (1997) were then compared to the computer-simulated drainage basin model developed by Howard (1994). The simulated morphology for 40 km diameter crater, analog to Siloe Patera, shows that with the progression of modification the crater reaches in a stage where the rim become rounded with a very minimum height difference from the surrounding area (Craddock et al., 2018). This simulated result of similar size crater is consistent with the Siloe Patera and suggest that it is a degraded impact crater. Based on the findings, Garcia (2018) suggested that the depth observed at the northern plateau (level of irregular mounts) is to be the original depth of the crater whereas the maximum depth at the southern floor reflects modified depth from a post-collapse activity that formed the southern depression. Brugman (2014) calculated the slightly higher depth-to-diameter ratio (d/D = 0.066) of Siloe Patera considering the diameter (d = 26.3 km) and depth of southern collapse (D = ~1700 m). However, in this study, the northern plateau level was considered as the original depth (D = ~1000 m) and diameters (d = ~35 km) result in a depth-to-diameter ratio (d/D = ~0.028) consistent to similar-sized moderately altered crater's depth diameter ratio (d/D = 0.032; Brugman, 2014). As mentioned earlier, Siloe Patera still preserves impact ejecta (though altered in some extent) spreading single-direction (unidirectional) from the south-western rim that is interpreted as multilayer rampart sinuous ejecta [MLERS] (e.g., Robbins and Hynek, 2012a) resulting from a low-angle impact to the target surface. A similar type of multilayer, prominently unidirectional, and rampart-sinuous (MLERS) ejecta (with hummocky broad lobes and slump deposits) is also seen for another adjacent complex impact crater (centered 31.92°N and 6.18°E) located just 160 km south of Siloe Patera (Robbins and Hynek, 2012a; Garcia, 2018). It is also possible that, if any, Siloe Patera had a rampart butterfly ejecta blanket from the same impact origin on the opposite side of the lobate deposit of the depression which might have been erased or obscured by subsequent impact and modification (Garcia, 2018). Thus, this evidence supports that Siloe Patera could be a degraded impact crater that experienced with subsequent modification and

post-collapse event. The present study hypothesizes that Siloe Patera has formed as an impact crater with the original depth correspond to the base of northern plateau and then experienced an interior collapse in southern depression as evident by the higher depth-to-diameter ratio of southern depression (uncommon to many typical impact craters), regional north-south slope, and present of subtle northeast-southwest (NE-SW) trending depression in southern part.

It is possible that the southern collapsed depression can be formed by demagmatization of underneath lava, removal and melting of cryospheric ice and/or combination of both. This study did not find any visible lava vent or fissure in the structure (in either THEMIS, CTX, or HiRISE resolution) except possible flow features and possible block materials on the southern depression. The lower thermal inertia values in flow feature (Fig. 4.16) cast doubt about their volcanic origin since volcanic materials are composed of competent rocks and block materials with higher thermal inertia values. However, it is possible that the lava flow has been originated as fissure lava from some fault along the rim and floor intersection. The fissure of the lava flow may have been buried by subsequent material deposits, modification by fluvial and/or glacial rework, or obscured by dust mantling whereas the lower thermal inertia also resulted from subsequent fluvial/glacial modifications to original competent volcanic rock or dust mantling. However, if these flow features were originated by volcanic activities, the lava flow was effusive type (as evident from the nature of the possible flow feature), not an explosive supervolcanic eruption. Considering these uncertain volcanic signatures, this study searched for an alternative formation mechanism e.g., alike a thermokarsts structure by ice removal or accumulated subsurface snow and ice melting. To test ice removal (and melting) as the possible cause of southern collapse depressions (both interior and NE-SW tending collapse or boomerang lake) the study calculated the volume of depressions and the volume of pore space correspond to amount of total void space that can be filled with cryospheric

ice (Fig. 4.3). Since the study considered the base of the northern plateau to be the floor of the impact crater, the contour line -3200m was fixed as the reference plane for the interior southern depression whereas the -2400m contour line was considered as reference plane line for rest of the other depressions. The southern collapse depressions (including boomerang lake) have an area of ~11,000 km^2 and a depression volume of ~2,500 km^3. The calculated total void space underneath the southern collapse depressions is ~10,000 km^3 (Fig. 4.21). The result, thus, showed there is a plethora of void space underneath the southern depression so that the cryospheric ice removal and subsurface ice melting can be a potential cause for the depressions to form like a thermokarst feature. Figure 4.21 indicates porosity declines as a function of depth on Mars according to equations described by Clifford (1993) and the volume of cryospheric subsurface ice as increasing the depth from the surface. The study also tested the total volume of ice that could have been removed for the entire collapse including both north and south interior collapse and the NE-SE tending collapse (boomerang lake). The total collapse depressions have an area of ~12500 km^2 and a depression volume of ~9000 km^3. The calculated total void space underneath the total collapse depressions is ~12,000 km^3. However, the entire depression has unlikely been formed by ice removal and since pieces of evidence showed that the northern depression has possibly formed by impact cratering, this study discounts that the entire Siloe Patera has formed by collapse event.

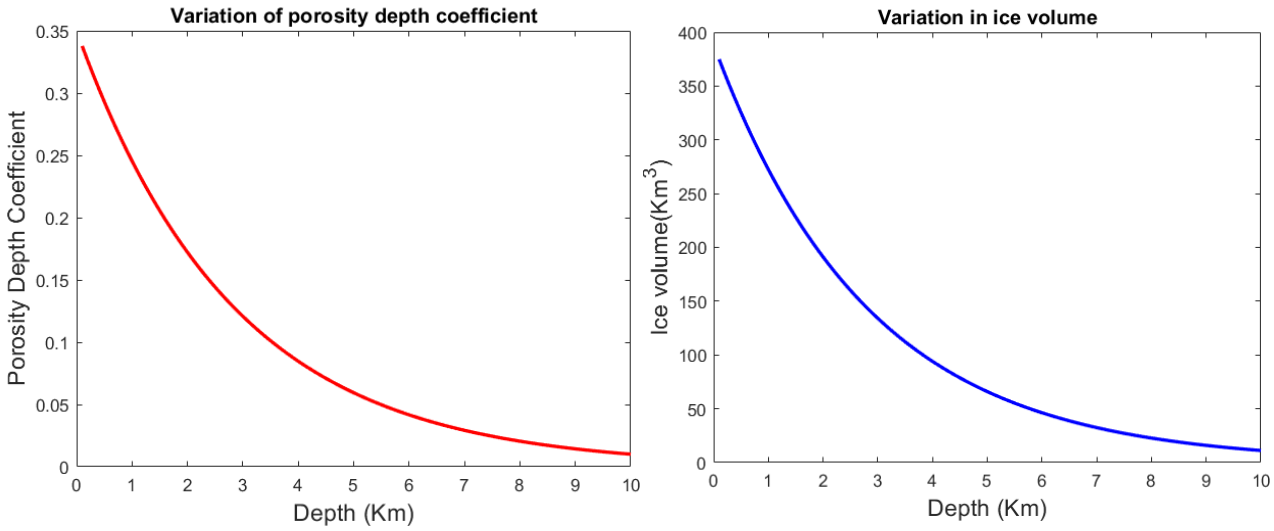

Fig. 4.21: The martian subsurface void space was calculated as porosity declines as a function of depth according to equations described by Clifford (1993) (a). The study calculated a surface area over the southern depressions around ~11,100 km^2. The cumulative maximum volume of cryospheric ice content was calculated as a function of depth assuming that all the subsurface void spaces are entirely filled with ice or snow (b). The total volume of ice volume was calculated considering a certain number of equal depth stake layers (i.e., 100) from the surface up to 10 km (b). The figure was recreated after Michalski and Bleacher (2013).

The polygonal mounts (irregular) on the northern plateau of the caldera interior floor were suggested as pyroclastic deposits from the volcano (Michalski and Bleacher, 2013) or consistent to the fracture fault block like the dewatering collapsed at the Circum-Chryse Planitia region of Mars and periglacial surface modification (Garcia, 2018). Since the study rules out Siloe Patera as a supervolcanic caldera, this study discounts that the hummocky terrain result from the caldera formation itself and rather that these are deposits of another origin. Though the hummocky terrains could be resulting from subsequent peri-glacial surface reworking after impact cratering; the presence of the possible flow feature and block materials in the southern depression (Fig. 4.14) indicate volcanic activities. The lava might have flowed from the southwestern portion of the rim (possibly as fissure flow along possible faults or fractures in curvature between rim and floor) to the downslope into the northeastern area. Thus, the possible volcanic flow feature and the subtle

northeast-southwest (NE-SW) trending depression that holds boomerang lake and FSV system cast doubt on the process of dewatering as the potential cause for the collapse event. Moreover, the dewatering associated features commonly possess large outflow channels (e.g., Michalski and Bleacher, 2013), chaos terrain, interior terraces, polygonally fractured floor, and an array of fractured polygonal collapse features seen in well-known dewatering features in the Chryse region of Mars (e.g., Sharp, 1973; Chapman and Tanaka, 2002; Glotch and Christensen, 2005; Rodriguez et al., 2005; Meresse et al., 2008; Roda et al., 2016). Albeit having the volume of depressions very consistent of the martian dewatering features, Siloe Patera (unlike other proposed caldera e.g., Eden Patera) lacks outflow channels (Michalski and Bleacher, 2013), chaos terrain, interior terraces, and fretted terrains within the depression which made it inconsistent to the typical well-known martian dewatering features. This study, therefore, rules out the dewatering process as a potential cause of formation. Considering the presence of all evidence, the study emphasizes that ice-removal, due to accumulated subsurface snow and ice melting due to volcanic heating that formed the boomerang lake and FSV system, is the potential cause of collapse with a possibility in conjunction with magma migration at shallow depth resulting effusive lava flow and volcanic heating. Siloe Patera by itself might have held water for some time as indicated by many sinuous fresh shallow inflow channels cut on the southern, northeastern, northwestern, and northern wall due to the melting of subsurface ice. The subtle NE-SW-trending depression can also be considered as evidence of sagging due to demagmatization at shallow depth responsible for the collapse and resulted in an effusive type lava flow. Thus, this study hypothesizes that the collapse feature has initiated with demagmatization at shallow depth resulting effusive surface lava flow and consequent volcanic heating that melted the accumulated subsurface snow and ice further strengthen the collapsed event and subsequently formed the boomerang lake and FSV system during the Hesperian-Amazonian periods. The present study also acknowledges that episodic impact cratering (as presence both on the southern basin and

the floor of boomerang lake) during Hesperian and Amazonian periods might have also triggered the subsurface ice melting through heating from the impact crater. As the ice melting continued water had accumulated in the boomerang lake and southern basin of Siloe Patera. The overflow of ice melted water through the fresh shallow valleys from the boomerang lake and breached into the basin of Siloe Patera in the north and another unnamed basin in the south formed deltaic deposits in the deep basins of standing water. The sedimentary outwash has formed due to water reworking in Siloe Patera. The collapse event is further strengthened by the presence of possible faults and fractures (Michalski and Bleacher, 2013). If these had formed during collapse event, it can be due to partial surface collapse or potential small seismic disturbances associated with volcanic activity and/or ice removal on the southern depressions. Alternatively, the fractures on crater fill materials (Fig. 4.19) are interpreted to have been formed from the brittle deformation of surface glacial ice due to gravitational stress coupled with seasonal repeated heating and cooling derived thermal stress (Mellon, 1997) as similar features seen on terrestrial debris cover in glacial landforms (Levy et al., 2006). The lower elevation surface surrounding hummocky surface in northern plateau displays a relatively smooth surface while the floor of southern depression has a rougher surface with possible flow features, block materials, and prominent linear to curvilinear ridges, fractures, and linear shallow valley-like features indicating distinct geological processes involved (Fig. 14). While it can be peri-glacier melt responsible for the hummocky terrain and smooth surface on the northern plateau, the presence of deep depressions, possible effusive flow features and block materials, and subtle northeast-southwest-trending depression consistent to water in boomerang lake and FSV system from accumulated ice melting, this study reinterprets that the southern depression has formed by a collapse event. The evidence of discontinuous linear ridges and crater fill, and lobate debris apron, collectively named brain terrain, on interior floor strengthen surface modification after the collapse (e.g., Michalski and Bleacher, 2013; Garcia, 2018) in the late Amazonian period. A similar type of

discontinuous linear ridges features and brain-terrain investigated at the martian mid-to-high latitudes was interpreted as formation and modification by a combination of glacial and thermal-contraction cracking in late Amazonian period (Levy et al., 2009b).

The spire in the floor of the southern depression (formed by slumping of rim materials due to collapse event) consists of broken multiple disconnected parts: one isolated mount and another elongated mount. The subsequent modifications after the collapse are inferred from the presence of disconnected mounts within the southern interior portion of the depression. Although isolated mounts can be found on the floor of an impact crater (e.g., Smith, 1976), the isolated mount, in this case, does not sufficiently prove that the southern depression has formed due to meteorite impacts. Dust mantling of surface and the subsequent medication by fluvial and glacial rework could be a potential reason for having lower thermal inertia values consistent with poorly consolidated materials of the flow feature on the floor. The study, therefore, hypothesizes that southern flow features are from the result of the effusive lava flows during collapse event due to demagmatization in shallow depth that had been experienced with subsequent glacial modification. A reasonable question may be where the vent of the effusive lava flow is? The study hypotheses that the vent of effusive flow has been altered, erased, and/or obscured by subsequent modifications by glacial reworking during late Amazonian periods as evident from the presence of brain terrains. This subsequent glacial or ice-related modification and reworking are consistent with prior literature indicating that the martian middle and high latitude have been shaped substantially by glacial processes during late Amazonian epoch (e.g., Mustard et al., 2001; Kreslavsky and Head, 2002; Head et al., 2003; Kuzmin, 2005; Head et al., 2006; Forget et al., 2006; Fastook and Head, 2008; Head and Marchant, 2009; Levy et al., 2009b). The study acknowledges that the layered and friable deposits in Arabia Terra can be sourced from pyroclastic explosive volcanic activities (Michalski and Bleacher,

2013) that dominated in the earlier history of Mars (Reimers and Komar, 1979). Noteworthy here, based on the findings of thermophysical and morphological properties the study of Bandfield et al. (2013) showed that the older regions of martian surface are composed of poorly consolidated fine-grained materials of volcanoclastic origin whereas the younger surface is dominated with blocky materials and effusive lava flow. This implies that early Mars was dominated by the explosive volcanism which has undergone subsequent modification by other geologic processes (e.g., Bandfield et al., 2013). The friable materials on the other martian volcanic caldera are pre-dated from the recent effusive type large shield volcanos e.g., Tharsis and Elysium (Robbins et al., 2011). Robbins et al. (2011) interpret that the transition of pyroclastic deposits from explosive volcanism to effusive lava flow occurred during the Hesperian era around ~3.2 to 3.5 Ga. It is clear, thus, that the earlier martian volcanic activities are explosive in style followed by the comparatively recent (Hesperian-Amazonian) dominance of effusive lava flow (e.g., Reimers and Komar, 1979; Robbins et al., 2011). A consistent lower thermal inertia in the study area support that the friable layered deposit in Arabia Terra region might have been sourced from the explosive volcanism of earlier martian history. However, this study is concerned with whether Siloe Patera is a potential source of this pyroclastic materials in Arabia Terra i.e., the feature is supervolcanic caldera or not. Based on above discussions, it can be interpreted that Siloe Patera is not a supervolcanic caldera construct (rather a degraded impact carter) though it may have experienced effusive lava flow subsequently as evident from the presence of possible flow features, putative block materials, and northeast-southwest-trending depression on the southern depression floor. Siloe Patera has experienced a collapse event through subsurface ice melting due to volcanic heating and episodic impact cratering followed by a comparatively recent glacial modification. The interpretation of this study is consistent with the prior literature that indicated the Arabia Terra region contains both pyroclastic deposits and effusive lava flows (e.g., Mouginis-Mark et al., 1988; Fergason and Christensen, 2008; Robbins et al.,

2011), valley systems and fluvial activities in the Hesperian-Amazonian periods (e.g., Wilson et al., 2016), and recent late Amazonian glacial modification and reworking to shape martian mid-latitude (e.g., Mustard et al., 2001; Kreslavsky and Head, 2002; Head et al., 2003; Kuzmin, 2005; Head et al., 2006; Forget et al., 2006; Fastook and Head, 2008; Head and Marchant, 2009; Levy et al., 2009b).

The study can now lay out some of the main details of the geological history of Siloe Patera, even though the precise timing of events is not entirely clear. The late Noachian to early Hesperian feature at Siloe Patera formed first as an impact crater, which later may have been modified by the Noachian-Hesperian fluvial activities and/or the periglacial reworking. The southern caldera depression developed subsequently like thermokarst features, experienced collapse through subsurface ice-removal and melting forming boomerang lake and FSV system due to possibility with demagmatization at a shallow depth that produced effusive volcanic lava flow and volcanic heating (in the Hesperian or Amazonian epoch). The overflow of the boomerang lake has produced a delta on the basin of southern depression. Following the formation of Siloe Patera, the depression complex held water for some time, as indicated by many sinuous inflow channels cut on the southern and northern wall (may be experienced with glacial melt) and also water flowed into the depression through the fresh shallow valley of boomerang lake. Followed by a collapse event the depressions had experienced a glacial reworking during the late Amazonian period. A central spire formed during southern caldera collapse. Later, sand ripples developed on the southern caldera floor, and there have been a few small cratering events near and within Siloe Patera.

5. Summary and conclusion

The present study has analyzed surficial geology, including possible geologic history, of Siloe Patera at Arabia Terra by combining an analysis of spectral units, elevated bulk-silica content, mosaics of nighttime and daytime IR, and thermal inertia characteristics using THEMIS-TIR. Mineralogy of olivine, phyllosilicate, and hydrated silicates phases were identified using CRISM-NIR, whereas local geologic features were interpreted from CTX and HiRISE data. There are four different spectral units: the purple unit, fuchsia/magenta unit, yellow/amber unit, and pale-brown or green (typical terrain) unit, which are typical of the study:

Purple unit: Olivine-bearing unit on eastern and northeastern rims and scarps has WAC absorption to longer wavelength, consistent to lower silica content, has comparatively "higher" (than other identified units in the study area) thermal inertia indicating weakly indurated materials, and NIR index confirms the presence of olivine phase.

Fuchsia unit: This unit covers part of the southwestern rim and scarp and adjacent caldera floor. This unit has alternate WAC absorption to longer wavelength together with a shorter wavelength, consistent to lower silica content in most of the unit, but, spatially co-located with higher silica content in limited areas. This unit has "higher" thermal inertia (comparing the identified units in the study area) indicating surface materials like the purple unit, and NIR index confirms the presence of the olivine-rich surface.

Yellow/amber unit: This unit covers the caldera floor of southern depression near the south-central high area (the spire), and has WAC absorption to shorter wavelength, which is consistent with elevated silica content. This unit includes the transverse ripple on the edge of central peak, whose thermal inertia indicating the presence of fine-grained sands (including ripple sands). This unit has weak signatures for the phyllosilicate index.

Pale brown/green (typical terrain) unit: This unit is a washed-out or widely deposited material on most of the floor surface and northwestern rim and scarp of this patera. This unit has WAC absorption in a shorter wavelength, consistent to elevated silica content, and lower thermal inertia suggesting fine grain dust, positive abortion to phyllosilicate index, as well in some areas it has hydrated phyllosilicate phase, spatially adjacent to the network of channels and gullies.

In line with the overall finding of this study, after forming as an impact crater possibly in the late Noachian to early Hesperian epoch and subsequent fluvial and/or periglacial modification, Siloe Patera experienced a collapse event due to subsurface accumulated ice melting and removal due to volcanic heating from younger effusive lava-flow and possible episodic impact cratering during the Hesperian-Amazonian periods. Subsequently, boomerang lake has formed, and an overflow of the lake produced deltaic deposits on the southern basin of Siloe Patera. The depression also has gone through sedimentary outwash formation and later the floor of the depression experienced glacial reworking in the late Amazonian period. Therefore, the weight of evidence tends to confirm that Siloe Patera is formed initially as an impact crater and then later stages of collapse event.

Acknowledgments

The author would like to thank the team members of 2001 Mars Odyssey and Mars Reconnaissance Orbiter (MRO) spacecraft missions for targeting, collecting, and archiving THEMIS, CRISM, CTX, and HiRISE datasets used in the present study. JMARS, ISIS3, Ames Stereo Pipelines (ASP), Davinci, GDAL, THMPROC, MARSTHERM, ENVI, ArcGIS, and QGIS software/tools were used for data processing and analysis. Special thanks to the team of Arizona State University's Mars Space Flight Facility. The authors are also grateful to Dr. Mark R. Salvatore and Dr. Joshua L. Bandfield for providing useful information on data processing. Finally, we would like to thank the anonymous reviewer(s) for the critical review of this paper.

References

Achille, G.D., Hynek, B.M., 2010. Ancient ocean on Mars supported by global distribution of deltas and valleys. Nature Geoscience 3, 459–463. https://doi.org/10.1038/ngeo891

Adeli, S., Hauber, E., Kleinhans, M., Le Deit, L., Platz, T., Fawdon, P., Jaumann, R., 2016. Amazonian-aged fluvial system and associated ice-related features in Terra Cimmeria, Mars. Icarus 277, 286–299. https://doi.org/10.1016/j.icarus.2016.05.020

Amador, E.S., Bandfield, J.L., 2016. Elevated bulk-silica exposures and evidence for multiple aqueous alteration episodes in Nili Fossae, Mars. Icarus 276, 39–51. https://doi.org/10.1016/j.icarus.2016.04.015

Anguita, F., Anguita, J., Castilla, G., Casa, M.-A.D.L., Domínguez, J.-M., Herrera, R., Llanes, P., López, M., Martínez, V., 1997. Arabia Terra, Mars: Tectonic and Palaeoclimatic Evolution of a Remarkable Sector of Martian Lithosphere. Earth, Moon, and Planets 77, 55–72. https://doi.org/10.1023/A:1006143106970

Baird, A.K., Toulmin, P., Clark, B.C., Rose, H.J., Keil, K., Christian, R.P., Gooding, J.L., 1976. Mineralogic and Petrologic Implications of Viking Geochemical Results From Mars: Interim Report. Science 194, 1288–1293. https://doi.org/10.1126/science.194.4271.1288

Bandfield, J.L., 2002. Global mineral distributions on Mars. Journal of Geophysical Research: Planets 107, 9-1-9–20. https://doi.org/10.1029/2001JE001510

Bandfield, J.L., Edwards, C.S., Montgomery, D.R., Brand, B.D., 2013. The dual nature of the martian crust: Young lavas and old clastic materials. Icarus 222, 188–199. https://doi.org/10.1016/j.icarus.2012.10.023

Bandfield, J.L., Hamilton, V.E., Christensen, P.R., McSween, H.Y., 2004a. Identification of quartzofeldspathic materials on Mars. Journal of Geophysical Research: Planets 109. https://doi.org/10.1029/2004JE002290

Bandfield, J.L., Rogers, D., Smith, M.D., Christensen, P.R., 2004b. Atmospheric correction and surface spectral unit mapping using Thermal Emission Imaging System data. Journal of Geophysical Research: Planets 109. https://doi.org/10.1029/2004JE002289

Barlow, N.G., Bradley, T.L., 1990. Martian impact craters: Correlations of ejecta and interior morphologies with diameter, latitude, and terrain. Icarus 87, 156–179. https://doi.org/10.1016/0019-1035(90)90026-6

Beyer, R.A., Alexandrov, O., Moratto, Z.M., 2014. Aligning Terrain Model and Laser Altimeter Point Clouds with the Ames Stereo Pipeline. Presented at the Lunar and Planetary Science Conference, p. 2902.

Broxton, M.J., Edwards, L.J., 2008. The Ames Stereo Pipeline: Automated 3D Surface Reconstruction from Orbital Imagery. Presented at the Lunar and Planetary Science Conference, p. 2419.

Brugman, K., 2014. Understanding the History of Arabia Terra, Mars Through Crater-Based Tests. Undergraduate Honors Theses. University of Colorado Boulder.

Carr, M.H., 1973. Volcanism on Mars. Journal of Geophysical Research (1896-1977) 78, 4049–4062. https://doi.org/10.1029/JB078i020p04049

Carr, M.H., 1986. Mars: A water-rich planet? Icarus 68, 187–216. https://doi.org/10.1016/0019-1035(86)90019-9

Carr, M.H., 2007. The Surface of Mars. Cambridge University Press. Cambridge

Carr, M.H., Head, J.W., 2003. Basal melting of snow on early Mars: A possible origin of some valley networks. Geophysical Research Letters 30. https://doi.org/10.1029/2003GL018575

Chapman, M.G., Tanaka, K.L., 2002. Related Magma–Ice Interactions: Possible Origins of Chasmata, Chaos, and Surface Materials in Xanthe, Margaritifer, and Meridiani Terrae, Mars. Icarus 155, 324–339. https://doi.org/10.1006/icar.2001.6735

Chesner, C.A., 2012. The Toba Caldera Complex. Quaternary International, The Toba Volcanic Super-eruption of 74,000 Years Ago: Climate Change, Environments, and Evolving Humans 258, 5–18. https://doi.org/10.1016/j.quaint.2011.09.025

Christensen, P.R., Bandfield, J.L., Hamilton, V.E., Ruff, S.W., Kieffer, H.H., Titus, T.N., Malin, M.C., Morris, R.V., Lane, M.D., Clark, R.L., Jakosky, B.M., Mellon, M.T., Pearl, J.C., Conrath, B.J., Smith, M.D., Clancy, R.T., Kuzmin, R.O., Roush, T., Mehall, G.L., Gorelick, N., Bender, K., Murray, K., Dason, S., Greene, E., Silverman, S., Greenfield, M., 2001. Mars Global Surveyor Thermal Emission Spectrometer experiment: Investigation description and surface science results. Journal of Geophysical Research: Planets 106, 23823–23871. https://doi.org/10.1029/2000JE001370

Christensen, P.R., Engle, E., Anwar, S., Dickenshied, S., Noss, D., Gorelick, N., Weiss-Malik, M., 2009. JMARS - A Planetary GIS. AGU Fall Meeting Abstracts 22, IN22A-06.

Christensen, P.R., Jakosky, B.M., Kieffer, H.H., Malin, M.C., McSween, H.Y., Nealson, K., Mehall, G.L., Silverman, S.H., Ferry, S., Caplinger, M., Ravine, M., 2004. The Thermal Emission Imaging System (THEMIS) for the Mars 2001 Odyssey Mission. Space Science Reviews 110, 85–130. https://doi.org/10.1023/B:SPAC.0000021008.16305.94

Clifford, S.M., 1993. A model for the hydrologic and climatic behavior of water on Mars. Journal of Geophysical Research: Planets 98, 10973–11016. https://doi.org/10.1029/93JE00225

Clifford, S.M., Lasue, J., Heggy, E., Boisson, J., McGovern, P., Max, M.D., 2010. Depth of the Martian cryosphere: Revised estimates and implications for the existence and detection of subpermafrost groundwater. Journal of Geophysical Research (Planets) 115, E07001. https://doi.org/10.1029/2009JE003462

Craddock, R.A., Bandeira, L., Howard, A.D., 2018. An Assessment of Regional Variations in Martian Modified Impact Crater Morphology. Journal of Geophysical Research: Planets 123, 763–779. https://doi.org/10.1002/2017JE005412

Craddock, R.A., Maxwell, T.A., 2012. Resurfacing of the Martian Highlands in the Amenthes and Tyrrhena region. Journal of Geophysical Research: Solid Earth 14265–14278. https://doi.org/10.1029/JB095iB09p14265@10.1002/(ISSN)2169-9356.MARS4

Craddock, R.A., Maxwell, T.A., Howard, A.D., 1997. Crater morphometry and modification in the Sinus Sabaeus and Margaritifer Sinus regions of Mars. Journal of Geophysical Research: Planets 102, 13321–13340. https://doi.org/10.1029/97JE01084

Davis, J.M., Balme, M., Grindrod, P.M., Williams, R.M.E., Gupta, S., 2016. Extensive Noachian fluvial systems in Arabia Terra: Implications for early Martian climate. Geology 44, 847–850. https://doi.org/10.1130/G38247.1

Davis, P.A., Soderblom, L.A., 1984. Modeling crater topography and albedo from monoscopic Viking Orbiter images: 1. Methodology. Journal of Geophysical Research: Solid Earth 89, 9449–9457. https://doi.org/10.1029/JB089iB11p09449

Delamere, W.A., Tornabene, L.L., McEwen, A.S., Becker, K., Bergstrom, J.W., Bridges, N.T., Eliason, E.M., Gallagher, D., Herkenhoff, K.E., Keszthelyi, L., Mattson, S., McArthur, G.K., Mellon, M.T., Milazzo, M., Russell, P.S., Thomas, N., 2010. Color imaging of Mars by the High Resolution Imaging Science Experiment (HiRISE). Icarus, MRO/HiRISE Studies of Mars 205, 38–52. https://doi.org/10.1016/j.icarus.2009.03.012

Delgado, F., Pavez, A., 2015. New insights into La Pacana caldera inner structure based on a gravimetric study (central Andes, Chile). Andean Geology 42, 313–328. https://doi.org/10.5027/andgeoV42n3-a02

Dohm, J.M., Barlow, N.G., Anderson, R.C., Williams, J.-P., Miyamoto, H., Ferris, J.C., Strom, R.G., Taylor, G.J., Fairén, A.G., Baker, V.R., Boynton, W.V., Keller, J.M., Kerry, K., Janes, D., Rodriguez, J.A.P., Hare, T.M., 2007. Possible ancient giant basin and related water enrichment in the Arabia Terra province, Mars. Icarus 190, 74–92. https://doi.org/10.1016/j.icarus.2007.03.006

Edgett, K.S., Parker, T.J., 1997. Water on early Mars: Possible subaqueous sedimentary deposits covering ancient cratered terrain in western Arabia and Sinus Meridiani. Geophysical Research Letters 24, 2897–2900. https://doi.org/10.1029/97GL02840

Edwards, C.S., Bandfield, J.L., Christensen, P.R., Fergason, R.L., 2009. Global distribution of bedrock exposures on Mars using THEMIS high-resolution thermal inertia. Journal of Geophysical Research: Planets 114. https://doi.org/10.1029/2009JE003363

Edwards, C.S., Christensen, P.R., Hill, J., 2014. Correction to "Mosaicking of global planetary image datasets: 2. Modeling of wind streak thicknesses observed in Thermal Emission Imaging System (THEMIS) daytime and nighttime infrared data." Journal of Geophysical Research: Planets 119, 1086–1087. https://doi.org/10.1002/2014JE004651

Edwards, C.S., Ehlmann, B.L., 2015. Carbon sequestration on Mars. Geology 43, 863–866. https://doi.org/10.1130/G36983.1

Edwards, C.S., Nowicki, K.J., Christensen, P.R., Hill, J., Gorelick, N., Murray, K., 2011. Mosaicking of global planetary image datasets: 1. Techniques and data processing for Thermal Emission Imaging System (THEMIS) multi-spectral data. Journal of Geophysical Research: Planets 116. https://doi.org/10.1029/2010JE003755

Ehlmann, B.L., Edwards, C.S., 2014. Mineralogy of the Martian Surface. Annual Review of Earth and Planetary Sciences 42, 291–315. https://doi.org/10.1146/annurev-earth-060313-055024

Ehlmann, B.L., Mustard, J.F., Swayze, G.A., Clark, R.N., Bishop, J.L., Poulet, F., Marais, D.J.D., Roach, L.H., Milliken, R.E., Wray, J.J., Barnouin-Jha, O., Murchie, S.L., 2009. Identification of hydrated silicate minerals on Mars using MRO-CRISM: Geologic context near Nili Fossae and implications for aqueous alteration. Journal of Geophysical Research: Planets 114. https://doi.org/10.1029/2009JE003339

Emran, A., King, D.T., Jr., Marzen, L.J., 2018b. Surficial Geology of Siloe Patera at Arabia Terra, Mars. AGU Fall Meeting Abstracts 53.

Emran, A., King, D.T., Marzen, L.J., Coker, C.W., Wright, S.P., 2018a. Remote Sensing Characterization of Siloe Patera, Mars. LPI Contributions 2066, 7017.

Fassett, C.I., Dickson, J.L., Head, J.W., Levy, J.S., Marchant, D.R., 2010. Supraglacial and proglacial valleys on Amazonian Mars. Icarus 208, 86–100. https://doi.org/10.1016/j.icarus.2010.02.021

Fassett, C.I., Head, J.W., 2007. Layered mantling deposits in northeast Arabia Terra, Mars: Noachian-Hesperian sedimentation, erosion, and terrain inversion. Journal of Geophysical Research: Planets 112. https://doi.org/10.1029/2006JE002875

Fastook, J.L., Head, J.W., 2008. Dichotomy Boundary Glaciation Models: Implications for Timing and Glacial Processes. AGU Fall Meeting Abstracts 41, P41A-1354.

Fergason, R.L, Hare, T.M., Laura, J., 2018. HRSC and MOLA blended digital elevation model at 200m v2, Astrogeology PDS Annex, U.S.

Fergason, R.L., Christensen, P.R., 2008. Formation and erosion of layered materials: Geologic and dust cycle history of eastern Arabia Terra, Mars. Journal of Geophysical Research: Planets 113. https://doi.org/10.1029/2007JE002973

Fergason, R.L., Christensen, P.R., Kieffer, H.H., 2006. High-resolution thermal inertia derived from the Thermal Emission Imaging System (THEMIS): Thermal model and applications. Journal of Geophysical Research: Planets 111. https://doi.org/10.1029/2006JE002735

Fergason, R.L., Laura, J.R., Hare, T.M., 2017. THEMIS-derived thermal inertia on Mars: Improved and flexible algorithm. Lunar and Planetary Science, XLVIII, Abstract #1563.

Forget, F., Haberle, R.M., Montmessin, F., Levrard, B., Head, J.W., 2006. Formation of Glaciers on Mars by Atmospheric Precipitation at High Obliquity. Science 311, 368–371. https://doi.org/10.1126/science.1120335

Fraeman, A.A., Ehlmann, B.L., Arvidson, R.E., Edwards, C.S., Grotzinger, J.P., Milliken, R.E., Quinn, D.P., Rice, M.S., 2016. The stratigraphy and evolution of lower Mount Sharp from spectral, morphological, and thermophysical orbital data sets. Journal of Geophysical Research: Planets 121, 1713–1736. https://doi.org/10.1002/2016JE005095

Francis, P., 1993. Volcanoes. A planetary perspective. Oxford (UK): Clarendon Press.

Francis, P.W., Wood, C.A., 1982. Absence of silicic volcanism on Mars: Implications for crustal composition and volatile abundance. Journal of Geophysical Research: Solid Earth 87, 9881–9889. https://doi.org/10.1029/JB087iB12p09881

Garcia, G.C., 2018. Identifying Evidence for Explosive Volcanism on Mars Through Geomorphologic and Thermophysical Observations. Unpublished MS Thesis, Boise State University, Boise, Idaho, USA.

Gillespie, A.R., Kahle, A.B., Walker, R.E., 1986. Color enhancement of highly correlated images. I. Decorrelation and HSI contrast stretches. Remote Sensing of Environment 20, 209–235. https://doi.org/10.1016/0034-4257(86)90044-1

Glotch, T.D., Christensen, P.R., 2005. Geologic and mineralogic mapping of Aram Chaos: Evidence for a water-rich history. Journal of Geophysical Research: Planets 110. https://doi.org/10.1029/2004JE002389

Goudge, T.A., Milliken, R.E., Head, J.W., Mustard, J.F., Fassett, C.I., 2017. Sedimentological evidence for a deltaic origin of the western fan deposit in Jezero crater, Mars and implications for future exploration. Earth and Planetary Science Letters 458, 357–365. https://doi.org/10.1016/j.epsl.2016.10.056

Grant, J.A., Schultz, P.H., 1990. Gradational epochs on Mars: Evidence from West-Northwest of Isidis Basin and Electris. Icarus 84, 166–195. https://doi.org/10.1016/0019-1035(90)90164-5

Greeley, R., Spudis, P.D., 1981. Volcanism on Mars. Reviews of Geophysics 19, 13–41. https://doi.org/10.1029/RG019i001p00013

Gulick, V.C., 2001. Origin of the valley networks on Mars: a hydrological perspective. Geomorphology 37, 241–268. https://doi.org/10.1016/S0169-555X(00)00086-6

Hartmann, W.K., Neukum, G., 2001. Cratering Chronology and the Evolution of Mars. Space Science Reviews 96, 165–194. https://doi.org/10.1023/A:1011945222010

Head, J.W., Marchant, D.R., 2009. Inventory of Ice-related Deposits on Mars: Evidence for Burial and Long-Term Sequestration of Ice in Non-Polar Regions and Implications for the Water Budget and Climate Evolution. Presented at the Lunar and Planetary Science Conference, p. 1356.

Head, J.W., Marchant, D.R., Agnew, M.C., Fassett, C.I., Kreslavsky, M.A., 2006. Extensive valley glacier deposits in the northern mid-latitudes of Mars: Evidence for Late Amazonian obliquity-driven climate change. Earth and Planetary Science Letters 241, 663–671. https://doi.org/10.1016/j.epsl.2005.11.016

Head, J.W., Mustard, J.F., Kreslavsky, M.A., Milliken, R.E., Marchant, D.R., 2003. Recent ice ages on Mars. Nature 426, 797. https://doi.org/10.1038/nature02114

Hill, J., Edwards, C.S., Christensen, P.R., 2014. Mapping the Martian Surface with THEMIS Global Infrared Mosaics. Presented at the Eighth International Conference on Mars, p. 1141.

Hill, J.R., Christensen, P.R., 2017. Well-preserved low thermal inertia ejecta deposits surrounding young secondary impact craters on Mars. Journal of Geophysical Research: Planets 122, 1276–1299. https://doi.org/10.1002/2016JE005210

Howard, A.D., 1994. A detachment-limited model of drainage basin evolution. Water Resources Research 30, 2261–2285. https://doi.org/10.1029/94WR00757

Huang, J., Edwards, C.S., Ruff, S.W., Christensen, P.R., Xiao, L., 2013. A new method for the semiquantitative determination of major rock-forming minerals with thermal infrared multispectral data: Application to THEMIS infrared data. Journal of Geophysical Research: Planets 118, 2146–2152. https://doi.org/10.1002/jgre.20160

Hulme, G., 1974. The Interpretation of Lava Flow Morphology. Geophysical Journal of the Royal Astronomical Society 39, 361–383. https://doi.org/10.1111/j.1365-246X.1974.tb05460.x

Hunt, G., 1977. Spectral signatures of particulate minerals in the visible and near infrared. GEOPHYSICS 42, 501–513. https://doi.org/10.1190/1.1440721

Hynek, B.M., Phillips, R.J., 2001. Evidence for extensive denudation of the Martian highlands. Geology 29, 407–410. https://doi.org/10.1130/0091-7613(2001)029<0407:EFEDOT>2.0.CO;2

Hynek, B.M., Phillips, R.J., Arvidson, R.E., 2003. Explosive volcanism in the Tharsis region: Global evidence in the Martian geologic record. Journal of Geophysical Research: Planets 108. https://doi.org/10.1029/2003JE002062

Jakosky, B.M., Mellon, M.T., Kieffer, H.H., Christensen, P.R., Varnes, E.S., Lee, S.W., 2000. The thermal inertia of Mars from the Mars Global Surveyor Thermal Emission Spectrometer. Journal of Geophysical Research: Planets 105, 9643–9652. https://doi.org/10.1029/1999JE001088

Jakosky, Bruce M. 1986. On the Thermal Properties of Martian Fines. *Icarus* 66 (1):117–24. https://doi.org/10.1016/0019-1035(86)90011-4.

Jones, A.P., McEwen, A.S., Tornabene, L.L., Baker, V.R., Melosh, H.J., Berman, D.C., 2011. A geomorphic analysis of Hale crater, Mars: The effects of impact into ice-rich crust. Icarus 211, 259–272. https://doi.org/10.1016/j.icarus.2010.10.014

Kerber, L., Head, J.W., Madeleine, J.-B., Forget, F., Wilson, L., 2012. The dispersal of pyroclasts from ancient explosive volcanoes on Mars: Implications for the friable layered deposits. Icarus 219, 358–381. https://doi.org/10.1016/j.icarus.2012.03.016

Kieffer, H.H., Martin, T.Z., Peterfreund, A.R., Jakosky, B.M., Miner, E.D., Palluconi, F.D., 1977. Thermal and albedo mapping of Mars during the Viking primary mission. Journal of Geophysical Research 82, 4249–4291. https://doi.org/10.1029/JS082i028p04249

Kreslavsky, M.A., Head, J.W., 2002. Mars: Nature and evolution of young latitude-dependent water-ice-rich mantle. Geophysical Research Letters 29, 14-1-14–4. https://doi.org/10.1029/2002GL015392

Kuzmin, R.O., 2005. 7 Ground Ice in the Martian Regolith, in: Tokano, T. (Ed.), Water on Mars and Life, Advances in Astrobiology and Biogeophysics. Springer Berlin Heidelberg, Berlin, Heidelberg, pp. 155–189. https://doi.org/10.1007/978-3-540-31538-4_7

Laura, J., Fergason, R.L., 2016. Modeling martian thermal inertia in a distributed memory high performance computing environment, in: 2016 IEEE International Conference on Big Data (Big Data). Presented at the 2016 IEEE International Conference on Big Data (Big Data), pp. 2919–2928. https://doi.org/10.1109/BigData.2016.7840942

Levy, J., Head, J., Marchant, D., 2009a. Thermal contraction crack polygons on Mars: Classification, distribution, and climate implications from HiRISE observations. Journal of Geophysical Research: Planets 114. https://doi.org/10.1029/2008JE003273

Levy, J., Head, J.W., Marchant, D.R., 2010. Concentric crater fill in the northern mid-latitudes of Mars: Formation processes and relationships to similar landforms of glacial origin. Icarus 209, 390–404. https://doi.org/10.1016/j.icarus.2010.03.036

Levy, J.S., Fassett, C.I., Head, J.W., Schwartz, C., Watters, J.L., 2014. Sequestered glacial ice contribution to the global Martian water budget: Geometric constraints on the volume of remnant, midlatitude debris-covered glaciers. Journal of Geophysical Research: Planets 119, 2188–2196. https://doi.org/10.1002/2014JE004685

Levy, J.S., Head, J.W., Marchant, D.R., 2009b. Concentric crater fill in Utopia Planitia: History and interaction between glacial "brain terrain" and periglacial mantle processes. Icarus 202, 462–476. https://doi.org/10.1016/j.icarus.2009.02.018

Levy, J.S., Marchant, D.R., Head, J.W., 2006. Distribution and origin of patterned ground on Mullins Valley debris-covered glacier, Antarctica: the roles of ice flow and sublimation. Antarctic Science 18, 385–397. https://doi.org/10.1017/S0954102006000435

Malin, M.C., Bell, J.F., Cantor, B.A., Caplinger, M.A., Calvin, W.M., Clancy, R.T., Edgett, K.S., Edwards, L., Haberle, R.M., James, P.B., Lee, S.W., Ravine, M.A., Thomas, P.C., Wolff, M.J., 2007. Context Camera Investigation on board the Mars Reconnaissance Orbiter. Journal of Geophysical Research: Planets 112. https://doi.org/10.1029/2006JE002808

Mangold, N., 2012. Fluvial landforms on fresh impact ejecta on Mars. Planetary and Space Science 62, 69–85. https://doi.org/10.1016/j.pss.2011.12.009

Mangold, N., Allemand, P., 2001. Topographic analysis of features related to ice on Mars. Geophysical Research Letters 28, 407–410. https://doi.org/10.1029/2000GL008491

Marchant, D.R., Head, J.W., 2007. Antarctic dry valleys: Microclimate zonation, variable geomorphic processes, and implications for assessing climate change on Mars. Icarus 192, 187–222. https://doi.org/10.1016/j.icarus.2007.06.018

Marchant, D.R., Lewis, A.R., Phillips, W.M., Moore, E.J., Souchez, R.A., Denton, G.H., Sugden, D.E., Potter, N., Landis, G.P., 2002. Formation of patterned ground and sublimation till over Miocene glacier ice in Beacon Valley, southern Victoria Land, Antarctica. GSA Bulletin 114, 718–730. https://doi.org/10.1130/0016-7606(2002)114<0718:FOPGAS>2.0.CO;2

McEwen, A.S., Eliason, E.M., Bergstrom, J.W., Bridges, N.T., Hansen, C.J., Delamere, W.A., Grant, J.A., Gulick, V.C., Herkenhoff, K.E., Keszthelyi, L., Kirk, R.L., Mellon, M.T., Squyres, S.W., Thomas, N., Weitz, C.M., 2007. Mars Reconnaissance Orbiter's High Resolution Imaging Science Experiment (HiRISE). Journal of Geophysical Research: Planets 112. https://doi.org/10.1029/2005JE002605

McGill, G.E., 2000. Crustal history of north central Arabia Terra, Mars. Journal of Geophysical Research: Planets 105, 6945–6959. https://doi.org/10.1029/1999JE001175

McGuire, P.C., Bishop, J.L., Brown, A.J., Fraeman, A.A., Marzo, G.A., Frank Morgan, M., Murchie, S.L., Mustard, J.F., Parente, M., Pelkey, S.M., Roush, T.L., Seelos, F.P., Smith, M.D., Wendt, L., Wolff, M.J., 2009. An improvement to the volcano-scan algorithm for atmospheric correction of CRISM and OMEGA spectral data. Planetary and Space Science 57, 809–815. https://doi.org/10.1016/j.pss.2009.03.007

Mellon, M.T., 1997. Small-scale polygonal features on Mars: Seasonal thermal contraction cracks in permafrost. Journal of Geophysical Research: Planets 102, 25617–25628. https://doi.org/10.1029/97JE02582

Mellon, M.T., Jakosky, B.M., Kieffer, H.H., Christensen, P.R., 2000. High-Resolution Thermal Inertia Mapping from the Mars Global Surveyor Thermal Emission Spectrometer. Icarus 148, 437–455. https://doi.org/10.1006/icar.2000.6503

Meresse, S., Costard, F., Mangold, N., Masson, P., Neukum, G., 2008. Formation and evolution of the chaotic terrains by subsidence and magmatism: Hydraotes Chaos, Mars. Icarus 194, 487–500. https://doi.org/10.1016/j.icarus.2007.10.023

Michael, G.G., 2013. Planetary surface dating from crater size–frequency distribution measurements: Multiple resurfacing episodes and differential isochron fitting. Icarus 226, 885–890. https://doi.org/10.1016/j.icarus.2013.07.004

Michalski, J.R., Bleacher, J.E., 2013. Supervolcanoes within an ancient volcanic province in Arabia Terra, Mars. Nature 502, 47–52. https://doi.org/10.1038/nature12482

Michalski, J.R., Bleacher, J.E., 2014. Plains Style Caldera Complexes: Evidence for Ancient, Explosive Volcanism on Mars. AGU Fall Meeting Abstracts 33, P33E-03.

Moore, J.M., 1990. Nature of the mantling deposit in the heavily cratered terrain of northeastern Arabia, Mars. Journal of Geophysical Research: Solid Earth 95, 14279–14289. https://doi.org/10.1029/JB095iB09p14279

Moratto, Z.M., Broxton, M.J., Beyer, R.A., Lundy, M., Husmann, K., 2010. Ames Stereo Pipeline, NASA's Open Source Automated Stereogrammetry Software. Presented at the Lunar and Planetary Science Conference, p. 2364.

Morgan, G.A., Head, J.W., 2009. Sinton crater, Mars: Evidence for impact into a plateau icefield and melting to produce valley networks at the Hesperian–Amazonian boundary. Icarus 202, 39–59. https://doi.org/10.1016/j.icarus.2009.02.025

Morschhauser, A., Lesur, V., Grott, M., 2014. A spherical harmonic model of the lithospheric magnetic field of Mars. Journal of Geophysical Research: Planets 119, 1162–1188. https://doi.org/10.1002/2013JE004555

Mouginis-Mark, P.J., Wilson, L., Zimbelman, J.R., 1988. Polygenic eruptions on Alba Patera, Mars. Bull Volcanol 50, 361–379. https://doi.org/10.1007/BF01050636

Murchie, S., Arvidson, R., Bedini, P., Beisser, K., Bibring, J.-P., Bishop, J., Boldt, J., Cavender, P., Choo, T., Clancy, R.T., Darlington, E.H., Marais, D.D., Espiritu, R., Fort, D., Green, R., Guinness, E., Hayes, J., Hash, C., Heffernan, K., Hemmler, J., Heyler, G., Humm, D., Hutcheson, J., Izenberg, N., Lee, R., Lees, J., Lohr, D., Malaret, E., Martin, T., McGovern, J.A., McGuire, P., Morris, R., Mustard, J., Pelkey, S., Rhodes, E., Robinson, M., Roush, T., Schaefer, E., Seagrave, G., Seelos, F., Silverglate, P., Slavney, S., Smith, M., Shyong, W.-J., Strohbehn, K., Taylor, H., Thompson, P., Tossman, B., Wirzburger, M., Wolff, M., 2007. Compact Reconnaissance Imaging Spectrometer for Mars (CRISM) on Mars Reconnaissance Orbiter (MRO). Journal of Geophysical Research: Planets 112. https://doi.org/10.1029/2006JE002682

Murphy, N.W., Jakosky, B.M., Rafkin, S.C., Larsen, K.W., Putzig, N.E., Mellon, M.T., 2007. Thermophysical properties of the Isidis basin, Mars. Journal of Geophysical Research: Planets 112. https://doi.org/10.1029/2005JE002586

Mustard, J.F., Cooper, C.D., 2005. Joint analysis of ISM and TES spectra: The utility of multiple wavelength regimes for Martian surface studies. Journal of Geophysical Research: Planets 110. https://doi.org/10.1029/2004JE002355

Mustard, J.F., Cooper, C.D., Rifkin, M.K., 2001. Evidence for recent climate change on Mars from the identification of youthful near-surface ground ice. Nature 412, 411. https://doi.org/10.1038/35086515

Neukum, G., R. Jaumann, HRSC Co-Investigator and Experiment Team., 2004. HRSC: The High-Resolution Stereo Camera of Mars Express. In A. Wilson (Ed.), Mars Express: The Scientific Payload, ESA, Noordwijk, The Netherlands, pp. 17-35

Palluconi, F.D., Kieffer, H.H., 1981. Thermal inertia mapping of Mars from 60°S to 60°N. Icarus 45, 415–426. https://doi.org/10.1016/0019-1035(81)90044-0

Pelkey, S.M., Mustard, J.F., Murchie, S., Clancy, R.T., Wolff, M., Smith, M., Milliken, R., Bibring, J.-P., Gendrin, A., Poulet, F., Langevin, Y., Gondet, B., 2007. CRISM multispectral summary products: Parameterizing mineral diversity on Mars from reflectance. Journal of Geophysical Research: Planets 112. https://doi.org/10.1029/2006JE002831

Plescia, J.B., Golombek, M.P., 1986. Origin of planetary wrinkle ridges based on the study of terrestrial analogs. GSA Bulletin 97, 1289–1299. https://doi.org/10.1130/0016-7606(1986)97<1289:OOPWRB>2.0.CO;2

Putzig, N.E., Barratt, E.M., Mellon, M.T., Michaels, T.I., 2013. MARSTHERM: A Web-based System Providing Thermophysical Analysis Tools for Mars Research. AGU Fall Meeting Abstracts 43, P43C-2023.

Putzig, N.E., Mellon, M.T., Herkenhoff, K.E., Phillips, R.J., Davis, B.J., Ewer, K.J., Bowers, L.M., 2014. Thermal behavior and ice-table depth within the north polar erg of Mars. Icarus, Third Planetary Dunes Systems 230, 64–76. https://doi.org/10.1016/j.icarus.2013.07.010

Putzig, N.E., Mellon, M.T., Kretke, K.A., Arvidson, R.E., 2005. Global thermal inertia and surface properties of Mars from the MGS mapping mission. Icarus 173, 325–341. https://doi.org/10.1016/j.icarus.2004.08.017

Quantin-Nataf, C., Lozac'h, L., Thollot, P., Loizeau, D., Bultel, B., Fernando, J., Allemand, P., Dubuffet, F., Poulet, F., Ody, A., Clenet, H., Leyrat, C., Harrisson, S., 2018. MarsSI: Martian surface data processing information system. Planetary and Space Science, Enabling Open and Interoperable Access to Planetary Science and Heliophysics Databases and Tools 150, 157–170. https://doi.org/10.1016/j.pss.2017.09.014

Raitala, J., 1990. Wrinkle ridges on mars. Advances in Space Research 10, 71–73. https://doi.org/10.1016/0273-1177(90)90329-X

Ramsey, M.S., Christensen, P.R., 1998. Mineral abundance determination: Quantitative deconvolution of thermal emission spectra. Journal of Geophysical Research: Solid Earth 103, 577–596. https://doi.org/10.1029/97JB02784

Reimers, C.E., Komar, P.D., 1979. Evidence for explosive volcanic density currents on certain Martian volcanoes. Icarus 39, 88–110. https://doi.org/10.1016/0019-1035(79)90103-9

Robbins, S.J., Achille, G.D., Hynek, B.M., 2011. The volcanic history of Mars: High-resolution crater-based studies of the calderas of 20 volcanoes. Icarus 211, 1179–1203. https://doi.org/10.1016/j.icarus.2010.11.012

Robbins, S.J., Hynek, B.M., 2012a. A new global database of Mars impact craters ≥1 km: 1. Database creation, properties, and parameters. Journal of Geophysical Research: Planets 117. https://doi.org/10.1029/2011JE003966

Robbins, S.J., Hynek, B.M., 2012b. A new global database of Mars impact craters ≥1 km: 2. Global crater properties and regional variations of the simple-to-complex transition diameter. Journal of Geophysical Research: Planets 117. https://doi.org/10.1029/2011JE003967

Robbins, S.J., Hynek, B.M., 2013. Utility of laser altimeter and stereoscopic terrain models: Application to Martian craters. Planetary and Space Science 86, 57–65. https://doi.org/10.1016/j.pss.2013.06.019

Robinson, M.S., Mouginis-Mark, P.J., Zimbelman, J.R., Wu, S.S.C., Ablin, K.K., Howington-Kraus, A.E., 1993. Chronology, Eruption Duration, and Atmospheric Contribution of the Martian Volcano Apollinaris Patera. Icarus 104, 301–323. https://doi.org/10.1006/icar.1993.1103

Roda, M., Kleinhans, M.G., Zegers, T.E., Govers, R., 2016. Origin of circular collapsed landforms in the Chryse region of Mars. Icarus 265, 70–78. https://doi.org/10.1016/j.icarus.2015.10.020

Rodriguez, J.A.P., Sasaki, S., Kuzmin, R.O., Dohm, J.M., Tanaka, K.L., Miyamoto, H., Kurita, K., Komatsu, G., Fairén, A.G., Ferris, J.C., 2005. Outflow channel sources, reactivation, and chaos formation, Xanthe Terra, Mars. Icarus 175, 36–57. https://doi.org/10.1016/j.icarus.2004.10.025

Ruff, S.W., Christensen, P.R., Blaney, D.L., Farrand, W.H., Johnson, J.R., Michalski, J.R., Moersch, J.E., Wright, S.P., Squyres, S.W., 2006. The rocks of Gusev Crater as viewed by the Mini-TES instrument. Journal of Geophysical Research: Planets 111. https://doi.org/10.1029/2006JE002747

Salamunićcar, G., Lončarić, S., Pina, P., Bandeira, L., Saraiva, J., 2011. MA130301GT catalogue of Martian impact craters and advanced evaluation of crater detection algorithms using diverse topography and image datasets. Planetary and Space Science 59, 111–131. https://doi.org/10.1016/j.pss.2010.11.003

Salvatore, M.R., Goudge, T.A., Bramble, M.S., Edwards, C.S., Bandfield, J.L., Amador, E.S., Mustard, J.F., Christensen, P.R., 2018. Bulk mineralogy of the NE Syrtis and Jezero crater regions of Mars derived through thermal infrared spectral analyses. Icarus 301, 76–96. https://doi.org/10.1016/j.icarus.2017.09.019

Salvatore, M.R., Mustard, J.F., Wyatt, M.B., Murchie, S.L., 2010. Definitive evidence of Hesperian basalt in Acidalia and Chryse planitiae. Journal of Geophysical Research: Planets 115. https://doi.org/10.1029/2009JE003519

Schultz, P.H., Lutz, A.B., 1988. Polar wandering of Mars. Icarus 73, 91–141. https://doi.org/10.1016/0019-1035(88)90087-5

Segura, T.L., Toon, O.B., Colaprete, A., Zahnle, K., 2002. Environmental Effects of Large Impacts on Mars. Science 298, 1977–1980. https://doi.org/10.1126/science.1073586

Self, S., 2006. The effects and consequences of very large explosive volcanic eruptions. Philosophical Transactions of the Royal Society A: Mathematical, Physical and Engineering Sciences 364, 2073–2097. https://doi.org/10.1098/rsta.2006.1814

Sharp, R.P., 1973. Mars: Fretted and chaotic terrains. Journal of Geophysical Research (1896-1977) 78, 4073–4083. https://doi.org/10.1029/JB078i020p04073

Sleep, N.H., 1994. Martian plate tectonics. Journal of Geophysical Research: Planets 99, 5639–5655. https://doi.org/10.1029/94JE00216

Smith, D.E., Zuber, M.T., Frey, H.V., Garvin, J.B., Head, J.W., Muhleman, D.O., Pettengill, G.H., Phillips, R.J., Solomon, S.C., Zwally, H.J., Banerdt, W.B., Duxbury, T.C., Golombek, M.P.,

Lemoine, F.G., Neumann, G.A., Rowlands, D.D., Aharonson, O., Ford, P.G., Ivanov, A.B., Johnson, C.L., McGovern, P.J., Abshire, J.B., Afzal, R.S., Sun, X., 2001. Mars Orbiter Laser Altimeter: Experiment summary after the first year of global mapping of Mars. Journal of Geophysical Research: Planets 106, 23689–23722. https://doi.org/10.1029/2000JE001364

Smith, E.I., 1976. Comparison of the crater morphology-size relationship for Mars, Moon, and Mercury. Icarus 28, 543–550. https://doi.org/10.1016/0019-1035(76)90127-5

Smith, M.R., Bandfield, J.L., Cloutis, E.A., Rice, M.S., 2013. Hydrated silica on Mars: Combined analysis with near-infrared and thermal-infrared spectroscopy. Icarus 223, 633–648. https://doi.org/10.1016/j.icarus.2013.01.024

Soare, R.J., Osinski, G.R., Roehm, C.L., 2008. Thermokarst lakes and ponds on Mars in the very recent (late Amazonian) past. Earth and Planetary Science Letters 272, 382–393. https://doi.org/10.1016/j.epsl.2008.05.010

Tanaka, K.L., 2000. Dust and Ice Deposition in the Martian Geologic Record. Icarus 144, 254–266. https://doi.org/10.1006/icar.1999.6297

Tanaka, K.L., Skinner, J.A., Hare, T.M., Joyal, T., Wenker, A., 2003. Resurfacing history of the northern plains of Mars based on geologic mapping of Mars Global Surveyor data. Journal of Geophysical Research: Planets 108. https://doi.org/10.1029/2002JE001908

Tanaka, K.L., Skinner, J.A., Jr., Dohm, J.M., Irwin, R.P., III, Kolb, E.J., Fortezzo, C.M., Platz, T., Michael, G.G., and Hare, T.M., 2014, Geologic map of Mars: U.S. Geological Survey Scientific Investigations Map 3292, scale 1:20,000,000, pamphlet 43 p., https://dx.doi.org/10.3133/sim3292.

Thomson, J.L., Salisbury, J.W., 1993. The mid-infrared reflectance of mineral mixtures (7–14 μm). Remote Sensing of Environment 45, 1–13. https://doi.org/10.1016/0034-4257(93)90077-B

Tizzani, P., Berardino, P., Casu, F., Euillades, P., Manzo, M., Ricciardi, G.P., Zeni, G., Lanari, R., 2007. Surface deformation of Long Valley caldera and Mono Basin, California, investigated with the SBAS-InSAR approach. Remote Sensing of Environment 108, 277–289. https://doi.org/10.1016/j.rse.2006.11.015

Toon, O.B., Segura, T., Zahnle, K., 2010. The Formation of Martian River Valleys by Impacts. Annual Review of Earth and Planetary Sciences 38, 303–322. https://doi.org/10.1146/annurev-earth-040809-152354

Vergniolle, S., Jaupart, C., 1986. Separated two-phase flow and basaltic eruptions. Journal of Geophysical Research: Solid Earth 91, 12842–12860. https://doi.org/10.1029/JB091iB12p12842

Vincent, R.K., Thomson, F., 1972. Spectral compositional imaging of silicate rocks. Journal of Geophysical Research 77, 2465–2472. https://doi.org/10.1029/JB077i014p02465

Viviano-Beck, C.E., Murchie, S.L., Beck, A.W., Dohm, J.M., 2017. Compositional and structural constraints on the geologic history of eastern Tharsis Rise, Mars. Icarus 284, 43–58. https://doi.org/10.1016/j.icarus.2016.09.005

Viviano-Beck, C.E., Seelos, F.P., Murchie, S.L., Kahn, E.G., Seelos, K.D., Taylor, H.W., Taylor, K., Ehlmann, B.L., Wiseman, S.M., Mustard, J.F., Morgan, M.F., 2014. Revised CRISM spectral parameters and summary products based on the currently detected mineral diversity on Mars. Journal of Geophysical Research: Planets 119, 1403–1431. https://doi.org/10.1002/2014JE004627

Walter, L.S., Salisbury, J.W., 1989. Spectral characterization of igneous rocks in the 8- to 12-μm region. Journal of Geophysical Research: Solid Earth 94, 9203–9213. https://doi.org/10.1029/JB094iB07p09203

Watters, T.R., 1988. Wrinkle ridge assemblages on the terrestrial planets. Journal of Geophysical Research: Solid Earth 93, 10236–10254. https://doi.org/10.1029/JB093iB09p10236
Watters, T.R., 1993. Compressional tectonism on Mars. Journal of Geophysical Research: Planets 98, 17049–17060. https://doi.org/10.1029/93JE01138
Wilhelms, D.E., Baldwin, R.J., 1989. The role of igneous sills in shaping the Martian uplands. Presented at the Lunar and Planetary Science Conference Proceedings, pp. 355–365.
Wilkes, C.A., 2014. Evidence for a Possible Supervolcano on Mars at Siloe Patera. Unpublished MS Thesis, Auburn University, Auburn, Alabama, USA
Wilkes, C.A., King, Jr., D.T., Wright, S.P., 2013. Investigation of Siloe Patera and the Surrounding Area: Possible Evidence of an Ancient Volcanic Caldera on Mars. Lunar and Planetary Science Meeting Abstracts 3034.
Williams, R.M.E., Moersch, J.E., Fergason, R.L., 2018. Thermophysical Properties of Martian Fluvial Sinuous Ridges: Inferences on 'Inverted Channel' Induration Agent. Earth and Space Science 0. https://doi.org/10.1029/2018EA000402
Wilson, S.A., Howard, A.D., Moore, J.M., Grant, J.A., 2016. A cold-wet middle-latitude environment on Mars during the Hesperian-Amazonian transition: Evidence from northern Arabia valleys and paleolakes. Journal of Geophysical Research: Planets 121, 1667–1694. https://doi.org/10.1002/2016JE005052
Zabrusky, K., Andrews-Hanna, J.C., Wiseman, S.M., 2012. Reconstructing the distribution and depositional history of the sedimentary deposits of Arabia Terra, Mars. Icarus 220, 311–330. https://doi.org/10.1016/j.icarus.2012.05.007
Zimbelman, J.R., Clifford, S.M., Williams, S.H., 1989. Concentric crater fill on Mars - an aeolian alternative to ice-rich mass wasting. Presented at the Lunar and Planetary Science Conference Proceedings, pp. 397–407.
Zuber, M.T., 2001. The crust and mantle of Mars. Nature 412(6843), 220–227. https://doi.org/10.1038/35084163
Zurek, R.W., Smrekar, S.E., 2007. An overview of the Mars Reconnaissance Orbiter (MRO) science mission. Journal of Geophysical Research: Planets 112. https://doi.org/10.1029/2006JE002701

Chapter 5: Conclusion

The planet Mars has been one of the most curious planets in the solar system. The recent influx of spacecraft data enabled scientists to explore the surface and atmosphere of the planet in a very efficient way with great detail and comprehensive methods. Mars has a variety of surface features like our home planet Earth. The planet has undergone different geological processes and the processes have induced modifications. Mars has volcanos, mountains, impact craters, dune fields, and extensive fluvial networks. Studying the surface of the planet demands integration of thermophysical, morphological, stratigraphic, and mineralogical information collected from different spacecraft missions e.g., rovers, landers, and orbital remote sensing. Accurate characterization of the surface of the planet reveals its geologic history, environmental conditions, and its atmosphere and climate. The domain of the martian remote sensing dataset covers a range of the electromagnetic spectrum including visible and near-infrared (VNIR), thermal infrared (TIR), and radar observations onboard satellites.

The present study aimed at characterizing surface geology of two different parts of the planet; Hargraves crater in Nili Fossae area and Siloe Patera in the Arabia Terra region. Identifying dunes (barchan and barchanoids) using a semi-automated object-based image analysis technique and its validation is the prime objective of the first project. The project used a higher resolution (~6 meters/pixel) images from the Context Camera (CTX; Malin et al., 2007) onboard the Mars Reconnaissance Orbiter (MRO) spacecraft. The relatively accurate and validated result of this study supports the application of an object-based image analysis technique in other areas of the planet. In addition, the project has also constrained thermophysical characteristics (i.e., thermal inertia) of dune

surfaces to analyze the grain-size distribution of constituent dune materials from thermal infrared (TIR) images of the Thermal Emission Imaging System (THEMIS; Christensen et al., 2004) sensor. The bulk mineralogy of the dune materials and its surrounding geologic units were analyzed to infer the source provenance of dune materials. Mineralogy of these units, including the dune field, have been analyzed from the thermal infrared (TIR) hyperspectral data of the Thermal Emission Spectrometer (TES; Christensen et al., 2001) instrument. The second project (i.e., Siloe Patera) aimed at resolving the debated geological history of Siloe Patera with the integration of near-infrared (NIR) and thermal infrared (TIR) datasets. The project addresses the surficial geology of the Late Noachian to Early Hesperian Siloe Patera by combining analysis of spectral units, bulk-silica content, and thermophysical characteristics (e.g., thermal inertia) using THEMIS-TIR dataset. In addition, the mineralogy of olivine, phyllosilicate, and hydrated silicates phases were investigated using near-infrared (NIR) data from the Compact Reconnaissance Imaging Spectrometer for Mars (CRISM; Murchie et al., 2007) instrument. Local geologic features were interpreted from the Mars Reconnaissance Orbiter (MRO) onboard the High Resolution Imaging Science Experiment (HiRISE; McEwen et al., 2007) and the Context Camera (CTX) images.

Having many advantages over pixel-based photo interpretation, the object-based dune identification has produced a method that provides quick, accurate, and reliable results in detecting dunes at Hargraves crater. The study found an average thermal inertia value of 243±23 $Jm^{-2}K^{-1}s^{-0.5}$ for the dune materials at the study area indicating a surface composed of an effective grain-size of ~230 μm. This thermal inertia value suggests that the dune materials are composed of fine sand-sized grains and moderately indurated with small granules or unconsolidated materials. Compositional analysis indicated that the dune materials are composed of a mixture of feldspar, olivine, and pyroxene minerals having a relatively lower bulk-silica content. The dunes were labeled

as active (stability index of 2) and do not appear to have been influenced by subsurface water ice or volatiles. The study emphasizes that with the accurate dune identification using a semi-automated method coupled with the compositional and thermophysical characteristics for individual martian dune fields would provide an excellent contribution for a better understanding of surface and atmospheric characteristics of the planet at a local scale.

The second project discusses four different spectral units in Siloe Patera which were leveled as purple, fuschia/magenta, yellow/amber, and pale-brown or green units. Purple is an olivine-bearing unit on the eastern and northeastern rims and scarps; fuschia/magenta is a mafic rock-rich unit on the southwestern rim and scarp and adjacent caldera floor. Yellow/amber is a unit on the southern caldera floor which includes probable lava flows and dune sands; pale-brown and green is a glacial outwash deposit on the caldera floor. The study concludes that the late Noachian to early Hesperian Siloe Patera has initially formed as an impact crater that has experienced a subsequent collapse event possibly due to the combination of magma and ice migration underneath the crust in Hesperian-Amazonian periods. If volcanism was involved in the formation of the collapse, then the volcanism type was effusive lava flow in the interior floors. Water might have filled in the depression; however, a glacial reworking dominated during the late Amazonian period. Recent small impact cratering and aeolian medication have been active.

References

Christensen, P. R., J. L. Bandfield, V. E. Hamilton, S. W. Ruff, H. H. Kieffer, T. N. Titus, M. C. Malin, et al. 2001. Mars Global Surveyor Thermal Emission Spectrometer Experiment: Investigation Description and Surface Science Results. *Journal of Geophysical Research: Planets* 106 (E10):23823–71. https://doi.org/10.1029/2000JE001370.

Christensen, P.R., Jakosky, B.M., Kieffer, H.H., Malin, M.C., McSween, H.Y., Nealson, K., Mehall, G.L., Silverman, S.H., Ferry, S., Caplinger, M., Ravine, M., 2004. The Thermal Emission Imaging System (THEMIS) for the Mars 2001 Odyssey Mission. Space Science Reviews 110, 85–130. https://doi.org/10.1023/B:SPAC.0000021008.16305.94

Malin, Michael C., James F. Bell, Bruce A. Cantor, Michael A. Caplinger, Wendy M. Calvin, R. Todd Clancy, Kenneth S. Edgett, et al. 2007. Context Camera Investigation on Board the Mars Reconnaissance Orbiter. *Journal of Geophysical Research: Planets* 112 (E5):E05S04. https://doi.org/10.1029/2006JE002808.

McEwen, A.S., Eliason, E.M., Bergstrom, J.W., Bridges, N.T., Hansen, C.J., Delamere, W.A., Grant, J.A., Gulick, V.C., Herkenhoff, K.E., Keszthelyi, L., Kirk, R.L., Mellon, M.T., Squyres, S.W., Thomas, N., Weitz, C.M., 2007. Mars Reconnaissance Orbiter's High Resolution Imaging Science Experiment (HiRISE). Journal of Geophysical Research: Planets 112. https://doi.org/10.1029/2005JE002605

Murchie, S., Arvidson, R., Bedini, P., Beisser, K., Bibring, J.-P., Bishop, J., Boldt, J., Cavender, P., Choo, T., Clancy, R.T., Darlington, E.H., Marais, D.D., Espiritu, R., Fort, D., Green, R., Guinness, E., Hayes, J., Hash, C., Heffernan, K., Hemmler, J., Heyler, G., Humm, D., Hutcheson, J., Izenberg, N., Lee, R., Lees, J., Lohr, D., Malaret, E., Martin, T., McGovern, J.A., McGuire, P., Morris, R., Mustard, J., Pelkey, S., Rhodes, E., Robinson, M., Roush, T., Schaefer, E., Seagrave, G., Seelos, F., Silverglate, P., Slavney, S., Smith, M., Shyong, W.-J., Strohbehn, K., Taylor, H., Thompson, P., Tossman, B., Wirzburger, M., Wolff, M., 2007. Compact Reconnaissance Imaging Spectrometer for Mars (CRISM) on Mars Reconnaissance Orbiter (MRO). Journal of Geophysical Research: Planets 112. https://doi.org/10.1029/2006JE002682

Chapter 6: Bibliography

Abuodha, J.O.Z., 2003. Grain size distribution and composition of modern dune and beach sediments, Malindi Bay coast, Kenya. Journal of African Earth Sciences 36, 41–54. https://doi.org/10.1016/S0899-5362(03)00016-2

Achille, G.D., Hynek, B.M., 2010. Ancient ocean on Mars supported by global distribution of deltas and valleys. Nature Geoscience 3, 459–463. https://doi.org/10.1038/ngeo891

Adeli, S., Hauber, E., Kleinhans, M., Le Deit, L., Platz, T., Fawdon, P., Jaumann, R., 2016. Amazonian-aged fluvial system and associated ice-related features in Terra Cimmeria, Mars. Icarus 277, 286–299. https://doi.org/10.1016/j.icarus.2016.05.020

Ahrens, C.J., Titus, T.N., 2014. An Assessment of the Reliability of Mineral Abundance Estimates Derived from TES Data over Dune Sites. Presented at the Eighth International Conference on Mars, p. 1012.

Amador, E.S., Bandfield, J.L., 2016. Elevated bulk-silica exposures and evidence for multiple aqueous alteration episodes in Nili Fossae, Mars. Icarus 276, 39–51. https://doi.org/10.1016/j.icarus.2016.04.015

Anguita, F., Anguita, J., Castilla, G., Casa, M.-A.D.L., Domínguez, J.-M., Herrera, R., Llanes, P., López, M., Martínez, V., 1997. Arabia Terra, Mars: Tectonic and Palaeoclimatic Evolution of a Remarkable Sector of Martian Lithosphere. Earth, Moon, and Planets 77, 55–72. https://doi.org/10.1023/A:1006143106970

Baatz, M., Hoffmann, C., Willhauck, G., 2008. Progressing from object-based to object-oriented image analysis, in: Object-Based Image Analysis, Lecture Notes in Geoinformation and Cartography. Springer, Berlin, Heidelberg, pp. 29–42. https://doi.org/10.1007/978-3-540-77058-9_2

Baird, A.K., Toulmin, P., Clark, B.C., Rose, H.J., Keil, K., Christian, R.P., Gooding, J.L., 1976. Mineralogic and Petrologic Implications of Viking Geochemical Results From Mars: Interim Report. Science 194, 1288–1293. https://doi.org/10.1126/science.194.4271.1288

Baldridge, A. M., 2007. Thermal infrared spectral studies of sulfates and chlorides: Applications to salts on the Martian surface. Thesis, Ariz. State Univ., Tempe. Pp, 204.

Bandeira, L., Marques, J.S., Saraiva, J., Pina, P., 2010. Automated Detection of Sand Dunes on Mars, in: Image Analysis and Recognition, Lecture Notes in Computer Science. Presented at the International Conference Image Analysis and Recognition, Springer, Berlin, Heidelberg, pp. 306–315. https://doi.org/10.1007/978-3-642-13775-4_31

Bandeira, L., Marques, J.S., Saraiva, J., Pina, P., 2011. Automated Detection of Martian Dune Fields. IEEE Geoscience and Remote Sensing Letters 8, 626–630. https://doi.org/10.1109/LGRS.2010.2098390

Bandfield, J.L., 2002. Global mineral distributions on Mars. Journal of Geophysical Research: Planets 107, 9-1-9–20. https://doi.org/10.1029/2001JE001510

Bandfield, J.L., Christensen, P.R., Smith, M.D., 2000b. Spectral data set factor analysis and end-member recovery: Application to analysis of Martian atmospheric particulates. Journal of Geophysical Research: Planets 105, 9573–9587. https://doi.org/10.1029/1999JE001094

Bandfield, J.L., Deanne Rogers, A., Edwards, C.S., 2011. The role of aqueous alteration in the formation of martian soils. Icarus 211, 157–171. https://doi.org/10.1016/j.icarus.2010.08.028

Bandfield, J.L., Edwards, C.S., Montgomery, D.R., Brand, B.D., 2013. The dual nature of the martian crust: Young lavas and old clastic materials. Icarus 222, 188–199. https://doi.org/10.1016/j.icarus.2012.10.023

Bandfield, J.L., Hamilton, V.E., Christensen, P.R., 2000a. A Global View of Martian Surface Compositions from MGS-TES. Science 287, 1626–1630. https://doi.org/10.1126/science.287.5458.1626

Bandfield, J.L., Hamilton, V.E., Christensen, P.R., McSween, H.Y., 2004a. Identification of quartzofeldspathic materials on Mars. Journal of Geophysical Research: Planets 109. https://doi.org/10.1029/2004JE002290

Bandfield, J.L., Rogers, D., Smith, M.D., Christensen, P.R., 2004b. Atmospheric correction and surface spectral unit mapping using Thermal Emission Imaging System data. Journal of Geophysical Research: Planets 109. https://doi.org/10.1029/2004JE002289

Bandfield, Joshua L., Deanne Rogers, Michael D. Smith, and Philip R. Christensen, 2004. Atmospheric Correction and Surface Spectral Unit Mapping Using Thermal Emission Imaging System Data. Journal of Geophysical Research: Planets 109 (E10):E10008. https://doi.org/10.1029/2004JE002289.

Banks, M.E., Fenton, L.K., Bridges, N.T., Geissler, P.E., Chojnacki, M., Runyon, K.D., Silvestro, S., Zimbelman, J.R., 2018. Patterns in Mobility and Modification of Middle- and High-Latitude Southern Hemisphere Dunes on Mars. Journal of Geophysical Research: Planets 123, 3205–3219. https://doi.org/10.1029/2018JE005747

Barlow, N., 2008. Mars: An Introduction to its Interior, Surface and Atmosphere. Cambridge University Press, Cambridge: UK. ISBN 978-0-521-85226-5.

Barlow, N.G., Bradley, T.L., 1990. Martian impact craters: Correlations of ejecta and interior morphologies with diameter, latitude, and terrain. Icarus 87, 156–179. https://doi.org/10.1016/0019-1035(90)90026-6

Beveridge, C., Kocurek, G., Ewing, R.C., Lancaster, N., Morthekai, P., Singhvi, A.K., Mahan, S.A., 2006. Development of spatially diverse and complex dune-field patterns: Gran Desierto Dune Field, Sonora, Mexico. Sedimentology 53, 19. https://doi.org/10.1111/j.1365-3091.2006.00814.x

Beyer, R.A., O. Alexandrov, and Z. Moratto., 2014. Aligning terrain model and laser altimeter point clouds with the Ames Stereo Pipeline. Lunar Planet. Sci., 45. Abstract 2902. https://www.hou.usra.edu/meetings/lpsc2014/pdf/2902.pdf

Bibring, J.-P., A. Soufflot, M. Berthé, Y. Langevin, B. Gondet, P. Drossart, M. Bouyé, et al., 2004. OMEGA: Observatoire Pour La Minéralogie, l'Eau, Les Glaces et l'Activité. In Mars Express - The Scientific Payload, European Space Agency Special Publication, SP-1240, edited, pp. 37-49, ESA. http://adsabs.harvard.edu/abs/2004ESASP1240...37B.

Blair, Terence C., and John G. McPherson., 1994. Alluvial Fans and Their Natural Distinction from Rivers Based on Morphology, Hydraulic Processes, Sedimentary Processes, and Facies Assemblages. Journal of Sedimentary Research 64 (3a):450–89. https://doi.org/10.1306/D4267DDE-2B26-11D7-8648000102C1865D.

Blaschke, T., 2010. Object based image analysis for remote sensing. ISPRS Journal of Photogrammetry and Remote Sensing 65, 2–16. https://doi.org/10.1016/j.isprsjprs.2009.06.004

Blaschke, T., Hay, G.J., Kelly, M., Lang, S., Hofmann, P., Addink, E., Queiroz Feitosa, R., van der Meer, F., van der Werff, H., van Coillie, F., Tiede, D., 2014. Geographic Object-Based Image Analysis – Towards a new paradigm. ISPRS Journal of Photogrammetry and Remote Sensing 87, 180–191. https://doi.org/10.1016/j.isprsjprs.2013.09.014

Blaschke, T., Strobl, J., 2002. What's wrong with pixels? Some recent developments interfacing remote sensing and GIS. GIS–Zeitschrift für Geoinformationssysteme, 14 (6), 12-17

Bramble, Michael S., John F. Mustard, and Mark R. Salvatore., 2017. The Geological History of Northeast Syrtis Major, Mars. Icarus 293 (Supplement C):66–93. https://doi.org/10.1016/j.icarus.2017.03.030.

Broxton, M.J., and L.J. Edwards., 2008. The Ames Stereo Pipeline: automated 3D surface reconstruction from orbital imagery. Lunar Planet. Sci., 39, Abstract 2419 http://adsabs.harvard.edu/abs/2008LPI....39.2419B.

Brugman, K., 2014. Understanding the History of Arabia Terra, Mars Through Crater-Based Tests. Undergraduate Honors Theses. University of Colorado Boulder.

Burnett, C., Blaschke, T., 2003. A multi-scale segmentation/object relationship modelling methodology for landscape analysis. Ecological Modelling, Landscape Theory and Landscape Modelling 168, 233–249. https://doi.org/10.1016/S0304-3800(03)00139-X

Cannon, K., Mustard, J., Osinski, G., Tornabene, L., Parman, S., Amador, E., Brown, A., Viviano-Beck, C., Ehlmann, B., Sapers, H., Pontefract, A., Marais, D.D., Mangold, N., Wiseman, S., 2015. An Ancient Crustal Stratigraphy in the Nili Fossae Troug Clays, Carbonates, Impacts and Volcanics. In 2nd Mars 2020 Landing Site Workshop.

Canup, R.M. and C.B. Agnor., 2000. Accretion of the terrestrial planets and the Earth–Moon system. In Origin of the Earth and Moon, edt. R.M. Canup and K. Righter. Tucson, AZ: University of Arizona Press.

Carr, M.H., 1973. Volcanism on Mars. Journal of Geophysical Research (1896-1977) 78, 4049–4062. https://doi.org/10.1029/JB078i020p04049

Carr, M.H., 1980. The Morphology of the Martian Surface. Space Science Review 25 (3): 231-284 https://doi.org/10.1007/BF00221929

Carr, M.H., 1986. Mars: A water-rich planet? Icarus 68, 187–216. https://doi.org/10.1016/0019-1035(86)90019-9

Carr, M.H., 2007. The Surface of Mars. Cambridge University Press. Cambridge

Carr, M.H., 2012. Formation of Martian flood features by release of water from confined aquifers. Journal of Geophysical Research: Solid Earth 2995–3007. https://doi.org/10.1029/JB084iB06p02995@10.1002/(ISSN)2169-9356.MARSVOL1

Carr, M.H., 2012. The fluvial history of Mars. Philosophical Transactions of the Royal Society of London Series A 370, 2193–2215. https://doi.org/10.1098/rsta.2011.0500

Carr, M.H., Head, J.W., 2003. Basal melting of snow on early Mars: A possible origin of some valley networks. Geophysical Research Letters 30. https://doi.org/10.1029/2003GL018575

Carr, M.H., Head, J.W., 2003. Oceans on Mars: An assessment of the observational evidence and possible fate. Journal of Geophysical Research: Planets 108. https://doi.org/10.1029/2002JE001963

Carr, M.H., Head, J.W., 2010. Geologic history of Mars. Earth and Planetary Science Letters, Mars Express after 6 Years in Orbit: Mars Geology from Three-Dimensional Mapping by the High Resolution Stereo Camera (HRSC) Experiment 294, 185–203. https://doi.org/10.1016/j.epsl.2009.06.042

Castilla, G., Hay, G.J., 2008. Image objects and geographic objects, in: Object-Based Image Analysis, Lecture Notes in Geoinformation and Cartography. Springer, Berlin, Heidelberg, pp. 91–110. https://doi.org/10.1007/978-3-540-77058-9_5

Chambers, John E., 2004. Planetary Accretion in the Inner Solar System. Earth and Planetary Science Letters 223 (3):241–52. https://doi.org/10.1016/j.epsl.2004.04.031.

Chapman, M.G., Tanaka, K.L., 2002. Related Magma–Ice Interactions: Possible Origins of Chasmata, Chaos, and Surface Materials in Xanthe, Margaritifer, and Meridiani Terrae, Mars. Icarus 155, 324–339. https://doi.org/10.1006/icar.2001.6735

Chesner, C.A., 2012. The Toba Caldera Complex. Quaternary International, The Toba Volcanic Super-eruption of 74,000 Years Ago: Climate Change, Environments, and Evolving Humans 258, 5–18. https://doi.org/10.1016/j.quaint.2011.09.025

Christensen, P. R., J. L. Bandfield, V. E. Hamilton, S. W. Ruff, H. H. Kieffer, T. N. Titus, M. C. Malin, et al., 2001. Mars Global Surveyor Thermal Emission Spectrometer Experiment: Investigation Description and Surface Science Results. Journal of Geophysical Research: Planets 106 (E10):23823–71. https://doi.org/10.1029/2000JE001370.

Christensen, P.R., Bandfield, J.L., Hamilton, V.E., Howard, D.A., Lane, M.D., Piatek, J.L., Ruff, S.W., Stefanov, W.L., 2000. A thermal emission spectral library of rock-forming minerals. Journal of Geophysical Research: Planets 105, 9735–9739. https://doi.org/10.1029/1998JE000624

Christensen, P.R., Bandfield, J.L., Hamilton, V.E., Ruff, S.W., Kieffer, H.H., Titus, T.N., Malin, M.C., Morris, R.V., Lane, M.D., Clark, R.L., Jakosky, B.M., Mellon, M.T., Pearl, J.C., Conrath, B.J., Smith, M.D., Clancy, R.T., Kuzmin, R.O., Roush, T., Mehall, G.L., Gorelick, N., Bender, K., Murray, K., Dason, S., Greene, E., Silverman, S., Greenfield, M., 2001. Mars Global Surveyor Thermal Emission Spectrometer experiment: Investigation description and surface science results. Journal of Geophysical Research: Planets 106, 23823–23871. https://doi.org/10.1029/2000JE001370

Christensen, P.R., Engle, E., Anwar, S., Dickenshied, S., Noss, D., Gorelick, N., Weiss-Malik, M., 2009. JMARS - A Planetary GIS. AGU Fall Meeting Abstracts 22, IN22A-06.

Christensen, P.R., Fergason, R.L., Edwards, C.S., Hill, J., 2013. THEMIS-Derived Thermal Inertia Mosaic of Mars: Product Description and Science Results. Presented at the Lunar and Planetary Science Conference, p. 2822.

Christensen, P.R., Jakosky, B.M., Kieffer, H.H., Malin, M.C., McSween, H.Y., Nealson, K., Mehall, G.L., Silverman, S.H., Ferry, S., Caplinger, M., Ravine, M., 2004. The Thermal Emission Imaging System (THEMIS) for the Mars 2001 Odyssey Mission. Space Science Reviews 110, 85–130. https://doi.org/10.1023/B:SPAC.0000021008.16305.94

Christensen, Philip R. 1988. Global Albedo Variations on Mars: Implications for Active Aeolian Transport, Deposition, and Erosion. Journal of Geophysical Research: Solid Earth 93 (B7):7611–24. https://doi.org/10.1029/JB093iB07p07611.

Christensen, Philip R., 1998. Variations in Martian Surface Composition and Cloud Occurrence Determined from Thermal Infrared Spectroscopy: Analysis of Viking and Mariner 9 Data. Journal of Geophysical Research: Planets 103 (E1):1733–46. https://doi.org/10.1029/97JE02114.

Christensen, Philip R., Bruce M. Jakosky, Hugh H. Kieffer, Michael C. Malin, Harry Y. Mcsween Jr, Kenneth Nealson, Greg L. Mehall, et al., 2004. The Thermal Emission Imaging System (Themis) for the Mars 2001 Odyssey Mission. In 2001 Mars Odyssey, 85–130. Springer, Dordrecht. https://doi.org/10.1007/978-0-306-48600-5_3.

Christensen, Philip R., Joshua L. Bandfield, James F. Bell III, Noel Gorelick, Victoria E. Hamilton, Anton Ivanov, Bruce M. Jakosky, et al., 2003. Morphology and Composition of the Surface of Mars: Mars Odyssey THEMIS Results. Science 300 (5628):2056–61. https://doi.org/10.1126/science.1080885.

Clifford, S.M., 1993. A model for the hydrologic and climatic behavior of water on Mars. Journal of Geophysical Research: Planets 98, 10973–11016. https://doi.org/10.1029/93JE00225

Clifford, S.M., Lasue, J., Heggy, E., Boisson, J., McGovern, P., Max, M.D., 2010. Depth of the Martian cryosphere: Revised estimates and implications for the existence and detection of subpermafrost groundwater. Journal of Geophysical Research (Planets) 115, E07001. https://doi.org/10.1029/2009JE003462

Courville, S.W., Putzig, N.E., Hoover, R., Fenton, L.K., 2016. Thermophysical Variation within Dune Fields in the Southern Hemisphere of Mars. AGU Fall Meeting Abstracts 21, P21A-2073.

Craddock, R.A., Bandeira, L., Howard, A.D., 2018. An Assessment of Regional Variations in Martian Modified Impact Crater Morphology. Journal of Geophysical Research: Planets 123, 763–779. https://doi.org/10.1002/2017JE005412

Craddock, R.A., Maxwell, T.A., 2012. Resurfacing of the Martian Highlands in the Amenthes and Tyrrhena region. Journal of Geophysical Research: Solid Earth 14265–14278. https://doi.org/10.1029/JB095iB09p14265@10.1002/(ISSN)2169-9356.MARS4

Craddock, R.A., Maxwell, T.A., Howard, A.D., 1997. Crater morphometry and modification in the Sinus Sabaeus and Margaritifer Sinus regions of Mars. Journal of Geophysical Research: Planets 102, 13321–13340. https://doi.org/10.1029/97JE01084

Darwish, A., Leukert, K., Reinhardt, W., 2003. Image segmentation for the purpose of object-based classification, in: IGARSS 2003. 2003 IEEE International Geoscience and Remote Sensing Symposium. Proceedings (IEEE Cat. No.03CH37477). Presented at the IGARSS 2003. 2003 IEEE International Geoscience and Remote Sensing Symposium. Proceedings (IEEE Cat. No.03CH37477), pp. 2039–2041. https://doi.org/10.1109/IGARSS.2003.1294332

Davis, J.M., Balme, M., Grindrod, P.M., Williams, R.M.E., Gupta, S., 2016. Extensive Noachian fluvial systems in Arabia Terra: Implications for early Martian climate. Geology 44, 847–850. https://doi.org/10.1130/G38247.1

Davis, P.A., Soderblom, L.A., 1984. Modeling crater topography and albedo from monoscopic Viking Orbiter images: 1. Methodology. Journal of Geophysical Research: Solid Earth 89, 9449–9457. https://doi.org/10.1029/JB089iB11p09449

Delamere, W.A., Tornabene, L.L., McEwen, A.S., Becker, K., Bergstrom, J.W., Bridges, N.T., Eliason, E.M., Gallagher, D., Herkenhoff, K.E., Keszthelyi, L., Mattson, S., McArthur, G.K., Mellon, M.T., Milazzo, M., Russell, P.S., Thomas, N., 2010. Color imaging of Mars by the High Resolution Imaging Science Experiment (HiRISE). Icarus, MRO/HiRISE Studies of Mars 205, 38–52. https://doi.org/10.1016/j.icarus.2009.03.012

Delgado, F., Pavez, A., 2015. New insights into La Pacana caldera inner structure based on a gravimetric study (central Andes, Chile). Andean Geology 42, 313–328. https://doi.org/10.5027/andgeoV42n3-a02

Dinwiddie, Robert, Philip Eales, David Hughes, Iain Nicolson, Ian Ridpath, Robin Scagell, Giles Sparrow, Pam Spence, Carole Stott, and Kevin Tildsley., 2012. In Universe. edt. Martin Rees. Revised, Updated ed. edition. New York: DK.

Dohm, J.M., Barlow, N.G., Anderson, R.C., Williams, J.-P., Miyamoto, H., Ferris, J.C., Strom, R.G., Taylor, G.J., Fairén, A.G., Baker, V.R., Boynton, W.V., Keller, J.M., Kerry, K., Janes, D., Rodriguez, J.A.P., Hare, T.M., 2007. Possible ancient giant basin and related water enrichment in the Arabia Terra province, Mars. Icarus 190, 74–92. https://doi.org/10.1016/j.icarus.2007.03.006

Edgett, K.S., Christensen, P.R., 1991. The particle size of Martian aeolian dunes. Journal of Geophysical Research: Planets 96, 22765–22776. https://doi.org/10.1029/91JE02412

Edgett, K.S., Malin, M.C., 2000. New views of Mars eolian activity, materials, and surface properties: Three vignettes from the Mars Global Surveyor Mars Orbiter Camera. Journal of Geophysical Research: Planets 105, 1623–1650. https://doi.org/10.1029/1999JE001152

Edgett, K.S., Parker, T.J., 1997. Water on early Mars: Possible subaqueous sedimentary deposits covering ancient cratered terrain in western Arabia and Sinus Meridiani. Geophysical Research Letters 24, 2897–2900. https://doi.org/10.1029/97GL02840

Edwards, C. S., K. J. Nowicki, P. R. Christensen, J. Hill, N. Gorelick, and K. Murray., 2011. Mosaicking of Global Planetary Image Datasets: 1. Techniques and Data Processing for Thermal Emission Imaging System (THEMIS) Multi-Spectral Data. Journal of Geophysical Research: Planets 116 (E10):E10008. https://doi.org/10.1029/2010JE003755.

Edwards, C.S., Bandfield, J.L., Christensen, P.R., Fergason, R.L., 2009. Global distribution of bedrock exposures on Mars using THEMIS high-resolution thermal inertia. Journal of Geophysical Research: Planets 114. https://doi.org/10.1029/2009JE003363

Edwards, C.S., Christensen, P.R., Hill, J., 2014. Correction to "Mosaicking of global planetary image datasets: 2. Modeling of wind streak thicknesses observed in Thermal Emission Imaging System (THEMIS) daytime and nighttime infrared data." Journal of Geophysical Research: Planets 119, 1086–1087. https://doi.org/10.1002/2014JE004651

Edwards, C.S., Ehlmann, B.L., 2015. Carbon sequestration on Mars. Geology 43, 863–866. https://doi.org/10.1130/G36983.1

Edwards, C.S., Nowicki, K.J., Christensen, P.R., Hill, J., Gorelick, N., Murray, K., 2011. Mosaicking of global planetary image datasets: 1. Techniques and data processing for Thermal Emission Imaging System (THEMIS) multi-spectral data. Journal of Geophysical Research: Planets 116. https://doi.org/10.1029/2010JE003755

Ehlmann, B.L., Edwards, C.S., 2014. Mineralogy of the Martian Surface. Annual Review of Earth and Planetary Sciences 42, 291–315. https://doi.org/10.1146/annurev-earth-060313-055024

Ehlmann, B.L., Mustard, J.F., Swayze, G.A., Clark, R.N., Bishop, J.L., Poulet, F., Marais, D.J.D., Roach, L.H., Milliken, R.E., Wray, J.J., Barnouin-Jha, O., Murchie, S.L., 2009. Identification of hydrated silicate minerals on Mars using MRO-CRISM: Geologic context near Nili Fossae and implications for aqueous alteration. Journal of Geophysical Research: Planets 114. https://doi.org/10.1029/2009JE003339

Ehlmann, Bethany L., and John F. Mustard., 2012. An In-Situ Record of Major Environmental Transitions on Early Mars at Northeast Syrtis Major. Geophysical Research Letters 39 (11):L11202. https://doi.org/10.1029/2012GL051594

Ehlmann, Bethany L., John F. Mustard, Caleb I. Fassett, Samuel C. Schon, James W. Head III, David J. Des Marais, John A. Grant, and Scott L. Murchie., 2008. Clay Minerals in Delta Deposits and Organic Preservation Potential on Mars. Nature Geoscience 1 (6):ngeo207. https://doi.org/10.1038/ngeo207.

Ehlmann, Bethany L., John F. Mustard, Gregg A. Swayze, Roger N. Clark, Janice L. Bishop, Francois Poulet, David J. Des Marais, et al., 2009. Identification of Hydrated Silicate Minerals on Mars Using MRO-CRISM: Geologic Context near Nili Fossae and Implications for Aqueous Alteration. Journal of Geophysical Research: Planets 114 (E2):E00D08. https://doi.org/10.1029/2009JE003339.

Elbelrhiti, H., Andreotti, B., Claudin, P., 2008. Barchan dune corridors: Field characterization and investigation of control parameters. Journal of Geophysical Research: Earth Surface 113 (F2). https://doi.org/10.1029/2007JF000767

Emran, A., King, D.T., Jr., Marzen, L.J., 2018b. Surficial Geology of Siloe Patera at Arabia Terra, Mars. AGU Fall Meeting Abstracts 53.

Emran, A., King, D.T., Marzen, L.J., Coker, C.W., Wright, S.P., 2018a. Remote Sensing Characterization of Siloe Patera, Mars. LPI Contributions 2066, 7017.

Emran, A., Marzen, L.J., King, D.T., 2019. Automated Object-Based Identification of Dunes at Hargraves Crater, Mars. Presented at the Lunar and Planetary Science Conference, p. 1157.

Ewing, R.C., Kocurek, G., Lake, L.W., 2006. Pattern analysis of dune-field parameters. Earth Surface Processes and Landforms 31, 1176–1191. https://doi.org/10.1002/esp.1312

Fassett, C.I., Dickson, J.L., Head, J.W., Levy, J.S., Marchant, D.R., 2010. Supraglacial and proglacial valleys on Amazonian Mars. Icarus 208, 86–100. https://doi.org/10.1016/j.icarus.2010.02.021

Fassett, C.I., Head, J.W., 2007. Layered mantling deposits in northeast Arabia Terra, Mars: Noachian-Hesperian sedimentation, erosion, and terrain inversion. Journal of Geophysical Research: Planets 112. https://doi.org/10.1029/2006JE002875

Fassett, C.I., Head, J.W., 2008. Valley network-fed, open-basin lakes on Mars: Distribution and implications for Noachian surface and subsurface hydrology. Icarus 198, 37–56. https://doi.org/10.1016/j.icarus.2008.06.016

Fassett, Caleb I., and James W. Head., 2005. Fluvial Sedimentary Deposits on Mars: Ancient Deltas in a Crater Lake in the Nili Fossae Region. Geophysical Research Letters 32 (14):L14201. https://doi.org/10.1029/2005GL023456.

Fastook, J.L., Head, J.W., 2008. Dichotomy Boundary Glaciation Models: Implications for Timing and Glacial Processes. AGU Fall Meeting Abstracts 41, P41A-1354.

Faure, G and T.M. Mensing., 2008. Introduction to Planetary Science: The Geological Prspective. Springer Netherlands. doi 10.1007/978-1-4020-5544-7

Feely, K.C., Christensen, P.R., 1999. Quantitative compositional analysis using thermal emission spectroscopy: Application to igneous and metamorphic rocks. Journal of Geophysical Research: Planets 104, 24195–24210. https://doi.org/10.1029/1999JE001034

Fenton, L. K., Gullikson, A. L., Hayward, R. K., Charles, H., Titus, T. N., 2019. The Mars Global Digital Dune Database (MGD^3): Composition and Stability. Presented at the Lunar and Planetary Science Conference, p. 1115.

Fenton, L.K., Hayward, R.K., 2010. Southern high latitude dune fields on Mars: Morphology, aeolian inactivity, and climate change. Geomorphology, Planetary Dune Systems 121, 98–121. https://doi.org/10.1016/j.geomorph.2009.11.006

Fenton, L.K., Michaels, T.I., Beyer, R.A., 2014a. Inverse maximum gross bedform-normal transport 1: How to determine a dune-constructing wind regime using only imagery. Icarus, Third Planetary Dunes Systems 230, 5–14. https://doi.org/10.1016/j.icarus.2013.04.001

Fenton, L.K., Michaels, T.I., Chojnacki, M., Beyer, R.A., 2014b. Inverse maximum gross bedform-normal transport 2: Application to a dune field in Ganges Chasma, Mars and comparison with HiRISE repeat imagery and MRAMS. Icarus, Third Planetary Dunes Systems 230, 47–63. https://doi.org/10.1016/j.icarus.2013.07.009

Fenton, L.K., Toigo, A.D., Richardson, M.I., 2005. Aeolian processes in Proctor Crater on Mars: Mesoscale modeling of dune-forming winds. Journal of Geophysical Research (Planets) 110, E06005. https://doi.org/10.1029/2004JE002309

Fergason, R.L, Hare, T.M., Laura, J., 2018. HRSC and MOLA blended digital elevation model at 200m v2, Astrogeology PDS Annex, U.S.

Fergason, R.L., Christensen, P.R., 2008. Formation and erosion of layered materials: Geologic and dust cycle history of eastern Arabia Terra, Mars. Journal of Geophysical Research: Planets 113. https://doi.org/10.1029/2007JE002973

Fergason, R.L., Christensen, P.R., Kieffer, H.H., 2006. High-resolution thermal inertia derived from the Thermal Emission Imaging System (THEMIS): Thermal model and applications. Journal of Geophysical Research: Planets 111. https://doi.org/10.1029/2006JE002735

Fergason, R.L., Laura, J.R., Hare, T.M., 2017. THEMIS-derived thermal inertia on Mars: Improved and flexible algorithm. Lunar and Planetary Science, XLVIII, Abstract #1563.

Fisher, P., 1997. The pixel: A snare and a delusion. International Journal of Remote Sensing 18, 679–685. https://doi.org/10.1080/014311697219015

Foody, G.M., 2002. Status of land cover classification accuracy assessment. Remote Sensing of Environment 80, 185–201. https://doi.org/10.1016/S0034-4257(01)00295-4

Forget, F., Haberle, R.M., Montmessin, F., Levrard, B., Head, J.W., 2006. Formation of Glaciers on Mars by Atmospheric Precipitation at High Obliquity. Science 311, 368–371. https://doi.org/10.1126/science.1120335

Fraeman, A.A., Ehlmann, B.L., Arvidson, R.E., Edwards, C.S., Grotzinger, J.P., Milliken, R.E., Quinn, D.P., Rice, M.S., 2016. The stratigraphy and evolution of lower Mount Sharp from spectral, morphological, and thermophysical orbital data sets. Journal of Geophysical Research: Planets 121, 1713–1736. https://doi.org/10.1002/2016JE005095

Francis, P., 1993. Volcanoes. A planetary perspective. Oxford (UK): Clarendon Press.

Francis, P.W., Wood, C.A., 1982. Absence of silicic volcanism on Mars: Implications for crustal composition and volatile abundance. Journal of Geophysical Research: Solid Earth 87, 9881–9889. https://doi.org/10.1029/JB087iB12p09881

Garcia, G.C., 2018. Identifying Evidence for Explosive Volcanism on Mars Through Geomorphologic and Thermophysical Observations. Unpublished MS Thesis, Boise State University, Boise, Idaho, USA.

Gardin, E., Allemand, P., Quantin, C., Silvestro, S., Delacourt, C., 2012. Dune fields on Mars: Recorders of a climate change? Planetary and Space Science, Titan Through Time: A Workshop on Titan's Formation, Evolution and Fate 60, 314–321. https://doi.org/10.1016/j.pss.2011.10.004

Gillespie, A.R., Kahle, A.B., Walker, R.E., 1986. Color enhancement of highly correlated images. I. Decorrelation and HSI contrast stretches. Remote Sensing of Environment 20, 209–235. https://doi.org/10.1016/0034-4257(86)90044-1

Gillespie, Alan R., 1992. Enhancement of Multispectral Thermal Infrared Images: Decorrelation Contrast Stretching. Remote Sensing of Environment 42 (2):147–55. https://doi.org/10.1016/0034-4257(92)90098-5.

Glotch, T.D., Christensen, P.R., 2005. Geologic and mineralogic mapping of Aram Chaos: Evidence for a water-rich history. Journal of Geophysical Research: Planets 110. https://doi.org/10.1029/2004JE002389

Glotch, T.D., Morris, R.V., Christensen, P.R., Sharp, T.G., 2004. Effect of precursor mineralogy on the thermal infrared emission spectra of hematite: Application to Martian hematite mineralization. Journal of Geophysical Research: Planets 109. https://doi.org/10.1029/2003JE002224

Golder, K., 2013. Geomorphology of Eridania Basin, Mars: A Study of the Evolution of Chaotic Terrain and a Paleolake. Masters Theses. Wesleyan University, Connecticut, USA.

Goudge, T. A., B. L. Ehlmann, C. I. Fassett, J. W. Head, J. F. Mustard, N. Mangold, S. Gupta, R. E. Milliken,and A. J., 2017b. Jezero Crater, Mars, as a Compelling Site for Future In Situ Exploration. In 48th Lunar and Planetary Science Conference, 20-24 Mar. 2017. The Woodlands, TX; United States. https://ntrs.nasa.gov/search.jsp?R=20170002464.

Goudge, T.A., Milliken, R.E., Head, J.W., Mustard, J.F., Fassett, C.I., 2017. Sedimentological evidence for a deltaic origin of the western fan deposit in Jezero crater, Mars and implications for future exploration. Earth and Planetary Science Letters 458, 357–365. https://doi.org/10.1016/j.epsl.2016.10.056

Goudge, T.A., Mustard, J.F., Head, J.W., Fassett, C.I., Wiseman, S.M., 2015. Assessing the mineralogy of the watershed and fan deposits of the Jezero crater paleolake system, Mars. Journal of Geophysical Research: Planets 120, 775–808. https://doi.org/10.1002/2014JE004782

Goudge, Timothy A., John F. Mustard, James W. Head, Mark R. Salvatore, and Sandra M. Wiseman., 2015a. Integrating CRISM and TES Hyperspectral Data to Characterize a Halloysite-Bearing Deposit in Kashira Crater, Mars. Icarus 250 (Supplement C):165–87. https://doi.org/10.1016/j.icarus.2014.11.034.

Goudge, Timothy A., Ralph E. Milliken, James W. Head, John F. Mustard, and Caleb I. Fassett., 2017a. Sedimentological Evidence for a Deltaic Origin of the Western Fan Deposit in Jezero Crater, Mars and Implications for Future Exploration. Earth and Planetary Science Letters 458 (Supplement C):357–65. https://doi.org/10.1016/j.epsl.2016.10.056.

Grant, J.A., Schultz, P.H., 1990. Gradational epochs on Mars: Evidence from West-Northwest of Isidis Basin and Electris. Icarus 84, 166–195. https://doi.org/10.1016/0019-1035(90)90164-5

Greeley, R., Bridges, N.T., Kuzmin, R.O., Laity, J.E., 2002. Terrestrial analogs to wind-related features at the Viking and Pathfinder landing sites on Mars. Journal of Geophysical Research: Planets 107, 5-1-5–22. https://doi.org/10.1029/2000JE001481

Greeley, R., Iversen, J.D., 1987. Wind as a Geological Process: On Earth, Mars, Venus and Titan. Cambridge University Press, Cambridge.

Greeley, R., Kraft, M., Sullivan, R., Wilson, G., Bridges, N., Herkenhoff, K., Kuzmin, R.O., Malin, M., Ward, W., 1999. Aeolian features and processes at the Mars Pathfinder landing site. Journal of Geophysical Research: Planets 104, 8573–8584. https://doi.org/10.1029/98JE02553

Greeley, R., Kuzmin, R.O., Haberle, R.M., 2001. Aeolian Processes and their Effects on Understanding the Chronology of Mars. Space Science Reviews 96, 393–404. https://doi.org/10.1023/A:1011917910624

Greeley, R., Spudis, P.D., 1981. Volcanism on Mars. Reviews of Geophysics 19, 13–41. https://doi.org/10.1029/RG019i001p00013

Greeley, R., Thompson, S.D., 2003. Mars: Aeolian features and wind predictions at the Terra Meridiani and Isidis Planitia potential Mars Exploration Rover landing sites. Journal of Geophysical Research (Planets) 108, 8093. https://doi.org/10.1029/2003JE002110

Gulick, V.C., 2001. Origin of the valley networks on Mars: a hydrological perspective. Geomorphology 37, 241–268. https://doi.org/10.1016/S0169-555X(00)00086-6

Gullikson, A.L., Hayward, R.K., Titus, T.N., Charles, H., Fenton, L.K., Hoover, R.H., Putzig, N.E., 2018. Mars global digital dune database (MGD3)—Composition, stability, and thermal inertia (USGS Numbered Series No. 2018–1164), Open-File Report. U.S. Geological Survey, Reston, VA.

Gupta, R.P., 1991. Remote Sensing Geology. Springer-Verlag, Berlin Heidelberg.

Gwinner, K., R. Jaumann, E. Hauber, H. Hoffmann, C. Heipke, J. Oberst, G. Neukum, et al., 2016. The High Resolution Stereo Camera (HRSC) of Mars Express and Its Approach to Science Analysis and Mapping for Mars and Its Satellites. Planetary and Space Science 126 (July): 93–138. https://doi.org/10.1016/j.pss.2016.02.014.

Haberle, Robert M., and Bruce M. Jakosky., 1991. Atmospheric Effects on the Remote Determination of Thermal Inertia on Mars. Icarus 90 (2):187–204. https://doi.org/10.1016/0019-1035(91)90100-8.

Hartmann, W.K., Neukum, G., 2001. Cratering Chronology and the Evolution of Mars. Space Science Reviews 96, 165–194. https://doi.org/10.1023/A:1011945222010

Hay, G.J., Castilla, G., 2008. Geographic Object-Based Image Analysis (GEOBIA): A new name for a new discipline, in: Object-Based Image Analysis, Lecture Notes in Geoinformation and Cartography. Springer, Berlin, Heidelberg, pp. 75–89. https://doi.org/10.1007/978-3-540-77058-9_4

Hayashi, Joan N., Bruce M. Jakosky, and Robert M. Haberle., 1995. Atmospheric Effects on the Mapping of Martian Thermal Inertia and Thermally Derived Albedo. Journal of Geophysical Research: Planets 100 (E3):5277–84. https://doi.org/10.1029/94JE02449.

Hayward, R.K., Fenton, L., Titus, T.N., 2014. Mars Global Digital Dune Database (MGD3): Global dune distribution and wind pattern observations. Icarus 230, 9. https://doi.org/10.1016/j.icarus.2013.04.011

Hayward, R.K., Mullins, K.F., Fenton, L.K., Hare, T.M., Titus, T.N., Bourke, M.C., Colaprete, A., Christensen, P.R., 2007. Mars global digital dune database and initial science results. Journal of Geophysical Research E: Planets 112. https://doi.org/10.1029/2007JE002943

Hayward, R.K., Titus, T.N., Michaels, T.I., Fenton, L.K., Colaprete, A., Christensen, P.R., 2009. Aeolian dunes as ground truth for atmospheric modeling on Mars. Journal of Geophysical Research E: Planets 114. https://doi.org/10.1029/2009JE003428

Head, J.W., Hiesinger, H., Ivanov, M.A., Kreslavsky, M.A., Pratt, S., Thomson, B.J., 1999. Possible Ancient Oceans on Mars: Evidence from Mars Orbiter Laser Altimeter Data. Science 286, 2134–2137. https://doi.org/10.1126/science.286.5447.2134

Head, J.W., Marchant, D.R., 2009. Inventory of Ice-related Deposits on Mars: Evidence for Burial and Long-Term Sequestration of Ice in Non-Polar Regions and Implications for the Water Budget and Climate Evolution. Presented at the Lunar and Planetary Science Conference, p. 1356.

Head, J.W., Marchant, D.R., Agnew, M.C., Fassett, C.I., Kreslavsky, M.A., 2006. Extensive valley glacier deposits in the northern mid-latitudes of Mars: Evidence for Late Amazonian obliquity-driven climate change. Earth and Planetary Science Letters 241, 663–671. https://doi.org/10.1016/j.epsl.2005.11.016

Head, J.W., Mustard, J.F., Kreslavsky, M.A., Milliken, R.E., Marchant, D.R., 2003. Recent ice ages on Mars. Nature 426, 797. https://doi.org/10.1038/nature02114

Hill, J., Edwards, C.S., Christensen, P.R., 2014. Mapping the Martian Surface with THEMIS Global Infrared Mosaics. Presented at the Eighth International Conference on Mars, p. 1141.

Hill, J.R., Christensen, P.R., 2017. Well-preserved low thermal inertia ejecta deposits surrounding young secondary impact craters on Mars. Journal of Geophysical Research: Planets 122, 1276–1299. https://doi.org/10.1002/2016JE005210

Hooper, D.M., McGinnis, R.N., Necsoiu, M., 2012. Volcaniclastic aeolian deposits at Sunset Crater, Arizona: terrestrial analogs for Martian dune forms. Earth Surface Processes and Landforms 37, 1090–1105. https://doi.org/10.1002/esp.3238

Howard, A.D., 1994. A detachment-limited model of drainage basin evolution. Water Resources Research 30, 2261–2285. https://doi.org/10.1029/94WR00757

Howard, Alan D., Jeffrey M. Moore, and Rossman P. Irwin., 2005. An Intense Terminal Epoch of Widespread Fluvial Activity on Early Mars: 1. Valley Network Incision and Associated

Deposits. Journal of Geophysical Research: Planets 110 (E12):E12S14. https://doi.org/10.1029/2005JE002459.
Hoyt, W.G., Wesley, W.G., 1977. Lowell and Mars. American Journal of Physics 45, 316–317. https://doi.org/10.1119/1.10630
Huang, J., Edwards, C.S., Ruff, S.W., Christensen, P.R., Xiao, L., 2013. A new method for the semiquantitative determination of major rock-forming minerals with thermal infrared multispectral data: Application to THEMIS infrared data. Journal of Geophysical Research: Planets 118, 2146–2152. https://doi.org/10.1002/jgre.20160
Hugenholtz, C.H., Levin, N., Barchyn, T.E., Baddock, M.C., 2012. Remote sensing and spatial analysis of aeolian sand dunes: A review and outlook. Earth-Science Reviews 111, 319–334. https://doi.org/10.1016/j.earscirev.2011.11.006
Hulme, G., 1974. The Interpretation of Lava Flow Morphology. Geophysical Journal of the Royal Astronomical Society 39, 361–383. https://doi.org/10.1111/j.1365-246X.1974.tb05460.x
Hunt, G., 1977. Spectral signatures of particulate minerals in the visible and near infrared. GEOPHYSICS 42, 501–513. https://doi.org/10.1190/1.1440721
Hynek, B.M., Phillips, R.J., 2001. Evidence for extensive denudation of the Martian highlands. Geology 29, 407–410. https://doi.org/10.1130/0091-7613(2001)029<0407:EFEDOT>2.0.CO;2
Hynek, B.M., Phillips, R.J., 2003. New data reveal mature, integrated drainage systems on Mars indicative of past precipitation. Geology 31, 757–760. https://doi.org/10.1130/G19607.1
Hynek, B.M., Phillips, R.J., Arvidson, R.E., 2003. Explosive volcanism in the Tharsis region: Global evidence in the Martian geologic record. Journal of Geophysical Research: Planets 108. https://doi.org/10.1029/2003JE002062
Irwin, R.P., Howard, A.D., Maxwell, T.A., 2004. Geomorphology of Ma'adim Vallis, Mars, and associated paleolake basins. Journal of Geophysical Research: Planets 109. https://doi.org/10.1029/2004JE002287
Irwin, Rossman P., Alan D. Howard, Robert A. Craddock, and Jeffrey M. Moore., 2005. An Intense Terminal Epoch of Widespread Fluvial Activity on Early Mars: 2. Increased Runoff and Paleolake Development. Journal of Geophysical Research: Planets 110 (E12):E12S15. https://doi.org/10.1029/2005JE002460.
Ivanov, M.A., Hiesinger, H., Erkeling, G., Hielscher, F.J., Reiss, D., 2012. Major episodes of geologic history of Isidis Planitia on Mars. Icarus 218, 24–46. https://doi.org/10.1016/j.icarus.2011.11.029
Jakosky, B.M., Mellon, M.T., Kieffer, H.H., Christensen, P.R., Varnes, E.S., Lee, S.W., 2000. The thermal inertia of Mars from the Mars Global Surveyor Thermal Emission Spectrometer. Journal of Geophysical Research: Planets 105, 9643–9652. https://doi.org/10.1029/1999JE001088
Jakosky, Bruce M. 1986. On the Thermal Properties of Martian Fines. *Icarus* 66 (1):117–24. https://doi.org/10.1016/0019-1035(86)90011-4.
Jakosky, Bruce M., Michael T. Mellon, Hugh H. Kieffer, Philip R. Christensen, E. Stacy Varnes, and Steven W. Lee., 2000. The Thermal Inertia of Mars from the Mars Global Surveyor Thermal Emission Spectrometer. Journal of Geophysical Research: Planets 105 (E4):9643–52. https://doi.org/10.1029/1999JE001088.
Jarell, Elizabeth M., 2015. Using Curiosity to Search for Life. Mars Daily. Last Accessed October 25, 2017. http://www.marsdaily.com/reports/Using_Curiosity_to_Search_for_Life_
Jaumann, R., G. Neukum, T. Behnke, T. C. Duxbury, K. Eichentopf, J. Flohrer, S. v. Gasselt, et al., 2007. The High-Resolution Stereo Camera (HRSC) Experiment on Mars Express: Instrument

Aspects and Experiment Conduct from Interplanetary Cruise through the Nominal Mission. Planetary and Space Science 55 (7): 928–52. https://doi.org/10.1016/j.pss.2006.12.003.

Jaumann, R., Tirsch, D., Hauber, E., Ansan, V., Di Achille, G., Erkeling, G., Fueten, F., Head, J., Kleinhans, M.G., Mangold, N., Michael, G.G., Neukum, G., Pacifici, A., Platz, T., Pondrelli, M., Raack, J., Reiss, D., Williams, D.A., Adeli, S., Baratoux, D., de Villiers, G., Foing, B., Gupta, S., Gwinner, K., Hiesinger, H., Hoffmann, H., Deit, L.L., Marinangeli, L., Matz, K.-D., Mertens, V., Muller, J.P., Pasckert, J.H., Roatsch, T., Rossi, A.P., Scholten, F., Sowe, M., Voigt, J., Warner, N., 2015. Quantifying geological processes on Mars—Results of the high resolution stereo camera (HRSC) on Mars express. Planetary and Space Science 112, 53–97. https://doi.org/10.1016/j.pss.2014.11.029

Jerolmack, D.J., Mohrig, D., Grotzinger, J.P., Fike, D.A., Watters, W.A., 2006. Spatial grain size sorting in eolian ripples and estimation of wind conditions on planetary surfaces: Application to Meridiani Planum, Mars. Journal of Geophysical Research: Planets 111. https://doi.org/10.1029/2005JE002544

Johnson, J.R., Hörz, F., Lucey, P.G., Christensen, P.R., 2002. Thermal infrared spectroscopy of experimentally shocked anorthosite and pyroxenite: Implications for remote sensing of Mars. Journal of Geophysical Research: Planets 107, 3-1-3–14. https://doi.org/10.1029/2001JE001517

Jones, A.P., McEwen, A.S., Tornabene, L.L., Baker, V.R., Melosh, H.J., Berman, D.C., 2011. A geomorphic analysis of Hale crater, Mars: The effects of impact into ice-rich crust. Icarus 211, 259–272. https://doi.org/10.1016/j.icarus.2010.10.014

Kerber, L., Head, J.W., 2012. A progression of induration in Medusae Fossae Formation transverse aeolian ridges: evidence for ancient aeolian bedforms and extensive reworking. Earth Surface Processes and Landforms 37, 422–433. https://doi.org/10.1002/esp.2259

Kerber, L., Head, J.W., Madeleine, J.-B., Forget, F., Wilson, L., 2012. The dispersal of pyroclasts from ancient explosive volcanoes on Mars: Implications for the friable layered deposits. Icarus 219, 358–381. https://doi.org/10.1016/j.icarus.2012.03.016

Kieffer, H. H., S. C. Chase, E. Miner, G. Münch, and G. Neugebauer., 1973. Preliminary Report on Infrared Radiometric Measurements from the Mariner 9 Spacecraft. Journal of Geophysical Research 78 (20):4291–4312. https://doi.org/10.1029/JB078i020p04291.

Kieffer, H.H., Martin, T.Z., Peterfreund, A.R., Jakosky, B.M., Miner, E.D., Palluconi, F.D., 1977. Thermal and albedo mapping of Mars during the Viking primary mission. Journal of Geophysical Research 82, 4249–4291. https://doi.org/10.1029/JS082i028p04249

Kirk, R. L., E. Howington-Kraus, M. R. Rosiek, J. A. Anderson, B. A. Archinal, K. J. Becker, D. A. Cook, et al., 2008. Ultrahigh Resolution Topographic Mapping of Mars with MRO HiRISE Stereo Images: Meter-Scale Slopes of Candidate Phoenix Landing Sites. Journal of Geophysical Research: Planets 113 (E3): E00A24. https://doi.org/10.1029/2007JE003000.

Kocurek, G., Ewing, R.C., 2005. Aeolian dune field self-organization – implications for the formation of simple versus complex dune-field patterns. Geomorphology 72, 94–105. https://doi.org/10.1016/j.geomorph.2005.05.005

Koeppen, W.C., Hamilton, V.E., 2008. Global distribution, composition, and abundance of olivine on the surface of Mars from thermal infrared data. Journal of Geophysical Research: Planets 113. https://doi.org/10.1029/2007JE002984

Kreslavsky, M.A., Head, J.W., 2002. Mars: Nature and evolution of young latitude-dependent water-ice-rich mantle. Geophysical Research Letters 29, 14-1-14–4. https://doi.org/10.1029/2002GL015392

Kuzmin, R.O., 2005. 7 Ground Ice in the Martian Regolith, in: Tokano, T. (Ed.), Water on Mars and Life, Advances in Astrobiology and Biogeophysics. Springer Berlin Heidelberg, Berlin, Heidelberg, pp. 155–189. https://doi.org/10.1007/978-3-540-31538-4_7

Lapotre, M.G.A., Ehlmann, B.L., Minson, S.E., Arvidson, R.E., Ayoub, F., Fraeman, A.A., Ewing, R.C., Bridges, N.T., 2017. Compositional variations in sands of the Bagnold Dunes, Gale crater, Mars, from visible-shortwave infrared spectroscopy and comparison with ground truth from the Curiosity rover. Journal of Geophysical Research: Planets 122, 2489–2509. https://doi.org/10.1002/2016JE005133

Lapotre, M.G.A., Ewing, R.C., Weitz, C.M., Lewis, K.W., Lamb, M.P., Ehlmann, B.L., Rubin, D.M., 2018. Morphologic Diversity of Martian Ripples: Implications for Large-Ripple Formation. Geophysical Research Letters 45, 10,229-10,239. https://doi.org/10.1029/2018GL079029

Laura, J., Fergason, R.L., 2016. Modeling martian thermal inertia in a distributed memory high performance computing environment, in: 2016 IEEE International Conference on Big Data (Big Data). Presented at the 2016 IEEE International Conference on Big Data (Big Data), pp. 2919–2928. https://doi.org/10.1109/BigData.2016.7840942

Lawson, C.L., Hanson, R.J., 1995. Solving Least Squares Problems. Prentice-Hall, Englewood Cliffs, NJ, pp 340.

Levy, J., Head, J., Marchant, D., 2009a. Thermal contraction crack polygons on Mars: Classification, distribution, and climate implications from HiRISE observations. Journal of Geophysical Research: Planets 114. https://doi.org/10.1029/2008JE003273

Levy, J., Head, J.W., Marchant, D.R., 2010. Concentric crater fill in the northern mid-latitudes of Mars: Formation processes and relationships to similar landforms of glacial origin. Icarus 209, 390–404. https://doi.org/10.1016/j.icarus.2010.03.036

Levy, J.S., Fassett, C.I., Head, J.W., Schwartz, C., Watters, J.L., 2014. Sequestered glacial ice contribution to the global Martian water budget: Geometric constraints on the volume of remnant, midlatitude debris-covered glaciers. Journal of Geophysical Research: Planets 119, 2188–2196. https://doi.org/10.1002/2014JE004685

Levy, J.S., Head, J.W., Marchant, D.R., 2009b. Concentric crater fill in Utopia Planitia: History and interaction between glacial "brain terrain" and periglacial mantle processes. Icarus 202, 462–476. https://doi.org/10.1016/j.icarus.2009.02.018

Levy, J.S., Marchant, D.R., Head, J.W., 2006. Distribution and origin of patterned ground on Mullins Valley debris-covered glacier, Antarctica: the roles of ice flow and sublimation. Antarctic Science 18, 385–397. https://doi.org/10.1017/S0954102006000435

Lewis, Kevin W., and Oded Aharonson., 2006. Stratigraphic Analysis of the Distributary Fan in Eberswalde Crater Using Stereo Imagery. Journal of Geophysical Research: Planets 111 (E6):E06001. https://doi.org/10.1029/2005JE002558.

Lorenz, R.D., Wall, S., Radebaugh, J., Boubin, G., Reffet, E., Janssen, M., Stofan, E., Lopes, R., Kirk, R., Elachi, C., Lunine, J., Mitchell, K., Paganelli, F., Soderblom, L., Wood, C., Wye, L., Zebker, H., Anderson, Y., Ostro, S., Allison, M., Boehmer, R., Callahan, P., Encrenaz, P., Ori, G.G., Francescetti, G., Gim, Y., Hamilton, G., Hensley, S., Johnson, W., Kelleher, K., Muhleman, D., Picardi, G., Posa, F., Roth, L., Seu, R., Shaffer, S., Stiles, B., Vetrella, S., Flamini, E., West, R., 2006. The Sand Seas of Titan: Cassini RADAR Observations of Longitudinal Dunes. Science 312, 724–727. https://doi.org/10.1126/science.1123257

Malin, M.C., Bell, J.F., Cantor, B.A., Caplinger, M.A., Calvin, W.M., Clancy, R.T., Edgett, K.S., Edwards, L., Haberle, R.M., James, P.B., Lee, S.W., Ravine, M.A., Thomas, P.C., Wolff, M.J.,

2007. Context Camera Investigation on board the Mars Reconnaissance Orbiter. Journal of Geophysical Research (Planets) 112, E05S04. https://doi.org/10.1029/2006JE002808

Malin, M.C., Bell, J.F., Cantor, B.A., Caplinger, M.A., Calvin, W.M., Clancy, R.T., Edgett, K.S., Edwards, L., Haberle, R.M., James, P.B., Lee, S.W., Ravine, M.A., Thomas, P.C., Wolff, M.J., 2007. Context Camera Investigation on board the Mars Reconnaissance Orbiter. Journal of Geophysical Research: Planets 112. https://doi.org/10.1029/2006JE002808

Malin, M.C., Danielson, G.E., Ingersoll, A.P., Masursky, H., Veverka, J., Ravine, M.A., Soulanille, T.A., 1992. Mars Observer camera. Journal of Geophysical Research: Planets 97, 7699–7718. https://doi.org/10.1029/92JE00340

Malin, Michael C., and Kenneth S. Edgett., 2003. Evidence for Persistent Flow and Aqueous Sedimentation on Early Mars. Science 302 (5652):1931–34. https://doi.org/10.1126/science.1090544.

Malin, Michael C., James F. Bell, Bruce A. Cantor, Michael A. Caplinger, Wendy M. Calvin, R. Todd Clancy, Kenneth S. Edgett, et al., 2007. Context Camera Investigation on Board the Mars Reconnaissance Orbiter. Journal of Geophysical Research: Planets 112 (E5):E05S04. https://doi.org/10.1029/2006JE002808.

Mangold, N., 2012. Fluvial landforms on fresh impact ejecta on Mars. Planetary and Space Science 62, 69–85. https://doi.org/10.1016/j.pss.2011.12.009

Mangold, N., Allemand, P., 2001. Topographic analysis of features related to ice on Mars. Geophysical Research Letters 28, 407–410. https://doi.org/10.1029/2000GL008491

Mangold, N., Baratoux, D., Arnalds, O., Bardintzeff, J.-M., Platevoet, B., Grégoire, M., Pinet, P., 2011. Segregation of olivine grains in volcanic sands in Iceland and implications for Mars. Earth and Planetary Science Letters 310, 233–243. https://doi.org/10.1016/j.epsl.2011.07.025

Mangold, N., F. Poulet, J. F. Mustard, J.-P. Bibring, B. Gondet, Y. Langevin, V. Ansan, et al., 2007. Mineralogy of the Nili Fossae Region with OMEGA/Mars Express Data: 2. Aqueous Alteration of the Crust. Journal of Geophysical Research: Planets 112 (E8):E08S04. https://doi.org/10.1029/2006JE002835.

Mangold, N., Poulet, F., Mustard, J.F., Bibring, J.-P., Gondet, B., Langevin, Y., Ansan, V., Masson, P., Fassett, C., Head, J.W., Hoffmann, H., Neukum, G., 2007. Mineralogy of the Nili Fossae region with OMEGA/Mars Express data: 2. Aqueous alteration of the crust. Journal of Geophysical Research: Planets 112. https://doi.org/10.1029/2006JE002835

Mangold, N., Poulet, F., Mustard, J.F., Bibring, J.-P., Gondet, B., Langevin, Y., Ansan, V., Masson, P., Fassett, C., Head, J.W., Hoffmann, H., Neukum, G., 2007. Mineralogy of the Nili Fossae region with OMEGA/Mars Express data: 2. Aqueous alteration of the crust. Journal of Geophysical Research: Planets 112. https://doi.org/10.1029/2006JE002835

Marchant, D.R., Head, J.W., 2007. Antarctic dry valleys: Microclimate zonation, variable geomorphic processes, and implications for assessing climate change on Mars. Icarus 192, 187–222. https://doi.org/10.1016/j.icarus.2007.06.018

Marchant, D.R., Lewis, A.R., Phillips, W.M., Moore, E.J., Souchez, R.A., Denton, G.H., Sugden, D.E., Potter, N., Landis, G.P., 2002. Formation of patterned ground and sublimation till over Miocene glacier ice in Beacon Valley, southern Victoria Land, Antarctica. GSA Bulletin 114, 718–730. https://doi.org/10.1130/0016-7606(2002)114<0718:FOPGAS>2.0.CO;2

McEwen, A.S., Eliason, E.M., Bergstrom, J.W., Bridges, N.T., Hansen, C.J., Delamere, W.A., Grant, J.A., Gulick, V.C., Herkenhoff, K.E., Keszthelyi, L., Kirk, R.L., Mellon, M.T., Squyres, S.W., Thomas, N., Weitz, C.M., 2007. Mars Reconnaissance Orbiter's High Resolution Imaging Science Experiment (HiRISE). Journal of Geophysical Research: Planets 112. https://doi.org/10.1029/2005JE002605

McGill, G.E., 2000. Crustal history of north central Arabia Terra, Mars. Journal of Geophysical Research: Planets 105, 6945–6959. https://doi.org/10.1029/1999JE001175

McGuire, P.C., Bishop, J.L., Brown, A.J., Fraeman, A.A., Marzo, G.A., Frank Morgan, M., Murchie, S.L., Mustard, J.F., Parente, M., Pelkey, S.M., Roush, T.L., Seelos, F.P., Smith, M.D., Wendt, L., Wolff, M.J., 2009. An improvement to the volcano-scan algorithm for atmospheric correction of CRISM and OMEGA spectral data. Planetary and Space Science 57, 809–815. https://doi.org/10.1016/j.pss.2009.03.007

Mellon, M.T., 1997. Small-scale polygonal features on Mars: Seasonal thermal contraction cracks in permafrost. Journal of Geophysical Research: Planets 102, 25617–25628. https://doi.org/10.1029/97JE02582

Mellon, M.T., Jakosky, B.M., Kieffer, H.H., Christensen, P.R., 2000. High-Resolution Thermal Inertia Mapping from the Mars Global Surveyor Thermal Emission Spectrometer. Icarus 148, 437–455. https://doi.org/10.1006/icar.2000.6503

Mellon, Michael T., and Bruce M. Jakosky., 1993. Geographic Variations in the Thermal and Diffusive Stability of Ground Ice on Mars. Journal of Geophysical Research: Planets 98 (E2):3345–64. https://doi.org/10.1029/92JE02355.

MER., 2013. The Mars Exploration Rover Mission. NASA Report. November 2013, 20. Last Accessed October 25, 2017. https://mars.nasa.gov/mer/home/resources/

Meresse, S., Costard, F., Mangold, N., Masson, P., Neukum, G., 2008. Formation and evolution of the chaotic terrains by subsidence and magmatism: Hydraotes Chaos, Mars. Icarus 194, 487–500. https://doi.org/10.1016/j.icarus.2007.10.023MERLithograph.pdf

Michael, G.G., 2013. Planetary surface dating from crater size–frequency distribution measurements: Multiple resurfacing episodes and differential isochron fitting. Icarus 226, 885–890. https://doi.org/10.1016/j.icarus.2013.07.004

Michalski, J.R., Bleacher, J.E., 2013. Supervolcanoes within an ancient volcanic province in Arabia Terra, Mars. Nature 502, 47–52. https://doi.org/10.1038/nature12482

Michalski, J.R., Bleacher, J.E., 2014. Plains Style Caldera Complexes: Evidence for Ancient, Explosive Volcanism on Mars. AGU Fall Meeting Abstracts 33, P33E-03.

Michalski, J.R., Kraft, M.D., Diedrich, T., Sharp, T.G., Christensen, P.R., 2003. Thermal emission spectroscopy of the silica polymorphs and considerations for remote sensing of Mars. Geophysical Research Letters 30. https://doi.org/10.1029/2003GL018354

Michalski, J.R., Kraft, M.D., Sharp, T.G., Williams, L.B., Christensen, P.R., 2006. Emission spectroscopy of clay minerals and evidence for poorly crystalline aluminosilicates on Mars from Thermal Emission Spectrometer data. Journal of Geophysical Research: Planets 111. https://doi.org/10.1029/2005JE002438

Michalski, J.R., Kraft, M.D., Sharp, T.G., Williams, L.B., Christensen, P.R., 2005. Mineralogical constraints on the high-silica martian surface component observed by TES. Icarus 174, 161–177. https://doi.org/10.1016/j.icarus.2004.10.022

Moore, J.M., 1990. Nature of the mantling deposit in the heavily cratered terrain of northeastern Arabia, Mars. Journal of Geophysical Research: Solid Earth 95, 14279–14289. https://doi.org/10.1029/JB095iB09p14279

Moratto, Z.M., Broxton, M.J., Beyer, R.A., Lundy, M., Husmann, K., 2010. Ames Stereo Pipeline, NASA's Open Source Automated Stereogrammetry Software. Presented at the Lunar and Planetary Science Conference, p. 2364.

Moratto, Z.M., M.J. Broxton, R.A. Beyer, M. Lundy, K., 2010. HusmannAmes Stereo Pipeline, NASA's open source automated stereogrammetry software. Lunar Planet. Sci., 41, Article Abstract 2364. http://adsabs.harvard.edu/abs/2010LPI....41.2364M

Morgan, G.A., Head, J.W., 2009. Sinton crater, Mars: Evidence for impact into a plateau icefield and melting to produce valley networks at the Hesperian–Amazonian boundary. Icarus 202, 39–59. https://doi.org/10.1016/j.icarus.2009.02.025

Morschhauser, A., Lesur, V., Grott, M., 2014. A spherical harmonic model of the lithospheric magnetic field of Mars. Journal of Geophysical Research: Planets 119, 1162–1188. https://doi.org/10.1002/2013JE004555

Mouginis-Mark, P.J., Wilson, L., Zimbelman, J.R., 1988. Polygenic eruptions on Alba Patera, Mars. Bull Volcanol 50, 361–379. https://doi.org/10.1007/BF01050636

Murchie, S., Arvidson, R., Bedini, P., Beisser, K., Bibring, J.-P., Bishop, J., Boldt, J., Cavender, P., Choo, T., Clancy, R.T., Darlington, E.H., Marais, D.D., Espiritu, R., Fort, D., Green, R., Guinness, E., Hayes, J., Hash, C., Heffernan, K., Hemmler, J., Heyler, G., Humm, D., Hutcheson, J., Izenberg, N., Lee, R., Lees, J., Lohr, D., Malaret, E., Martin, T., McGovern, J.A., McGuire, P., Morris, R., Mustard, J., Pelkey, S., Rhodes, E., Robinson, M., Roush, T., Schaefer, E., Seagrave, G., Seelos, F., Silverglate, P., Slavney, S., Smith, M., Shyong, W.-J., Strohbehn, K., Taylor, H., Thompson, P., Tossman, B., Wirzburger, M., Wolff, M., 2007. Compact Reconnaissance Imaging Spectrometer for Mars (CRISM) on Mars Reconnaissance Orbiter (MRO). Journal of Geophysical Research: Planets 112. https://doi.org/10.1029/2006JE002682

Murphy, N. W., B. M. Jakosky, S. C. R. Rafkin, K. Larsen, N. E. Putzig, and M. T. Mellon., 2005. Thermophysical Properties of the Surface of Isidis Basin, Mars. Lunar Planet. Sci., 2005. Abstract 2218. https://www.lpi.usra.edu/meetings/lpsc2005/pdf/2218.pdf

Murphy, N.W., Jakosky, B.M., Rafkin, S.C., Larsen, K.W., Putzig, N.E., Mellon, M.T., 2007. Thermophysical properties of the Isidis basin, Mars. Journal of Geophysical Research: Planets 112. https://doi.org/10.1029/2005JE002586

Murphy, Nathaniel W., Bruce M. Jakosky, Scot C. Rafkin, Kristopher W. Larsen, Nathaniel E. Putzig, and Michael T. Mellon., 2007. Thermophysical Properties of the Isidis Basin, Mars. Journal of Geophysical Research: Planets 112 (E5):E05004. https://doi.org/10.1029/2005JE002586.

Mustard, J. F., B. L. Ehlmann, S. L. Murchie, F. Poulet, N. Mangold, J. W. Head, J.-P. Bibring, and L. H. Roach., 2009. Composition, Morphology, and Stratigraphy of Noachian Crust around the Isidis Basin. Journal of Geophysical Research: Planets 114 (E2):E00D12. https://doi.org/10.1029/2009JE003349.

Mustard, J.F., Cooper, C.D., 2005. Joint analysis of ISM and TES spectra: The utility of multiple wavelength regimes for Martian surface studies. Journal of Geophysical Research: Planets 110. https://doi.org/10.1029/2004JE002355

Mustard, J.F., Cooper, C.D., Rifkin, M.K., 2001. Evidence for recent climate change on Mars from the identification of youthful near-surface ground ice. Nature 412, 411. https://doi.org/10.1038/35086515

Neukum, G., R. Jaumann, HRSC Co-Investigator and Experiment Team., 2004. HRSC: The High-Resolution Stereo Camera of Mars Express. In A. Wilson (Ed.), Mars Express: The Scientific Payload, ESA, Noordwijk, The Netherlands (2004), pp. 17-35.

Nimmo, F., Tanaka, K., 2005. Early Crustal Evolution of Mars. Annual Review of Earth and Planetary Sciences 33, 133–161. https://doi.org/10.1146/annurev.earth.33.092203.122637

Ori, Gian Gabriele, Lucia Marinangeli, and Antonio Baliva., 2000. Terraces and Gilbert-Type Deltas in Crater Lakes in Ismenius Lacus and Memnonia (Mars). Journal of Geophysical Research: Planets 105 (E7):17629–41. https://doi.org/10.1029/1999JE001219.

Osinski, G.R., Tornabene, L.L., Grieve, R.A.F., 2011. Impact ejecta emplacement on terrestrial planets. Earth and Planetary Science Letters 310, 167–181. https://doi.org/10.1016/j.epsl.2011.08.012

Palluconi, F.D., Kieffer, H.H., 1981. Thermal inertia mapping of Mars from 60°S to 60°N. Icarus 45, 415–426. https://doi.org/10.1016/0019-1035(81)90044-0

Pelkey, S. M., J. F. Mustard, S. Murchie, R. T. Clancy, M. Wolff, M. Smith, R. Milliken, et al., 2007. CRISM Multispectral Summary Products: Parameterizing Mineral Diversity on Mars from Reflectance. Journal of Geophysical Research: Planets 112 (E8):E08S14. https://doi.org/10.1029/2006JE002831.

Pelkey, Shannon M, Bruce M Jakosky, and Philip R Christensen., 2003. Surficial Properties in Melas Chasma, Mars, from Mars Odyssey THEMIS Data. Icarus 165 (1):68–89. https://doi.org/10.1016/S0019-1035(03)00152-0.

Piqueux, S., Christensen, P.R., 2011. Temperature-dependent thermal inertia of homogeneous Martian regolith. Journal of Geophysical Research: Planets 116. https://doi.org/10.1029/2011JE003805

Plescia, J.B., Golombek, M.P., 1986. Origin of planetary wrinkle ridges based on the study of terrestrial analogs. GSA Bulletin 97, 1289–1299. https://doi.org/10.1130/0016-7606(1986)97<1289:OOPWRB>2.0.CO;2

Pont, S.C. du, Narteau, C., Gao, X., 2014. Two modes for dune orientation. Geology 42, 743–746. https://doi.org/10.1130/G35657.1

Presley, M.A., Christensen, P.R., 1997. Thermal conductivity measurements of particulate materials 1. A review. Journal of Geophysical Research: Planets 102, 6535–6549. https://doi.org/10.1029/96JE03302

Putzig, N.E., Barratt, E.M., Mellon, M.T., Michaels, T.I., 2013. MARSTHERM: A Web-based System Providing Thermophysical Analysis Tools for Mars Research Abstract P43C-2023. Poster presented at the AGU Fall Meeting in San Frnacisco, Decemeber 12. http://nathaniel.putzig.com/research/agu2013/Putzig_et_al_2013_AGU_abstract.pdf

Putzig, N.E., Barratt, E.M., Mellon, M.T., Michaels, T.I., 2013. MARSTHERM: A Web-based System Providing Thermophysical Analysis Tools for Mars Research. AGU Fall Meeting Abstracts 43, P43C-2023.

Putzig, N.E., Mellon, M.T., Herkenhoff, K.E., Phillips, R.J., Davis, B.J., Ewer, K.J., Bowers, L.M., 2014. Thermal behavior and ice-table depth within the north polar erg of Mars. Icarus, Third Planetary Dunes Systems 230, 64–76. https://doi.org/10.1016/j.icarus.2013.07.010

Putzig, N.E., Mellon, M.T., Kretke, K.A., Arvidson, R.E., 2005. Global thermal inertia and surface properties of Mars from the MGS mapping mission. Icarus 173, 325–341. https://doi.org/10.1016/j.icarus.2004.08.017

Putzig, Nathaniel E., and Michael T. Mellon., 2007. Apparent Thermal Inertia and the Surface Heterogeneity of Mars. Icarus 191 (1):68–94. https://doi.org/10.1016/j.icarus.2007.05.013.

Putzig, Nathaniel E., Michael T. Mellon, Katherine A. Kretke, and Raymond E. Arvidson., 2005. Global Thermal Inertia and Surface Properties of Mars from the MGS Mapping Mission. Icarus 173 (2):325–41. https://doi.org/10.1016/j.icarus.2004.08.017.

Putzig, Nathaniel E., Michael T. Mellon, Kenneth E. Herkenhoff, Roger J. Phillips, Brian J. Davis, Kenneth J. Ewer, and Lauren M. Bowers., 2014. Thermal Behavior and Ice-Table Depth within the North Polar Erg of Mars. Icarus, Third Planetary Dunes Systems, 230 (Supplement C):64–76. https://doi.org/10.1016/j.icarus.2013.07.010.

Quantin-Nataf, C., L. Lozac'h, P. Thollot, D. Loizeau, B. Bultel, J. Fernando, P. Allemand, et al., 2018. MarsSI: Martian Surface Data Processing Information System. Planetary and Space Science,

Enabling Open and Interoperable Access to Planetary Science and Heliophysics Databases and Tools, 150 (January): 157–70. https://doi.org/10.1016/j.pss.2017.09.014.

Quinn, D. P., and B. L. Ehlmann., 2014. Structural Constraints on the Origin of the Sulfate-Bearing Unit at Northeast Syrtis Major. In 8th International Conference on Mars, held July 14-18, 2014 in Pasadena, California. LPI Contribution No. 1791 (1437). http://adsabs.harvard.edu/abs/2014LPICo1791.1437Q.

Raitala, J., 1990. Wrinkle ridges on mars. Advances in Space Research 10, 71–73. https://doi.org/10.1016/0273-1177(90)90329-X

Ramirez, R.M., Kopparapu, R., Zugger, M.E., Robinson, T.D., Freedman, R., Kasting, J.F., 2014. Warming early Mars with CO_2 and H_2. Nature Geoscience 7, 59–63. https://doi.org/10.1038/ngeo2000

Ramsey, M.S., Christensen, P.R., 1998. Mineral abundance determination: Quantitative deconvolution of thermal emission spectra. Journal of Geophysical Research: Solid Earth 103, 577–596. https://doi.org/10.1029/97JB02784

Rangarajan, V.G., Bharti, R., Mondal, S.K., Pradhan, C., Dutta, S., 2018. Remote Sensing for Martian Studies: Inferences from Syrtis Major. J Indian Soc Remote Sens 46, 1537–1551. https://doi.org/10.1007/s12524-018-0826-7

Reimers, C.E., Komar, P.D., 1979. Evidence for explosive volcanic density currents on certain Martian volcanoes. Icarus 39, 88–110. https://doi.org/10.1016/0019-1035(79)90103-9

Robbins, S.J., Achille, G.D., Hynek, B.M., 2011. The volcanic history of Mars: High-resolution crater-based studies of the calderas of 20 volcanoes. Icarus 211, 1179–1203. https://doi.org/10.1016/j.icarus.2010.11.012

Robbins, S.J., Hynek, B.M., 2012a. A new global database of Mars impact craters ≥1 km: 1. Database creation, properties, and parameters. Journal of Geophysical Research: Planets 117. https://doi.org/10.1029/2011JE003966

Robbins, S.J., Hynek, B.M., 2012b. A new global database of Mars impact craters ≥1 km: 2. Global crater properties and regional variations of the simple-to-complex transition diameter. Journal of Geophysical Research: Planets 117. https://doi.org/10.1029/2011JE003967

Robbins, S.J., Hynek, B.M., 2013. Utility of laser altimeter and stereoscopic terrain models: Application to Martian craters. Planetary and Space Science 86, 57–65. https://doi.org/10.1016/j.pss.2013.06.019

Robinson, M.S., Mouginis-Mark, P.J., Zimbelman, J.R., Wu, S.S.C., Ablin, K.K., Howington-Kraus, A.E., 1993. Chronology, Eruption Duration, and Atmospheric Contribution of the Martian Volcano Apollinaris Patera. Icarus 104, 301–323. https://doi.org/10.1006/icar.1993.1103

Roda, M., Kleinhans, M.G., Zegers, T.E., Govers, R., 2016. Origin of circular collapsed landforms in the Chryse region of Mars. Icarus 265, 70–78. https://doi.org/10.1016/j.icarus.2015.10.020

Rodriguez, J.A.P., Sasaki, S., Kuzmin, R.O., Dohm, J.M., Tanaka, K.L., Miyamoto, H., Kurita, K., Komatsu, G., Fairén, A.G., Ferris, J.C., 2005. Outflow channel sources, reactivation, and chaos formation, Xanthe Terra, Mars. Icarus 175, 36–57. https://doi.org/10.1016/j.icarus.2004.10.025

Rogers, A. Deanne, and Joshua L. Bandfield. 2009. Mineralogical Characterization of Mars Science Laboratory Candidate Landing Sites from THEMIS and TES Data. Icarus 2 (203):437–53. https://doi.org/10.1016/j.icarus.2009.04.020.

Rogers, A.D., Aharonson, O., 2008. Mineralogical composition of sands in Meridiani Planum determined from Mars Exploration Rover data and comparison to orbital measurements. Journal of Geophysical Research: Planets 113. https://doi.org/10.1029/2007JE002995

Rogers, A.D., Bandfield, J.L., Christensen, P.R., 2007. Global spectral classification of Martian low-albedo regions with Mars Global Surveyor Thermal Emission Spectrometer (MGS-TES) data. Journal of Geophysical Research: Planets 112. https://doi.org/10.1029/2006JE002726

Rogers, A.D., Christensen, P.R., 2007. Surface mineralogy of Martian low-albedo regions from MGS-TES data: Implications for upper crustal evolution and surface alteration. Journal of Geophysical Research: Planets 112. https://doi.org/10.1029/2006JE002727

Rogers, A.D., Fergason, R.L., 2011. Regional-scale stratigraphy of surface units in Tyrrhena and Iapygia Terrae, Mars: Insights into highland crustal evolution and alteration history. Journal of Geophysical Research: Planets 116. https://doi.org/10.1029/2010JE003772

Ruff, S.W., 2004. Spectral evidence for zeolite in the dust on Mars. Icarus 168, 131–143. https://doi.org/10.1016/j.icarus.2003.11.003

Ruff, S.W., Christensen, P.R., Blaney, D.L., Farrand, W.H., Johnson, J.R., Michalski, J.R., Moersch, J.E., Wright, S.P., Squyres, S.W., 2006. The rocks of Gusev Crater as viewed by the Mini-TES instrument. Journal of Geophysical Research: Planets 111. https://doi.org/10.1029/2006JE002747

Ryan, C.H., Tornabene, L.L., Cannon, K.M., Mustard, J.F., Sapers, H.M., Osinski, G.R., 2017. Geomorphological Mapping of Hargraves Ejecta in the Nili Fossae Trough: Insight into Impact Processes at Potential Mars 2020 Landing Site. Presented at the Lunar and Planetary Science Conference, p. 2861.

Ryan, C.H., Tornabene, L.L., Osinski, G.R., Cannon, K.M., Mustard, J.F., MacRae, R.A., Corney, R., Sapers, H.M., 2016. Geomorphological Mapping of the Hargraves Ejecta and Polygonal Terrain Associated with the Candidate Mars 2020 Landing Site, Nili Fossae Trough. Presented at the Lunar and Planetary Science Conference, p. 2524.

Sagan, C., Veverka, J., Fox, P., Dubisch, R., Lederberg, J., Levinthal, E., Quam, L., Tucker, R., Pollack, J.B., Smith, B.A., 1972. Variable features on Mars: Preliminary mariner 9 television results. Icarus 17, 346–372. https://doi.org/10.1016/0019-1035(72)90005-X

Salamunićcar, G., Lončarić, S., Pina, P., Bandeira, L., Saraiva, J., 2011. MA130301GT catalogue of Martian impact craters and advanced evaluation of crater detection algorithms using diverse topography and image datasets. Planetary and Space Science 59, 111–131. https://doi.org/10.1016/j.pss.2010.11.003

Salvatore, M.R., Goudge, T.A., Bramble, M.S., Edwards, C.S., Bandfield, J.L., Amador, E.S., Mustard, J.F., Christensen, P.R., 2018. Bulk mineralogy of the NE Syrtis and Jezero crater regions of Mars derived through thermal infrared spectral analyses. Icarus 301, 76–96. https://doi.org/10.1016/j.icarus.2017.09.019

Salvatore, M.R., Kraft, M.D., Edwards, C.S., Christensen, P.R., 2016. The geologic history of Margaritifer basin, Mars. Journal of Geophysical Research: Planets 121, 273–295. https://doi.org/10.1002/2015JE004938

Salvatore, M.R., Mustard, J.F., Head, J.W., Rogers, A.D., Cooper, R.F., 2014. The dominance of cold and dry alteration processes on recent Mars, as revealed through pan-spectral orbital analyses. Earth and Planetary Science Letters 404, 261–272. https://doi.org/10.1016/j.epsl.2014.08.006

Salvatore, M.R., Mustard, J.F., Wyatt, M.B., Murchie, S.L., 2010. Definitive evidence of Hesperian basalt in Acidalia and Chryse planitiae. Journal of Geophysical Research: Planets 115. https://doi.org/10.1029/2009JE003519

Schon, Samuel C., James W. Head, and Caleb I. Fassett., 2012. An Overfilled Lacustrine System and Progradational Delta in Jezero Crater, Mars: Implications for Noachian Climate. Planetary and Space Science 67 (1):28–45. https://doi.org/10.1016/j.pss.2012.02.003.

Schultz, P.H., Lutz, A.B., 1988. Polar wandering of Mars. Icarus 73, 91–141. https://doi.org/10.1016/0019-1035(88)90087-5

Schultz, Richard A., and Herbert V. Frey., 1990. A New Survey of Multiring Impact Basins on Mars. Journal of Geophysical Research: Solid Earth 95 (B9):14175–89. https://doi.org/10.1029/JB095iB09p14175.

Scott, D.H., and Carr, M.H., (1978) Geologic map of Mars. USGS Miscellaneous Investigations Series, Map I-1083. https://www.usgs.gov/media/images/geologic-map-mars (accessed 4.11.19).

Seelos, F.P., IV, Arvidson, R.E., 2003. Bounded Variable Least Squares -- Application of a Constrained Optimization Algorithm to the Analysis of TES Emissivity Spectra. Presented at the Lunar and Planetary Science Conference.

Sefton-Nash, E., Teanby, N.A., Newman, C., Clancy, R.A., Richardson, M.I., 2014. Constraints on Mars' recent equatorial wind regimes from layered deposits and comparison with general circulation model results. Icarus, Third Planetary Dunes Systems 230, 81–95. https://doi.org/10.1016/j.icarus.2013.11.014

Segura, T.L., Toon, O.B., Colaprete, A., Zahnle, K., 2002. Environmental Effects of Large Impacts on Mars. Science 298, 1977–1980. https://doi.org/10.1126/science.1073586

Self, S., 2006. The effects and consequences of very large explosive volcanic eruptions. Philosophical Transactions of the Royal Society A: Mathematical, Physical and Engineering Sciences 364, 2073–2097. https://doi.org/10.1098/rsta.2006.1814

Sharp, R.P., 1973. Mars: Fretted and chaotic terrains. Journal of Geophysical Research (1896-1977) 78, 4073–4083. https://doi.org/10.1029/JB078i020p04073

Sholes, S.F., Chevrier, V.F., Tullis, J.A., 2013. Object based image analysis for remote sensing of planetary surfaces. 44th Lunar and Planetary Science Conference, Houston, Texas.

Silvestro, S., Di Achille, G., Ori, G.G., 2010. Dune morphology, sand transport pathways and possible source areas in east Thaumasia Region (Mars). Geomorphology, Planetary Dune Systems 121, 84–97. https://doi.org/10.1016/j.geomorph.2009.07.019

Silvestro, S., Vaz, D.A., Ewing, R.C., Rossi, A.P., Fenton, L.K., Michaels, T.I., Flahaut, J., Geissler, P.E., 2013. Pervasive aeolian activity along rover Curiosity's traverse in Gale Crater, Mars. Geology 41, 483–486. https://doi.org/10.1130/G34162.1

Sleep, N.H., 1994. Martian plate tectonics. Journal of Geophysical Research: Planets 99, 5639–5655. https://doi.org/10.1029/94JE00216

Smith, B.A., Soderblom, L.A., Banfield, D., Barnet, C., Basilevsky, A.T., Beebe, R.F., Bollinger, K., Boyce, J.M., Brahic, A., Briggs, G.A., Brown, R.H., Chyba, C., Collins, s A., Colvin, T., Cook, A.F., Crisp, D., Croft, S.K., Cruikshank, D., Cuzzi, J.N., Danielson, G.E., Davies, M.E., Jong, E.D., Dones, L., Godfrey, D., Goguen, J., Grenier, I., Haemmerle, V.R., Hammel, H., Hansen, c J., Helfenstein, c P., Howell, C., Hunt, G.E., Ingersoll, A.P., Johnson, T.V., Kargel, J., Kirk, R., Kuehn, D.I., Limaye, S., Masursky, H., McEwen, A., Morrison, D., Owen, T., Owen, W., Pollack, J.B., Porco, C.C., Rages, K., Rogers, P., Rudy, D., Sagan, C., Schwartz, J., Shoemaker, E.M., Showalter, M., Sicardy, B., Simonelli, D., Spencer, J., Sromovsky, L.A., Stoker, C., Strom, R.G., Suomi, V.E., Synott, S.P., Terrile, R.J., Thomas, P., Thompson, W.R., Verbiscer, A., Veverka, J., 1989. Voyager 2 at Neptune: Imaging Science Results. Science 246, 1422–1449. https://doi.org/10.1126/science.246.4936.1422

Smith, D.E., Zuber, M.T., Frey, H.V., Garvin, J.B., Head, J.W., Muhleman, D.O., Pettengill, G.H., Phillips, R.J., Solomon, S.C., Zwally, H.J., Banerdt, W.B., Duxbury, T.C., Golombek, M.P., Lemoine, F.G., Neumann, G.A., Rowlands, D.D., Aharonson, O., Ford, P.G., Ivanov, A.B., Johnson, C.L., McGovern, P.J., Abshire, J.B., Afzal, R.S., Sun, X., 2001. Mars Orbiter Laser

Altimeter: Experiment summary after the first year of global mapping of Mars. Journal of Geophysical Research 106, 23689–23722. https://doi.org/10.1029/2000JE001364
Smith, E.I., 1976. Comparison of the crater morphology-size relationship for Mars, Moon, and Mercury. Icarus 28, 543–550. https://doi.org/10.1016/0019-1035(76)90127-5
Smith, M.D., Bandfield, J.L., Christensen, P.R., 2000. Separation of atmospheric and surface spectral features in Mars Global Surveyor Thermal Emission Spectrometer (TES) spectra. Journal of Geophysical Research: Planets 105, 9589–9607. https://doi.org/10.1029/1999JE001105
Smith, M.R., Bandfield, J.L., Cloutis, E.A., Rice, M.S., 2013. Hydrated silica on Mars: Combined analysis with near-infrared and thermal-infrared spectroscopy. Icarus 223, 633–648. https://doi.org/10.1016/j.icarus.2013.01.024
Soare, R.J., Osinski, G.R., Roehm, C.L., 2008. Thermokarst lakes and ponds on Mars in the very recent (late Amazonian) past. Earth and Planetary Science Letters 272, 382–393. https://doi.org/10.1016/j.epsl.2008.05.010
Strahler, A.H., Woodcock, C.E., Smith, J.A., 1986. On the nature of models in remote sensing. Remote Sensing of Environment 20, 121–139. https://doi.org/10.1016/0034-4257(86)90018-0
Tanaka, K.L., 1986. The stratigraphy of Mars. Proceedings of Lunar Planetary Science Conference, 17th, Part 1. Journal of Geophysical Research, 91, supplemental, E139-E158.
Tanaka, K.L., 2000. Dust and Ice Deposition in the Martian Geologic Record. Icarus 144, 254–266. https://doi.org/10.1006/icar.1999.6297
Tanaka, K.L., Scott, D.H., Greeley, R., 1992. Global Stratigraphy. Mars, edited by H.H. Hieffer et al., pp. 345-382, University of Arizona Press, Tuscon.
Tanaka, K.L., Skinner, J.A., Hare, T.M., Joyal, T., Wenker, A., 2003. Resurfacing history of the northern plains of Mars based on geologic mapping of Mars Global Surveyor data. Journal of Geophysical Research: Planets 108. https://doi.org/10.1029/2002JE001908
Tanaka, K.L., Skinner, J.A., Jr., Dohm, J.M., Irwin, R.P., III, Kolb, E.J., Fortezzo, C.M., Platz, T., Michael, G.G., and Hare, T.M., 2014, Geologic map of Mars: U.S. Geological Survey Scientific Investigations Map 3292, scale 1:20,000,000, pamphlet 43 p., https://dx.doi.org/10.3133/sim3292.
Telfer, M.W., Parteli, E.J.R., Radebaugh, J., Beyer, R.A., Bertrand, T., Forget, F., Nimmo, F., Grundy, W.M., Moore, J.M., Stern, S.A., Spencer, J., Lauer, T.R., Earle, A.M., Binzel, R.P., Weaver, H.A., Olkin, C.B., Young, L.A., Ennico, K., Runyon, K., The New Horizons Geology, G. and I.S.T.T., 2018. Dunes on Pluto. Science 360, 992–997. https://doi.org/10.1126/science.aao2975
THEMIS User Guide, 2006. Thermal Emission Imaging System 2001 Mars Odyssey: Themis Geometric Processing User's Guide. Last Accessed May 23, 2019. Available at https://static.mars.asu.edu/pds/ODTGEO_v2/document/geometry.pdf
Thomson, J.L., Salisbury, J.W., 1993. The mid-infrared reflectance of mineral mixtures (7–14 μm). Remote Sensing of Environment 45, 1–13. https://doi.org/10.1016/0034-4257(93)90077-B
Tizzani, P., Berardino, P., Casu, F., Euillades, P., Manzo, M., Ricciardi, G.P., Zeni, G., Lanari, R., 2007. Surface deformation of Long Valley caldera and Mono Basin, California, investigated with the SBAS-InSAR approach. Remote Sensing of Environment 108, 277–289. https://doi.org/10.1016/j.rse.2006.11.015
Toon, O.B., Segura, T., Zahnle, K., 2010. The Formation of Martian River Valleys by Impacts. Annual Review of Earth and Planetary Sciences 38, 303–322. https://doi.org/10.1146/annurev-earth-040809-152354
Tzotsos, A., Argialas, D., 2008. Support Vector Machine Classification for Object-Based Image Analysis, in: Object-Based Image Analysis, Lecture Notes in Geoinformation and

Cartography. Springer, Berlin, Heidelberg, pp. 663–677. https://doi.org/10.1007/978-3-540-77058-9_36

Vaz, D.A., Sarmento, P.T.K., Barata, M.T., Fenton, L.K., Michaels, T.I., 2015. Object-based Dune Analysis: Automated dune mapping and pattern characterization for Ganges Chasma and Gale crater, Mars. Geomorphology 250, 128–139. https://doi.org/10.1016/j.geomorph.2015.08.021

Vaz, D.A., Silvestro, S., 2014. Mapping and characterization of small-scale aeolian structures on Mars: An example from the MSL landing site in Gale Crater. Icarus, Third Planetary Dunes Systems 230, 151–161. https://doi.org/10.1016/j.icarus.2013.08.007

Vergniolle, S., Jaupart, C., 1986. Separated two-phase flow and basaltic eruptions. Journal of Geophysical Research: Solid Earth 91, 12842–12860. https://doi.org/10.1029/JB091iB12p12842

Vincent, R.K., Thomson, F., 1972. Spectral compositional imaging of silicate rocks. Journal of Geophysical Research 77, 2465–2472. https://doi.org/10.1029/JB077i014p02465

Viviano-Beck, C. E., S. L. Murchie, A. W. Beck, and J. M. Dohm., 2017. Compositional and Structural Constraints on the Geologic History of Eastern Tharsis Rise, Mars. Icarus 284 (Supplement C):43–58. https://doi.org/10.1016/j.icarus.2016.09.005.

Viviano-Beck, C.E., Seelos, F.P., Murchie, S.L., Kahn, E.G., Seelos, K.D., Taylor, H.W., Taylor, K., Ehlmann, B.L., Wiseman, S.M., Mustard, J.F., Morgan, M.F., 2014. Revised CRISM spectral parameters and summary products based on the currently detected mineral diversity on Mars. Journal of Geophysical Research: Planets 119, 1403–1431. https://doi.org/10.1002/2014JE004627

Walter, L.S., Salisbury, J.W., 1989. Spectral characterization of igneous rocks in the 8- to 12-μm region. Journal of Geophysical Research: Solid Earth 94, 9203–9213. https://doi.org/10.1029/JB094iB07p09203

Ward, A.W., Doyle, K.B., Helm, P.J., Weisman, M.K., Witbeck, N.E., 1985. Global map of eolian features on Mars. Journal of Geophysical Research 90, 19.

Watters, T.R., 1988. Wrinkle ridge assemblages on the terrestrial planets. Journal of Geophysical Research: Solid Earth 93, 10236–10254. https://doi.org/10.1029/JB093iB09p10236

Watters, T.R., 1993. Compressional tectonism on Mars. Journal of Geophysical Research: Planets 98, 17049–17060. https://doi.org/10.1029/93JE01138

Wenk, H.-R., Bulakh, A., 2016. Minerals: Their Constitution and Origin, 2 edition. ed. Cambridge University Press, Cambridge.

Wichman, R.W., Schultz, P.H., 1989. Sequence and mechanisms of deformation around the Hellas and Isidis Impact Basins on Mars. Journal of Geophysical Research 94, 17333. https://doi.org/10.1029/JB094iB12p17333

Wilhelms, D.E., Baldwin, R.J., 1989. The role of igneous sills in shaping the Martian uplands. Presented at the Lunar and Planetary Science Conference Proceedings, pp. 355–365.

Wilkes, C.A., 2014. Evidence for a Possible Supervolcano on Mars at Siloe Patera. Unpublished MS Thesis, Auburn University, Auburn, Alabama, USA

Wilkes, C.A., King, Jr., D.T., Wright, S.P., 2013. Investigation of Siloe Patera and the Surrounding Area: Possible Evidence of an Ancient Volcanic Caldera on Mars. Lunar and Planetary Science Meeting Abstracts 3034.

Williams, R.M.E., Moersch, J.E., Fergason, R.L., 2018. Thermophysical Properties of Martian Fluvial Sinuous Ridges: Inferences on 'Inverted Channel' Induration Agent. Earth and Space Science 0. https://doi.org/10.1029/2018EA000402

Wilson, S.A., Howard, A.D., Moore, J.M., Grant, J.A., 2016. A cold-wet middle-latitude environment on Mars during the Hesperian-Amazonian transition: Evidence from northern Arabia valleys and paleolakes. Journal of Geophysical Research: Planets 121, 1667–1694. https://doi.org/10.1002/2016JE005052

Wilson, S.A., Zimbelman, J.R., 2004. Latitude-dependent nature and physical characteristics of transverse aeolian ridges on Mars. Journal of Geophysical Research: Planets 109, E10. https://doi.org/10.1029/2004JE002247

Wyatt, M.B., Hamilton, V.E., McSween, H.Y., Christensen, P.R., Taylor, L.A., 2001. Analysis of terrestrial and Martian volcanic compositions using thermal emission spectroscopy: 1. Determination of mineralogy, chemistry, and classification strategies. Journal of Geophysical Research: Planets 106, 14711–14732. https://doi.org/10.1029/2000JE001356

Yu, X., Hörst, S.M., He, C., McGuiggan, P., Crawford, B., 2018. Where Does Titan Sand Come From: Insight From Mechanical Properties of Titan Sand Candidates. Journal of Geophysical Research: Planets 123, 2310–2321. https://doi.org/10.1029/2018JE005651

Zabrusky, K., Andrews-Hanna, J.C., Wiseman, S.M., 2012. Reconstructing the distribution and depositional history of the sedimentary deposits of Arabia Terra, Mars. Icarus 220, 311–330. https://doi.org/10.1016/j.icarus.2012.05.007

Zimbelman, J.R., Clifford, S.M., Williams, S.H., 1989. Concentric crater fill on Mars - an aeolian alternative to ice-rich mass wasting. Presented at the Lunar and Planetary Science Conference Proceedings, pp. 397–407.

Zuber, M.T., 2001. The crust and mantle of Mars. Nature 412(6843), 220–227. https://doi.org/10.1038/35084163

Zubrin, Robert, and Richard Wagner., 1997. The Case for Mars: The Plan to Settle the Red Planet and Why We Must. New York: Touchstone.

Zurek, R.W., Smrekar, S.E., 2007. An overview of the Mars Reconnaissance Orbiter (MRO) science mission. Journal of Geophysical Research: Planets 112. https://doi.org/10.1029/2006JE002701